ELECTROCATALYSIS IN ALKALINE MEDIA AND ANION EXCHANGE MEMBRANES FOR ALKALINE FUEL CELLS

A Dissertation

Presented to the Faculty of the Graduate School

of Cornell University

In Partial Fulfillment of the Requirements for the Degree of

Doctor of Philosophy

by

Jimmy John

August 2013

ELECTROCATALYSIS IN ALKALINE MEDIA AND ANION EXCHANGE MEMBRANES FOR ALKALINE FUEL CELLS

Jimmy John, Ph.D.

Cornell University 2013

The central theme of this thesis is the investigations of fundamental processes of relevance to the operation of fuel cells in alkaline media. In this respect, broadly speaking, aspects of electrocatalysis in alkaline media and phenomena active in hydroxide-conducting anion exchange membranes were explored.

Specifically, the electrocatalytic oxidation of formate on platinum in alkaline media was examined in detail. Results from a suite of electrochemical measurements, complemented with in situ mass-spectrometric measurements in the form of differential electrochemical mass spectrometry (DEMS), revealed a highly adsorbate-mediated reaction mechanism of formate oxidation. In a comparative analysis of results, the relative inactivity of formate towards oxidation, vis-à-vis formic acid in acidic media, is inferred to be due to the slow kinetics associated with the rate-determining steps of the formation of an electro-active adsorbate from formate and its subsequent oxidation. This mechanistic study is detailed in Chapter 3.

A prototypical quaternary-ammonium based anion exchange membrane material was the subject of electroanalytical investigations into the processes relevant to the application of anion exchange membranes in fuel cells. The uptake of carbonate ions, and any subsequent carbonate precipitation in the membrane, was studied using the electrochemical quartz crystal microbalance (EQCM) technique. The EQCM studies demonstrated reversible carbonate and formate (produced simultaneously with carbonate by the oxidation of methanol) exchange in the membrane. The studies, further, established that the membranes exhibit a finite capacity of carbonate/formate uptake which would preclude any precipitation. On an associated aspect, acoustic impedance measurements showed the membranes to undergo swelling on hydration. Further, during the EQCM measurements, the extent of swelling in the membrane changed

dynamically in response to the electrochemically driven anion exchange process in the membrane. The results from these studies are documented in Chapter 4.

Physical and charge transport in the membrane were probed by employing redox active molecules which are neutral and negatively charged, respectively, and the applicable transport mechanisms inferred from the electrochemical studies. Preliminary results from ex-situ microscopic/spectroscopic studies targeting a more detailed physicochemical understanding of the membrane phenomena are also documented. These studies are intended to be a prelude to a comprehensive in situ characterization of the membrane in the future that will be needed to critically address the form-function relationships in these material systems. The transport and the ex-situ studies form the subject matter of Chapter 5.

As for the methodologies employed in this work, the theoretical and the experimental aspects of the DEMS and the EQCM techniques are presented in Chapter 2. On a related note, the development of advanced in situ FTIR setups is described in Chapter 6. The preliminary testing of these setups is also reported. It is expected that, in the future, these advanced spectroscopic tools would be an invaluable aid in examining electrochemical interfaces. The final chapter deals with the rotating disc electrode voltammteric studies of the oxidation of hydrogen in the presence of carbon monoxide on platinum lead (PtPb) intermetallic in acidic media. This study was motivated by the promising electrocatalytic activity of the PtPb intermetallic for formic acid and methanol oxidation in acidic media.

BIOGRAPHICAL SKETCH

The author hails from the city of Thiruvananthapuram in the southern Indian state of Kerala. He pursued the integrated Master's degree in chemistry at Indian Institute of Technology in Kanpur (IIT-K) starting 2003. The summer research internships he did at McMaster University, Canada (2006) under Prof. Gillian Goward studying metal organic frameworks for hydrogen storage and at National University of Singapore, Singapore (2007) under Prof. B.V.R. Chowdari exploring lithium-ion batteries were invaluable in exposing him to the field of electrochemical energy research. He graduated from IIT-K in 2008. Fuel cells, in particular, captured his attention and he had the wonderful opportunity to pursue graduate research in the same area when he joined the laboratory of Prof. Héctor D. Abruña in the Department of Chemistry and Chemical Biology at Cornell University in 2008. He received his Ph.D. in August 2013. Since the time he was introduced to it in Prof. Abruña's laboratory, he has been fascinated by electrochemistry and he hopes to remain a life-long student of the subject.

ACKNOWLEDGMENTS

I will be forever grateful to Prof. Héctor D. Abruña for having me in his laboratory. Through his teaching and mentoring, I was introduced to the perennially fascinating world of electrochemistry. He has been a great source of encouragement and support throughout my graduate career at Cornell. I also greatly appreciate the freedom he has given me in pursuing my research ideas and fostering my growth as a researcher. Time and again, his professional advice has helped me move forward in my Ph.D. I am also deeply indebted to him for facilitating career opportunities for me. Not to forget, I would also like to thank him for throwing the best summer parties at his house!

It was a pleasure to have as my special committee members Prof. Francis J. DiSalvo and Prof. Richard G. Hennig. They have provided me with wonderful support and advice in my graduate research. Invariably, I have come out of discussions with them with new insights on my research. I am fortunate to have had the opportunity to learn from their tremendous knowledge and experience. I would also like to acknowledge the whole-hearted support that I received from Prof. Geoffrey W. Coates on the anion exchange membrane project.

Dr. Hongsen Wang and Dr. Eric D. Rus have been such amazing mentors to me in the Abruña lab and for that I cannot thank them enough. I believe, as a budding researcher, I have greatly benefited from the uncompromising scientific rigor and the decisiveness they exercise in both experiments and analysis; not to speak of their incredible research skills.

I was fortunate to have as my collaborator in the anion exchange membrane project Kristina from the Coates group. She was very accommodating of my requests for samples and patiently answered my innumerable questions on polymer chemistry. I am really grateful to her for all the wonderful help she extended to the membrane project over the past few years. I would also like to acknowledge the efforts of Dr. Henry A. Kostalik IV from the Coates group, who initiated me to the membrane project.

The ex-situ TEM studies of the membrane material would not have been possible without the help of Alex (Yingchao Yu) who was kind enough to examine the samples under the

microscope. Suggestions from Dr. Teressa Porri at Nanobiotechnology Center (NBTC) were very useful in optimizing the spin-coating of the membrane material onto electrodes. I would also like to thank Dr. Jonathan Shu and Dr. Steve Kriske at Cornell Center for Materials Research (CCMR) for their assistance in using the facility equipments.

I found extremely patient and supportive senior researchers in Dr. Dave Finkelstein and Dr. Michele Tague as I was learning the ropes in the Abruña lab. Dr. Finkelstein taught me the highly useful technique of rotating disc electrode voltammetry; while, Dr. Tague showed me how to operate the electrochemical quartz crystal microbalance setup. I would also like to thank all the Abruña group members – both past and present – for making it such a joy to work in the lab. In particular, I would like to thank Nicole Ritzert for extending an inexhaustible amount of help around in the lab to the group members.

Suzanne at Energy Materials Center at Cornell (EMC2) has been such a great resource for graduate students at the center. I would like to thank her for efficiently processing all my center-related travel and equipment acquisition requests. Pat, in her capacity as the graduate field coordinator, has been an indispensable part of my graduate life at Cornell helping me keep track of and meet the department and the graduate school requirements as I worked towards my Ph. D. degree. I also appreciate the help from Kelly at the Abruña lab in placing orders through e-shop.

I was fortunate to have such wonderful friends and colleagues in Dr. Amrita Haldar, Dr. Hoang Van Le, Dr. Joanna Tan, Dr. Sean Conte and Dr. Swapna Lekkala. They have made my stay at Cornell a memorable experience with their delightful company and selfless support. In particular, Amrita and Hoang are amazing human beings whom I greatly respect and admire.

Even outside Cornell, there have been so many wonderful people in my life whose support, advice and friendship I would like to gratefully acknowledge – my parents who have always supported me, my wonderful sister – Julie –who always had my back and whom I greatly admire, my brother-in-law – Jubin – for all his help, advice and support during my stay here in the United States. Allen, my wonderful nephew of five years old, is a source of joy, amazement and pride for me as I see him grow up. I would also like to thank my relatives at Corning, NY –

the family of Dr. Sam George – for all the invaluable help and support over the past few years. The visits to Corning helped me not miss my home too much. My childhood friends – Rameez and Tony – have always been very understanding and supportive of my career goals. I would like to thank them for being always there for me.

I also met many amazing people when I was at IIT-K. I am glad to have found such good friends as Dr. Karthik Uppulury and Satish during my stay there. Among the teachers at IIT-K, I would like to specially mention Prof. Pinaki Gupta-Bhaya who is an amazing person and an extraordinary teacher. I still remember the excitement that I felt listening to him explain the laws of thermodynamics in his sophomore physical chemistry class. I appreciate the support and the encouragement of my undergraduate thesis advisor, Prof. S. Sundar Manoharan. I am thankful to him for giving me the opportunity to work in his research lab. I would also like to thank Prof. Gillian Goward, McMaster University, Canada and Prof. B.V.R. Chowdari, NUS, Singapore for giving me the opportunities to engage in summer undergraduate research.

Last but not the least I would like to acknowledge the funding sources and the Cornell facilities – the Department of Chemistry and Chemical Biology at Cornell University for the teaching assistantship, EMC2 for the research assistantship, the International Precious Metal Institute for the very generous graduate research award, NBTC and CCMR at Cornell for access to the various fabrication and characterization tools. This material is based upon work supported as part of the Energy Materials Center at Cornell (EMC^2), an Energy Frontier Research Center funded by the U.S. Department of Energy, Office of Science, Office of Basic Energy Sciences under Award Number DE-SC0001086. This work made use of the Nanobiotechnology Center shared research facilities at Cornell. This work made use of the Cornell Center for Materials Research Shared Facilities which are supported through the NSF MRSEC program (DMR-1120296).

TABLE OF CONTENTS

LIST OF FIGURES

Chapter 1: Introduction

Chapter 2: Methodology

Chapter 3: Formate electro-oxidation on Pt in alkaline media

LIST OF TABLES

LIST OF ABBREVIATIONS

(A)AEM	(alkaline) anion exchange membrane
ADC	analog-to-digital converter
AFC	alkaline fuel cell
BVD	Butterworth-Van-Dyke
CCM	catalyst coated membrane
CV	cyclic voltammetry
DEMS	differential electrochemical mass spectrometry
DI	de-ionized
DPSCC	double potential step chronocoulometry
ECSA	electrochemical surface area
EDX	energy-dispersive X-ray spectroscopy
FTIR	Fourier transform infrared spectroscopy
HAADF	high-angle annular dark-field imaging
HOR	hydrogen oxidation reaction
H.P.	high pass (filter)
ICE	internal combustion engine
IEC	ion-exchange capacity
IR	infrared
IRRAS	infrared reflection absorption spectroscopy
L.P.	low pass (filter)
MCT	mercury-cadmium-telluride
MEA	membrane electrode assembly
MSCV	mass-spectrometric cyclic voltammogram
ORR	oxygen reduction reaction
PDS	potential difference spectrum
PEM	proton exchange membrane
PEM	photoelastic modulator
PM-IRRAS	polarization-modulation infrared reflection absorption spectroscopy
RDE	rotating disc electrode
RHE	reversible hydrogen electrode
SEM	secondary electron multiplier
SNR	signal-to-noise ratio
SOM	small organic molecule
SPE	solid polymer electrolyte
STEM	scanning transmission electron microscopy
TEM	transmission electron microscopy
TMPD	N,N,N′,N′-tetramethyl-p-phenylenediamine

CHAPTER 1
INTRODUCTION

1.1 Motivation

In recent years, there has been a global impetus to promote sustainable energy use in all aspects of human living. A major focus of this effort has been the electrification of transport that can, in conjunction with sustainable methods of electricity generation, redress the deleterious environmental impact of the fossil-fuel powered vehicles currently in use. In terms of research and development, three categories of alternative energy conversion/storage systems are currently being evaluated viz. low temperature (< 100 °C) fuel cells, rechargeable batteries and supercapacitors. Simplified operation schemes of each of these systems are shown in Figure 1.1 and Figure 1.2.

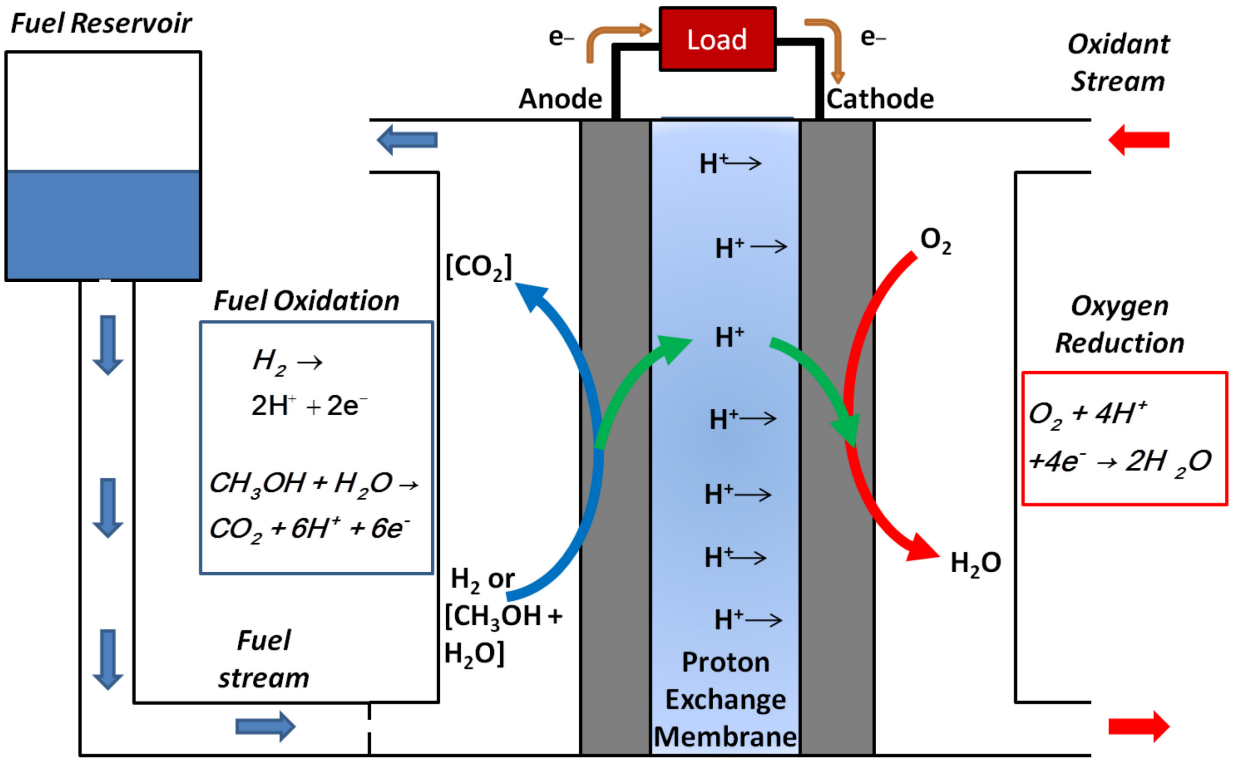

Figure 1.1: Schematic of a proton exchange membrane fuel cell (PEMFC).

Fuel cell is an energy conversion device where the chemical energy stored in the fuel (typically hydrogen and small organic molecules) and the oxidant (generally air or oxygen) are converted into electrical energy for immediate use (see Figure 1.1). Rechargeable batteries and supercapacitors are energy storage systems. The former converts the chemical energy stored during the charging process into current in the external circuit via electrochemical reactions (see Figure 1.2a). Supercapacitors store the electrical energy supplied during the charging process either electrochemically (akin to batteries) or electrostatically by charge separation (see Figure 1.2b) or by both methods (as in pseudocapacitors).

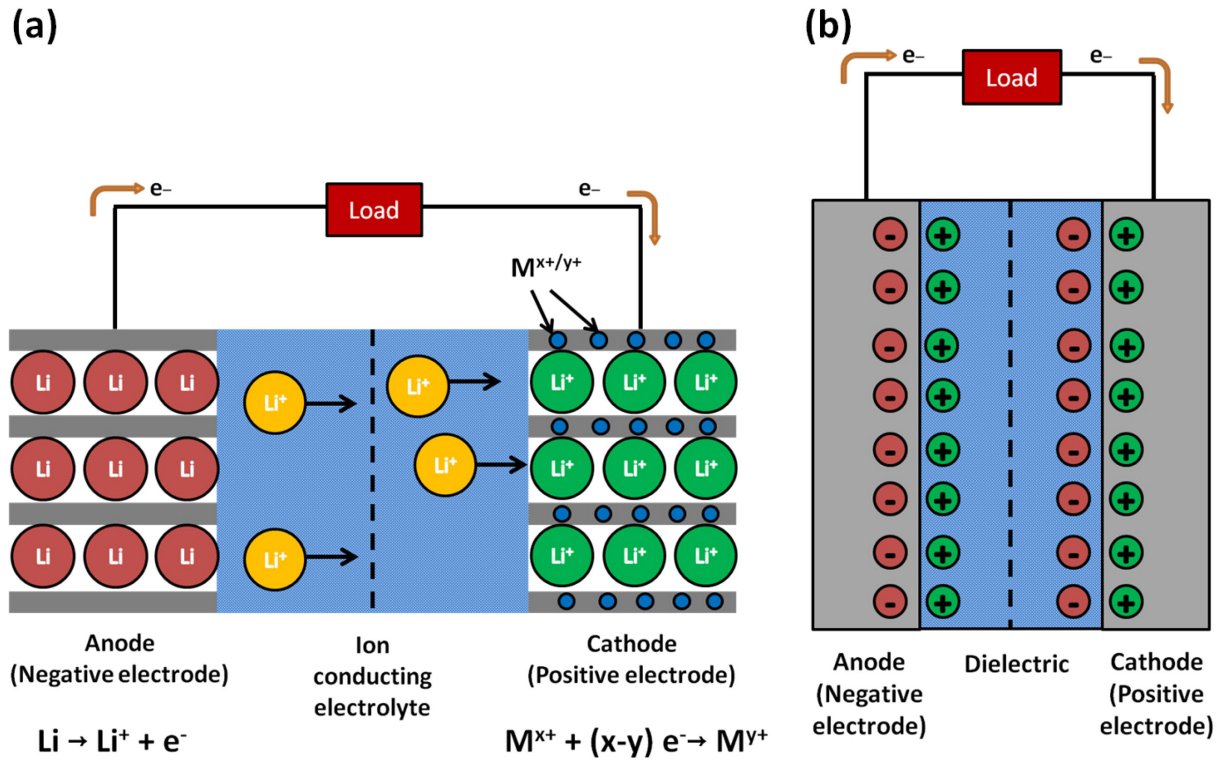

Figure 1.2: Operational scheme of (a) Li-ion rechargeable cell and (b) capacitor showing the discharge process. In (a) **M** represents an electroactive motif that undergoes changes in its oxidation state during the charge/discharge process.

The fuel cells can be operated at either high temperature (200-900 °C) or low temperature (60-90 °C) regimes depending on the application space. The proton exchange membrane fuel cell

(PEMFC) shown in Figure 1.1 is an example of a low-temperature fuel cell. High temperature fuel cells are employed to meet stationary energy demands and low temperature fuel cells are being researched and developed for transportation and portable applications. The latter systems have been specifically targeted for deployment in automobiles[1–3] and form the broad motivational basis for the research presented in this thesis.

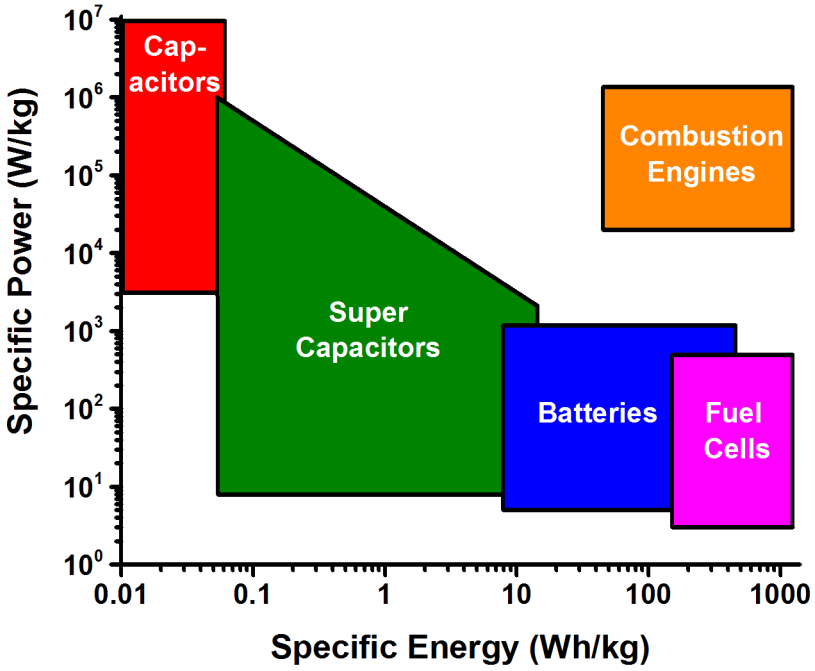

Figure 1.3: Ragone plot showing the performance regimes of common energy conversion / storage systems (based on the values from ref. [1]).

Electrification of transportation presents a unique combination of recharging, power and energy demands due to the general expectation that an automobile can (1) be driven as desired, (2) travel far and fast as needed, and (3) be recharged quickly. The power and energy demands that can be met by the three energy systems introduced above, in comparison to the internal combustion engines (ICE) currently in use, are shown in the so-called Ragone plot (Figure 1.3).[1] It should be noted that, in a sense, higher values of specific power and specific energy of a particular energy system represent the ability of an automobile utilizing that particular energy

system to go faster and farther, respectively. It is clear from the Ragone plot that, as it stands currently, there is no one alternative energy system that alone can deliver the performance of an ICE. In fact, the alternative energy systems, as of now, occupy zones in the power-energy space that are more or less mutually exclusive. However, it should be pointed out that, unlike the ICEs, the alternative energy systems are not limited by the Carnot cycle and hence, their efficiencies can be much higher.

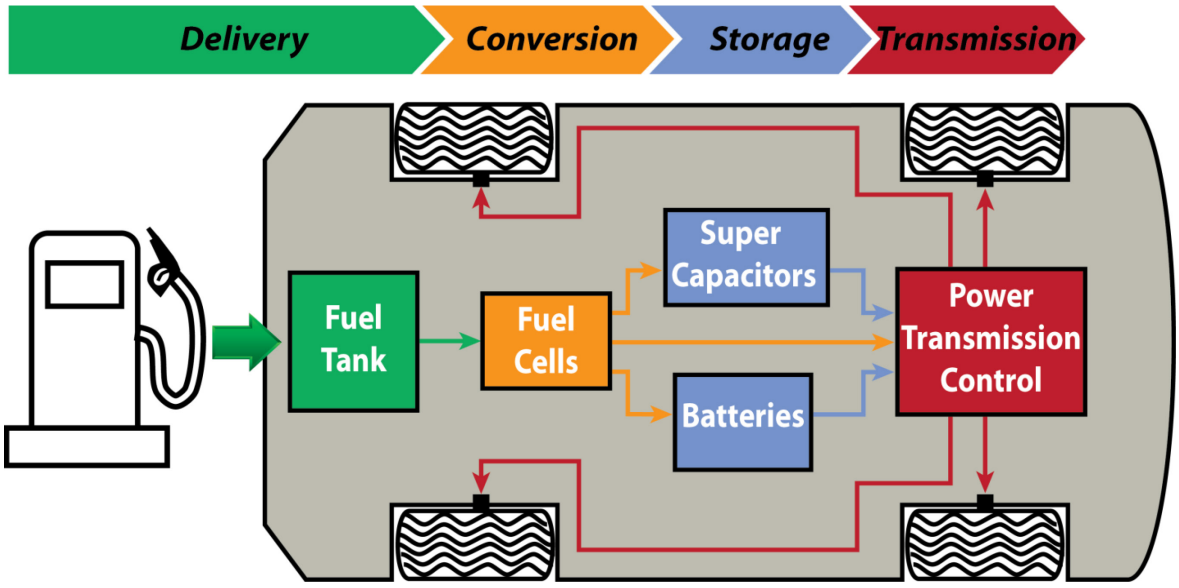

Figure 1.4: A hypothetical scheme for automobile electrification depicting the layout of the various energy devices on the chassis of the vehicle.

Fuel cells can have specific energy values comparable to that of ICEs but low power rating. The reverse is true for capacitors and, to a large extent, for supercapacitors. Rechargeable batteries straddle the two performance regimes of fuel cells and supercapacitors. Given this current alternative energy landscape for electrification of automobiles, a synergetic drive system drawing upon the intrinsic advantages of each energy system seems to be inevitable. A hypothetical scheme for automobile electrification is depicted in Figure 1.4 where, in general, fuel cells due to their higher specific energy values can provide the extended range while

batteries and supercapacitors can meet the power demands associated with acceleration and maintaining high speeds.

A fuel cell, due to its operational paradigm, is uniquely suited to be deployed at the top of the process-flow for the automobile electrification scheme. In a fuel cell system, the energy storage is decoupled from the energy conversion process. It should be remembered that a fuel cell is a thermodynamically open system whereas batteries and supercapacitors are closed systems. For a fuel cell system, the process of storing energy is just the replenishment of the fuel tank with fuel while the energy conversion occurs in the fuel cell itself. Hence, the use of fuel cells affords two important advantages vis-à-vis batteries and supercapacitors: (1) fast recharging (refueling) times (< 5min) and (2) enhanced range (~ 300 mi) comparable to ICE-powered cars.[2] Another desirable aspect of a fuel cell, which it shares with the ICE, is the independence from the electricity grid due to the use of fuels as energy carriers. In all of these respects, leveraging the shared operational features of fuel cells with the ICEs in the automobile electrification scheme represents an easier and logical technology transition from fossil-fuel powered automobiles to sustainable electric vehicles. Of course, as mentioned earlier, this approach envisages the incorporation of batteries and supercapacitors into the electrical drive system that can handle dynamic power demands while fuel cells act to provide the primary electrical energy.

1.2 Alkaline Fuel Cells

1.2.1 Introduction

The low temperature fuel cells are generally classified into two major subtypes based on the mobile ions in the electrolyte medium that are integral to the electrode reactions. There are acidic fuel cells where H^+ are the mobile species and alkaline fuel cells (AFCs) where OH^- are more often than not the ionic species of interest. Historically, AFCs employing a liquid

electrolyte, called the traditional AFCs, were the first to be deployed in a practical application (Figure 1.5). The famous Apollo series of space missions utilized AFCs for energy generation from on-board H_2 and O_2 supplies.[4] H_2O generated at the anode was also recovered for further use. The AFCs used in these space missions had some of the highest power densities reported (> 5 W/cm^2) so far for any fuel cell system.[5] For traditional AFCs, the liquid electrolyte is saturated KOH solution in a porous matrix such as the asbestos separator employed in Apollo missions.

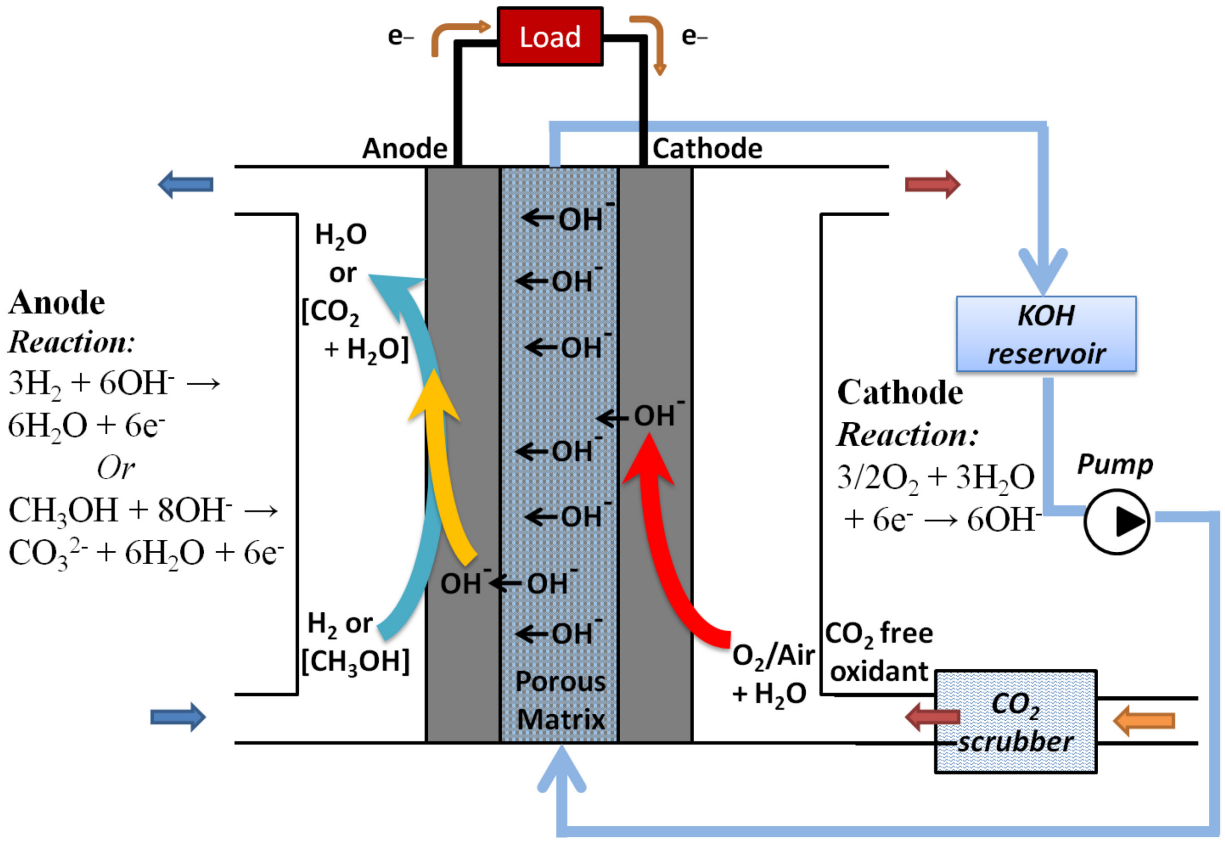

Figure 1.5: Schematic of a traditional liquid electrolyte alkaline fuel cell.

Early in the development of AFCs, it was realized that, due to the alkaline operating conditions, the electrolyte contamination by CO_2 in the feed streams was going to be an issue. This is the so-called 'carbonation' phenomenon (Figure 1.6) by which CO_2 dissolved in the liquid electrolyte is converted into CO_3^{2-} (Equation 1.1) and, over time, precipitates out as the

carbonate salt (Equation 1.2). The precipitate blocks ion conduction pathways in the porous matrix and leads to eventual device failure.

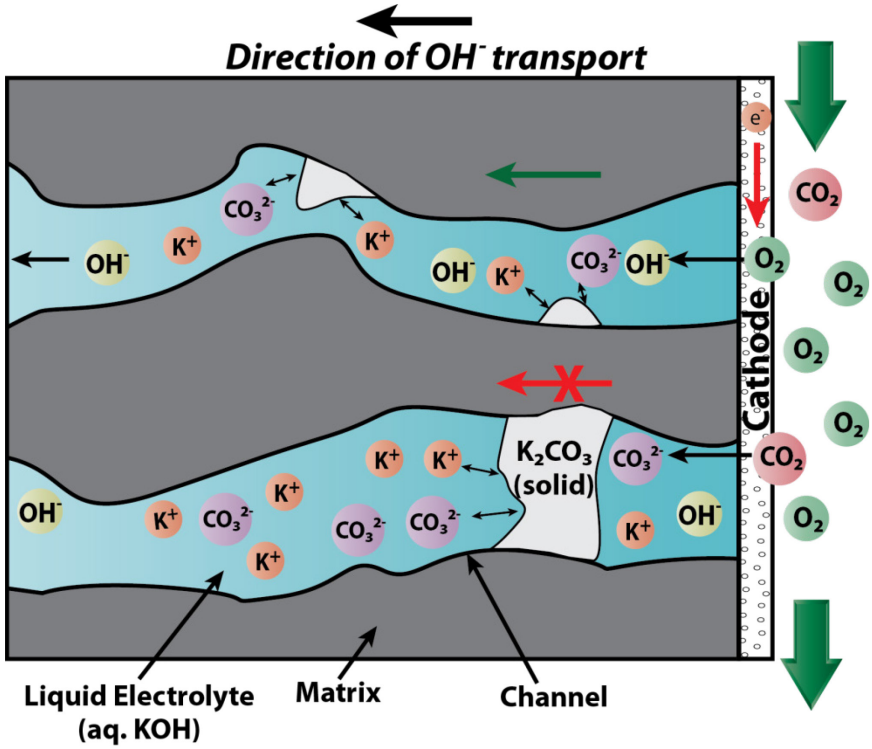

Figure 1.6: Depiction of carbonation phenomenon in a traditional liquid electrolyte AFC.

Equation 1.1: $$CO_{2(aq)} + 2OH^{-}_{(aq)} \rightarrow CO^{2-}_{3(aq)} + H_2O$$

Equation 1.2: $$2K^{+}_{(aq)} + CO^{2-}_{3(aq)} \rightarrow K_2CO_3 \downarrow$$

It is evident why the traditional AFCs were so successfully employed in the space missions where highly pure gases were used and the environmental conditions were strictly regulated. For terrestrial usage, AFCs became less attractive due to the carbonation issue. The workarounds included circulating the liquid electrolyte to prevent buildup of carbonate precipitate and passing the gas feed streams through CO_2 scrubbers to remove CO_2 (Figure 1.5). However, with the development of proton exchange membranes (PEM) such as the highly successful Nafion, compact all solid-state devices could be realized; albeit under acidic operating conditions. Hence, over the last few decades, research and development of fuel cells have

concentrated heavily on PEMFCs and the latter have attained high technological maturity. Meanwhile, the traditional AFCs, due to the complexity associated with their terrestrial operation, lost mainstream interest in the fuel cell community.

1.2.2 Electrocatalysis in Alkaline Media

The phenomenon that lies at the heart of a fuel cell operation is the electrocatalysis of the electrode reactions (Figure 1.7). Traditionally, Pt is used as electrocatalyst to drive both fuel oxidation at the anode and oxygen reduction at the cathode. On Pt, hydrogen oxidation is highly facile whereas oxygen reduction has very slow kinetics. A significant fraction of the performance losses of fuel cells results from the high overpotential associated with the oxygen reduction reaction even on the state-of-the art Pt catalysts. In the case of "direct" fuel cells, where fuels such as methanol are directly oxidized, the performance losses are even higher due to the sluggish kinetics of fuel oxidation at the anode. Hence, better electrocatalysts are needed to improve fuel cell performance.

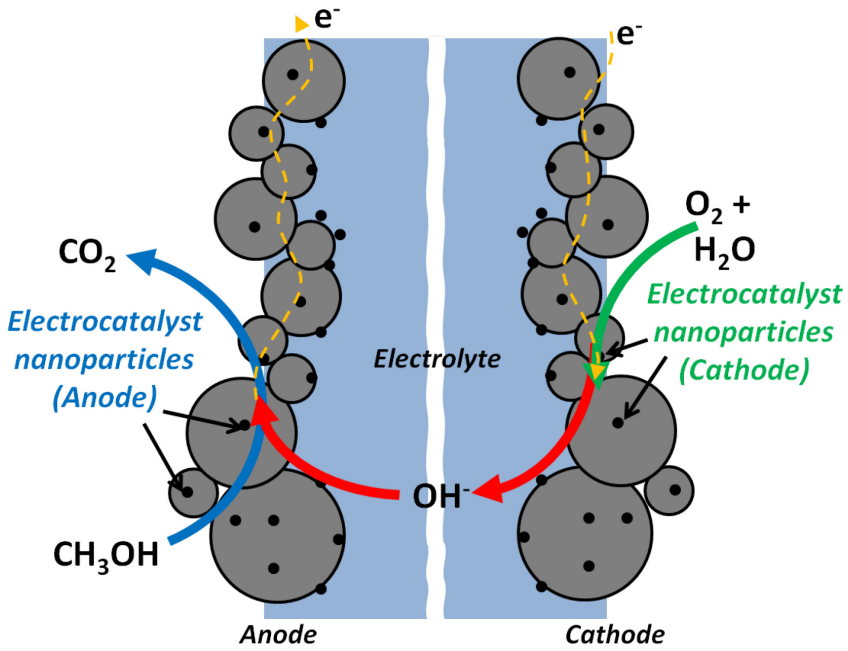

Figure 1.7: Fuel cell processes in an alkaline fuel cell.

The real advantage of operating fuel cells under alkaline conditions comes from the potential to explore a wider array of metals and alloys for use as electrocatalysts, than in acidic media. This advantage stems from the relative stability of non-noble metals such as Ag, Ni, Cu and others in basic media vis-à-vis acidic media. It is apparent that, since non-precious metal catalysts can be explored, alkaline fuel cells afford potential cost benefits. A brief discussion of electrocatalysis in alkaline media is included below. For a comprehensive overview, relevant literature can be referred to.[6–8]

At the cathode side, the veracity of better oxygen reduction kinetics on Pt in alkaline media vis-à-vis acidic media is still a matter of debate.[7] Nevertheless, the use of less expensive electrocatalysts for the oxygen reduction reaction (ORR) either in the form of Pt alloys or non-Pt based materials seems to be well-substantiated. [7,8] In the category of Pt based catalysts, Pd-monolayer/Pt(111), Pt-Cr-Ta alloy and Pt-Ag alloys have been suggested. In fact, Pt-Au alloys were used as ORR catalysts in AFCs of Apollo missions.[4] As a Pt-free catalyst, Ag is especially attractive for ORR since it has been reported to have activity comparable to that of Pt in alkaline medium while being substantially less expensive than Pt.[7] Unlike Pt, Ag is also selective for ORR. This can mitigate performance losses due to fuel crossover from the anode to the cathode especially for direct methanol fuel cells. Alloys of Ag with Co and Pb, Ag-W_2C composite, MnO_x, metal macrocycles, lanthanum strontium manganese oxides are some of the other Pt-free catalysts that have been reported in the literature.[8]

Just as in the case of the ORR activity of Pt and related materials, claims of enhanced electrocatalysis of fuel oxidation on Pt need to be verified by future research. However, the oxidation of adsorbed CO on Pt has been established to occur at significantly lower potentials in alkaline media, compared to acidic media.[9] This is beneficial for H_2 oxidation at the anode since

Pt can be expected to be more tolerant to CO poisoning. The enhanced activity of Pt for CO oxidation is also advantageous for the oxidation of small organic molecules such as formate and methanol since the reaction pathways for these molecules involve the formation of adsorbed CO as an intermediate.[7,10] The option of exploring catalyst candidates that are less expensive than Pt also remains an attractive feature for anode electrocatalysis. For the hydrogen oxidation reaction (HOR), Ni has often been reported as a cost-effective alternative for Pt in alkaline medium. However, the catalytic activity of Ni seems to be highly dependent on the morphology of the catalyst particles and the pretreatment methods employed.[11] A related system of Cr-decorated Ni has also been reported to show promising HOR activity.[12] Some of the alternative catalysts studied for methanol oxidation are Pd-Co_3O_4, Pt-Ru, Pt-Au and Au-Ru alloys, Ni and Ni-Pd alloys, and La-Sr-oxides.[6–8] For the oxidation of higher alcohols, some promising candidates have been reported such as Pt-ZrO_2/C, Hypermec (Ni-Fe-Co alloy), Pd alloys (with Ag, Au and Ru), Pd-NiO, Pd-(Ni-Zn-P)/C for ethanol oxidation and Pd-Ni for ethylene glycol.[6–8] It should be mentioned that in all these cases the efficacy of the catalysts to effect complete oxidation of the molecule remains an important metric that needs to be critically evaluated in the future.

1.2.3 Development of Alkaline Anion Exchange Membrane for AFCs

To leverage the favorable electrocatalytic effects in alkaline media for AFCs, the carbonation issue needs to be critically addressed. As mentioned earlier, although the modification of liquid electrolyte system can mitigate the carbonation to an extent, the deployment of an OH^- conducting polymer electrolyte membranes known as alkaline anion exchange membranes in AFCs (analogous to PEM in PEMFCs) represents an effective approach to fundamentally prevent carbonate precipitation in AFCs. The schematic of an AAEM depicted in Figure 1.8 illustrates this approach. The underlying cause for the buildup of fatal amounts of

carbonate precipitate in the traditional liquid electrolyte AFCs is the presence of mobile cations (K^+) that can combine with CO_3^{2-} to initiate precipitate growth (Equation 1.1 and Equation 1.2). However, in an AAEM, the cationic sites (functional units) are immobilized on a polymer backbone (structural unit). Since the cations are spatially separated, even if CO_3^{2-} anions associate themselves with the cationic sites, carbonate precipitation would not occur. As illustrated in Figure 1.8, in such a scenario, OH^- conduction can still occur; thus, preventing a catastrophic device failure.

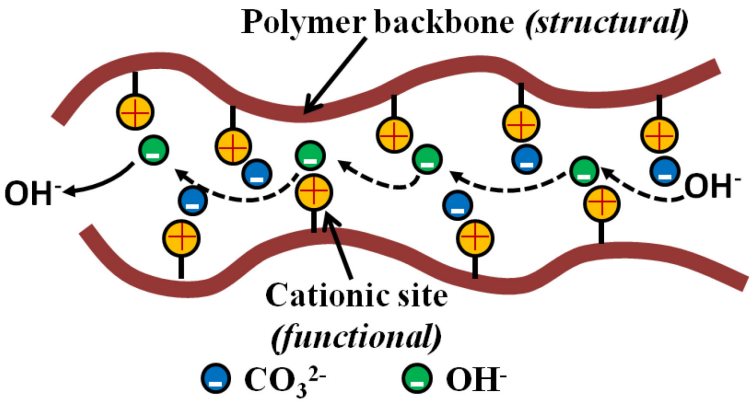

Figure 1.8: Schematic of an alkaline anion exchange membrane.

Compared to PEMFCs (Figure 1.1), AFCs employing AAEMs (AAEM-AFCs) should, in principle, exhibit lower fuel crossover due to the favorable direction of electro-osmotic drag of water molecules. To elaborate, in PEMFCs, protons generated at the anode are transported along with the associated water molecules across the membrane to the cathode. This consequently results in the increased crossover of the dissolved fuel (importantly in liquid fuels such as methanol) from the anode to the cathode. This leads to a mixed potential at the cathode and, as a result, the device voltage drops. It is evident that, due to the direction of OH^- transport (from cathode to anode) in AFCs (Figure 1.5), the electro-osmotic drag in AAEM-AFCs should serve to mitigate fuel crossover. Finally, compared to traditional AFCs, AAEM-AFCs, due to the use

of solid polymer electrolyte (SPE) membranes, should be easier to fabricate as all solid state components are employed. Device components will also be less prone to corrosion due to the absence of caustic liquid electrolyte.[6]

The recent development of AAEMs that can potentially address the carbonation issue has given a much-needed impetus to the research in AFCs that was largely overshadowed over the last few decades by the success of PEMFCs.[6] Due to its nascent stage, research in AAEMs, till now, has largely focused on the materials aspects which involve the synthesis and ex-situ characterization of prospective cationic polyelectrolyte membranes. The viability of a candidate AAEM has been evaluated mostly by ex-situ techniques and along few, albeit important, vectors such as ionic conductivity, mechanical strength and chemical stability.

A series of recent reviews provide comprehensive treatments of the various AAEM systems studied and evaluated by the community.[13–15] AAEMs can be homogeneous or heterogeneous membranes or inter-penetrating polymer networks. Homogeneous membranes, as the name suggests, are macroscopically single phase materials whereas the heterogeneous membranes and the inter-penetrating polymer networks are composed of two or more bulk phases. Heterogeneous membranes also require the addition of KOH solution to ensure ionic conductivity. Of all the categories, homogeneous membranes are the most promising and are the only AAEM subtype discussed herein.

For the sake of current discussion, a summary of the most promising AAEM systems and their typical structural and functional motifs are shown in Figure 1.9. The functional units are quaternary hetero-cations; typically, quaternary ammoniums (R_4N^+ where Rs are alkyl substitutions and need not be identical) or phosphoniums (R_4P^+). Ion-exchange capacity (IEC) is the number of moles of the cationic groups per unit mass of the dry polymer and is a measure of

the relative ratio of the functional part of the AAEM to its structural part. Evidently, IEC is tunable during the synthesis step. The structural units endow mechanical strength to AAEMs and are hydrophobic in nature. A higher IEC can ostensibly improve the ionic conductivity of the membrane. However, an increase in IEC often results in an increase in the swelling of the hydrated membrane due to enhanced water uptake in the hydrophilic regions (containing the functional unit) of the AAEM. Hence, the mechanical integrity of the membrane is generally compromised at very high IEC values. Consequently, the ratio of the structural to the functional part is optimized specific to the AAEM system for acceptable performance.

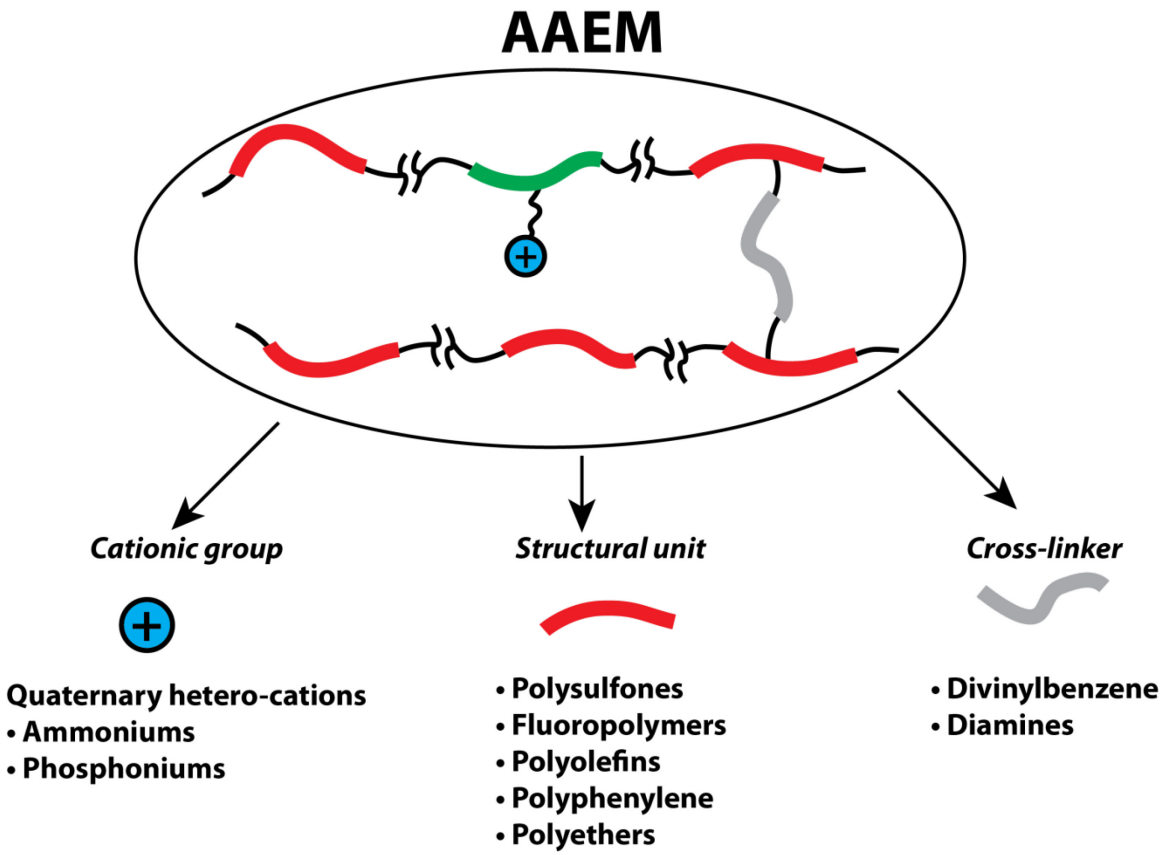

Figure 1.9: Component materials of prospective AAEM systems.

Cross-linkers can also be incorporated into the AAEM to preserve its structural integrity even at higher IEC values. Future progress in optimizing AAEM systems may involve tailoring

the polymer morphology, rather than increasing IEC values, to achieve high ionic conductivity without compromising the mechanical strength of the membrane.[16]

On the matter of OH^- conductivity in AAEMs, it is widely suspected that due to the lower mobility of OH^- vis-à-vis H^+, AAEMs will have lower ionic conductivity compared to PEMs.[17] However, it should be pointed out that currently there is only some rudimentary understanding of OH^- transport in solution, let alone in AAEMs.[18,19] The intrinsic limits of OH^- conductivity in AAEM systems can only be established by future fundamental studies in this direction. Nevertheless, it is still promising that, in the short span of AAEM development, there are already membranes reported with OH^- conductivity values competitive to those of the state-of-the-art Nafion membrane for PEMFCs.[16,20–23]

A critical issue that is a major focus of the ongoing research in AAEMs is that of the chemical degradation of the membrane under operating conditions of high pH (12-14) and temperature (60-90 °C). The underlying phenomenon is the loss of the functional form of the quaternary hetero-cations (R_4X^+ where X=N,P and Rs need not be identical) due to rearrangement, elimination or substitution reactions catalyzed by OH^-.[6,13–15] As an example, for quaternary ammoniums in the rearrangement reactions, the positive charge on the cation (R_4N^+) is discharged following the rearrangement of the latter to the neutral tertiary amine of the form R_3N. In case of substitutions and eliminations by OH^- attack, the heteroatom is itself separated from the polymer and lost as secondary (R_2NH) or tertiary amines (R_3N). Encouragingly, considerable progress has already been made on this front with membranes stable in 1-2 M KOH at 60 °C reported. [24,25] Particularly promising is the recently reported quaternary phosphonium based AAEM membrane that is found to be extremely stable (based on OH^- conductivity measurements) in 1M KOH at 80 °C for the duration of the test (22 days).[26]

1.3 Research Overview

The broad theme of the current work described in this thesis is the fundamental studies of the critical processes of relevance to AAEM-AFCs. The two main focuses are electrocatalysis in alkaline media and characterization (both electrochemical and ex-situ) of a prospective AAEM material. Electroanalytical studies of the oxidation of formate ($HCOO^-$) in alkaline medium on polycrystalline platinum form the basis of the current work in electrocatalysis and are described in chapter 3. The study of $HCOO^-$ oxidation on Pt as an electrocatalytic system is relevant since formate is a potential fuel in direct fuel cells. Recently, direct formate fuel cells have shown promising performance.[27,28] Additionally, the study of $HCOO^-$ oxidation is essential for understanding the oxidation of other SOMs such as methanol and ethanol since the oxidation of the latter molecules produce $HCOO^-$ as one of the incomplete oxidation products.[29–32]

In the field of AAEM research, there are critical voids in our knowledge of the processes and the phenomena active in an operational AAEM. There is still much to be learned about membrane transport mechanisms (both physical and charge transport) in these systems. Since the morphology of the polymer influences membrane properties, such as mechanical strength and ionic conductivity, studies aimed at examining the polymer microstructure are also relevant.[16] Although the prevention of carbonate precipitation is promised with the use of AAEMs in AFCs, this needs to be experimentally verified. Besides, the effect of carbonate and other anions such as formate – either incorporated into the membrane from the environment or generated from electrode reactions – on the functioning of the AAEM needs to be evaluated.

Using a prospective quaternary ammonium based AAEM material[20] as a template, the above-mentioned fundamental aspects of AAEM have been explored in the current work (chapters 4 and 5). Chapter 4 focuses on the electroanalytical studies of the carbonation/anion-

incorporation phenomenon in AAEM investigated using the electrochemical quartz crystal microbalance (EQCM) technique. Since AAEM materials generally undergo dimensional changes upon hydration (necessary for ionic conductivity), a related technique known as acoustic impedance spectroscopy (AIS) was also employed to monitor the swelling of the AAEM candidate material. Physical and charge transport studies of the AAEM material using redox active molecules as probes are detailed in Chapter 5. Also documented in this chapter are the preliminary results from the ex-situ characterization studies of the membrane material using FTIR and TEM.

The technical and the theoretical background for differential electrochemical mass spectrometry (DEMS) – utilized in the study of $HCOO^-$ oxidation on Pt – is given in the methodology chapter (chapter 2). In addition to DEMS, chapter 2 also describes the theoretical framework and the experimental aspects of the EQCM and the AIS techniques employed in the AAEM work. On a related note, the development and the preliminary testing of the advanced in situ FTIR configurations in the laboratory are described in chapter 6. These new experimental setups are expected to be of great value in the future for both electrocatalysis and AAEM research in the laboratory.

PtPb intermetallic has demonstrated excellent catalytic activity for both formic acid and methanol oxidation in acidic medium and significantly no adsorbed CO was detected during oxidation.[33–35] Based on this promising result, the hydrogen oxidation activity of the intermetallic and its tolerance to free CO in solution was investigated. The results from these studies are discussed in chapter 7.

1.4 References

(1) Winter, M.; Brodd, R. J. *Chemical Reviews* **2004**, *104*, 4245–4270.

(2) Wagner, F. T.; Lakshmanan, B.; Mathias, M. F. *The Journal of Physical Chemistry Letters* **2010**, *1*, 2204–2219.

(3) Debe, M. K. *Nature* **2012**, *486*, 43–51.

(4) Perry, M. L.; Fuller, T. F. *Journal of The Electrochemical Society* **2002**, *149*, S59.

(5) McLean, G. *International Journal of Hydrogen Energy* **2002**, *27*, 507–526.

(6) Varcoe, J. R.; Slade, R. C. T. *Fuel Cells* **2005**, *5*, 187–200.

(7) Spendelow, J. S.; Wieckowski, A. *Physical chemistry chemical physics : PCCP* **2007**, *9*, 2654–75.

(8) Yu, E. H.; Krewer, U.; Scott, K. *Energies* **2010**, *3*, 1499–1528.

(9) Couto, A.; Rincón, A.; Pérez, M. C.; Gutiérrez, C. *Electrochimica Acta* **2001**, *46*, 1285–1296.

(10) Christensen, P. A.; Hamnett, A.; Linares-Moya, D. *Physical chemistry chemical physics : PCCP* **2011**, *13*, 11739–47.

(11) Schulze, M.; Gülzow, E.; Steinhilber, G. *Applied Surface Science* **2001**, *179*, 251–256.

(12) Lu, S.; Pan, J.; Huang, A.; Zhuang, L.; Lu, J. *Proceedings of the National Academy of Sciences* **2008**, *105*, 20611–20614.

(13) Couture, G.; Alaaeddine, A.; Boschet, F.; Ameduri, B. *Progress in Polymer Science* **2011**, *36*, 1521–1557.

(14) Merle, G.; Wessling, M.; Nijmeijer, K. *Journal of Membrane Science* **2011**, *377*, 1–35.

(15) Wang, Y.-J.; Qiao, J.; Baker, R.; Zhang, J. *Chemical Society reviews* **2013**.

(16) Pan, J.; Chen, C.; Zhuang, L.; Lu, J. *Accounts of chemical research* **2012**, *45*, 473–81.

(17) Hibbs, M. R.; Hickner, M. A.; Alam, T. M.; McIntyre, S. K.; Fujimoto, C. H.; Cornelius, C. J. *Chemistry of Materials* **2008**, *20*, 2566–2573.

(18) Asthagiri, D.; Pratt, L. R.; Kress, J. D.; Gomez, M. A. *Proceedings of the National Academy of Sciences of the United States of America* **2004**, *101*, 7229–33.

(19) Tuckerman, M. E.; Chandra, A.; Marx, D. *Accounts of chemical research* **2006**, *39*, 151–8.

(20) Kostalik, H. A.; Clark, T. J.; Robertson, N. J.; Mutolo, P. F.; Longo, J. M.; Abruña, H. D.; Coates, G. W. *Macromolecules* **2010**, *43*, 7147–7150.

(21) Robertson, N. J.; Kostalik, H. A.; Clark, T. J.; Mutolo, P. F.; Abruña, H. D.; Coates, G. W. *Journal of the American Chemical Society* **2010**, *132*, 3400–4.

(22) Wang, J.; Zhao, Z.; Gong, F.; Li, S.; Zhang, S. *Macromolecules* **2009**, *42*, 8711–8717.

(23) Hibbs, M. R.; Fujimoto, C. H.; Cornelius, C. J. *Macromolecules* **2009**, *42*, 8316–8321.

(24) Thomas, O. D.; Soo, K. J. W. Y.; Peckham, T. J.; Kulkarni, M. P.; Holdcroft, S. *Journal of the American Chemical Society* **2012**, *134*, 10753–6.

(25) Gu, S.; Cai, R.; Luo, T.; Chen, Z.; Sun, M.; Liu, Y.; He, G.; Yan, Y. *Angewandte Chemie (International ed. in English)* **2009**, *48*, 6499–502.

(26) Noonan, K. J. T.; Hugar, K. M.; Kostalik, H. A.; Lobkovsky, E. B.; Abruña, H. D.; Coates, G. W. *Journal of the American Chemical Society* **2012**.

(27) Bartrom, A. M.; Haan, J. L. *Journal of Power Sources* **2012**, *214*, 68–74.

(28) Bartrom, A. M.; Ta, J.; Nguyen, T. Q.; Her, J.; Donovan, A.; Haan, J. L. *Journal of Power Sources* **2013**, *229*, 234–238.

(29) López-Atalaya, M.; Morallón, E.; Cases, F.; Vázquez, J. L.; Pérez, J. M. *Journal of Power Sources* **1994**, *52*, 109–117.

(30) Morallón, E.; Rodes, A.; Vázquez, J. L.; Pérez, J. M. *Journal of Electroanalytical Chemistry* **1995**, *391*, 149–157.

(31) Christensen, P. A.; Linares-Moya, D. *The Journal of Physical Chemistry C* **2010**, *114*, 1094–1101.

(32) Matsuoka, K.; Iriyama, Y.; Abe, T.; Matsuoka, M.; Ogumi, Z. *Electrochimica Acta* **2005**, *51*, 1085–1090.

(33) Casado-Rivera, E.; Volpe, D. J.; Alden, L.; Lind, C.; Downie, C.; Vázquez-Alvarez, T.; Angelo, A. C. D.; DiSalvo, F. J.; Abruña, H. D. *Journal of the American Chemical Society* **2004**, *126*, 4043–9.

(34) Wang, H.; Alden, L.; Disalvo, F. J.; Abruña, H. D. *Physical chemistry chemical physics : PCCP* **2008**, *10*, 3739–51.

(35) Matsumoto, F.; Roychowdhury, C.; DiSalvo, F. J.; Abruña, H. D. *Journal of The Electrochemical Society* **2008**, *155*, B148.

CHAPTER 2
METHODOLOGY

2.1 Differential Electrochemical Mass Spectrometry

2.1.1 Introduction

Due to the chemical non-specificity of electrochemical measurements, the identification and quantification of product species generated during an electrochemical reaction by combining electrochemical measurements with a chemical-species-sensitive technique is highly desirable. Differential electrochemical mass spectrometry (DEMS) represents such an approach. In essence, DEMS uses mass spectrometry to achieve the detection of volatile electro-generated species. The technique is differential since the product formation rates can be measured. Thus, DEMS is distinct from other mass spectrometric techniques where only the measurement of the integrated signal is possible. The history of DEMS began with the work of Bruckenstein and Gadde[1] whose implementation of in situ mass spectrometry was integrating in nature. Later, Wolter and Heitbaum[2,3] improved the technique to enable the measurement of product formation rates by the deployment of efficient pumping stages interfaced to the vacuum system.

In addition to the chemical specificity afforded by DEMS, it also has the advantage that the measured mass spectrometric currents, corresponding to the different product species, are unaffected by adventitious electrochemical processes – both Faradaic and non-Faradaic – such as double-layer charging and electrode surface processes. The latter processes can complicate the analysis of the electrochemical current responses. Hence, the mass spectrometric currents can be utilized to monitor, individually, the formation and, where calibration is possible, also the quantification of products. Due to the latter feature, DEMS measurements can be semi-

quantitative. DEMS is also highly sensitive and can detect products even in sub-nmol amounts. It is also highly versatile having been adapted to study a wide range of electrochemical systems such as fuel cells, batteries and photoelectrochemical cells.[4] It should also be noted that the DEMS technique is complimentary to in situ FTIR (discussed in chapter 6) in that the former detects only volatile product species while the latter targets mainly the detection of adsorbed species.

2.1.2 DEMS Cells

The process central to the applicability of mass spectrometry in studying electrochemical reactions, as realized in DEMS, is the transfer of the electro-generated volatile product species from the solution into the vacuum chamber of the mass spectrometer without compromising the operation of the latter. This is accomplished by the use of a suitable porous hydrophobic membrane acting as a barrier between the solution and the vacuum system. Hydrophobicity of the membrane, along with the presence of small pores (radius < 0.8 μm), prevents the bulk solvent from penetrating the membrane while allowing the permeation of the volatile species and, to some extent, the solvent molecules, through the pores, into the vacuum chamber.[2] Typically, Teflon membranes are used. For the current studies, the Teflon membranes (GORE-TEX) employed were ~ 75 μm thick with a mean pore size of ~ 20 nm and a porosity of 50%. There are a wide variety of DEMS cells reported in the literature.[4] However, for the purpose of the discussion, only the cells that were utilized in the current studies are described herein. The two cell types employed were the conventional cell and the dual thin layer flow cell. These are shown in Figure 2.1.

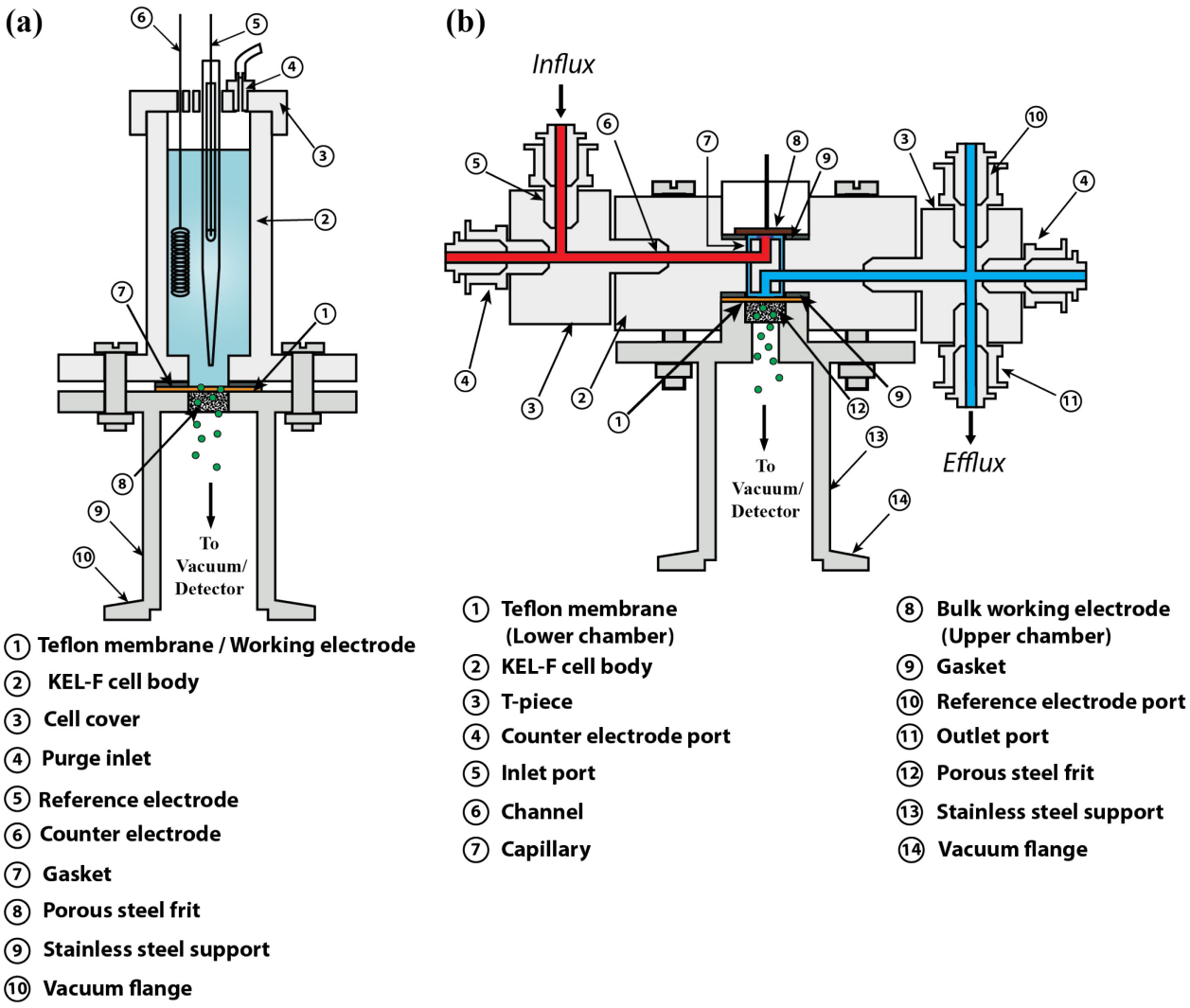

Figure 2.1: DEMS cells – (a) Conventional cell (b) Dual thin layer flow cell

(a) Conventional Cell

In a conventional cell (Figure 2.1a), the electrode material of interest is sputtered on the porous Teflon membrane. This way, the membrane also acts as the working electrode. Typically, the electrode material is sputtered to a nominal thickness of 30-80 nm on top of the membrane. The membrane is mechanically supported on a porous steel frit (diameter = 6 mm) embedded in a stainless steel support piece. The support piece is welded to a standard vacuum flange (DN 16, KF-ISO) that is used to connect to the vacuum chamber of the mass spectrometer system. The cell body is constructed out of Kel-F. To ensure a good seal between the cell body and the

membrane, a silicone or Teflon gasket of inner diameter 6 mm is sandwiched between the two. In this arrangement, a circular area 6 mm in diameter (~ 0.28 cm^2) of the electrode layer is exposed to the solution.

In the conventional cell, since the volatile products are electro-generated right at the membrane, the products partition rapidly into the vacuum chamber. Hence, the time delay between the mass spectrometric and the electrochemical signal is much smaller than the flow-type DEMS cells (vide infra). However, there are some disadvantages to this cell configuration. There is an absence of active mass transport which can result in the depletion of the reactant and build-up of the products at the electrode surface during the electrochemical reactions. Only porous electrodes can be used in this configuration. Due to the nature of preparation of porous electrodes, there is no real control over either the electrochemical surface area or the morphology of the electrode layer on top of the Teflon membrane as they will vary depending on the nature of the electrode material and the deposition protocol followed during the sputtering process. On a related aspect, there may be differences between the wettability of electrode layers made from different materials which will also affect the electrochemical response. The general point is that, everything else being the same, caution must be still be exercised when comparing results from different porous electrode systems. Additionally, the reaction equilibria can be affected due to the enhanced partitioning of the volatile species generated at or in the electrode layer into the vacuum chamber.[5] These effects are largely unstudied but should be kept in mind while analyzing and quantifying results.

(b) Dual Thin Layer Flow Cell

The dual thin layer flow cell (Figure 2.1b) that allows the use of bulk electrodes and the establishment of well-defined solution mass transport of species addresses the above-mentioned

problems of the conventional cell. Construction of this cell has been described in detail previously. [6,7] Briefly, the cell consists of a main cell body and two T-pieces attached to the latter. The main cell body has two chambers (upper and lower) and the latter are connected by a set of capillaries (0.5 mm in diameter). The solution is conveyed in and out of the chambers via larger channels (1.5 mm in diameter) that are connected to the channels in the t-pieces; thus, completing the solution flow path in the cell. The volume of solution in the chamber is ~3 μL. The entire cell is constructed out of Kel-F. In a typical cell assembly as shown in Figure 2.1b, a bulk working electrode is inserted into the upper chamber of the cell and in the lower chamber the porous Teflon membrane is introduced. Just as in the conventional cells, silicone or Teflon gaskets are used as spacers to help form good seals between the electrode/membrane and the cell. The Teflon membrane is interfaced to the vacuum chamber in a fashion similar to that of the conventional cell described previously. The T-pieces, in addition to directing solution flow in and out of the cell body, also have ports to connect the reference electrode and the counter electrodes. Two counter electrodes (one upstream and one downstream from the working electrode) are employed to mitigate the resistance effects in the thin layer flow cell.

It is apparent that the dual chambered construction of the cell spatially separates the process of electro-generation of volatile products (at the working electrode in the upper chamber) from that of the phase transfer of the volatile species from the solution into the vacuum (at the Teflon membrane in the lower chamber). This way the dual thin layer cell circumvents the mass transport problems associated with the conventional cell. The dual chambered construction also makes the cell experimentally versatile. By using a sputtered Teflon membrane in combination with a bulk electrode, the flow cell can be used for secondary detection of non-volatile species. In this arrangement, the sputtered Teflon membrane typically act as the primary working

electrode and the electro-generation of volatile species at the membrane electrode and the subsequent mass spectrometric detection happen just as in the conventional cell. Additionally, non-volatile product species can be detected electrochemically at the bulk electrode (detector electrode) downstream from the membrane electrode.

(c) DEMS Cell Configuration for Operation in Alkaline Media

Since the current work focuses on the study of fuel cell reactions in alkaline media, it is worthwhile to briefly review the mode of DEMS cell operation under alkaline conditions. Electro-oxidation of carbonaceous fuels typically generates CO_2 which in alkaline media is rapidly converted to the non-volatile CO_3^{2-} ion. Thus, for the mass spectrometric analysis of products including CO_2, the sputtered Teflon membrane needs to be employed as the working electrode. This ensures the rapid partitioning of the electro-generated CO_2 into the vacuum chamber before it can be wholly converted to CO_3^{2-} in the alkaline media. Both the conventional cell and the dual thin layer flow cell can be used in this fashion to detect CO_2.

2.1.3 DEMS Setup

Two experimental DEMS setups were used in the course of the current study – one employs a HiQuad (Pfeiffer) mass spectrometer and the other uses a PrismaPlus (Pfeiffer) mass spectrometer. A comparison of these setups is given in Table 2.1. Essentially, the HiQuad mass spectrometer has nominally better sensitivity and resolution. All the vacuum chamber components were obtained from Pfeiffer or Varian.

For purposes of describing the basic DEMS setup, the HiQuad setup is used as the template. The layout of the HiQuad setup is shown in Figure 2.2. The top panel (Figure 2.2a) depicts the mass spectrometer components while the bottom panel (Figure 2.2b) shows the pumping stages. Starting with the pumping station, the vacuum chamber is pumped by two

turbomolecular pumps. These pumps are backed by a 2-stage rotary vane pre-pump. The access of volatiles into the chamber is controlled by an angle valve. The chamber pressure is measured using a cold cathode/Pirani gauge. With the chamber closed, a pressure of ~ 10^{-8} mbar can be easily achieved in the vacuum chamber using the afore-mentioned pumping system. During the operation of the DEMS cell with the chamber open the pressure in the vacuum chamber is in the range 10^{-5} – 10^{-4} mbar.

Table 2.1: Comparison of the two laboratory DEMS setups

	HiQuad™ (Pfeiffer) mass spectrometer based DEMS setup	**PrismaPlus™ (Pfeiffer) mass spectrometer based DEMS setup**
Mass spectrometer system	HiQuad™ QMG 700 (Pfeiffer)	PrismaPlus™ QMG 220 M1 (Pfeiffer)
Mass range (amu)	1-128	1-100
Mass filter	Quadrupole rod system	Quadrupole rod system
Rod diameter (mm)	16	6
Rod length (mm)	300	100
Rod material	Molybdenum	Stainless steel
Ion source	Yttriated iridium filaments	Yttriated iridium filaments
Detectors	1. Faraday cup 2. 90° off-axis SEM*	1. Faraday cup 2. Continuous SEM*
Pumping station		
Turbo-pumps	1. Pfeiffer TMU 261 YP (N_2 - 210 l/s) 2. Pfeiffer TMU 071YP (N_2 - 60 l/s)	1. Varian 969-9008 (N_2 - 250 l/s) 2. Pfeiffer TMU 065UP (N_2 – 65 l/s)
Pre-pump	Pfeiffer DUO 010M (2-stage rotary vane – 12 m^3/hr)	Varian DS 202 (2-stage rotary vane – 9.85 m^3/hr)
Vacuum gauge	Pfeiffer PKR 521 (Combination Pirani / Cold cathode gauge – 1000 – 5 x 10^{-9} mbar)	1. Varian 525 (Cold cathode gauge – 10^{-2} – 10^{-8} mbar) 2. Varian Pirani gauge

Component specifications are nominal. *SEM – Secondary electron multiplier.

The neutral molecules entering the vacuum chamber from the DEMS cell are rapidly conveyed to the ion source where they are ionized by impinging electrons emitted from a filament (yttriated iridium). The typical ionization energy used is 65 eV. The stream of

positively charged ions exiting the ion source is then accelerated and focused by a series of appropriately biased orifice plates. The focused ion beam then enters the mass filter.

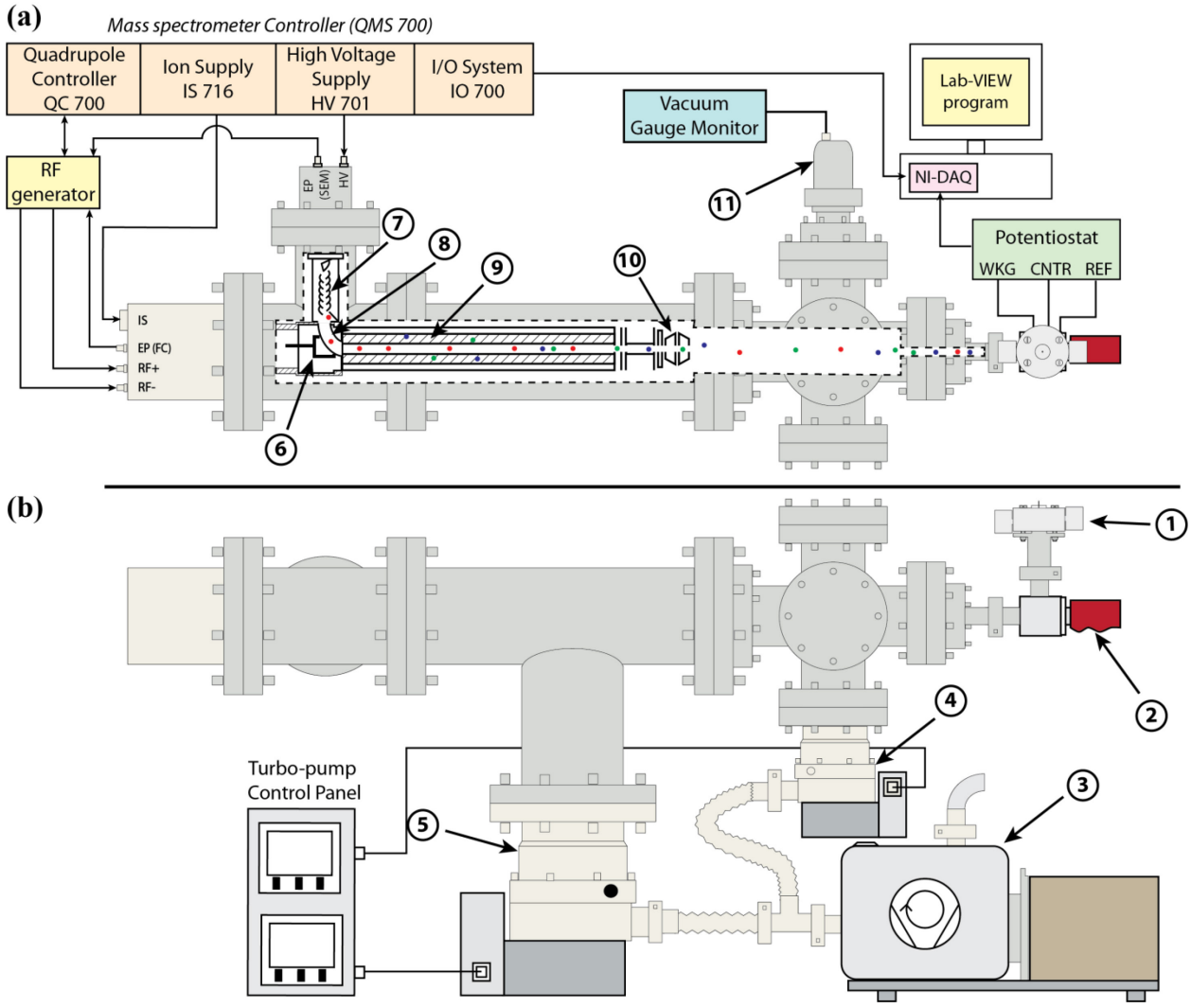

Figure 2.2: DEMS experimental setup based on HiQuad (Pfeiffer) mass spectrometer system. (a) Top view showing the electrical connections of the spectrometer and the data acquisition setup. The cut-out view (dotted-line enclosed region) depicts the mass spectrometric detection of molecules generated in the DEMS cell (b) Side view showing the mass spectrometer system interfaced with the pumping station. Components: 1 – DEMS cell, 2 – Angle valve, 3 – Roughing pump, 4 – Turbo pump (Low capacity), 5 – Turbo pump (High capacity), 6 – Faraday cup, 7 – Secondary electron multiplier, 8 – Deflection unit, 9 – Quadrupole Mass filter, 10 – Ion source, 11 – Vacuum gauge. Abbreviations: IS – Ion source, EP – Electrometer preamplifier, FC – Faraday cup, RF – Radio-frequency, SEM – Secondary electron multiplier, HV – High voltage.

The mass filter is a quadrupole rod system consisting of four identical cylindrical rods symmetrically arranged with their long axis parallel to each other. The rod material is either molybdenum or stainless steel. The diametrically opposite rods are electrically connected and an alternating ac voltage is applied to the pairs using an RF generator. The positively charged ions entering the rod system are subjected to an oscillating electric field. Depending on the applied voltage, only species (shown as red filled circles in Figure 2.2a) with a particular mass-to-charge ratio (m/z) will have stable trajectories and pass through the rod system. The rest of the ions will hit the rods and be neutralized. Thus, mass filtering is achieved. It should be mentioned that quadrupole rods in HiQuad system is three times longer than that in PrismaPlus endowing the former with much higher mass selectivity/resolution.

The mass-selected ions are detected using either a Faraday cup or a secondary electron multiplier (SEM). Ideally, the usage of a SEM requires chamber pressures less than 10^{-5} mbar. The SEM detector is more sensitive than the Faraday cup since the initial detection current from the impinging ion is amplified by the production of secondary electrons in the dynode array of the SEM. However, SEM is best used to detect species with low background signal.

The mass spectrometer controller in conjunction with the Quadera software (Pfeiffer) consolidates the operations of the different components of the mass spectrometer. Additionally, the controller outputs analog signals corresponding to the mass spectrometric ion currents. The mass spectrometer analog outputs from the controller and the analog outputs from the potentiostat interfaced with the DEMS cell are simultaneously acquired by a National Instruments data acquisition (NI-DAQ) card and recorded using a home-made LabVIEW program.

2.1.4 DEMS Calibration

In suitable cases, the DEMS setup can be calibrated for the quantification of a specific volatile product from the mass spectrometric current (I_{MS}). The necessary requirement is the availability of an electrochemical reaction that can exclusively create the volatile product of interest. In such a situation, the Faradaic current (I_F) observed is entirely due to the generation of the volatile product and can be related to the mass spectrometric current as follows.

Equation 2.1:

$$I_F = \frac{nI_{MS}}{K^*_{(m/z)}}$$

where n is the number moles of electrons required to produce one mole of the volatile product and $K^*_{(m/z)}$ is the calibration constant.

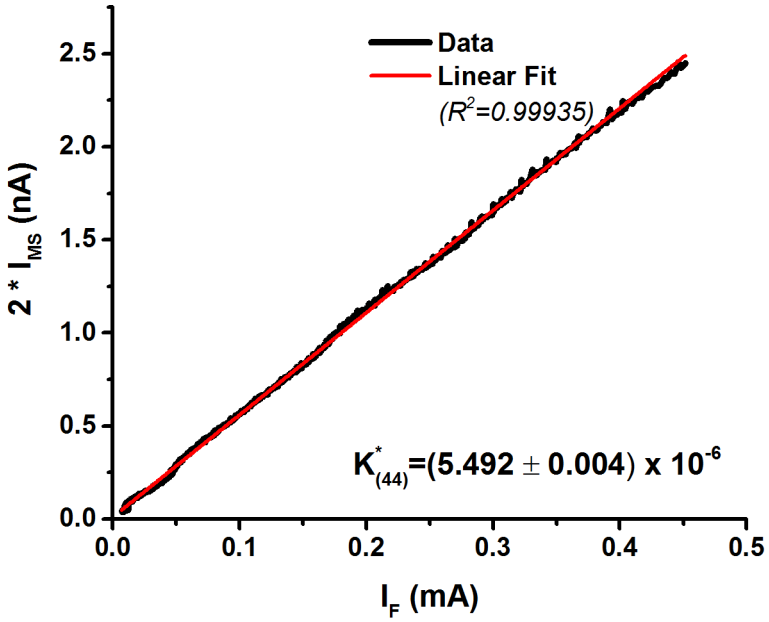

Figure 2.3: Calibration of DEMS setup for CO_2^+ (m/z=44). The slope yields the calibration constant $K^*_{(44)}$. The plot is based on the data collected during the oxidation of 50mM HCOOH in 0.1M H_2SO_4 at a Pt/C nanoparticle film deposited on a glassy carbon electrode. Scan rate: 1 mV/s. The potential range of the scan is from 0.28-0.65 V vs RHE. Flow rate ~ 8 µL/s.

It is assumed that non-Faradaic and parasitic Faradic contributions to I_F are either negligible or are properly compensated. The calibration constant $K^*_{(m/z)}$ is specific for a given

volatile species and under a given set of experimental conditions that include the solution flow rate and the mass spectrometer sensitivity. Two volatile species for which DEMS is commonly calibrated are H_2 and CO_2. H_2 is calibrated using the H^+ reduction reaction and CO_2 by either oxidation of adsorbed CO or more conveniently by the oxidation of HCOOH. It is to be noted that the electro-oxidation of HCOOH can only generate CO_2 as the product. Figure 2.3 shows the calibration curve for CO_2^+ (m/z =44) obtained using HCOOH oxidation at a Pt electrode. Good linearity between the Faradaic current and the mass spectrometric current is seen.

2.2 Electrochemical Quartz Crystal Microbalance

2.2.1 Theory

The electrochemical quartz crystal microbalance (EQCM) is essentially an extension of the quartz crystal microbalances, ubiquitously deployed as mass sensors for process monitoring in vacuum, gaseous or liquid environments. In essence, by using QCM in an electrochemical setup, EQCM allows for the monitoring of electrochemically driven mass changes. A brief description of the fundamental concepts and the experimental aspects of the EQCM technique is provided here. For a comprehensive treatment of the subject, the highly readable review by Buttry and Ward may be referred to.[8]

(a) Converse Piezo-electric Effect

The operation of the QCM is based on the converse phenomenon of piezo-electricity. Piezo-electricity is the effect in which a voltage/potential difference is developed between the opposite faces of a non-centrosymmetric crystal, such as quartz, on the application of a shear stress to the crystal faces. The converse piezo-electricity is the reverse effect wherein the crystal undergoes a shear deformation on application of a voltage between the opposite faces of the crystal. The piezoelectric effect originates in non-centrosymmetric crystals due to the presence of

a polar axis in the crystal along which there exists a net dipole moment. When the crystal undergoes shear deformation, the atoms in the crystal are displaced and the net dipole moment changes. As a result, net surface charges, opposite in sign, develops at the crystal faces giving rise to the voltage across the crystal.

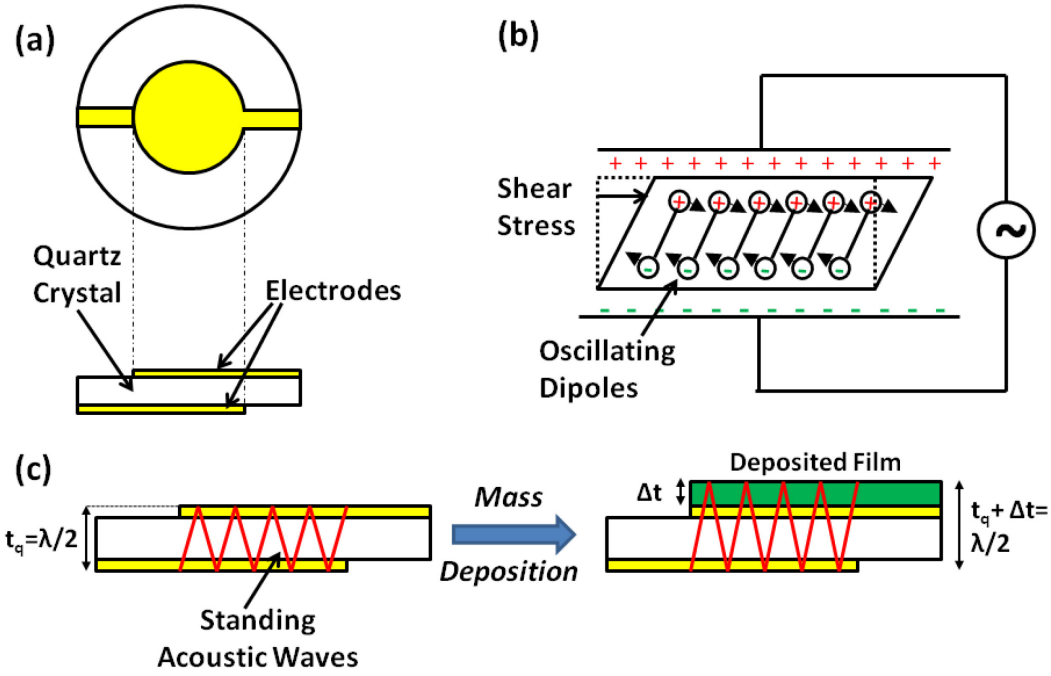

Figure 2.4: Operating principle of QCM: (a) typical QCM oscillator (b) converse piezo-electric effect (c) detection of mass changes at the crystal during the deposition process by shift in the resonant frequency of the crystal. Adapted from ref. [8].

In case of the QCM oscillator (Figure 2.4a), by virtue of the converse piezo-electric effect, the dipoles in the crystal now oscillate under the influence of the alternating electric field applied across the crystal by means of the metal film electrodes deposited on the crystal faces. The oscillating dipole results in the periodic displacement of atoms in the direction parallel to the crystal face. This concerted motion manifests itself as the periodic sheer deformation of the crystal (Figure 2.4b). The polarity of the applied electric field dictates the direction of the sheer

deformation while the magnitude of the applied voltage controls the amplitude of the crystal motion.

(b) Sauerbrey Equation

The oscillating dipoles in an operational QCM create transverse acoustic waves (Figure 2.4c) that travel through the crystal before getting reflected at the crystal faces. In order to establish standing wave condition required for steady state operation, the wavelength (λ) of the acoustic wave should be equal to $2t_q$ (where t_q is the thickness of the quartz crystal). This is the resonance condition for the bare oscillator without any mass loading. The resonant frequency (f_u) is given by

Equation 2.2:
$$f_u = \frac{\upsilon_q}{2t_q} = \left(\frac{\sqrt{\rho_q \mu_q}}{\rho_q} \right) \frac{1}{2t_q} = \left(\frac{z_q}{\rho_q} \right) \frac{1}{2t_q}$$

where υ_q is the speed of the acoustic wave in the quartz crystal. υ_q can be re-expressed in terms of the density, ρ_q and the shear modulus, μ_q of the quartz crystal as shown in Equation 2.2. The quantity $(\rho_q \mu_q)^{1/2}$ is known as the acoustic impedance of the quartz crystal, z_q.

When mass deposition occurs at the crystal face, the transverse waves propagate into the deposited medium provided the "no-slip" condition is satisfied. The "no-slip" condition stipulates that the atomic displacement and the shear stress vary continuously across the two media. Further, if the acoustic properties of the deposited medium are same as that of the quartz crystal, the deposited film can be considered as the extension of the quartz crystal oscillator and the whole system can be treated as a composite resonator. Based on these assumptions, the resonance condition for the composite resonator when a film of thickness Δt is deposited on the crystal is modified to $\lambda = 2(t_q + \Delta t)$. This amounts to a decrease in the resonance frequency (Δf)

related linearly to the mass increase *(Δm)* as expressed by the well-know Sauerbrey equation (Equation 2.3).

Equation 2.3:
$$\Delta f = -f_u \frac{\Delta t}{t_q} = -\left(\frac{2 f_u^2}{z_q}\right)\frac{\Delta m}{A} = -C_f \frac{\Delta m}{A}$$

where A is the area of the overlapping area between the electrodes that is piezoelectrically active and C_f is the sensitivity factor of the crystal. It is to be noted that C_f is an intrinsic parameter of the quartz crystal independent of the environment or the deposited medium. For a 5MHz AT-cut quartz crystal at room temperature, C_f =56.6 Hz/μg/cm^2.

For the Sauerbrey relation to be valid, the following conditions need to be met: (i) the deposited film is rigid (ii) the film has uniform thickness and (iii) low mass loading (less than 2% shift of the resonant frequency). A film is said to be rigid if it vibrates in phase with the crystal. Most metal and oxide films behave as rigid films in both gas and liquid environments. Polymers and biomolecules can behave as non-rigid films especially in liquids. Although the linear relationship between *Δf* and Δm is lost in such situations, the QCM still responds to mass changes in the film as observed by the shift in the resonant frequency. Importantly, in case of non-rigid films, the QCM is also sensitive to the rheological properties of the film and their changes such as swelling of polymer films by solvent. An analysis of the impedance response of the QCM can yield useful insights into such phenomena. This will be described later in this section.

(c) Electro-mechanical Model of QCM

It is highly instructive to analyze the operation of QCM in terms of its equivalent mechanical and electrical model (Figure 2.5). This serves two main purposes: (i) the mechanical model helps in the phenomenological understanding of the QCM operation (ii) the electrical

model forms the basis for the impedance analysis of the QCM response – relevant to the investigations of non-rigid films.

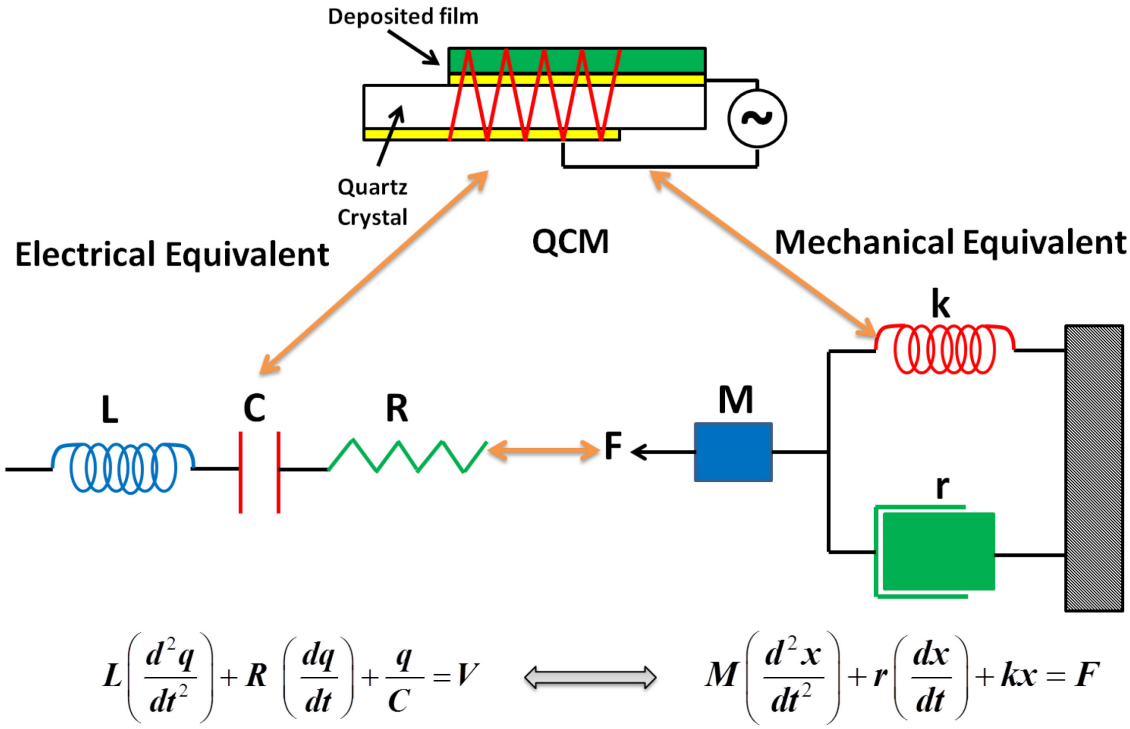

Figure 2.5: Electro-mechanical model of QCM. Adapted from ref. [8].

The general state of the QCM – a mass loaded quartz crystal interacting with the immersion medium- can be described, at the simplest level, as a damped harmonic oscillator. Mechanically, this is analogous to the motion of a mass under the combined action of a spring and a dashpot (damper) as shown in Figure 2.5. Mathematically, these two mechanical systems can be described by the same equation of force (Equation 2.4).

Equation 2.4:
$$M\left(\frac{d^2x}{dt^2}\right)+r\left(\frac{dx}{dt}\right)+kx=F$$

where M is the mass of the load, r is the coefficient of friction of the dashpot, k is the spring constant, x is the displacement of the mass, t is the time and F is the force applied.

Electrically, the QCM system is equivalent to the LCR circuit as shown in Figure 2.5 consisting of an inductor, a capacitor and a resistor in series. The relevant equation, in this case, is given below.

Equation 2.5: $$L\left(\frac{d^2q}{dt^2}\right)+R\left(\frac{dq}{dt}\right)+\left(\frac{1}{C}\right)q=V$$

where L is the inductance, R is the resistance, C is the capacitance, q is the charge, t is the time and V is the applied voltage. There is complete equivalence between the mechanical and the electrical models of the QCM as given by Equation 2.4 and Equation 2.5. This also entails that the corresponding pair of quantities in the equations are equivalent. To elaborate, the mass loading of the crystal is equivalent to an increase in the value of mass M attached to the spring or an increase in the inductance L in the LCR circuit. This equivalence relationship holds true for the other pairs of quantities – r and R, k and $1/C$ representing the dissipation or frictional losses to the environment and the spring constant or stiffness associated with the oscillator, respectively. The utility of this framework is readily apparent as the electrical quantities L, C and R of the composite resonator system can be directly measured experimentally (vide infra).

For a realistic model of the QCM, typically a capacitance C_0 is included in parallel to the LCR series. The C_0 models the cumulative parasitic capacitances of the quartz crystal-electrodes system, the crystal holder and the instrument cabling. The inclusion of C_0 in the electrical equivalent model previously discussed gives the widely applied Butterworth-Van-Dyke (BVD) model of the QCM (Figure 2.6). In this model, the LCR series is known as the motional arm and, as explained earlier, functionally represents the QCM.

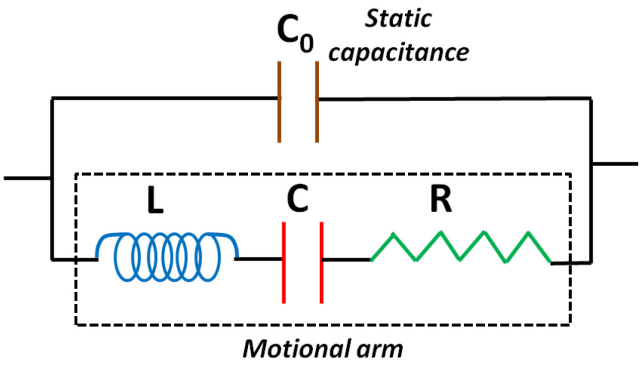

Figure 2.6: Butterworth-Van-Dyke (BVD) model of the QCM

(d) Operation of QCM in Liquid Immersion Medium

Introduction of the QCM into a liquid medium results in a frequency decrease due to the mass loading by the liquid. It also leads to increased dissipation (higher value of R) due to the viscous drag of the liquid medium on the motion of the crystal. The resulting frequency shift (Δf_L) has been treated theoretically[9,10] and is given by the equation

Equation 2.6:
$$\Delta f_L = -f_u^{3/2}\left(\frac{\rho_L \eta_L}{\pi \rho_q \mu_q}\right)^{1/2}$$

where ρ_L and η_L are the density and the viscosity of the liquid respectively; the other quantities are as defined in Equation 2.2. Typically, $|\Delta f_L|$ for water is about 700 – 800 Hz.

Generally, the contribution from the liquid medium to the QCM response is constant and, in the absence of any other complications such as non-rigid films, the Sauerbrey equation is still valid for mass changes at the quartz crystal immersed in the liquid. The BVD model (Figure 2.6) can be extended to include the effects of liquid immersion on the QCM operation as shown in Figure 2.7.[8] In this model, the mass change due to the deposition of the rigid film is represented by the inductance, L_f. Similarly, the mass loading and the viscous losses due to the liquid are represented by the inductance, L_L and R_L respectively.

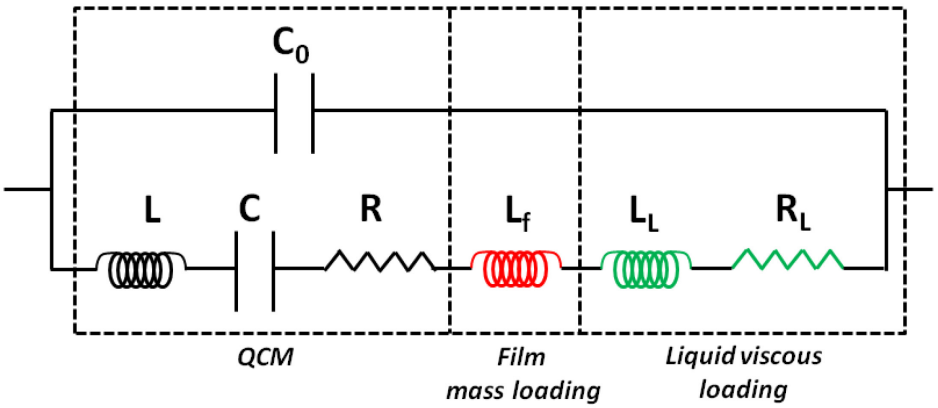

Figure 2.7: Electrical equivalent model for a rigid film-QCM composite resonator immersed in a liquid medium. Adapted from ref. [8].

(e) Viscoelastic Films

Viscoelastic materials exhibit both viscous (associated with fluids) and elastic (shown by solids) behaviors while undergoing deformation. Soft materials such as polymers and bio-molecular structures display significant viscoelastic effects especially when immersed in a liquid medium. The introduction of a viscoelastic/non-rigid film on the quartz crystal profoundly affects the QCM response. Most importantly, the linear relationship between Δf and Δm as expressed by the Sauerbrey equation is no longer valid. Hence, use of Δf to quantify mass changes is no longer straightforward. Due to the viscous nature of the film, there are severe dissipation losses or, equivalently, large increases in the value of R. Hence, monitoring R in these systems can yield important insights into the rheology of these materials.

In order to describe the system of a viscoelastic film on the quartz crystal in a liquid immersion medium the appropriate circuit elements representing the viscoelasticity of the film has to be included in addition to the liquid contribution. One of the possible models that can be applied is shown in Figure 2.8 (adapted from Buttry and Ward).[8] L_f, R_f and C_f represent the mass loading, the viscous losses and the elasticity of the film respectively. The other quantities are as defined previously.

It is to be noted that the changes in the viscoelasticity of the film can also be dynamically induced as in EQCM experiments where solvent and ionic transport in the film can be driven electrochemically.

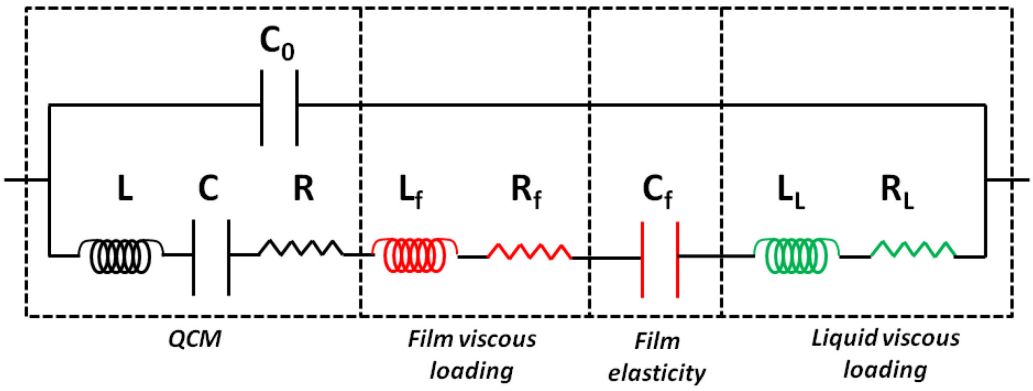

Figure 2.8: Electrical equivalent model for a viscoelastic film-QCM composite resonator immersed in a liquid medium. Adapted from ref. [8].

(f) Impedance Analysis

The study of viscoelastic films using the QCM technique is greatly aided by the impedance analysis of the composite resonator system. The impedance analysis is performed by casting the measurements in the form of diagnostic plots that are described below. Only selected aspects of these plots are dealt with here. For a detailed explanation of the plots, the review paper by Buttry and Ward may be referred to. [8]

The impedance response of an electrical circuit can be studied in terms of its total impedance Z or its admittance $Y=1/Z$. Z is composed of the real part – the resistance, R_v (to distinguish it from R in the BVD model) and the imaginary part – the reactance, X as in Equation 2.7 . Similarly, Y can be decomposed into its real part – the conductance, G and its imaginary part - the susceptance, B as in Equation 2.8. It is to be noted that all the quantities are dependent on the frequency ω at which the system is driven.

Equation 2.7: $$Z(\omega) = R_v(\omega) + jX(\omega)$$

Equation 2.8: $$Y(\omega) = G(\omega) + jB(\omega)$$

i. Admittance Locus

A plot of *G* vs *B* for a range of frequencies is known as the admittance locus. The admittance locus for a QCM resonator based on the BVD model is shown in Figure 2.9. The frequency increases clockwise. The plot helps in the diagnosis of the composite resonator. The radius of the circle is inversely related to the dissipation parameter *R*; thus, the smaller the radius, the higher the dissipation losses in the system.

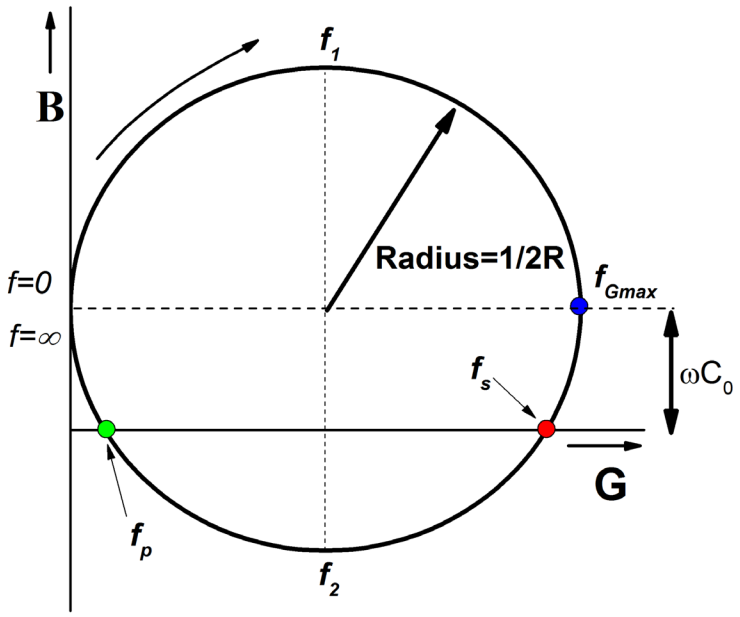

Figure 2.9: Admittance locus for a QCM resonator based on the BVD model. Adapted from ref. [8].

There are few frequencies of significance that are germane to the analysis. The resonance condition for the system is that the phase angle should be zero. This is tantamount to the condition *B*=0. As can be seen from Figure 2.9, this occurs at frequencies f_s and f_p known as the series and the parallel resonant frequency respectively. At f_s, the total reactance of the

motional arm is zero and at f_p, the total reactance of the entire network is zero. The QCMs are usually driven at the series resonance frequency f_s. It is to be noted that the f_s and f_p points are drawn closer together when R and/or C_0 increases. For large enough values of R and/or C_0, the resonance condition may not be satisfied at all. This can occur in the case of viscoelastic films. Hence, the admittance locus is very useful for diagnosing failures in the operation of the QCM. f_1 and f_2 are frequencies at which B attains the maximum and the minimum values respectively. These frequencies, along with f_{Gmax} (frequency at which G is maximum), are important in G-B plots which will be discussed later.

ii. $|Z|$-θ *Plot*

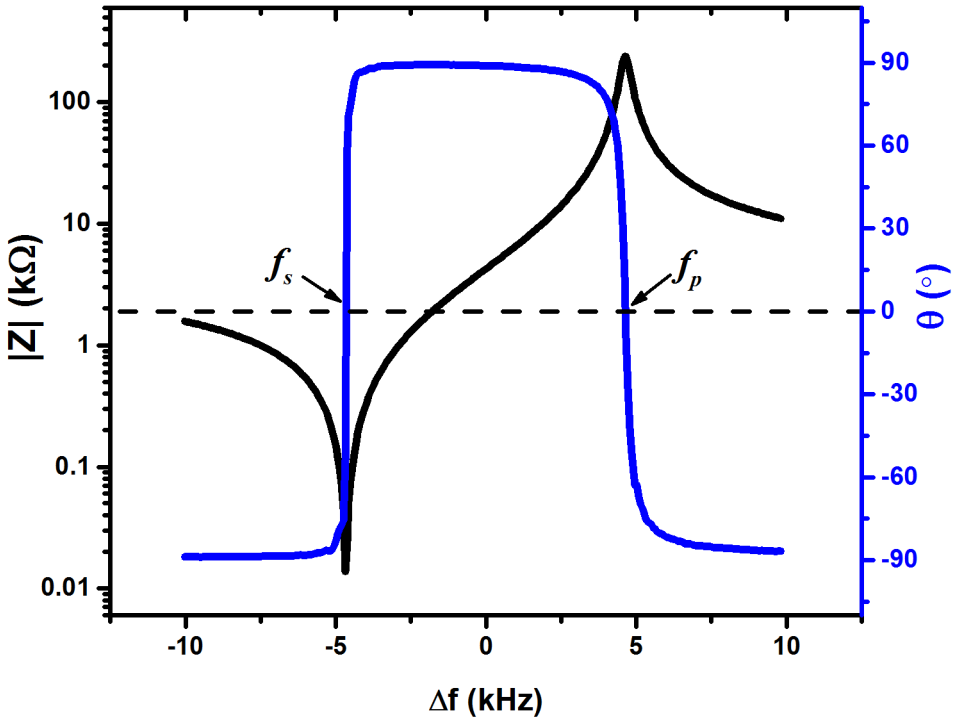

Figure 2.10: $|Z|$-θ plot for an unloaded QCM in air at room temperature.

To aid in the discussion, representative plots of the correlated quantities $|Z|$ and θ versus frequency for a bare QCM in air at room temperature are shown in Figure 2.10. As expected, it is seen that the minimum value of $|Z|$ occurs at the series resonance frequency f_s. Focusing on the θ

plot, at low and high frequencies $\theta \approx$ -90° indicating the capacitive nature of the total impedance at these frequencies. This will become apparent when studying the response of the circuit elements in the BVD model (Figure 2.6) at low and high frequencies. At low frequencies, the capacitance C in the motional arm dominates while at high frequencies it is the static capacitance C_0 that dominates. At intermediate frequencies, between f_s and f_p, θ is positive due to the contribution from the inductance L. It is clear that the composite resonator system can achieve the resonance condition only if the curve crosses the x-axis. Thus $|Z|$-θ plot can also used to diagnose operational failures of QCM.

iii. G-B Plot

The main utility of *G-B* plots lie in the measurement of the quality factor Q of the composite resonator. Q is a measure of the energy retained by the resonator. Q is defined as the ratio of the energy stored to the energy dissipated per oscillation. It can be expressed as

Equation 2.9:
$$Q = \frac{2\pi f_{G\max} L}{R} \approx \frac{f_{G\max}}{f_2 - f_1}$$

Evidently, a high value of R will result in low Q due to dissipative losses. In air, quartz crystals can achieve extremely high Q values; greater than 10^5. However, Q is reduced drastically in liquids; for instance, in water, $Q \approx 3000$. The presence of viscoelastic films results in a further decrease in the value of the quality factor compromising the mass-sensing capability of the QCM.

Using a *G-B* plot, it is straightforward to calculate Q from Equation 2.9. Figure 2.11 shows the *G-B* plot for the same resonator as in Figure 2.10. Q for this resonator was calculated to be about 77,000. As mentioned earlier, f_1 and f_2 are frequencies at which B has the minimum and the maximum value respectively. This is also clear from the susceptance (B) plot.

Importantly, f_2- f_1 is the full-width at half max (FWHM) for the conductance (G) peak. f_2- f_1 is also known as the resonator bandwidth. Apparently, a narrow conductance peak and consequently a small bandwidth will result in high Q. It is clear from Equation 2.9 that an increase in value of R will broaden the conductance peak. Thus, G-B plots also aid in the characterization of the composite resonator.

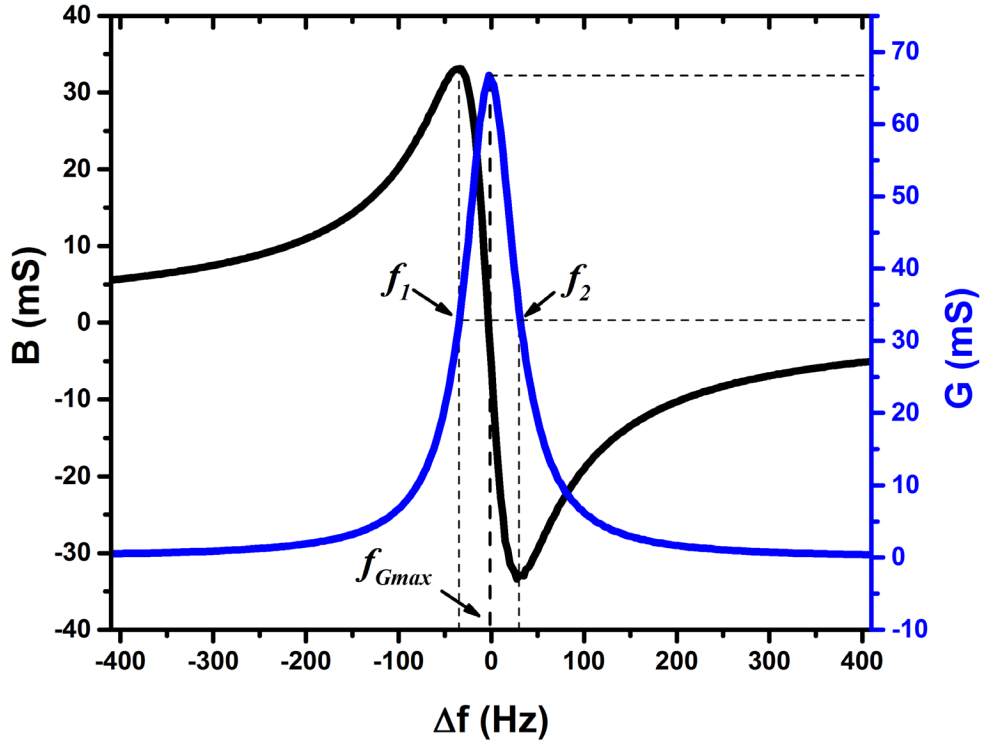

Figure 2.11: G-B plot for an unloaded QCM (same as in Figure 2.10) in air at room temperature.

2.2.2 Experimental

(a) Scheme

A typical EQCM experimental setup is depicted in Figure 2.12. The electrochemistry is conducted in a standard three-electrode configuration consisting of the working, the reference and the counter electrode. The front electrode of the QCM crystal in contact with the solution acts as the working electrode. The composite resonator is driven at the resonant frequency by the

oscillator circuit controlled by the QCM controller. The QCM controller also includes the frequency monitor module that measures the frequency changes. To avoid cross-talk between the electrochemical and the frequency measurements, the oscillator circuit is galvanically isolated from the electrochemical circuit. Finally, the electrochemical data from the potentiostat and the frequency information from the frequency monitor are collated using a software program in a computer. Details of the various components in the setup are discussed below.

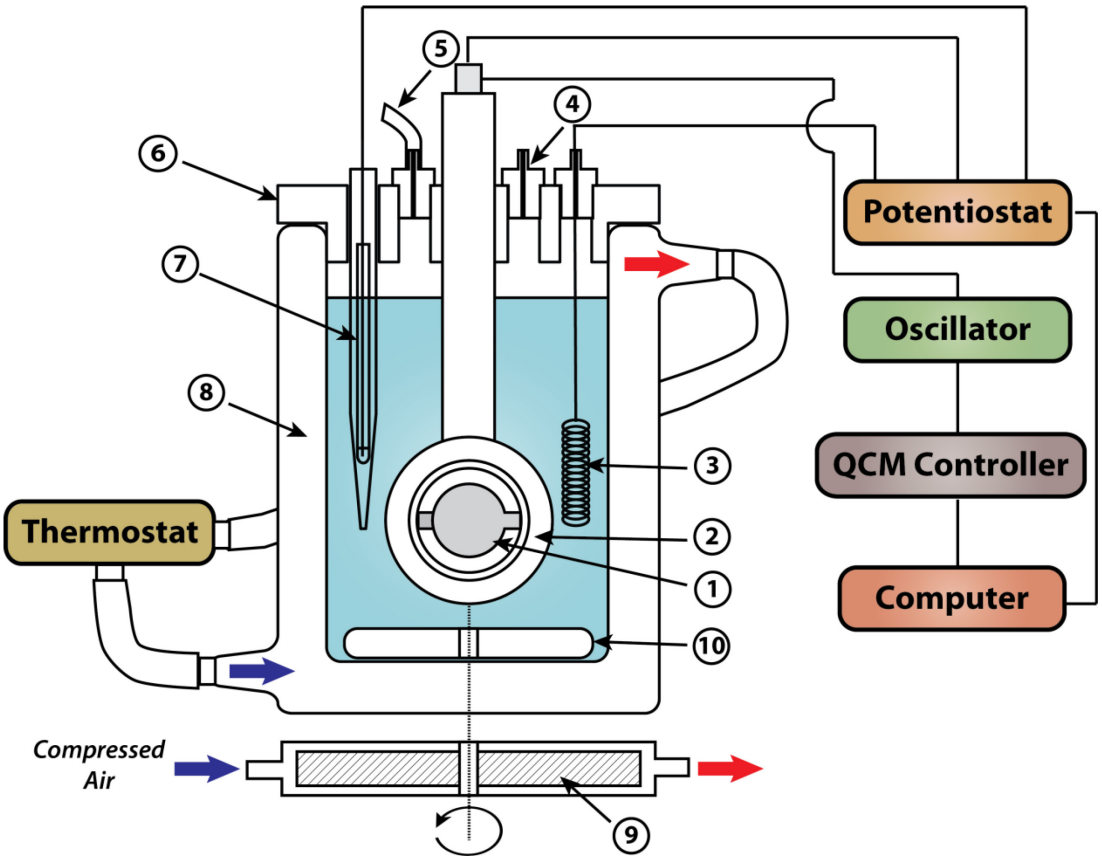

Figure 2.12: Experimental scheme for EQCM. 1 - Working electrode (front electrode of the QCM), 2 - QCM holder, 3 – Counter electrode, 4 – Purge gas outlet, 5 – Purge gas inlet, 6 – Cell cover, 7 – Reference electrode, 8 – Water jacket, 9 – Magnet, 10- Stir bar

(b) Cell

Due to the sensitivity of the QCM to temperature variations, a constant temperature is maintained in the glass electrochemical cell by employing a thermostat (Fischer Scientific

Model No. 9101) operating in conjunction with a water-cooled jacket enveloping the cell. The system is typically maintained at 25 °C. Stirring of the solution at a constant rate is useful to maintain a steady flow profile around the QCM and in mitigating frequency drifts/fluctuations from natural convection currents in the solution. A stir bar rotated by a magnet underneath the cell can be setup to achieve this. However, an electrically operated magnetic stirrer will introduce unwanted electrical noise in the frequency measurements. Hence, the magnet is driven by an air-jet from a compressed air supply. Typically, stirring rates of ~ 300 rpm are used. The rotation rate of the stir bar can be read using a laser tachometer. A home-made Teflon cell cover is used to hold the crystal holder and the auxiliary electrodes. It also has ports to allow purging the headspace with desired gases. Reversible hydrogen electrode (RHE) or Ag/AgCl electrode is used as the reference electrode. Generally, the reference electrode is separated from the solution in the main compartment by a salt bridge. Pt-wires are used as counter electrodes.

(c) Quartz Crystals

As mentioned earlier, the front electrode, in contact with the solution, of the quartz crystal acts as the working electrode. 5 MHz AT-cut quartz crystals with polished electrode surfaces where purchased from a series of vendors (Maxtek, Inficon, Tangidyne and Stanford Research Systems). It is important for the electrode surfaces to be polished since rough surfaces will have surface cavities that can trap liquid affecting the accuracy of the frequency measurements. The electrode materials were either Pt or Au (100-150 nm). To aid adhesion of the electrode material to the quartz crystal, a thin layer of Ti (15-20 nm) is deposited on the quartz crystal. Use of Cr as the adhesion layer is not recommended for EQCM experiments due to the diffusion of Cr to the electrode surface. In some cases, due to the need for metal electrodes other than Au or Pt for electrochemical experiments, thin films of metals are sputter-

deposited on top of the Au or Pt front electrode surface. All the quartz crystals used are 1" in diameter. The electrodes are arranged in the asymmetric keyhole configuration. For the commonly employed electrode configuration, the front electrode (solution side) is ≈ 0.5" in diameter (geometric area = 1.37 cm^2) and the back electrode is ≈ 0.25" in diameter (geometric area = 0.32 cm^2). In some cases, crystals with smaller front electrodes (≈ 0.25" in diameter) were used; the back electrodes are the same size in this case.

(d) QCM Measurement Systems

Two systems were used for the QCM measurements – Maxtek and Stanford Research Systems (SRS). The details of each system are given below.

i. Maxtek System

The crystals are mounted in a Teflon holder (Model No. TPS-550) that included the oscillator circuit. The holder is connected to the plating monitor (Model No. PM-740) using a shielded tri-axial cable. The frequency output from the plating monitor is transmitted via a RS-232 cable to the serial port of the computer. A home-made LabWindows program collects both the frequency and the electrochemical data.

ii. SRS System

This system has the benefit that the motional resistance *R* can be measured along with the resonant frequency. The crystals are mounted in a Teflon holder (Model No. O100RH). The oscillator circuit is in a separate electronics module (Model No. O100RXO) that is connected to the holder through a BNC connector. The electronics module achieves the galvanic isolation of the frequency measurement from the electrochemical measurement. The module outputs the frequency data through a RJ-45 connection, via a Cat-5 cable, to the QCM controller (Model No. QCM 200). The QCM controller transmits the data via a serial connection to the computer where

a SRS LabVIEW program (SRS QCM 200) collects the frequency and the resistance data. The electrochemical data is acquired using a separate home-made LabVIEW program.

(e) Electrochemical Measurement

The potentiostats employed were the Pine AFCBP1 Bipotentiostat and the BASi CV-27 voltammograph. The data was recorded by home-made LabVIEW/LabWindows programs using NI-DAQ cards to interface with the potentiostat.

(f) Impedance Analysis

Impedance analysis of the QCM composite resonators was carried out using Hewlett-Packard impedance analyzer (Model No. HP4194A). The 16047D test fixture (Hewlett-Packard) was used to connect the crystal to the analyzer. It is to be noted that for the impedance measurements the SRS crystal holder without the oscillator circuit need to be used as the impedance analyzer scans the frequency while acquiring the impedance response of the resonator. A standard operating procedure for impedance measurements can be closely modeled on the procedure detailed for the impedance characterization of a ceramic resonator included in the HP4194A manual (Section 3-3-2).

(g) EQCM Calibration

Theoretically, the calibration constant C_f (also known as the sensitivity factor) can be calculated using Equation 2.3. It is apparent that C_f is an intrinsic property of the quartz crystal independent of its environment. At 25 °C for a 5 MHz AT-cut quartz crystal, C_f = 56.6 Hz/μg/cm^2. However, in practice, especially for liquid operation C_f may be different from the theoretical value and may need to be determined experimentally. The calibration of the quartz crystal in the EQCM setup is achieved via the electrochemical deposition of thin layers of metals such as Ag[10,11] to introduce mass changes at the quartz crystal. A galvanostatic deposition

method is usually employed. In this case, the charge Q passed for the duration of deposition, t, can be directly calculated by $Q=I\,t$ where I is the current density. The mass change Δm at the electrode can then be calculated from Q using Equation 2.10.

Equation 2.10: $$Q = It = \left(\frac{\Delta m}{MW}\right) nF$$

where n is the number of electrons transferred per metal atom deposited, MW is the molar mass of the metal, and F is Faraday's constant. Finally, C_f (Hz/μg/cm^2) can be calculated from the slope S (Hz/s) of the Δf vs t plot as per Equation 2.11.

Equation 2.11: $$C_f = \frac{S\ n\ F}{I\ MW}$$

where F is in C/mol, I is in μA/cm^2 and MW is in g/mol.

Figure 2.13 shows the galvanostatic deposition of Ag on Pt QCM electrode for the purpose of calibration. In this case, the C_f was calculated to be 56.6 Hz/μg/cm^2 in agreement with the theoretical value. However, a similar calibration procedure using Cu deposition yielded C_f = 20.3 Hz/μg/cm^2. It is important to keep in mind that growth of metal layers electrochemically is influenced by a variety of factors such as the composition of the metal plating solution and the concentration of the components of the solution, the current density used and even the relative positions of the counter and the reference electrodes. These factors can affect the film growth; most importantly the roughness of the film. This can undesirably affect the calibration procedure since, as mentioned previously, rough surfaces introduce spurious effects in the frequency measurements. Hence, the validity of the calibration procedure as it relates to the system being studied should be carefully examined. Additionally, as should be evident, this calibration procedure is valid only for rigid films and is inapplicable to viscoelastic films.

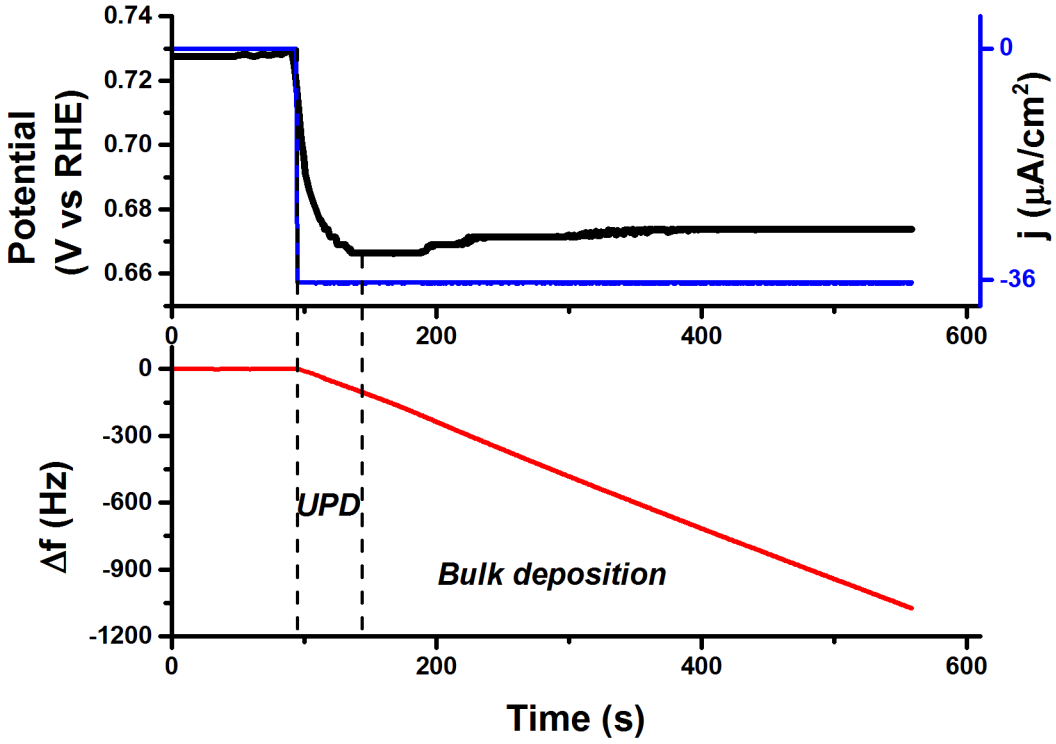

Figure 2.13: EQCM calibration using Ag deposition on a 5 MHz AT-cut Pt quartz crystal. 1 mM $AgNO_3$ in 0.1 M HNO_3. Current density: -36 μA/cm^2.

(h) Further Experimental Considerations

As noted earlier, temperature stabilization of the EQCM is critical for mitigating frequency drifts/fluctuations. Typically, it takes about 2-3 hrs for the thermostat to be effective in stabilizing the temperature of the solution and for the crystal to display a steady frequency. If the frequency continues to drift significantly, even at longer times, most likely the crystal holder is not sealed properly. In this case, there could be slow leakage of the solution into the crystal holder that will delay achieving steady state. This can be easily corrected by disassembling, cleaning and retightening the crystal holder. Additionally, there could be unwanted strain on the crystal due to its compression in the crystal holder and/or the sealing O-rings themselves may swell in contact with the solution causing the frequency to drift. These are more difficult to

counter. From a practical point of view, if the frequency drift is not significant over the time scale of the experiment then the frequency data can be corrected by subtracting the background.

2.3 References

(1) Bruckenstein, S.; Gadde, R. R. *Journal of the American Chemical Society* **1971**, *93*, 793–794.

(2) Wolter, O.; Heitbaum, J. *Berichte der Bunsengesellschaft für physikalische Chemie* **1984**, *88*, 2–6.

(3) Wolter, O.; Heitbaum, J. *Berichte der Bunsengesellschaft für physikalische Chemie* **1984**, *88*, 6–10.

(4) Baltruschat, H. *Journal of the American Society for Mass Spectrometry* **2004**, *15*, 1693–706.

(5) De Groot, M. .; Koper, M. T. . *Journal of Electroanalytical Chemistry* **2004**, *562*, 81–94.

(6) Jusys, Z.; Massong, H.; Baltruschat, H. *Journal of The Electrochemical Society* **1999**, *146*, 1093–1098.

(7) Wang, H.; Löffler, T.; Baltruschat, H. *Journal of Applied Electrochemistry* **2001**, *31*, 759–765.

(8) Buttry, D. A.; Ward, M. D. *Chemical Reviews* **1992**, *92*, 1355–1379.

(9) Kanazawa, K. K.; Gordon, J. G. *Analytical Chemistry* **1985**, *57*, 1770–1771.

(10) Bruckenstein, S.; Shay, M. *Electrochimica Acta* **1985**, *30*, 1295–1300.

(11) Gabrielli, C. *Journal of The Electrochemical Society* **1991**, *138*, 2657.

CHAPTER 3
FORMATE ELECTRO-OXIDATION ON PLATINUM IN ALKALINE MEDIA*

3.1 Introduction

From the perspective of fundamental electrocatalysis, the simplicity of its chemical structure prompts the study of the electro-oxidation of $HCOO^-$ as an archetype electrocatalytic reaction for small organic molecules (SOM) electrocatalysis in alkaline media. Further, the study assumes significance for the alkaline electrocatalysis of more complicated molecules such as CH_3OH[1–3] and C_2H_5OH[4] as their electro-oxidation generate, among other species, $HCOO^-$ as the incomplete oxidation intermediate/product. The study of $HCOO^-$ oxidation on Pt is particularly relevant for methanol oxidation in alkaline media as $HCOO^-$ is suspected to be the main product of the latter reaction.[5] On the applied research front, the study of $HCOO^-$ oxidation is motivated by the revived interest in alkaline fuel cell systems[6] which, in turn, is largely due to the successful deployment of alkaline anion exchange membranes (AAEMs)[7,8] in these systems. In this context, it should be highlighted that $HCOO^-$ itself is a viable fuel in these systems and direct formate fuel cells employing AAEMs have been demonstrated recently.[9,10]

The current study seeks to gain insight into the mechanism of $HCOO^-$ oxidation on Pt. Prior literature on formate electro-oxidation on Pt is scarce. The earliest work, as far as known, is by Buck and Griffith.[11] They observed low oxidation currents at very basic pHs (12-14) compared to acidic and neutral pHs. The system was also studied by Conway and Dzieciuch.[12] They performed a comparative study of decarboxylation reactions of trifluoroacetate and formate

*Adapted and reproduced in part with permission from John, J., Wang, H., Rus, E. D., & Abruña, H. D. (2012). Mechanistic Studies of Formate Oxidation on Platinum in Alkaline Medium. The Journal of Physical Chemistry C, 116(9), 5810–5820. doi:10.1021/jp211887x. Copyright 2012 American Chemical Society.

in aqueous (alkaline) and non-aqueous media. The reactions were found to be more complex in aqueous medium. Wetzel et al. investigated $HCOO^-$ oxidation on Pt in the pH region of 10 to 13.5.[13,14] They also observed low currents but reported an abrupt enhancement of the oxidation rate when the solution pH fell below ~12.6. Beden et al.[15] and Adzic et al.[16] saw particularly high activity of Pt for $HCOO^-$ oxidation in neutral medium vis-à-vis HCOOH in acidic medium. With the aim of understanding the role of $HCOO^-$ in methanol oxidation, an in-situ FTIR study of $HCOO^-$ oxidation on Pt was carried out recently by Christensen et al.[17] They were able to detect formation of adsorbed CO (CO_{ads}), both linear-bonded (CO_L) and bridge-bonded (CO_B), from adsorbed formate ($HCOO_{ads}$). However, the mechanism of the electro-oxidation itself is yet to be established.

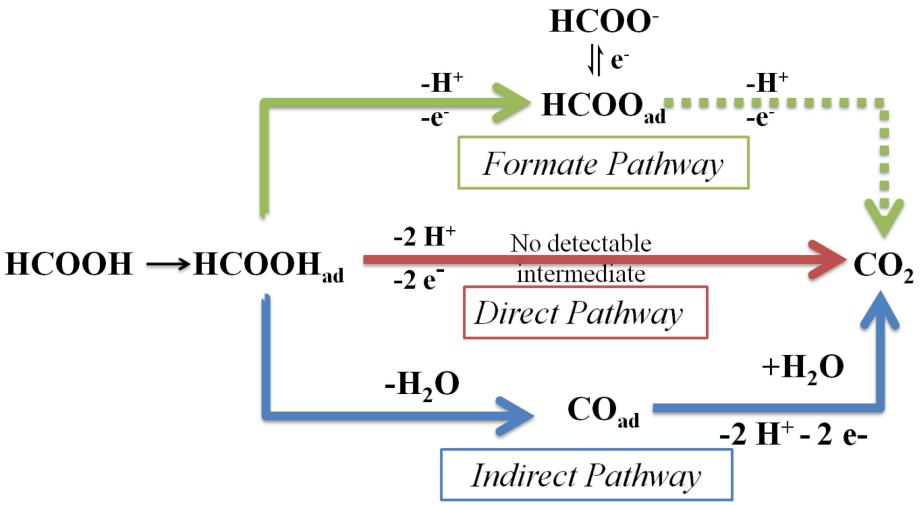

Figure 3.1: Proposed pathways for HCOOH oxidation

Prior to delving into the discussion of $HCOO^-$ oxidation, it is useful to review its counterpart in the acidic medium, viz. HCOOH electro-oxidation on Pt. Compared to $HCOO^-$ oxidation, HCOOH oxidation on Pt has been the subject of intensive research for over four decades.[18–31] Over the years, a dual path-way mechanism of HCOOH oxidation has come to be generally accepted.[19,26,30] A generalized scheme showing all the major pathways proposed in

literature so far is shown in Figure 3.1. The traditionally accepted dual-pathway mechanism encompasses the direct and the indirect pathways. In this scheme, HCOOH can undergo rapid and direct oxidation to CO_2 via the direct pathway. The reactive intermediate in this pathway is believed to be [Pt]-COOH. [19,26,30] Alternatively, HCOOH can decompose to the poisoning species, adsorbed CO (CO_{ads}), which can be subsequently oxidized to CO_2 at higher potentials. [26]

Recently, based predominantly on in-situ FTIR studies, a third pathway involving adsorbed formate ($HCOO_{ads}$) as the active intermediate has been proposed.[32–38] Due to the proposed involvement of $HCOO_{ads}$, insights into the prevalence and the role of this third pathway is likely to be of significance to $HCOO^-$ oxidation in alkaline medium and vice-versa. Hence, the current study would, additionally, serve to shed some light on the reactivity of $HCOO_{ads}$; albeit, with the important caveat that the investigations are done at basic pH (pH=14) where the electrochemical environment is vastly different compared to the acidic conditions for HCOOH oxidation.

3.2 Experimental

3.2.1 Electrochemical Measurements

Cyclic voltammetry by itself and in combination with DEMS were employed in this study. DEMS is particularly useful for monitoring product formation during $HCOO^-$ oxidation (in this case, CO_2 is the sole product) without interferences from the Pt-surface processes and the double-layer charging. Due to the low reactivity of $HCOO^-$, the latter processes contribute significantly to the measured current.

For conventional cyclic voltammetric studies, a standard three-electrode electrochemical cell was used. For adsorbate stripping experiments, without the mass spectrometric measurement, a home-made dual thin-layer DEMS flow cell was employed allowing for the

exchange of the analyte and the blank (supporting electrolyte) solutions. This cell has been described in section 2.1.2.b. To accomplish the fast exchange between the analyte and the blank solutions while maintaining the working electrode under potential control, a three way luer valve was used to switch between reservoirs of blank and analyte solutions. For these non-DEMS measurements, polycrystalline Pt disks (5 or 10 mm in diameter) were used as the working electrode. In case of the thin layer flow cell, used for adsorbate stripping experiments, a circular area, 6 mm in diameter, of the Pt disk is exposed to the solution.

Due to the rapid conversion of CO_2 to CO_3^{2-} in alkaline conditions, mass spectrometric detection of CO_2 is not possible using the dual thin-layer flow cell the configuration employed for the adsorbate stripping experiments described above. As elaborated in section 2.1.2.c, for alkaline operation of DEMS for CO_2 detection, the salient feature is the use of a catalyst sputtered porous membrane in lieu of the traditional disc electrode as the working electrode. Since CO_2 generation in this case occurs right on the porous membrane, the CO_2 can partition rapidly into the vacuum chamber for detection before being completely converted to CO_3^{2-} by the base in the solution. A porous Teflon membrane (GORETEX) onto which Pt was sputtered to an average thickness of 30 nm was used as the working electrode for this study. Using the operational paradigm mentioned above, the DEMS studies were carried out in both the conventional DEMS cell, where the solution is stagnant, for cyclic voltammetry and the dual thin-layer flow cell for adsorbate stripping. Additional details can be found in section 2.1.2.

Measurements were made using an EG&GModel 173 potentiostat/galvanostat and a Model 175 universal programmer. For some experiments, a Pine AFCBP1 Bipotentiostat, a PAR Model M-273 potentiostat or a BASi CV-27 voltammograph was also used. Data were recorded by home-made LabWindows/LabVIEW data acquisition programs using a NI-DAQ card. All

solutions were deaerated with high purity argon (Airgas) for at least 30 min prior to the experiment. Measurements were carried out at room temperature. A large area Pt wire was used as the counter electrode and a RHE as the reference electrode. All potentials are referenced to RHE. Where current densities (**j**) are reported, the currents (**i**) are always normalized to the geometric surface area of the working electrode.

3.2.2 DEMS Apparatus

The details of the mass spectrometer system and the associated components, used for DEMS studies, are described in section 2.1.3. Briefly, for the current study, both the Prisma Plus and the Hi-Quard mass spectrometer systems from Pfeiffer vacuum were used. Quadera software (supplied by Pfeiffer vaccum) was used to control the mass spectrometer. The analog output signals from the mass spectrometer were acquired using a NI-DAQ card and recorded by a home-made LabVIEW program which also simultaneously recorded data from the concomitant electrochemical measurements.

3.2.3 Reagents

Solutions were prepared with high purity de-ionized water (18 MΩ cm Millipore Milli-Q). HCOONa (≥99.0 % ACS Sigma Aldrich) and HCOOH (88 % AR ACS Mallinckrodt) were used to make the analyte solutions. For preparing supporting electrolyte of desired pH, NaOH (99 % AR ACS Mallinckrodt), H_2SO_4 (99.999 % Aldrich) and $HClO_4$ (70 % ACS Reagent Fisher Scientific) were used. In some experiments, a constant ionic strength was maintained by the addition of $NaClO_4$ (anhydrous 98.0-102.0 % ACS Alfa Aesar) to the solution.

3.2.4 Electrode Preparation

Prior to each experiment, where polycrystalline Pt disks were used, the working electrodes were polished with 1 μm diamond paste (METADI Buehler) to a mirror finish, rinsed

with ultrapure water, and sonicated in ultrapure water three times, each time for 10 min. Pt wire counter electrodes were also flame annealed in a propane flame to ensure cleanliness. For all working electrodes, electrochemical cycling over the potential window from +0.05 to +1.4 V vs RHE at 100 mV/s was also carried out in the respective supporting electrolyte until clean Pt cyclic voltammograms were obtained. The sputtered Pt membrane electrodes where cleaned by electrochemical cycling alone. When comparable experiments were carried out in acid and in base, the same experimental conditions were maintained including using the same electrochemical cell, working electrode, reference electrode (RHE) and counter electrode; except, of course, the analyte and the supporting electrolyte solutions.

3.3 Results and Discussion

3.3.1 Comparison of HCOOH and $HCOO^-$ Oxidation CVs

Representative cyclic voltammograms of HCOOH oxidation in acid and $HCOO^-$ oxidation in base on Pt are shown in Figure 3.2. Since the voltammetric features of HCOOH oxidation (Figure 3.2a) are relatively well understood, [18–31] it is worthwhile to review the same for the sake of comparing them to those of $HCOO^-$ oxidation. In the positive-going scan, the onset of oxidation occurs at about ~0.2 V (see inset to Figure 3.2a). There are two anodic peaks: (i) a small peak at ~0.56 V (**Peak 1a**) corresponding to the direct oxidation of HCOOH at Pt sites not blocked by CO_{ads}, and (ii) a larger peak at ~0.9 V (**Peak 2a**) that has contributions from both the direct pathway and the indirect pathway (oxidation of CO_{ads}, see Figure 3.1). The oxidation through the direct pathway is enhanced due to the removal of site-blocking CO_{ads} by electro-oxidation.

HCOOH can also be oxidized in the Pt-oxide region albeit at a lower rate. The onset of this oxidative process is seen at ~1.2 V. This is thought to be due to the presence of catalytically

active surface oxides that can oxidize HCOOH, presumably through an Eley-Rideal mechanism.[11,30,39]

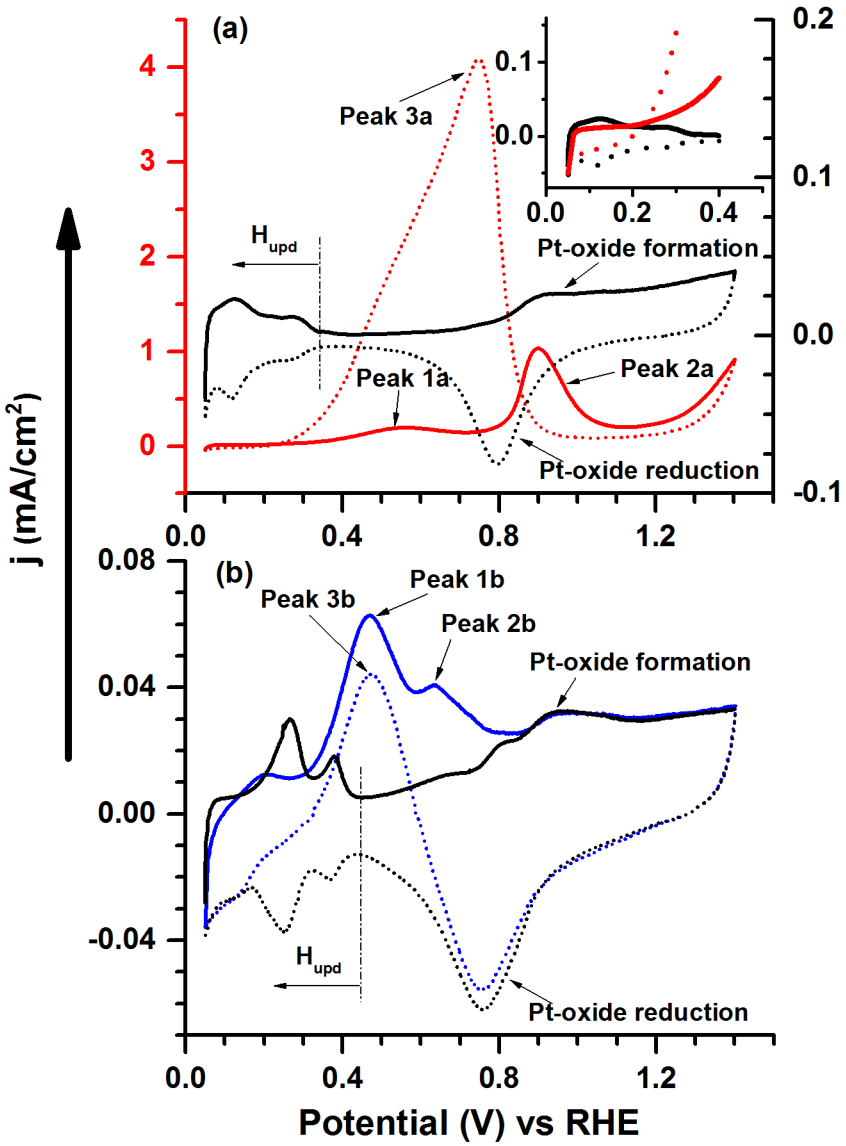

Figure 3.2: Cyclic voltammograms of (a) 0.2 M HCOOH in 1M $HClO_4$ (Red) on a polycrystalline Pt disk and (b) 0.2 M HCOONa in 1 M NaOH (Blue). Cyclic voltammograms of blank solutions (1 M $HClO_4$ and 1 M NaOH respectively) are shown in black. Inset to Figure 3.2a shows the H_{upd} region in 1 M $HClO_4$ (Black) and in the presence of 200 mM HCOOH (Red). Positive-going and negative-going segments of the cyclic voltammograms are shown by solid lines and broken lines respectively. Scan rate 20 mV/s.

In the negative-going scan, much higher currents are observed as a result of the facile electro-oxidation of HCOOH on the CO_{ads}-free Pt surface. As seen in Figure 3.2a, the onset of

the oxidation peak (**Peak 3a**) in the negative-going scan at ~0.9 V coincides with the incipient Pt-oxide reduction.

Since $HCOO^-$ oxidation would be affected by the Pt-surface processes, viz. H/OH adsorption-desorption and Pt-oxide formation/reduction, it is worthwhile to summarize from the literature the current understanding of these processes on Pt in alkaline medium vis-à-vis acidic medium.[40–42] In acid on Pt, H-adsorption/desorption and OH/O formation/reduction processes are well-separated on the potential scale by the traditional double-layer region where the surface is comparatively adsorbate-free. However, in alkaline medium, these processes are no longer separated; specifically, overlapping H and OH adsorption/desorption processes are thought to occur reversibly up to ~0.65 V vs RHE on Pt (100) and Pt (110) faces. The onset of OH adsorption on Pt in alkaline medium is quite early at ~0.35 V vs RHE.[42,43] An important consequence of this availability of OH_{ads} at low potentials is the well-documented earlier onset of CO oxidation on Pt in alkaline medium compared to acidic medium.[44–48]

While comparing the activities of HCOOH and $HCOO^-$ for oxidation (Figure 3.2), it is observed that the oxidative currents during $HCOO^-$ oxidation are significantly lower than those of HCOOH oxidation (~ 90x lower on comparing the peak currents for **Peak 3a** and **Peak 3b** in the negative-going scans) for the same bulk concentration of $HCOO^-$ and HCOOH. This indicates that $HCOO^-$ oxidation is more kinetically hindered than HCOOH oxidation. For $HCOO^-$ oxidation, two peaks (**Peak 1b** and **Peak 2b**) are observed in the positive-going scan and one peak (**Peak 3b**) in the negative-going scan (Figure 3.2b). The first peak (**Peak 1b**) in the positive-going scan and the peak (**Peak 3b**) in the negative-going scan occur at about the same potential (~0.47 V) and also have comparable peak currents. The second peak (**Peak 2b**) in the positive-going scan at ~0.63 V is smaller than the first peak (**Peak 1b**). Monitoring the CO_2

formation rate using DEMS serves to follow the $HCOO^-$ oxidation more easily as seen in Figure 3.3. Figure 3.3a shows a typical CV for $HCOO^-$ oxidation while the mass spectrometric cyclic voltammogram (MSCV) of CO_2 at m/z=44 (CO_2^+) recorded simultaneously is shown in Figure 3.3b. Based on the MSCV, the onset of $HCOO^-$ oxidation is observed at ~0.2 V. Also, no CO_2 is detected in the negative-going scan above ~0.7 V. It is apparent that $HCOO^-$ oxidation is completely suppressed in the Pt-oxide region. Hence it is concluded that $HCOO^-$ oxidation only occurs over a limited potential range approximately from 0.2 to 0.7 V.

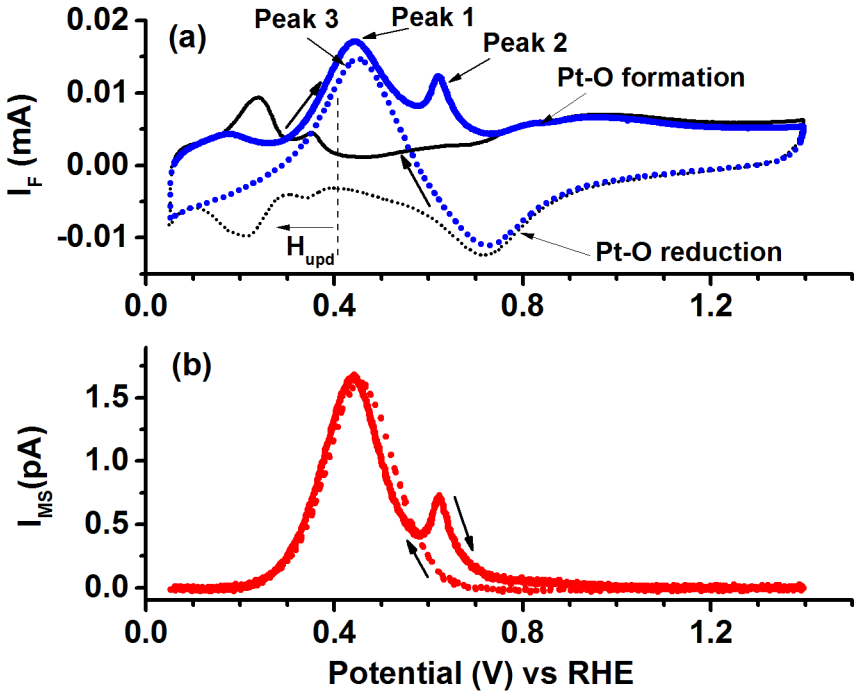

Figure 3.3: Simultaneously recorded (a) cylic voltammogram and (b) corresponding mass spectrometric cyclic voltammogram at m/z=44 (CO_2^+) for $HCOO^-$ oxidation on a Pt sputtered Teflon membrane in 0.1 M HCOONa + 1 M NaOH. Cyclic voltammogram of 1 M NaOH shown in black in (a). Positive-going and negative-going segments of the cyclic voltammograms are shown by solid lines and broken lines respectively. Scan rate: 10 mV/s.

It has been suggested that the dual pathway mechanism, active for HCOOH oxidation (Figure 3.1), is generally applicable to $HCOO^-$ oxidation.[18] In essence, analogous to HCOOH, it has been proposed that $HCOO^-$ can undergo oxidation either directly through a reactive

intermediate or indirectly through a chemisorbed or poisoning intermediate. The presence of a chemisorbed intermediate has been verified and identified as CO_{ads} by the recent in-situ FTIR study by Christensen et al.[17] The presence of the site-blocking CO_{ads} species is also apparent from the decrease of the Faradic charge under the broad H-desorption peak (~0.2 V) in the positive-going scan and the H-adsorption peaks in the range 0.05-0.3 V in the negative-going scan in Figure 3.2b. The identity of the reactive intermediate, if any, is yet to be established. It has been suggested that there are slow pre-chemical steps such as adsorption and/or formation of the reactive intermediate that could be rate-limiting.[11,49] Consequently, it has been proposed that the low activity of $HCOO^-$ can be attributed to such limiting processes in alkaline solution. [18,49] Guided by such proposals, the origins of the voltammetric features of $HCOO^-$ oxidation is sought in the current study.

Separation and identification of Faradaic processes associated with $HCOO^-$ oxidation is problematic due to the significant overlap between processes. Referring to Figure 3.3, it is clear that the potential ranges of the Faradaic processes underlying the two peaks (**Peak 1** and **Peak 2**) in the positive-going scan overlap considerably. Given that CO_{ads} formed from $HCOO^-$ has already been detected[17] and that the oxidation of bulk and adsorbed CO has already been observed at potentials at which **Peak 2** occurs,[48] it can be concluded that **Peak 2** has contributions from the oxidation of CO_{ads}. Due to similar peak positions and onset potentials, the oxidative process underlying **Peak 1** in the positive-going scan and **Peak 3** in the negative-going scan is inferred to be the same. As concluded earlier, based on the DEMS results (Figure 3.3b), this Faradaic process is active over a potential range approximately from 0.2 to 0.7 V. One possibility is the oxidation of CO_{ads}. It is well known that, on Pt, CO_{ads} can be oxidized at significantly more negative potentials (as low as 0.35 V [47]) in base than in acid. [44–48] Hence, we

should expect a contribution from CO_{ads} oxidation to **Peak 1**. However, CO_{ads} oxidation cannot account for the quite negative onset (~0.2 V) of $HCOO^-$ oxidation at which potential no OH-adsorption is expected to occur. [42,43] This is also supported by the findings from the in-situ FTIR study of $HCOO^-$ oxidation by Christensen et al.[17] where they observed CO_3^{2-} formation at a potential lower than the onset of OH-adsorption. Thus, it is inferred that this process involves the oxidation of $HCOO^-$ by another pathway not involving CO_{ads}. Hence, the current results also support, in essence, the dual pathway mechanism of $HCOO^-$ oxidation. In summary, it appears that **Peak 2** is mainly oxidation of CO_{ads} analogous to the indirect pathway of HCOOH oxidation. **Peak 1** corresponds mainly to an oxidative pathway likely not involving CO_{ads}. Since it is not certain that $HCOO^-$ is directly converted to CO_2 in this pathway, it is appropriate to call this oxidative process the *primary pathway* rather than the direct pathway. Following this convention, the traditional indirect pathway proceeding through CO_{ads} oxidation is designated as the *secondary pathway*.

On comparing CVs of $HCOO^-$ and HCOOH oxidation, we find notable differences (see Figure 3.2). In the case of HCOOH oxidation (Figure 3.2a), it is generally observed that the removal of the site-blocking CO_{ads} by electro-oxidation results in a significant enhancement of HCOOH oxidation. This is seen from the higher currents for the second peak (**Peak 2a**) compared to the first peak (**Peak 1a**) in the positive-going scan and also from the significantly higher currents during the negative-going scan. Analogously, in the case of $HCOO^-$ oxidation, if CO_{ads} were highly inhibitory, an increase in $HCOO^-$ oxidation rate is expected upon removal of CO_{ads}. However, as noted earlier, low currents are observed in both the positive and the negative-going scans for $HCOO^-$ oxidation. In fact from Figure 3.3b, it is seen that the peak currents, as indicated by the mass spectrometric currents, are comparable in the positive and the negative-

going scans. It is also noted that that the second peak (**Peak 2b**) is smaller than the first (**Peak 1b**) in the positive-going scan. From these observations, it seems that the surface blocking by CO_{ads} formation from $HCOO^-$ is not the primary reason for the apparent low activity of $HCOO^-$.

$HCOO^-$ oxidation is completely inhibited in the Pt-oxide region (see Figure 3.2 & Figure 3.3). This is in contrast to HCOOH in acid where Pt-oxide is catalytically active towards oxidation of HCOOH. [11,30,39] It may be that the Pt-oxide formed in alkaline solution is unreactive towards $HCOO^-$. It is also important to consider the charged nature of $HCOO^-$. In the Pt-oxide region, at potentials well positive of PZC, [50–52] it is possible that $HCOO^-$ behaves just as a spectator anion at the surface. Significantly, Vela et al., [53] studying HCOOH and HCOONa oxidation at Pd in acid and alkaline solutions by in-situ FTIR spectroscopy, showed the presence of a predominant surface configuration of $HCOO^-$ in alkaline solution with the two O-atoms bound strongly to the Pd surface and the C-H bond normal to the surface. Employing surface enhanced infra-red absorption (SEIRA) spectroscopy, a surface-sensitive in-situ FTIR technique, to study HCOOH oxidation in acid at Pt nanoparticles, Miki et al. show that $HCOO_{ads}$ is most likely to be in a bridging configuration on the Pt-surface with the molecular plane normal to the surface or slightly tilted.[32] Based on computational results, similar conclusions were reached by Neurock et al. [54] in the context of the role of $HCOO^-$ in HCOOH oxidation at Pt in acid. The overriding point of such studies is that the C-H bond activation by Pt in such a surface configuration would be difficult; consistent with the observed lack of activity for $HCOO^-$ oxidation in the Pt-oxide region. It is also interesting to note that $HCOO^-$ oxidation in the cathodic scan is initiated only after significant Pt-oxide reduction (see Figure 3.3). On the other hand, the onset of HCOOH oxidation coincides with the onset of the Pt-oxide reduction peak (see Figure 3.2a).

3.3.2 Concentration Dependence

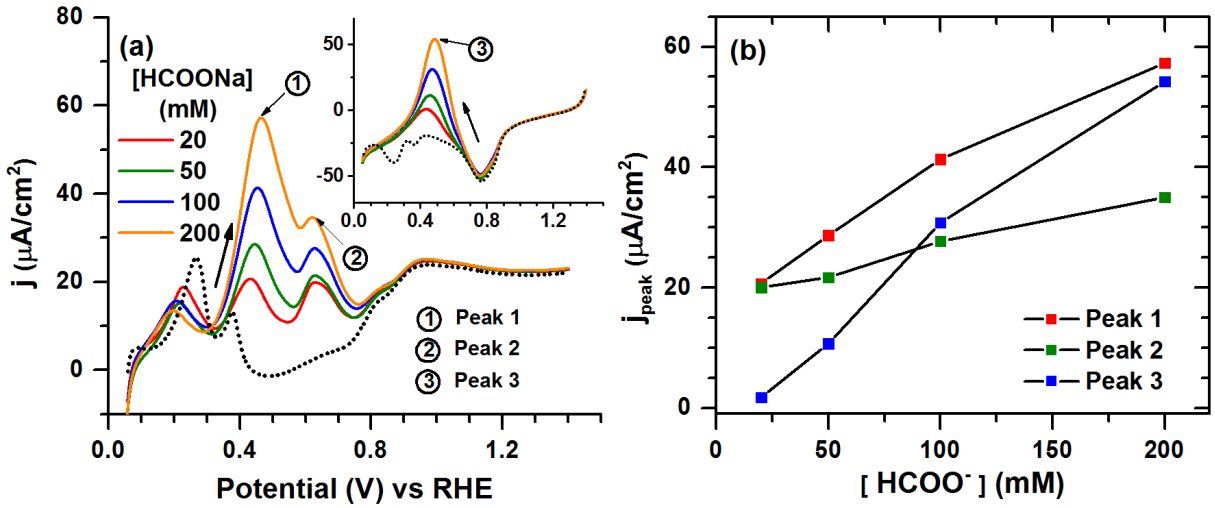

Figure 3.4: (a) Positive-going segments of cyclic voltammograms at different concentrations of HCOONa in 1 M NaOH with appropriate amounts of $NaClO_4$ added to keep the ionic strength constant at 1.2 M on a polycrystalline Pt disk. Inset shows the corresponding negative-going segments. Positive and negative-going segments of the cyclic voltammogram of 1 M NaOH + 0.2 M $NaClO_4$ are shown in dotted line. Scan rate 10 mV/s. (b) Peak currents ($\mathbf{j_{peak}}$) of the oxidation peaks in the positive and the negative-going scans plotted versus [$HCOO^-$].

To further understand the low activity of $HCOO^-$, the bulk concentration of $HCOO^-$ was varied while keeping [OH^-] the same and the ionic strength constant at 1.2 M (Figure 3.4a). This was achieved by the addition of appropriate amounts of $NaClO_4$ to the different analyte solutions. Examination of the anodic scans shows several trends in the voltammetric response (Figure 3.4b). Firstly, there is an increase of the first (**Peak 1**) and the second (**Peak 2**) peak currents in the positive-gong scan with [$HCOO^-$]. Since we expect $HCOO^-$ oxidation to be adsorbate mediated, it could be that there is an increase in the surface concentration of an active intermediate with [$HCOO^-$], dictated by an appropriate isotherm. Secondly, although both **Peak 1** and **Peak 2** increase, **Peak 1** increases faster than **Peak 2** with increasing [$HCOO^-$] i.e. the direct oxidation of $HCOO^-$ occurs to a greater extent than the oxidation of CO_{ads} at higher concentrations of $HCOO^-$. It is possible and likely that at high concentrations of $HCOO^-$, CO_{ads}

formed from $HCOO^-$ approaches the saturation coverage. Hence, the incremental increase in the charge of CO_{ads} oxidation would be less at higher [$HCOO^-$]. Thirdly, there is a progressive suppression of the H-desorption peak (~0.2 V) with [$HCOO^-$] possibly from increased CO_{ads} formation. The peak (**Peak 3**) in the negative-going scan (inset to Figure 3.4a), although smaller than **Peak 1**, also increases in magnitude with [$HCOO^-$]. It was previously noted (Figure 3.3) that the currents associated with **Peak 1** and **Peak 3** are comparable. Comparing the peak currents (Figure 3.4), we note that with decreasing [$HCOO^-$], **Peak 3** becomes smaller relative to **Peak 1**. This may be due to an increase in the inhibitory effects of OH adsorption at lower [$HCOO^-$] (vide infra).

3.3.3 Scan Rate Dependence

The effect of change in scan rate (**ν**) on $HCOO^-$ oxidation is shown in Figure 3.5. Since the oxidation currents (Figure 3.5a) are comparable to those from Pt-surface features, simultaneous MSCVs (Figure 3.5b) were recorded to separate out, in effect, the $HCOO^-$ oxidation currents. The mass spectrometric currents ($\mathbf{I_{MS}}$) were then used to investigate the variation of $HCOO^-$ oxidation peaks with **ν**. However, this method is limited to relatively low scan rates due to the limit imposed by the time response of the DEMS setup.

Of significance is the behavior of **Peak 1** in the positive-going scan and **Peak 3** in the negative-going scan with **ν**. **Peak 1** increases with increasing **ν** (Figure 3.5a). This is clearly seen in the corresponding mass spectrometric cyclic voltammograms of CO_2 at m/z=44 (Figure 3.5b). This is attributed to the time-dependent formation of the poisoning CO_{ads}. Longer the potential of the working electrode is held in the H_{upd} region, larger the amount of CO_{ads} formed. Thus, as the scan rate is increased, the amount of CO_{ads} formed decreases due to the decrease in the time required to traverse the H_{upd} region. Consequently, $HCOO^-$ oxidation is enhanced at

higher scan rates due to decreased surface blocking by CO_{ads}. Such an effect is also observed in case of HCOOH oxidation.[19,55,56] The former explanation is also consistent with the observation that only at low scan rates do we see a well-defined second peak, **Peak 2** (attributed mainly to CO_{ads} oxidation), in the positive-going scan.

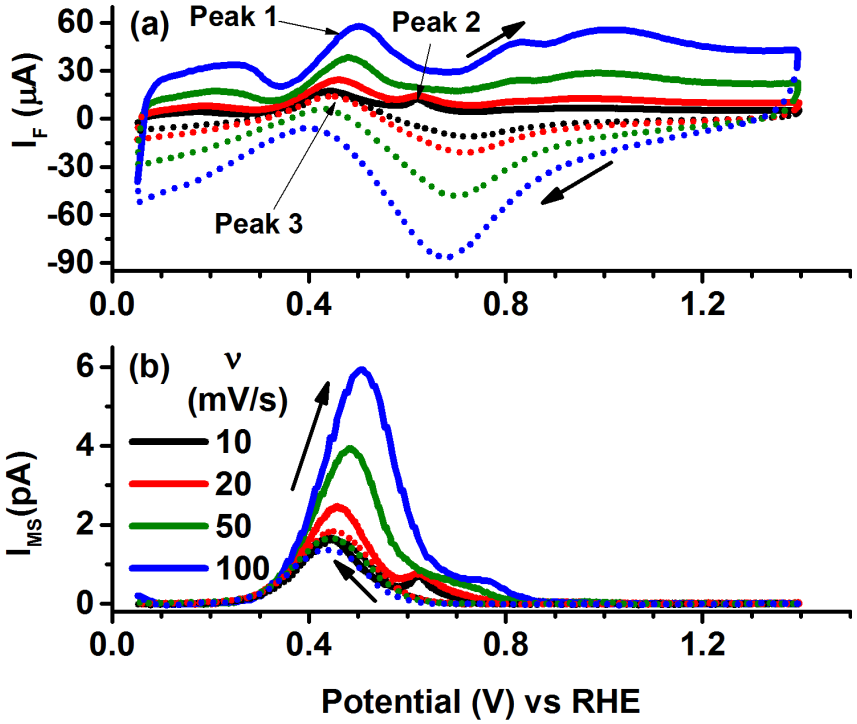

Figure 3.5: Simultaneously recorded (a) cyclic voltammograms and (b) corresponding mass spectrometric cyclic voltammograms at m/z=44 (CO_2^+) on a Pt sputtered Teflon membrane in 0.1 M HCOONa + 1 M NaOH at different scan rates (**ν**). Positive-going and negative-going segments of the cyclic voltammograms are shown by solid lines and broken lines respectively.

Interestingly, based on the mass spectrometric currents, $HCOO^-$ oxidation currents in the negative-going scans do not vary significantly with **ν** and are also smaller than that in the positive going scan (Figure 3.5b)**.** In fact, the negative-going scans in the MSCVs for different values of **ν** overlap to a large extent. This is most likely due to OH adsorption. This effect is explained as follows. As was mentioned earlier, OH adsorption occurs at all potentials beyond ~0.35 V. It is reasonable to assume that $HCOO^-$ is unlikely to displace the OH_{ads} already present. Thus, due to a lack of adsorption sites, $HCOO^-$ oxidation is inhibited in the negative-going scan.

Consequently, the $HCOO^-$ oxidation current in the negative-going scan would be smaller and independent of **v**. At the start of the positive-going scan (0.05 V vs RHE), however, no OH_{ads} is present. As the positive-going scan progresses, $HCOO^-$ in solution can better compete with OH^- for adsorption sites. This could explain the scan rate dependence of **Peak 1** in the positive-going scan and also the higher oxidation currents in the positive-going scan. It is noteworthy that, under similar basic conditions, CH_3OH which exhibits high activity on Pt also shows lower currents in the negative-going scan than in the positive-going scan.[57,58]

Interestingly, Buck and Griffith[11] observed an increase in the peak currents of $HCOO^-$ oxidation on decreasing the bulk pH from 14 to 10. This supports the idea of inhibition of $HCOO^-$ oxidation by OH adsorption. However, it is inherently difficult to isolate the effects of OH adsorption from adventitious processes. At lower pHs (pH < 13), due to the necessity of using a buffer system, the effect of the adsorption of counter ions other than OH^- needs to be considered. Moreover, even in a buffered system, the pH at the electrode surface can be sensitive to small changes in bulk pH.[14] As shown by Müller et al., [13] this becomes important for $HCOO^-$ oxidation since the changes in the surface pH could significantly change the relative concentrations of $HCOO^-$ and HCOOH near the electrode from their bulk solution values. In any case, it is clear that the effects of OH adsorption on $HCOO^-$ oxidation warrant careful study in the future.

3.3.4 Effect of CO_{ads}

(a) Cyclic Voltammetric Studies

It is known that the decomposition of HCOOH in acid to CO_{ads} (Figure 3.1) can take place in two ways.[26,59] First is the slow formation of CO_{ads} over a wide potential range (0.05 to 1.0 V) from the spontaneous dissociative adsorption of HCOOH. Another is the rapid

dehydration of HCOOH in the H_{upd} region (< 0.4 V). It is suspected that H_{ads} enhances the formation of CO_{ads} in this potential region.[19,26,31] It has been proposed that the latter method of CO_{ads} formation involves reduction of either the reactive intermediate Pt-COOH [19,26] or $HCOOH_{ads}$ [31] by H_{ads}. The effect of H_{ads} on the formation of CO_{ads} from HCOOH was studied by Capon and Parsons [19] by reversal of negative-going sweeps at different potentials ($\mathbf{E_{low}}$) in and near the H_{upd} region. The same strategy was followed to examine the analogous effect of H_{ads} on the formation of CO_{ads} from $HCOO^-$ and consequently on the primary and the secondary pathways of $HCOO^-$ oxidation. The results of such an experiment for HCOOH and $HCOO^-$ are shown in Figure 3.6a and Figure 3.6b, respectively.

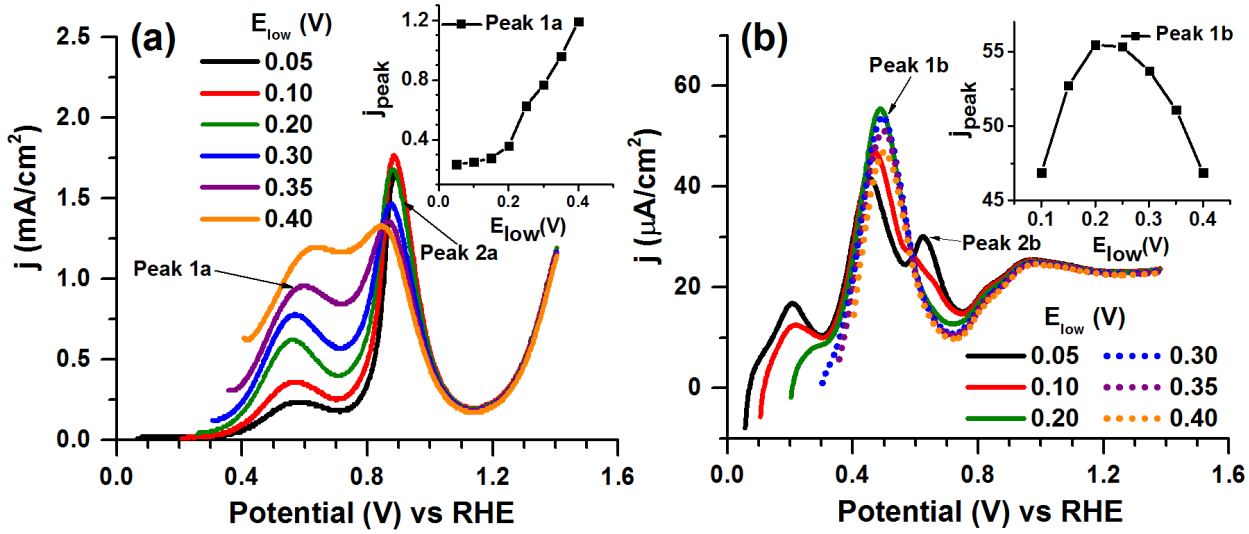

Figure 3.6: Positive-going segments of potential sweeps with different values for the lower limit of potential sweep ($\mathbf{E_{low}}$) (a) 0.1 M HCOOH in 1 M $HClO_4$ (b) 0.1 M HCOONa in 0.9 M NaOH. Scan rate 10 mV/s. Insets show plots of the peak currents for peaks Peak 1a and Peak 1b in the positive-going segment ($\mathbf{j_{peak}}$) versus $\mathbf{E_{low}}$.

The results for HCOOH agree with those reported by Capon and Parsons. [19] As the negative limit ($\mathbf{E_{low}}$) of the potential sweeps is shifted positive, there is an enhancement of the direct oxidation pathway. This is apparent from the increase in the peak current ($\mathbf{j_{peak}}$) of the first peak (**Peak 1a**) in the positive-going scan with increasing $\mathbf{E_{low}}$ (inset to Figure 3.6a). This is

clearly due to a decrease in the formation of site-blocking CO_{ads} with increasing $\mathbf{E_{low}}$. The second peak (**Peak 2a**) in the positive-going scan decreases to a small extent due to the decrease in CO_{ads} formation with $\mathbf{E_{low}}$.

Similarly, in the case of $HCOO^-$, the amount of CO_{ads} decreases with increasing $\mathbf{E_{low}}$. This is evident from the decrease in the second peak (**Peak 2b**) in the positive-going scan (Figure 3.6b). It is possible that CO_{ads} formation from $HCOO^-$ also involves H_{ads} just as in HCOOH. However, under the conditions of potential cycling employed, **Peak 2b** in the positive-going scan is not discernible when $\mathbf{E_{low}}$ is above 0.2 V. This could mean that, unlike the case of HCOOH, CO_{ads} formation from $HCOO^-$is restricted to low potentials in the H_{upd} region. The behavior of **Peak 1b** in the positive-going scan in the case of $HCOO^-$ oxidation is very revealing. Instead of a monotonically increasing peak, the first peak in the positive-going scan changes anomalously with $\mathbf{E_{low}}$. It grows initially, reaching a maximum at $\mathbf{E_{low}}\approx$0.2 V and then decreases. This is also shown more clearly in the plot of the peak current ($\mathbf{j_{peak}}$) with $\mathbf{E_{low}}$ (inset to Figure 3.6b). Such a behavior may be explained by the combined effect of inhibition of $HCOO^-$ adsorption by H and OH adsorption processes as follows. At quite low potentials ($\mathbf{E_{low}}\approx$0.05 V) in the H_{upd} region, H_{ads} can prevent the adsorption of $HCOO^-$. With increasing potential, however, more sites would be available for $HCOO^-$ to adsorb and undergo oxidation. Consequently, an increase in $HCOO^-$ oxidation is seen. However, at more positive potentials, $HCOO^-$ will have to compete with OH^- for adsorption sites; thus, $HCOO^-$ oxidation is again inhibited.

(b) Time Dependence of CO_{ads} Formation

The amount of CO_{ads} formed from HCOOH in the H_{upd} region, under potentiodynamic conditions, has been shown to be functions of both potential [59] and time.[19] Hence, it is

worthwhile to investigate such effects for CO_{ads} formation from $HCOO^-$. To this end, potential step – linear sweep voltammetric experiments were carried out.

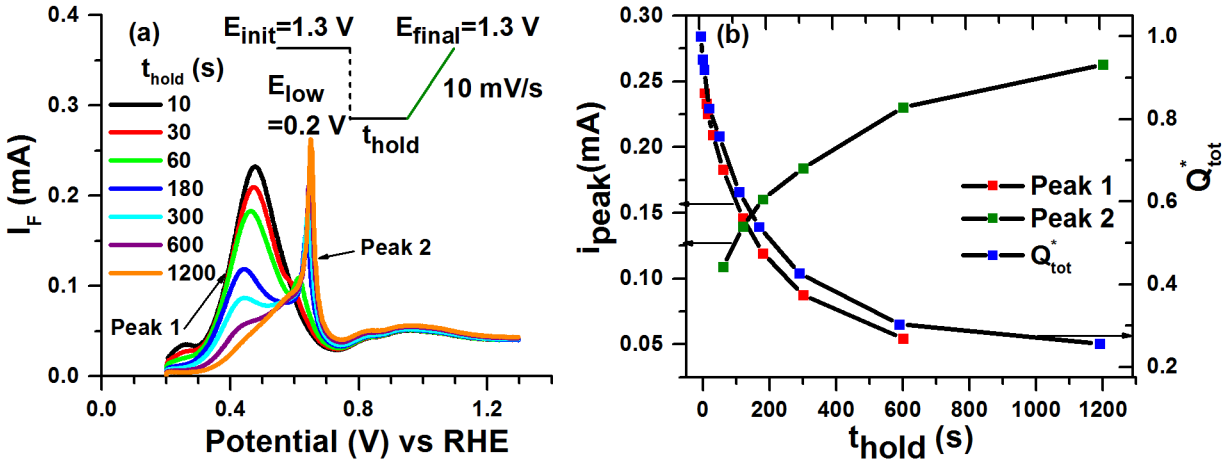

Figure 3.7: (a) Positive-going scans obtained after a potential step from 1.3 V to 0.2 V vs RHE and held for time $\mathbf{t_{hold}}$ at 0.2 V on Pt sputtered Teflon membrane in 0.1 M HCOONa + 1 M NaOH. Scan rate 10 mV/s. Inset shows the potential program followed. (b) Plots of the normalized charge of $HCOO^-$ oxidation, $\mathbf{Q_{tot}}^*$ and also the peak currents versus $\mathbf{t_{hold}}$.

For the time-dependent study of CO_{ads} formation, the potential program employed was as follows (see inset to Figure 3.7a). The potential of the working electrode was held initially ($\mathbf{E_{init}}$) at 1.3 V (where there is no oxidation of $HCOO^-$). The potential was then stepped to $\mathbf{E_{low}}$=0.20 V and held for varying amounts of time ($\mathbf{t_{hold}}$). The potential, $\mathbf{E_{low}}$, was chosen to minimize the effects from both H and OH adsorption as it was already indicated that $HCOO^-$ adsorption may be inhibited by the former processes. After time $\mathbf{t_{hold}}$, the potential was scanned from $\mathbf{E_{low}}$=0.20 V to $\mathbf{E_{final}}$=1.3 V. The positive-going scans thus obtained are shown in Figure 3.7a. The mass spectrometric current at m/z=44 (CO_2^+) recorded simultaneously can be used to obtain a measure of the total Faradaic charge of $HCOO^-$ oxidation ($\mathbf{Q_{tot}}$) through the primary and the secondary pathways from the mass spectrometric charge.

Briefly, for $HCOO^-$ oxidation, the mass spectrometric current ($\mathbf{I_{MS}}$) or the corresponding charge ($\mathbf{Q_{MS}}$) obtained by integration is linearly proportional to the Faradaic current ($\mathbf{I_F}$) or the Faradaic charge (in this case, $\mathbf{Q_{tot}}$) of $HCOO^-$ oxidation (Equation 3.1 & Equation 3.2).

Equation 3.1: $$I_F = \frac{nI_{MS}}{K^*_{44}}$$

Equation 3.2: $$Q_{tot} = \frac{nQ_{MS}}{K^*_{44}}$$

where **n** is the number of electrons involved in the oxidation of $HCOO^-$ (n=2, in this case) and $\mathbf{K^*_{44}}$ is the calibration constant.

For the purposes of analysis, $\mathbf{Q_{tot}}$, thus obtained, at a given time $\mathbf{t_{hold}}$, is normalized to the total charge at $\mathbf{t_{hold}}$=5 s to give the normalized total Faradaic charge, $\mathbf{Q^*_{tot}}$. The plot of $\mathbf{Q^*_{tot}}$ vs $\mathbf{t_{hold}}$ is shown in Figure 3.7b. The peak currents for the first (Peak 1) and the second (Peak 2) anodic peaks vs $\mathbf{t_{hold}}$ are also plotted (Figure 3.7b).

The Pt surface is gradually deactivated by CO_{ads} as shown by the overall decrease in the oxidation charge ($\mathbf{Q^*_{tot}}$) with time (Figure 3.7b). It is seen that substantial CO_{ads} formation occurs only at longer times; in the order of minutes. As seen from the $\mathbf{Q^*_{tot}}$ vs $\mathbf{t_{hold}}$ plot (Figure 3.7b), CO_{ads} formation approaches a saturation value only at times longer than 20 min. Under similar conditions of potential and concentration, saturation coverage of CO_{ads} from HCOOH is achieved in10s.[19,55,56] It is amply clear that CO_{ads} formation from $HCOO^-$ is quite slow vis-à-vis HCOOH.

The coupled behavior of **Peak 1** and **Peak 2** in the positive-going scans is apparent from Figure 3.7. As $\mathbf{t_{hold}}$ increases, **Peak 1** decreases and **Peak 2** increases and an isopotential point is obtained at ~0.6 V between **Peak 1** and **Peak 2**. This is also apparent from Figure 3.6b where the isopotential point, again at ~0.6 V, is clearly seen. Typically, an isopotential point is seen when

there are two adsorbed species such that their total area of coverage remains constant at all times.[60] In the context of the experiment, this would imply the presence of an adsorbate whose coverage is linearly dependent on the coverage of CO_{ads}. It is suspected that the adsorbate involved is the active intermediate in the primary pathway. This possibility is explored further in the adsorbate stripping experiments.

(c) Potential Dependence of CO_{ads} Formation

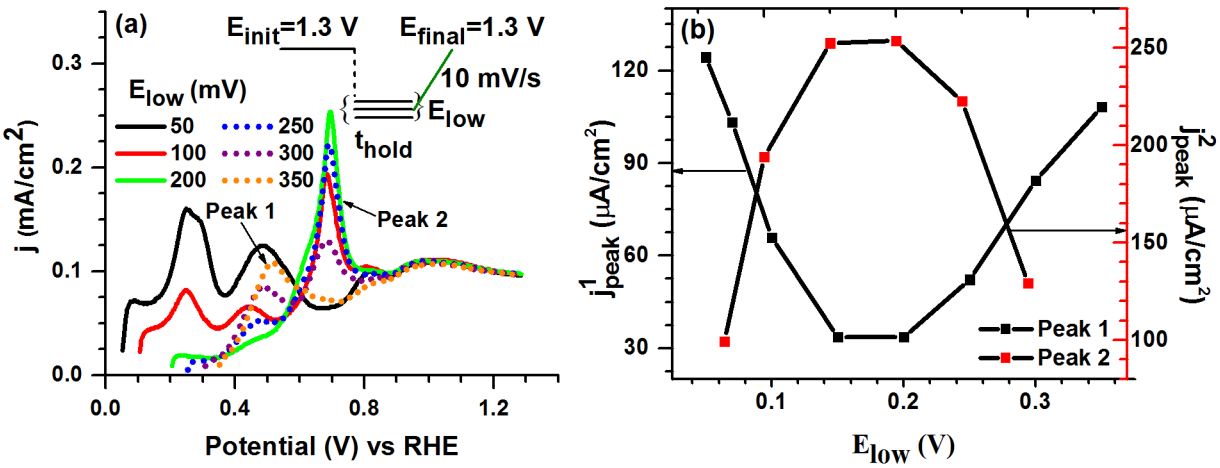

Figure 3.8: (a) Positive-going scans obtained after the potential step procedure shown in the inset was carried out in 0.1 M HCOONa + 0.9 M NaOH on a polycrystalline Pt disk for different values of $\mathbf{E_{low}}.\mathbf{t_{hold}}$=10 min. Scan rate 50 mV/s (b) Plot of the first ($\mathbf{j^1_{peak}}$) and the second ($\mathbf{j^2_{peak}}$) peak current density versus $\mathbf{E_{low}}$.

To study the potential dependence of CO_{ads} formation from $HCOO^-$, the previous potential step-scan procedure (inset to Figure 3.7) was modified to allow sufficient time for CO_{ads} formation. The potential program applied is shown in the inset of Figure 3.8a. From an initial potential of 1.3 V, the potential was stepped to a potential, $\mathbf{E_{low}}$ in the H_{upd} region and held for 10min ($\mathbf{t_{hold}}$) to allow sufficient time for CO_{ads} formation and then scanned anodically at 50 mV/s to 1.3 V. This procedure was repeated for different values of $\mathbf{E_{low}}$ ranging from 0.05 to 0.35 V vs RHE. Some representative positive-going sweeps obtained by this procedure are

shown in Figure 3.8a. The variation of the peak currents, $\mathbf{j^1_{peak}}$ and $\mathbf{j^2_{peak}}$, for the first (**Peak 1**) and the second peaks (**Peak 2**), respectively, in the positive-going scans with $\mathbf{E_{low}}$ are also plotted (Figure 3.8b). It is seen that the maximum CO_{ads} formation occurs over the potential range from 0.15 V to 0.2 V. Such a maximum for CO_{ads} formation from HCOOH has also been reported.[59] This has been attributed to a surface reaction, following Langmuir-Hinshelwood kinetics, that involves the reduction of either the reactive intermediate Pt-COOH[19,26] or $HCOOH_{ads}$[31] by H_{ads}. An analogous mechanism could be active in the case of $HCOO^-$. It is also to be noted that, although OH adsorption could inhibit $HCOO^-$ adsorption, the effect of the former should be negligible over the potential range (0.05-0.35 V) studied. Interestingly, **Peak 1** shows a trend opposite to that of **Peak 2** (Figure 3.8b) with the peak current ($\mathbf{j^1_{peak}}$) going through a minimum over the same potential range (0.15-0.2 V). This is further evidence for the strong correlation between the primary and the secondary pathways. Since $HCOO^-$ would not be able to displace the strongly bound CO_{ads}, the number of sites available for $HCOO^-$ adsorption and/or formation of the active intermediate in the primary pathway should be partly dictated by the coverage of CO_{ads} on Pt. This could explain the reciprocal relationship between **Peak 1** and **Peak 2**.

3.3.5 Adsorbate – Stripping Experiments

(a) Motivation

Since it has been indicated that $HCOO^-$ oxidation is highly adsborbate-mediated, stripping experiments were carried out. These experiments allow the delineation of the adsorbate contribution from that of the bulk $HCOO^-$ species to the Faradaic current measured. The DEMS flow cell described earlier (section 2.1.2.b) was employed for these experiments. Continuing the comparative treatment of HCOOH and $HCOO^-$ oxidation, the experiments were carried out in

both acid (1 M $HClO_4$) and base (1 M NaOH). The initial set of experiments, for both HCOOH and $HCOO^-$ oxidation, was carried out using a polycrystalline Pt bulk electrode without the DEMS measurement.

For $HCOO^-$ oxidation, the initial set of experiments was carried out using bulk Pt electrode as the working electrode in the upper chamber of the thin layer flow cell. As mentioned before, in this configuration, DEMS cannot be used to monitor CO_2 formation. Subsequent use of the Pt sputtered membrane as the working electrode in the bottom chamber allowed product monitoring for $HCOO^-$ oxidation using DEMS. The electrochemical measurements for $HCOO^-$ oxidation in both these configurations yielded the same qualitative results. Hence, for the purposes of the discussion, only the results from the DEMS stripping experiments for $HCOO^-$ oxidation are treated.

(b) Experimental Procedure

The potential profile applied to the working electrode and the solution exchange protocol followed during the adsorbate stripping experiment is depicted in Figure 3.9. At the start of the experiment, the working electrode is held at a potential, $\mathbf{E_{dose}}$ and exposed to the flow of blank solution (i.e. either 0.1 M H_2SO_4 or 1 M NaOH). Under potential control, the flow is then switched to the analyte solution (200 mM HCOOH in 0.1 M H_2SO_4 or 200 mM HCOONa in 1 M NaOH) for time $\mathbf{t_{dose}}$. Still maintaining potential control, at the end of time $\mathbf{t_{dose}}$, the flow is switched back to the blank solution and the cell flushed with blank solution for time $\mathbf{t_{hold}}$. Subsequently, a positive-going stripping scan is started from $\mathbf{E_{dose}}$ to the upper limit **(**1.4 V). A post-stripping scan from 0.05 V to 1.4 V was also performed to verify the absence of any electroactive adsorbates subsequent to stripping. A constant solution flow rate was maintained throughout. The dosing potentials ($\mathbf{E_{dose}}$) were sampled in the H_{upd} region.

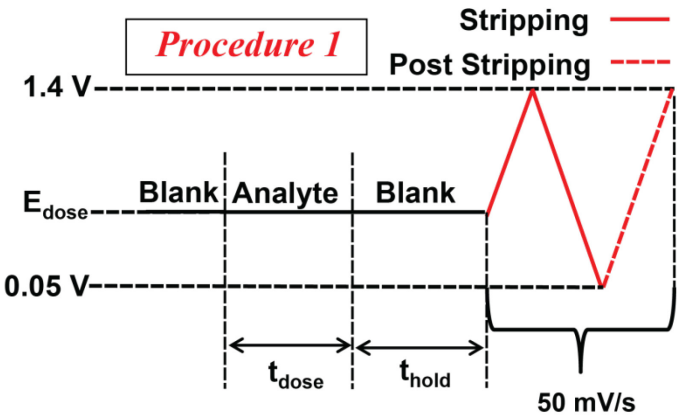

Figure 3.9: *Procedure 1*- Potential profile and solution flow program employed for the adsorbate stripping experiments.

(c) HCOOH Oxidation

It is instructive to discuss the adsorbate stripping for HCOOH oxidation first in order to contrast it with the results from $HCOO^-$ oxidation. For this experiment, procedure as depicted in Figure 3.9 is followed. The experimental parameters were: solution flow rate ~ 100 µL/s, t_{dose} ~ 5 s, t_{hold} ~ 120 s. The results are shown in Figure 3.10. In the case of acidic media (Figure 3.10a), there is only one stripping peak (**Peak A**) at ~0.7 V. This corresponds to the oxidation of CO_{ads}. No other stable adsorbate was detected. It is generally accepted that the reactive intermediate (Pt-COOH) in the direct pathway, once formed, is highly unstable immediately converting to the final oxidation product, CO_2.[26,30]

On plotting the peak current ($\mathbf{j_{peak}}$) for CO_{ads} stripping peak (**Peak A**) vs $\mathbf{E_{dose}}$, a maximum in CO_{ads} formation is observed at 0.2 V (Figure 3.10b). A similar maximum in CO_{ads} formation is reported by Sun and Yang.[59] They observed a maximum in the average rate of dissociative adsorption of HCOOH versus electrode potential for single crystal platinum electrodes. The current result provides additional support to the hypothesis that, at low potentials, H_{ads} is actively involved in the formation of CO_{ads}.[19,26,30]

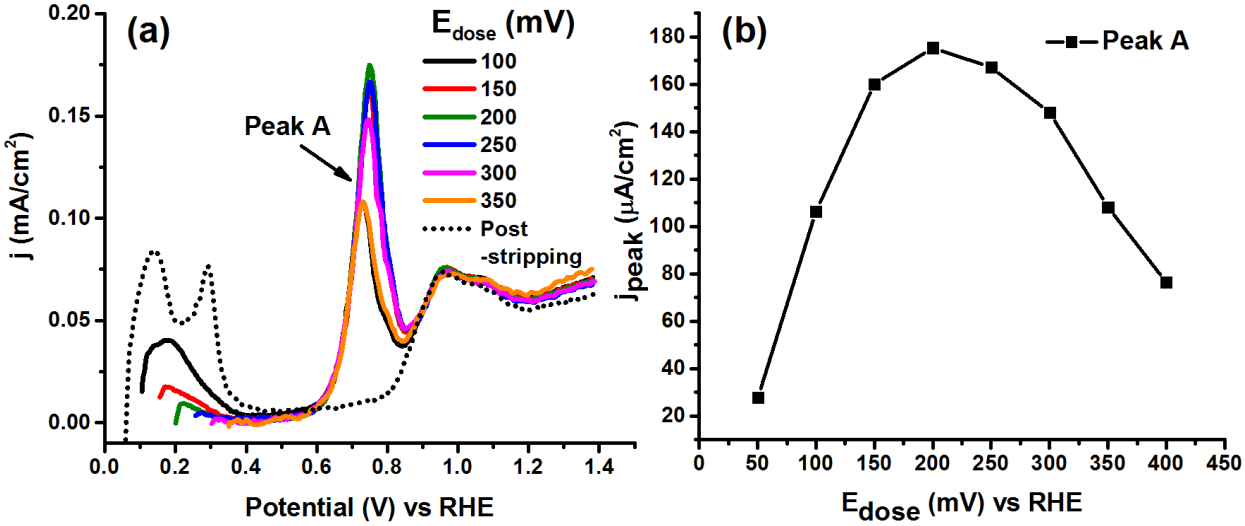

Figure 3.10: *Adsorbate stripping from HCOOH* – (a) Stripping scans at 50 mV/s obtained at a polycrystalline Pt disk for different values of $\mathbf{E_{dose}}$ following *Procedure 1* (Figure 3.9). Analyte solution: 0.2 M HCOOH in 0.1 M H_2SO_4, Blank solution: 0.1 M H_2SO_4. Solution flow rate: ~ 100 μL/s. $\mathbf{t_{dose}}$: ~ 5 s. $\mathbf{t_{hold}}$: ~ 120 s. Post stripping scans at 50 mV/s shown in black dotted line. (b) Plot of the peak current densities ($\mathbf{j_{peak}}$) versus $\mathbf{E_{dose}}$ for the stripping peak from (a).

(d) $HCOO^-$ Oxidation

Similar experiments, following *Procedure 1* (Figure 3.9), were carried out for $HCOO^-$ oxidation. The results from the DEMS adsorbate stripping experiments are shown in Figure 3.11. The mass spectrometric currents corresponding to the stripping scans at different values of $\mathbf{E_{dose}}$ are offset along the vertical axis for the sake of clarity. As mentioned previously, a Pt sputtered Teflon membrane was used as the working electrode for the detection of CO_2 in alkaline environment. The stripping scans for $HCOO^-$ show two broad peaks centered at ~0.5 V (**Peak B1**) and ~0.65 V (**Peak B2**). This is clearly seen from the mass spectrometric currents in Figure 3.11b. It should be noted that the potentials at which these stripping peaks occur match those of the first and the second peaks, respectively, in the positive-going scans in the presence of solution $HCOO^-$ (see Figure 3.3). This is further evidence that $HCOO^-$ oxidation is strongly mediated by adsorbates. For the sake of discussion, the adsorbates corresponding to **Peak B1** and **Peak B2** are called **X1** and **X2** respectively. Ostensibly, **X2** is CO_{ads}.

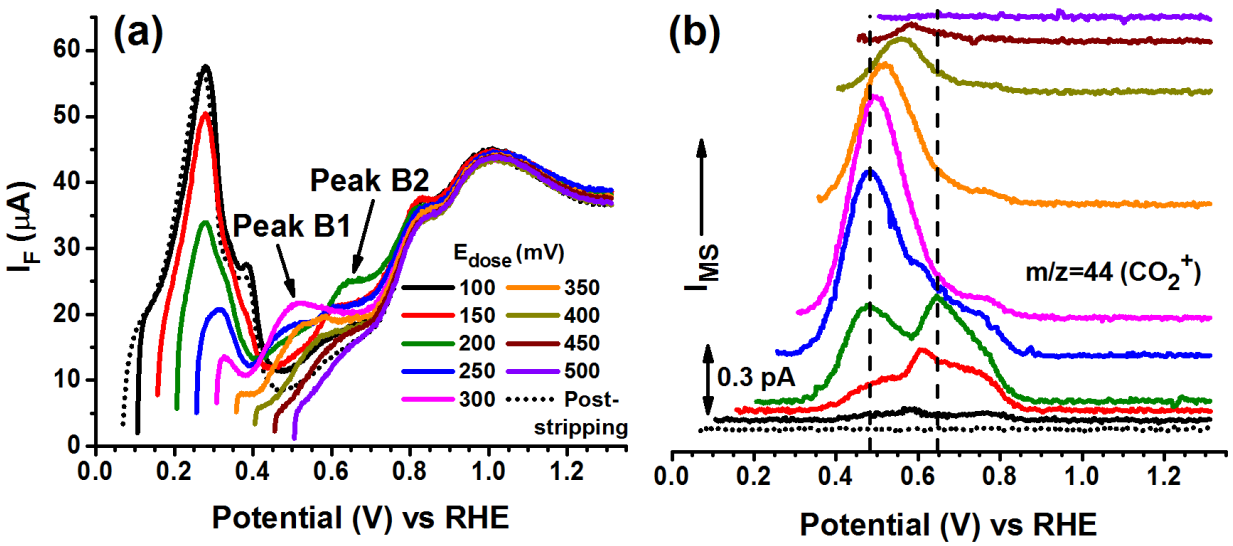

Figure 3.11: *Adsorbate stripping from HCOONa (Procedure 1)* – Analyte solution: 0.2 M HCOONa in 1 M NaOH, Blank solution: 1 M NaOH. Solution flow rate: ~ 15 µL/s. $\mathbf{t_{dose}}$: ~ 20 s. $\mathbf{t_{hold}}$: ~ 50 s. Post stripping scans at 50 mV/s shown in black dotted line. (a) Stripping scans at 50 mV/s obtained at the Pt-sputtered Teflon membrane for different values of $\mathbf{E_{dose}}$ following *Procedure 1* (Figure 3.9). (b) the corresponding mass spectrometric currents at m/z=44 (CO_2^+). The scans are offset for clarity. The legend is same as that of (a).

The mass spectrometric currents for different values of $\mathbf{E_{dose}}$ help to easily track qualitatively the relative amounts of **X1**and **X2**. At very low values of $\mathbf{E_{dose}}$ (~ 100 mV vs RHE), neither **X1** nor **X2** is formed in any significant quantity from $HCOO^-$. This is understandable since at these potentials the Pt surface has close to saturation coverage of H_{ads}. Hence, there may not be free sites available for $HCOO^-$ to adsorb. With further increase in $\mathbf{E_{dose}}$ (100 mV < $\mathbf{E_{dose}}$ < 200 mV), both **Peak B1** and **Peak B2** grow in intensity. However, from the relative peak ratios, it is evident that CO_{ads} is formed to a greater extent than **X1**. The availability of free sites at higher $\mathbf{E_{dose}}$ may allow adsorption of $HCOO^-$ at these potentials. It is also significant that there is preferred formation of CO_{ads} over **X1** in this potential range (100 mV < $\mathbf{E_{dose}}$ < 200 mV). This is in agreement with the results from the potential-step linear scan voltammetric experiments in the presence of $HCOO^-$ in solution discussed previously (Figure 3.8) where the maximum formation of CO_{ads} was shown to be in the range 0.15 – 0.2 V. Such observations strongly suggest the

catalytic role of H_{ads} in the decomposition of $HCOO^-$ to CO_{ads}. As $\mathbf{E_{dose}}$ (200 mV < $\mathbf{E_{dose}}$ < 300 mV) is increased further, the formation of CO_{ads} is inhibited and that of **X1** is enhanced as is apparent from the growth of **Peak B1** vis-à-vis **Peak B2**. It is possible that due to diminished availability of H_{ads} to catalyze the formation of CO_{ads} the adsorbed $HCOO^-$ preferentially forms **X1** at these potentials. Beyond $\mathbf{E_{dose}} \approx$ 300 mV, it is seen that the formation of **X1** is also inhibited. This is most likely due to the commencement of OH^- adsorption at these potentials that impedes $HCOO^-$ adsorption.

In contrast to HCOOH (Figure 3.10), the presence of two adsorbate stripping peaks **Peak B1** and **Peak B2** in case of $HCOO^-$ clearly signifies the existence of two stable electroactive adsorbates – **X1** and CO_{ads} (**X2**) - formed from $HCOO^-$. There are two possibilities as far as the identity of **X1** is concerned. It could be either $HCOO_{ads}$ or the active intermediate involved in the primary pathway. Of course, $HCOO_{ads}$ could also be the active intermediate. In order to elucidate the nature of the adsorbate, **X1**, a variation of the previous stripping experiment was carried out as per *Procedure 2* (Figure 3.12a). *Procedure 2* is the same as *Procedure 1* (Figure 3.9) except for an additional potential step at the end as detailed below. After holding the working electrode at potential $\mathbf{E_{dose}}$ for time $\mathbf{t_{hold}}$, the potential is stepped to 0.05 V and held for time $\mathbf{t_{step}}$. The stripping scan is then initiated from 0.05 V. As in the previous experiment, a constant flow rate of was maintained throughout the duration of the potential program.

The motivation for this experiment was to determine whether **X1** is weakly adsorbed or not. To aid discussion, the expected differences in the nature of the adsorbates on the Pt surface at the beginning of the stripping scans for the two procedures are schematically shown in Figure 3.12b. The rationale for the potential step to 0.05 V, after the initial adsorption of **X1** at a higher potential ($\mathbf{E_{dose}}$), was that, at such a low potential in the H_{upd} region, H_{ads} would displace any

weakly bound adsorbates. This would be the case for adsorption of anions such as $HCOO^-$. Consequently, **Peak B1** should be absent in the subsequent stripping scan, if **X1** is only weakly bound. Since CO_{ads} is strongly bound to Pt, it will not be displaced by H_{ads}. Hence, **Peak B2** should not change significantly by this procedure.

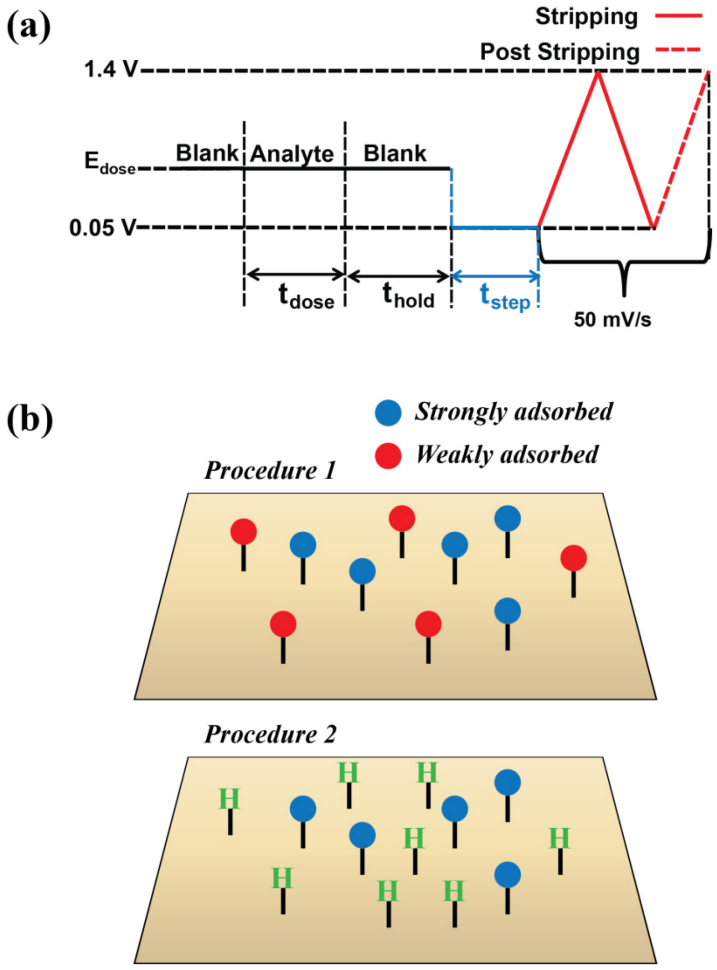

Figure 3.12: (a) *Procedure 2*- Modified potential profile and solution flow program for the adsorbate stripping experiment. The difference in procedure vis-à-vis *Procedure 1* (Figure 3.9) is highlighted in blue. (b) Schematic showing the differences in the surface states of Pt at the start of the stripping scans for *Procedure 1* and *Procedure 2*.

The stripping scans from the modified stripping experiment (*Procedure 2*) are shown in Figure 3.13. **Peak B1** was absent from the stripping scans. However, contrary to our expectations, **Peak B2** was also significantly enhanced. If we attribute **Peak B2** mainly to CO_{ads}

oxidation, the increase in charge under **Peak B2** from *Procedure 2* compared to *Procedure 1* implies that additional CO_{ads} is formed on stepping to low potential. This CO_{ads} has to originate from **X1** since the increase in charge under **Peak B2** is accompanied by the disappearance of **Peak B1**. At the same time, the latter phenomenon also shows that **X1** is not weakly adsorbed. This is so since if **X1** has to be converted to CO_{ads}, **X1** would have to be present at 0.05 V; hence, **X1** is not displaced by H_{ads}.

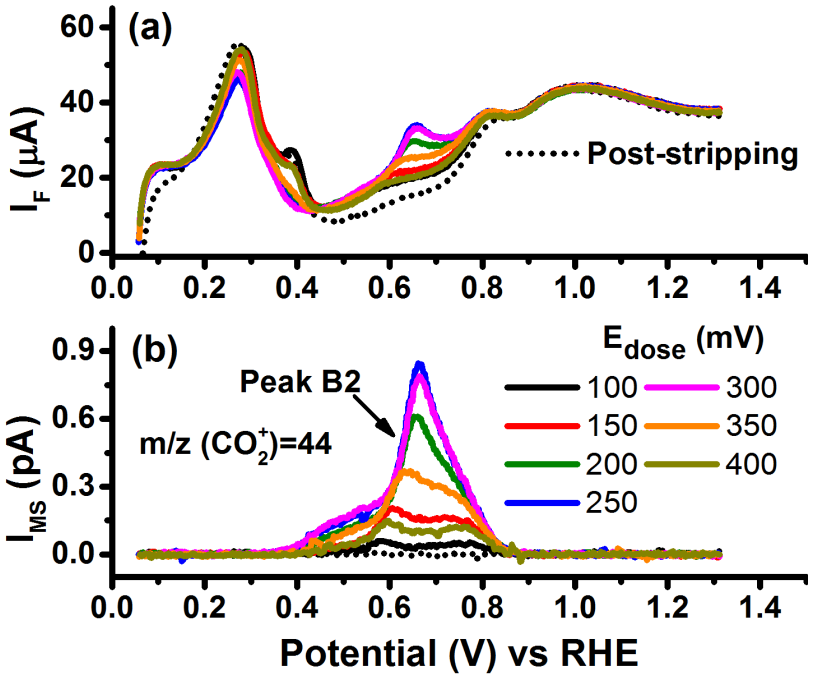

Figure 3.13: *Adsorbate stripping from HCOONa (Procedure 2)* – Analyte solution: 0.2 M HCOONa in 1 M NaOH, Blank solution: 1 M NaOH. Solution flow rate: ~ 15 μL/s. $\mathbf{t_{dose}}$: ~ 20 s. $\mathbf{t_{hold}}$: ~ 50 s. $\mathbf{t_{step}}$: ~ 50 s. Post stripping scans at 50 mV/s shown in black dotted line. (a) Stripping scans at 50 mV/s obtained at the Pt-sputtered Teflon membrane for different values of $\mathbf{E_{dose}}$ following *Procedure 2* (Figure 3.12a). (b) the corresponding mass spectrometric currents at m/z=44 (CO_2^+).

In view of the above-mentioned results, $HCOO_{ads}$ seems to be an unlikely candidate for **X1**. The implication that **X1** can be converted to CO_{ads} (**X2**) directly addresses the strong correlation observed between **Peak 1** and **Peak 2** in the potential step-scan experiments (Figure 3.7 & Figure 3.8). One possible scenario is the reduction of **X1** by H_{ads} to CO_{ads} in the low

potential region. As is apparent from the mass spectrometric currents in Figure 3.13b, the maximum CO_{ads} formation occurs at $\mathbf{E_{dose}} \approx 250$ mV - roughly halfway through the H_{upd} region. This observation again reinforces the idea of CO_{ads} formation being aided by the presence of H_{ads}.

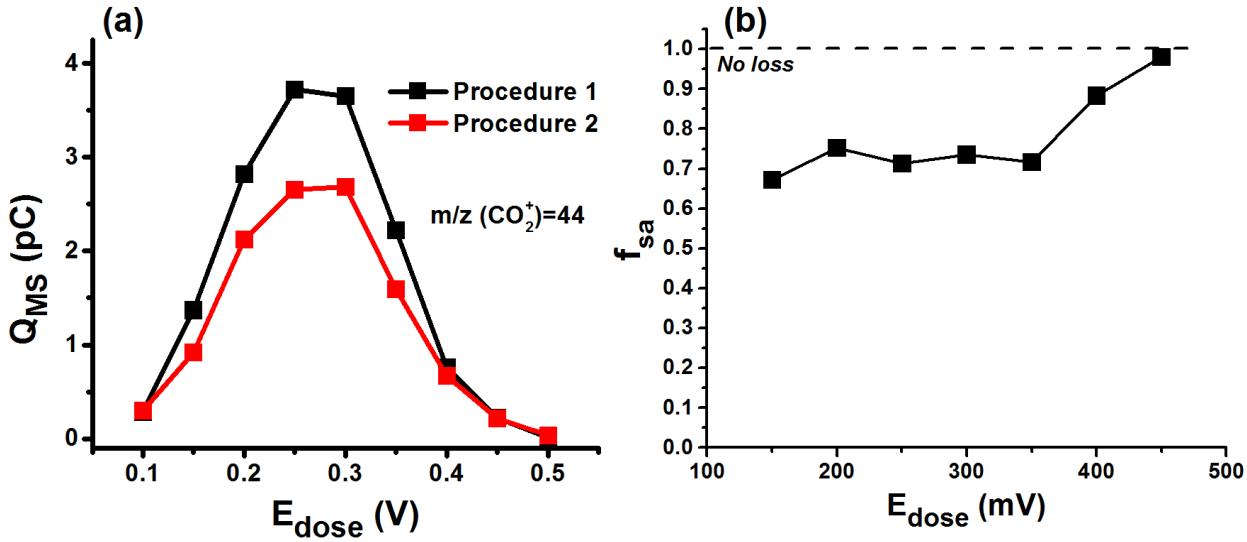

Figure 3.14: (a) Integrated mass spectrometric charge for CO_2 ($\mathbf{Q_{MS}}$) from the stripping scans following *Procedure 1* and *Procedure 2* at different values of $\mathbf{E_{dose}}$. (b) fraction ($\mathbf{f_{sa}}$) of the adsorbates retained after the potential step to 0.05 V vs RHE at different $\mathbf{E_{dose}}$ obtained from the ratio of the corresponding mass spectrometric charges ($\mathbf{Q_{MS}}$) following *Procedure 2* to that from *Procedure 1*.

It is instructive to compare the total mass spectrometric CO_2 (m/z=44) charge ($\mathbf{Q_{MS}}$) from the adsorbates in *Procedure 1* and *Procedure 2*. The quantity $\mathbf{Q_{MS}}$ is directly proportional to the amount of adsorbates formed since the end oxidation product of any adsorbate formed from $HCOO^-$ has to be CO_2. This is really useful since the fraction ($\mathbf{f_{sa}}$) of the adsorbates that are strongly bound to Pt can be found from the ratio of $\mathbf{Q_{MS}}$ for *Procedure 2* to *Procedure 1*. These quantities are compared for different values of $\mathbf{E_{dose}}$ for *Procedure 1* and *Procedure 2* in Figure 3.14. It is evident from the smaller values of $\mathbf{Q_{MS}}$ for *Procedure 2* vis-à-vis *Procedure 1* (Figure 3.14a) that a fraction of the adsorbates present at $\mathbf{E_{dose}}$ is weakly adsorbed and is displaced by H_{ads} on stepping the potential to 0.05 V. From Figure 3.14b, it is clear that most of the

adsorbates formed at $\mathbf{E_{dose}}$ are strongly bound (~ 70 %). This lends support to the idea that **X1** is a strongly adsorbed intermediate and that it is unlikely to be an anion such as $HCOO_{ads}$ which would be expected to be weakly bound.

3.3.6 Mechanism of $HCOO^-$ Oxidation

Based on the studies carried out so far, there is a significant amount of mechanistic details of the $HCOO^-$ oxidation that can be inferred. The results so far indicate that a dual pathway mechanism is active for $HCOO^-$ oxidation. However, unlike HCOOH oxidation, $HCOO^-$ oxidation seems to be highly mediated by adsorbates namely **X1** and CO_{ads} (**X2**). A tentative mechanism of $HCOO^-$ oxidation is shown in Figure 3.15.

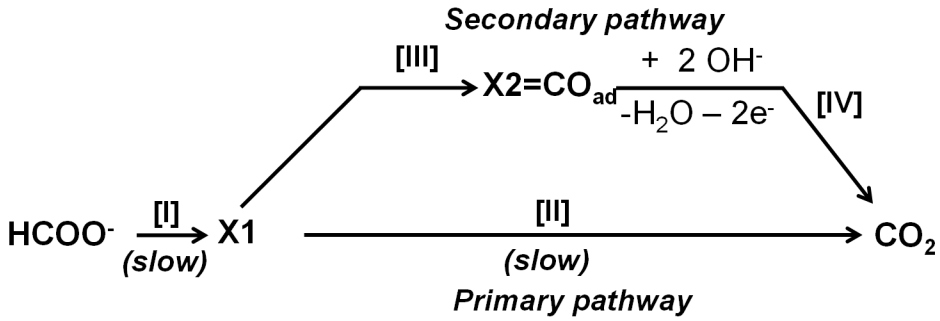

Figure 3.15: Proposed mechanism for $HCOO^-$ oxidation

X1 is proposed to be the precursor adsorbate for both the primary and the secondary pathways of $HCOO^-$ oxidation. It could either be oxidized to CO_2 (the primary pathway, reaction [II]) or converted to CO_{ads} (reaction [III]). CO_{ads}, thus formed, is oxidized (reaction [IV]) at higher potentials to CO_2 (the secondary pathway). Furthermore, it is indicated that both the formation of **X1** from $HCOO^-$ (reaction [I]) and the subsequent oxidation of **X1** (reaction [II]) by the primary pathway are kinetically slow. This is in contrast to the direct pathway in HCOOH oxidation, where formation of the reactive intermediate (Pt-COOH) and its subsequent oxidation are fast electrochemical steps.[26]

The proposed mechanism can be used to explain the observed voltammetric features of $HCOO^-$ oxidation. The overall low activity of $HCOO^-$ vis-à-vis HCOOH can be attributed to the slow kinetics of formation and oxidation of **X1** (reaction [I] and [II] respectively). Since no oxidation occurs in the negative-going scan above ~0.7 V (Figure 3.3), formation of **X1** is likely inhibited by Pt-oxide. It could also be that $HCOO^-$ transitions from an electroactive species to a spectator anion at potentials positive of PZC. [50–52] It was also seen that CO_{ads} formation from $HCOO^-$ was quite slow (Figure 3.7) vis-à-vis HCOOH in acid. Further, under potential cycling conditions, it was seen (Figure 3.3 and Figure 3.4) that **Peak 2** in the positive-going scan (mainly CO_{ads} oxidation) is always smaller than **Peak 1** (mainly primary pathway).

The slow kinetics of CO_{ads} formation is explained as follows. In the case of HCOOH, CO_{ads} can be formed from the reactive intermediate (Pt-COOH) or independently by spontaneous dissociative adsorption of HCOOH. [26] However, in the case of $HCOO^-$, formation of CO_{ads} is controlled primarily by the formation (reaction [I]) and subsequent conversion (reaction [III]) of **X1**. Since the formation of **X1** (reaction [I]) is kinetically limited, CO_{ads} formation would also be slow. It was also seen that a decrease in CO_{ads} formation did not appreciably enhance the oxidation of $HCOO^-$ through the primary pathway (Figure 3.6). This is so since the rate-limiting steps in the oxidation of $HCOO^-$ would be the reactions associated with **X1** (reactions [I] & [II]) and not the oxidation of CO_{ads}. Another interesting feature of the $HCOO^-$ oxidation was the strongly correlated behavior of **Peak 1** and **Peak 2** in the positive-going scans as seen in the potential step-scan experiments (Figure 3.7 & Figure 3.8). This is attributed to the partitioning of **X1** between the primary and the secondary pathways.

It is important to consider the effects of OH adsorption on $HCOO^-$ oxidation. As has already been noted, under potential cycling conditions, the oxidation currents in the negative-

going scans are generally smaller than those in the positive-going scans. This is attributed to the blocking of surface sites for $HCOO^-$ adsorption by OH_{ads} in the negative-going scan. Thus, OH adsorption can add to the kinetic complications in the formation of **X1** (reaction [I]). On the other hand, due to the presence of OH_{ads} at low potentials, the oxidation of CO_{ads} (reaction [IV]) is quite early at ~0.35 V vs RHE (see Figure 3.7).

The chemical identity of the proposed active intermediate **X1** needs to be established. As of now, **X1** appears to be a strongly adsorbed species that could be either oxidized to CO_2 or converted to **X2** (CO_{ads}). Mechanistically, it seems reasonable to propose an oxygen rich species with a strong Pt-C bond. The latter feature would be able to account for the strong adsorption of **X1**. Pt-COOH or an active complex of the form [Pt-CO….Pt-OH] could be two possible candidates. A future direction that needs to be pursued is the in-depth spectroscopic studies to unambiguously identify the chemical nature of **X1.**

3.4 Conclusions

The mechanistic studies conducted so far show that the oxidation of $HCOO^-$ in alkaline medium happens to a significantly lower extent when compared to HCOOH in acidic medium. A dual pathway mechanism (Figure 3.15), analogous to HCOOH oxidation, seems to be applicable for $HCOO^-$ oxidation. From combined cyclic voltammetric-DEMS studies, it was found that the activity of $HCOO^-$ is confined to the potential range ~0.2 -0.7 V vs RHE. Also, the formation of the active intermediate in $HCOO^-$ oxidation is indicated to be adversely affected by OH adsorption. Potential step-scan experiments revealed CO_{ads} formation from $HCOO^-$ to be slow. Moreover, it is observed that the primary and the secondary pathways of $HCOO^-$ oxidation are strongly correlated. Adsorbate stripping experiments showed the presence of a stable adsorbate,

X1 in addition to CO_{ads}. **X1** is shown to undergo oxidation in the same potential range in which the primary pathway is active. Additionally, **X1** can be converted to CO_{ads} in the presence of H_{ads}. Further studies are needed to identify the nature of this adsorbate. Based on the results obtained, a tentative mechanism is proposed. According to this mechanism, $HCOO^-$ oxidation is mediated exclusively by the formation of **X1** which is thought to serve as the precursor adsorbate for both the primary and the secondary pathways of $HCOO^-$ oxidation.

3.5 References

(1) Matsuoka, K.; Iriyama, Y.; Abe, T.; Matsuoka, M.; Ogumi, Z. *Electrochimica Acta* **2005**, *51*, 1085–1090.

(2) Morallón, E.; Rodes, A.; Vázquez, J. L.; Pérez, J. M. *Journal of Electroanalytical Chemistry* **1995**, *391*, 149–157.

(3) Christensen, P. A.; Linares-Moya, D. *The Journal of Physical Chemistry C* **2010**, *114*, 1094–1101.

(4) López-Atalaya, M.; Morallón, E.; Cases, F.; Vázquez, J. L.; Pérez, J. M. *Journal of Power Sources* **1994**, *52*, 109–117.

(5) Spendelow, J. S.; Wieckowski, A. *Physical chemistry chemical physics : PCCP* **2007**, *9*, 2654–75.

(6) Varcoe, J. R.; Slade, R. C. T. *Fuel Cells* **2005**, *5*, 187–200.

(7) Merle, G.; Wessling, M.; Nijmeijer, K. *Journal of Membrane Science* **2011**, *377*, 1–35.

(8) Couture, G.; Alaaeddine, A.; Boschet, F.; Ameduri, B. *Progress in Polymer Science* **2011**, *36*, 1521–1557.

(9) Bartrom, A. M.; Ta, J.; Nguyen, T. Q.; Her, J.; Donovan, A.; Haan, J. L. *Journal of Power Sources* **2013**, *229*, 234–238.

(10) Bartrom, A. M.; Haan, J. L. *Journal of Power Sources* **2012**, *214*, 68–74.

(11) Buck, R. P.; Griffith, L. R. *Journal of The Electrochemical Society* **1962**, *109*, 1005.

(12) Conway, B. E.; Dzieciuch, M. *Canadian Journal of Chemistry* **1963**, *41*, 38–54.

(13) Wetzel, R.; Günther, H.; Müller, L. *Journal of Electroanalytical Chemistry and Interfacial Electrochemistry* **1979**, *103*, 271–275.

(14) Günther, H.; Wetzel, R.; Müller, L. *Electrochimica Acta* **1979**, *24*, 237–238.

(15) Beden, B.; Lamy, C.; Leger, J. M. *Journal of Electroanalytical Chemistry and Interfacial Electrochemistry* **1979**, *101*, 127–131.

(16) Adžić, R. R.; Hofman, M. I.; Dražić, D. M. *Journal of Electroanalytical Chemistry and Interfacial Electrochemistry* **1980**, *110*, 361–368.

(17) Christensen, P. A.; Hamnett, A.; Linares-Moya, D. *Physical chemistry chemical physics : PCCP* **2011**, *13*, 11739–47.

(18) Capon, A.; Parson, R. *Journal of Electroanalytical Chemistry and Interfacial Electrochemistry* **1973**, *44*, 1–7.

(19) Capon, A.; Parsons, R. *Journal of Electroanalytical Chemistry and Interfacial Electrochemistry* **1973**, *45*, 205–231.

(20) Capon, A.; Parsons, R. *Journal of Electroanalytical Chemistry and Interfacial Electrochemistry* **1973**, *44*, 239–254.

(21) Clavilier, J.; Parsons, R.; Durand, R.; Lamy, C.; Leger, J. M. *Journal of Electroanalytical Chemistry* **1981**, *124*, 321–326.

(22) Beden, B.; Bewick, A.; Lamy, C. *Journal of Electroanalytical Chemistry and Interfacial Electrochemistry* **1983**, *148*, 147–160.

(23) Kunimatsu, K. *Journal of Electroanalytical Chemistry and Interfacial Electrochemistry* **1986**, *213*, 149–157.

(24) Kunimatsu, K.; Kita, H. *Journal of Electroanalytical Chemistry and Interfacial Electrochemistry* **1987**, *218*, 155–172.

(25) Corrigan, D. S.; Weaver, M. J. *Journal of Electroanalytical Chemistry and Interfacial Electrochemistry* **1988**, *241*, 143–162.

(26) Sun, S. G.; Clavilier, J.; Bewick, A. *Journal of Electroanalytical Chemistry and Interfacial Electrochemistry* **1988**, *240*, 147–159.

(27) Parsons, R.; VanderNoot, T. *Journal of Electroanalytical Chemistry and Interfacial Electrochemistry* **1988**, *257*, 9–45.

(28) Leung, L. W. H.; Weaver, M. J. *Langmuir* **1990**, *6*, 323–333.

(29) Iwasita, T.; Nart, F. C.; Lopez, B.; Vielstich, W. *Electrochimica Acta* **1992**, *37*, 2361–2367.

(30) Lu, G.; Crown, A.; Wieckowski, A. *The Journal of Physical Chemistry B* **1999**, *103*, 9700–9711.

(31) Wieckowski, A.; Sobkowski, J. *Journal of Electroanalytical Chemistry and Interfacial Electrochemistry* **1975**, *63*, 365–377.

(32) Miki, A.; Ye, S.; Osawa, M. *Chemical Communications* **2002**, *2002*, 1500–1501.

(33) Samjeské, G.; Osawa, M. *Angewandte Chemie (International ed. in English)* **2005**, *44*, 5694–8.

(34) Samjeské, G.; Miki, A.; Ye, S.; Yamakata, A.; Mukouyama, Y.; Okamoto, H.; Osawa, M. *The journal of physical chemistry. B* **2005**, *109*, 23509–16.

(35) Samjeské, G.; Miki, A.; Ye, S.; Osawa, M. *The journal of physical chemistry. B* **2006**, *110*, 16559–66.

(36) Miyake, H.; Okada, T.; Samjeské, G.; Osawa, M. *Physical chemistry chemical physics : PCCP* **2008**, *10*, 3662–9.

(37) Osawa, M.; Komatsu, K.-I.; Samjeské, G.; Uchida, T.; Ikeshoji, T.; Cuesta, A.; Gutiérrez, C. *Angewandte Chemie (International ed. in English)* **2011**, *50*, 1159–63.

(38) Cuesta, A.; Cabello, G.; Osawa, M.; Gutiérrez, C. *ACS Catalysis* **2012**, *2*, 728–738.

(39) Kutschker, A.; Vielstich, W. *Electrochimica Acta* **1962**, *8*, 985–989.

(40) Kita, H.; Ye, S.; Aramata, A.; Furuya, N. *Journal of Electroanalytical Chemistry and Interfacial Electrochemistry* **1990**, *295*, 317–331.

(41) Marinković, N. S.; Marković, N. M.; Adžić, R. R. *Journal of Electroanalytical Chemistry* **1992**, *330*, 433–452.

(42) Marković, N. M.; Gasteiger, H. A.; Ross, P. N. *The Journal of Physical Chemistry* **1996**, *100*, 6715–6721.

(43) Marković, N. M.; Sarraf, S. T.; Gasteiger, H. A.; Ross, P. N. *Journal of the Chemical Society, Faraday Transactions* **1996**, *92*, 3719.

(44) Spendelow, J. S.; Goodpaster, J. D.; Kenis, P. J. A.; Wieckowski, A. *The journal of physical chemistry. B* **2006**, *110*, 9545–55.

(45) Spendelow, J. S.; Lu, G. Q.; Kenis, P. J. A.; Wieckowski, A. *Journal of Electroanalytical Chemistry* **2004**, *568*, 215–224.

(46) Marković, N. M.; Lucas, C. A.; Rodes, A.; Stamenković, V. R.; Ross, P. N. *Surface Science* **2002**, *499*, L149–L158.

(47) García, G.; Koper, M. T. M. *Physical chemistry chemical physics : PCCP* **2008**, *10*, 3802–11.

(48) Couto, A.; Rincón, A.; Pérez, M. C.; Gutiérrez, C. *Electrochimica Acta* **2001**, *46*, 1285–1296.

(49) Munson, R. A. *Journal of The Electrochemical Society* **1964**, *111*, 372.

(50) Bockris, J. O.; Argade, S. D.; Gileadi, E. *Electrochimica Acta* **1969**, *14*, 1259–1283.

(51) Gileadi, E.; Argade, S. D.; Bockris, J. O. *The Journal of Physical Chemistry* **1966**, *70*, 2044–2046.

(52) Peretz, Y.; Yarnitzky, C. N. *Journal of Electroanalytical Chemistry* **2001**, *498*, 87–92.

(53) Vela, M. E.; Lezna, R. O.; De Tacconi, N. R.; Arvia, A. J.; Beden, B.; Hahn, F.; Lamy, C. *Journal of Electroanalytical Chemistry* **1992**, *323*, 289–302.

(54) Neurock, M.; Janik, M.; Wieckowski, A. *Faraday Discussions* **2009**, *140*, 363.

(55) Breiter, M. *Electrochimica Acta* **1963**, *8*, 457–470.

(56) Breiter, M. *Electrochimica Acta* **1963**, *8*, 447–456.

(57) Tripković, A. V.; Popović, K. D.; Momčilović, J. D.; Dražić, D. M. *Journal of Electroanalytical Chemistry* **1996**, *418*, 9–20.

(58) Tripković, A. V.; Popović, K. D.; Grgur, B. .; Blizanac, B.; Ross, P. N.; Marković, N. M. *Electrochimica Acta* **2002**, *47*, 3707–3714.

(59) Sun, S.; Yang, Y. *Journal of Electroanalytical Chemistry* **1999**, *467*, 121–131.

(60) Untereker, D. F.; Bruckenstein, S. *Analytical Chemistry* **1972**, *44*, 1009–1020.

CHAPTER 4
CHARACTERIZATION OF AN QUATERNARY AMMONIUM BASED ALKALINE ANION EXCHANGE MEMBRANE – PART I

4.1 Introduction

The alkaline anion exchange membrane (AAEM) material, depicted in Figure 4.1, is the focus of the current study. This material is unique in the sense that it is one of the few candidate AAEM materials that can be used as both the membrane and the ionomer (see Figure 4.1).[1] The latter form is generally defined to be the soluble form of the AAEM material. The material itself is chemically simple consisting of a polyethylene backbone (structural) functionalized with quaternary ammonium cationic groups (functional); the latter bestowing ionic conductivity on the material. It has good OH^- conductivity (~ 44 mS/cm at 20 °C) and the membrane form is mechanically stable.

The ionomer form has the important function of establishing an optimal interface between the membrane-electrode as shown in Figure 4.1. As explained below, this is easily realized for the current AAEM material since it is solvent-processable i.e. it can be dissolved in a suitable set of solvents. Solvent processability of the material allows catalyst inks (homogeneous mixtures of catalyst nanoparticles and the ionomer solution) to be prepared. The catalyst inks can then be directly applied on to the solid membrane forming the membrane-electrode interfaces. This method of fabrication of the membrane-electrode assembly (MEA) is known as the catalyst coated membrane (CCM) method. The solvent processability of the polymer also makes it the choice candidate for fundamental electroanalytical studies of the AAEM class of materials. Since the polymer can now be directly cast from the ionomer solution on to an electrode/substrate, the crucial membrane-electrode interface can be recreated and analyzed electrochemically.

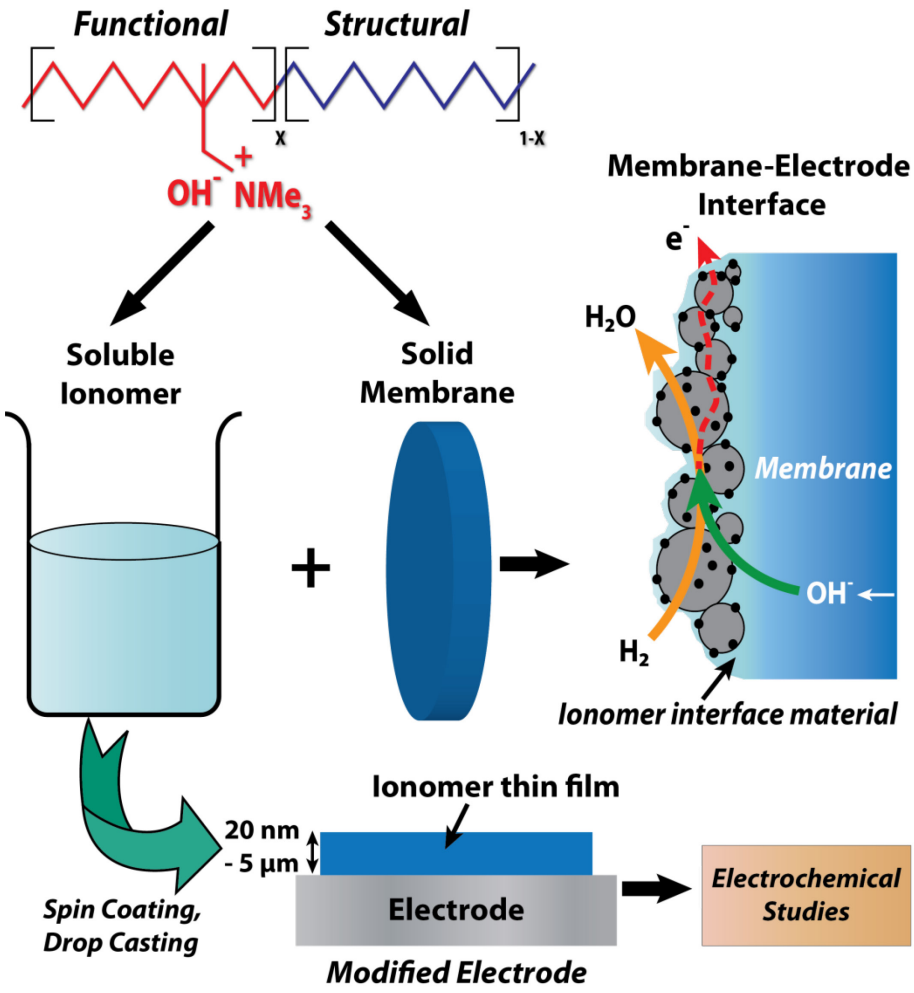

Figure 4.1: Structure of the AAEM material. Also, depicted are the solid and the soluble (the ionomer) forms and their application in the fabrication of the membrane-electrode assemblies (MEAs) and in electrochemical studies.

Currently in the field of AAEM research, there is much to be understood about the fundamental processes that are central to the operation of AAEM in a fuel cell. The OH^- transport mechanism, specifically, and charge transport in the membrane, in general, need to be understood. In the context of the solid polymer electrolyte (SPE), the effects of carbonate and anions, other than OH^-, generated as products of electrode reactions or incorporated from the environment, on the functioning of the membrane, need to be studied. There are early indications that the strategies to judiciously direct polymer morphology maybe central to the efforts in improving AAEMs in terms of their conductivity and mechanical stability.[2] Hence, it is critical

to understand how the polymer morphology affects the membrane performance. Due to the simplicity of its chemical structure, the AAEM material introduced above could serve as a model system for the analytical studies of quaternary ammonium based AAEMs. Thus, the results from the current set of electroanalytical studies are expected to contribute to the larger understanding of quaternary ammonium AAEM systems, specifically, and AAEM systems, in general.

In this chapter, the results from electrochemical quartz crystal microbalance (EQCM) studies aimed at understanding the anion exchange process in ionomer thin films is the topic of discussion. The EQCM investigations reported herein constitute the major portion of the current work on AAEM thin films. The next chapter documents results from physical and charge transport studies of the ionomer thin films along with some preliminary spectroscopy / microscopy characterization of the films.

4.2 Experimental

4.2.1 Sample Preparation

(a) Synthesis

The polymer was synthesized by the Coates group following the procedures described in the literature.[1] All the samples were prepared with a 1:3.75 molar ratio of functional to non-functional (structural) units (x=0.21 in Figure 4.1). This ratio afforded the best combination of mechanical stability and ionic conductivity.

(b) Handling

The polymer samples were received in the solid form. The counter-ion was I^-. It is important to note that the polymer samples are stable chemically in the I^- or the HCO_3^-/CO_3^{2-} form. However, the presence of OH^- ions in the membrane in the dry state can result in the

degradation of the sample. Hence, it is recommended to store the dry samples in either the I^- or the HCO_3^-/CO_3^{2-} form.

(c) Ion-exchange Procedure

The I^- form is not usually used to cast ionomer films that will be used for electrochemical experiments due to the strong adsorption of I^- on metal surfaces such as those of Pt and Au. Hence, typically, the I^- ions in the solid sample are exchanged out with CO_3^{2-} ions. In this form, the membrane is still air stable and can be used for electrochemical experiments. The samples in the I^- form are first immersed in 1M base (NaOH/KOH) for 20 min with stirring. The step is repeated with a fresh batch of base solution to ensure that all the I^- has been exchanged out by OH^-. The sample, in the OH^- form, is now immersed in 1M Na_2CO_3 and the ion-exchange carried out as previously. Finally, any excess base or carbonate is removed by soaking in de-ionized (DI) water with stirring for 20 min and the process repeated with a fresh batch of DI water for two more times.

It is important to perform the OH^- exchange first before the CO_3^{2-} exchange. There is some evidence, based on the solubility differences of the I^- and the CO_3^{2-} forms, to suggest that CO_3^{2-} may not be able to directly replace I^-. However, the reverse process seems to occur readily based on the ex-situ IR spectra of the dry samples (discussed in Section 5.3e). On a related note, OH^- can easily replace or be replaced by either I^- or CO_3^{2-}.[1]

(d) Solubility of the Polymer

For the preparation of the ionomer solution, the solubility of the initial batch of polymer sample (AAEM-I in Table 4.1) was found to be too low. Hence, it was sought to increase the polymer solubility by varying some of the parameters as detailed below.

i. Polymer Molecular Weight

The molecular weight of the polymer was found to be the dominant factor in determining polymer solubility. Accordingly, samples with lower molecular weights (calculated) were obtained. The details are given below in Table 4.1. The sample types are listed in the chronological order of synthesis.

Table 4.1: Molecular weights of AAEM samples used

Polymer Sample Type	**Sample Codes**	**Mol. Wt. (g/mol) (*Calculated*)**
AAEM-I	KMH-1-165	38,765
AAEM-II	KMH-2-243, KMH-2-252	23,259
AAEM-III	KMH-3-082	11,393

Decreasing the molecular weight increased the polymer solubility significantly. For instance, the maximum solubility of AAEM-I in n-propanol was 1 wt%; while, that of AAEM-II was ~ 5 wt%. Ionomer solutions with high polymer loadings (>1 wt %) are needed to make sufficiently thick films in the range of 200 nm – 1 μm, appropriate for the current study.

ii. Solvent

Based on the previous literature (supporting info of ref. [1]), n-propanol by itself and a mixture of n-propanol and water (1:1 v/v) were tried as solvent systems. A variety of other polar and non-polar solvents were also tested. However, the solvent did not seem to make any significant impact on the solubility of the high molecular weight polymer (AAEM-I). As mentioned previously, the lower molecular weight polymer samples (AAEM-II and III) showed significantly higher solubility and for these samples neat n-propanol was found to be suitable as the solvent.

iii. Nature of Counter-ion

A less intuitive observation was the effect of the incorporated anions in the polymer on its solubility in n-propanol. It was seen that the polymer in the I^- form was significantly less soluble than in the HCO_3^-/CO_3^{2-} form in n-propanol with the nominal concentration of the polymer in the mixture being the same. The reason for this difference in solubility is not clear. However, it is to be expected that the solvation energetics of the polymer will be different depending on the counter-ion. Based on the observations from the ex-situ TEM studies (section 5.3.6) of the polymer samples, a possible reason for the lower solubility of the I^- form could be the ability of I_3^-, which is formed from I^- upon air oxidation, to cross-link polymer chains. The cross-linked polymer chains, consequently, will be less soluble. However, this hypothesis needs to be verified experimentally.

(e) Preparation of Ionomer Solution

The wet polymer sample in the CO_3^{2-} form obtained after the ion-exchange procedure (*vide supra*) was dried between sheets of Kimwipes to remove most of the water. The sample was further dried overnight at room temperature by placing in a partially evacuated chamber. The dried sample was then weighed. It may be beneficial to dice the sample into smaller pieces if possible to aid polymer dissolution. Based on the measured weight and the desired wt % of the polymer in the final ionomer solution, an appropriate volume of n-propanol was added to the dried sample in a glass vial with a stir bar. To prevent contamination from adhesives in the cap vials, thermoset PTFE-lined caps were used to seal the vials. The cap-vial joint was further sealed with PTFE tape. The vial was then placed in a silicone oil bath on a magnetic stirrer with an automatic temperature feedback control (IKA Works Ceramag Midi with ETS-D4 temperature monitor). Typically, the temperature of the bath was set to ~ 80 °C. The solution

was left stirring at the elevated temperature for at least for 24 hrs. Depending on the concentration and the molecular weight of the polymer, and the nature of the counter-ion, the time required for complete polymer dissolution can vary. Typically, it was seen that for the high molecular weight sample (AAEM-I) for ~ 1 wt% polymer loading in the carbonate form, 2-3 days at ~ 80 °C were required. The low molecular weight samples (AAEM-II and III) in the carbonate form were observed visually to dissolve almost completely in 3-4 hrs even for high loading (~ 4 wt%). Even so, the solutions were still kept heated and stirred for at least 24 hrs before removing from the bath to ensure complete dissolution. The ionomer solutions were typically straw yellow to light brown in color. The color is suspected to be due to the residual catalyst in the ionomer from the synthesis step (see section 5.3.6).

It was observed, especially in case of the high molecular weight polymer solution and/or high polymer loading, that the polymer phase would separate out of the solution over time. This process of polymer aggregation is aided by the loss of solvent over time. Heating the ionomer solution can alleviate this problem to an extent. However, the most effective approach was to decrease the molecular weight of the polymer.

Filtration of the as-prepared ionomer solution was found to be critical to achieving uniform thin films by spin-coating (vide infra).Even a visibly homogeneous ionomer solution was found to have a significant amount of large particles (nominal particle size > 8 μm based on the pore sizes used for filtration). A good procedure is to start with glass wool filtration to sift out the coarse particles. A series of filtration steps with successively smaller pore size filters can then be attempted to further refine the solution. When using syringe filters, PTFE filters are preferred due to their hydrophobicity.

(f) Spin-coating of Ionomer Thin Films

For EQCM experiments, the spin-coating of ionomer thin films on the quartz crystals was performed using a commercial spin-coater (Laurell Model WS-400A-6NPP/LITE). The quartz crystals were cleaned initially in a chromerge bath. They were then washed with n-propanol and DI water and blow-dried using a jet of dry air/argon. The crystals were then mounted and secured on the chuck of the spin-coater. An aliquot of the ionomer solution, which was sonicated for 10-15 min beforehand, was then introduced onto the stationary substrate using a micro-pipette. For a 0.5" diameter electrode surface, about 40 μL of the solution is sufficient to cover the electrode surface. Immediately afterwards, the spin-coater program was initiated. The spin-coater was ramped up to its final speed where it is left for an appropriate amount of time so as to remove any residual solvent. A typical run would involve increasing the speed in increments of 200 rpm/s to a final speed of 1000 rpm with a total runtime of 5 min. The resulting film would then be dried in a slow jet of dry air/argon.

4.2.2 Film thickness measurement

The dry thicknesses of the spin-coated ionomer films on the quartz/RDE electrode substrates were measured by a contact profilometer (Tencor Alpha step 500). The films were always deposited on a pair of similar substrates and identical conditions of spin-coating were employed on both. One of the samples was used for profilometry and the other sample was used for electrochemical experiments. The thicknesses of both the film samples prepared under identical conditions were assumed to be the same.

For profilometry, step edges were created in the film using a pointed cotton or foam head swab lightly soaked in n-propanol. Line scans were performed across at different points along

the edges. The thickness readings were then averaged to determine the mean film thickness. The film thicknesses reported in the current study are always for the dry film.

The color of the film in ambient light also changes with the thickness due to interference effects. This effect was observed for films with thicknesses spanning a range of approximately 50 nm – 1 μm. Films in the thickness range 50-100 nm were golden in color, above 100 nm up to about 250 nm were purple and thicker films were straw green in color. These color variations can be used as visual guides for cursory estimates of film thickness.

4.2.3 Electrochemical Measurements

For a discussion of the theory of the EQCM technique and the related impedance analysis measurements, section 2.2.1 can be referred to. The experimental details are already documented in section 2.2.2. All the EQCM experiments were carried out in the water jacketed EQCM cell (section 2.2.2.b) at 25 °C.

4.2.4 Chemicals

Methanol (anhydrous AR ACS Macron chemicals), sodium formate (≥ 99.0% puriss p.a. ACS Sigma Aldrich), paraformaldehyde (~ 95% Fluka) were used for the studies. For ion-exchange procedure and for making supporting electrolyte solutions, sodium hydroxide (98.7% AR ACS Macron chemicals) and sodium carbonate (100.0% AR ACS Mallinckrodt) were employed. Solutions were prepared in high purity de-ionized water (18 MΩ cm Barnstead Nanopure Model No. 7148). High purity nitrogen, argon and carbon dioxide gases were obtained from Airgas.

4.3 Results and Discussion

4.3.1 Viscoelastic Effects in Ionomer Thin Films

Hydration of the AAEM is a prerequisite for ionic conductivity in the membrane. Drawing a parallel with Nafion, it has been proposed that hydration in AAEMs help in the formation of inter-connected hydrophilic domains that aid OH^- conductivity.[2,3] However, hydration or water uptake in the membrane also leads to significant swelling of the membrane. Excessive swelling leads to loss of mechanical strength of the membranes and can also cause a decrease in the ionic conductivity. Hence, the ionomer thin films in aqueous environment were expected to exhibit significant viscoelastic effects. Impedance measurements were carried out on a series of ionomer thin films of different thicknesses deposited on QCM electrodes. For a comparative study, measurements were carried out both in air and in water. An overview of the acoustic impedance measurement technique and the related data analysis can be found in section 2.2.1.f. The impedance analysis of the ionomer film modified QCM systems serves two functions: (i) diagnose the extent of viscoelastic effects in the thin films in a non-electrochemical aqueous environment (ii) guide the choice of the optimal thickness of the film for EQCM studies.

Figure 4.2 shows the relevant diagnostic plots for the series of ionomer thin films in air and water. For the θ-plots (Figure 4.2a and Figure 4.2b), the frequencies (**Δf**) are shown relative to $\mathbf{(f_{Zmin} + f_{Zmax})/2}$ for the particular composite resonator (the ionomer film modified QCM electrode) where $\mathbf{f_{Zmin}}$ and $\mathbf{f_{Zmax}}$ are the absolute frequencies at which the total impedance **Z** attains the minimum and the maximum values respectively. For those composite resonator systems where it is possible to achieve series and parallel resonances, $\mathbf{f_{Zmin}=f_s}$ and $\mathbf{f_{Zmax}=f_p}$ (where $\mathbf{f_s}$ and $\mathbf{f_p}$ are the series and the parallel resonance frequencies). This is not the case for relatively thick ionomer films as will be evident later on in the discussion.

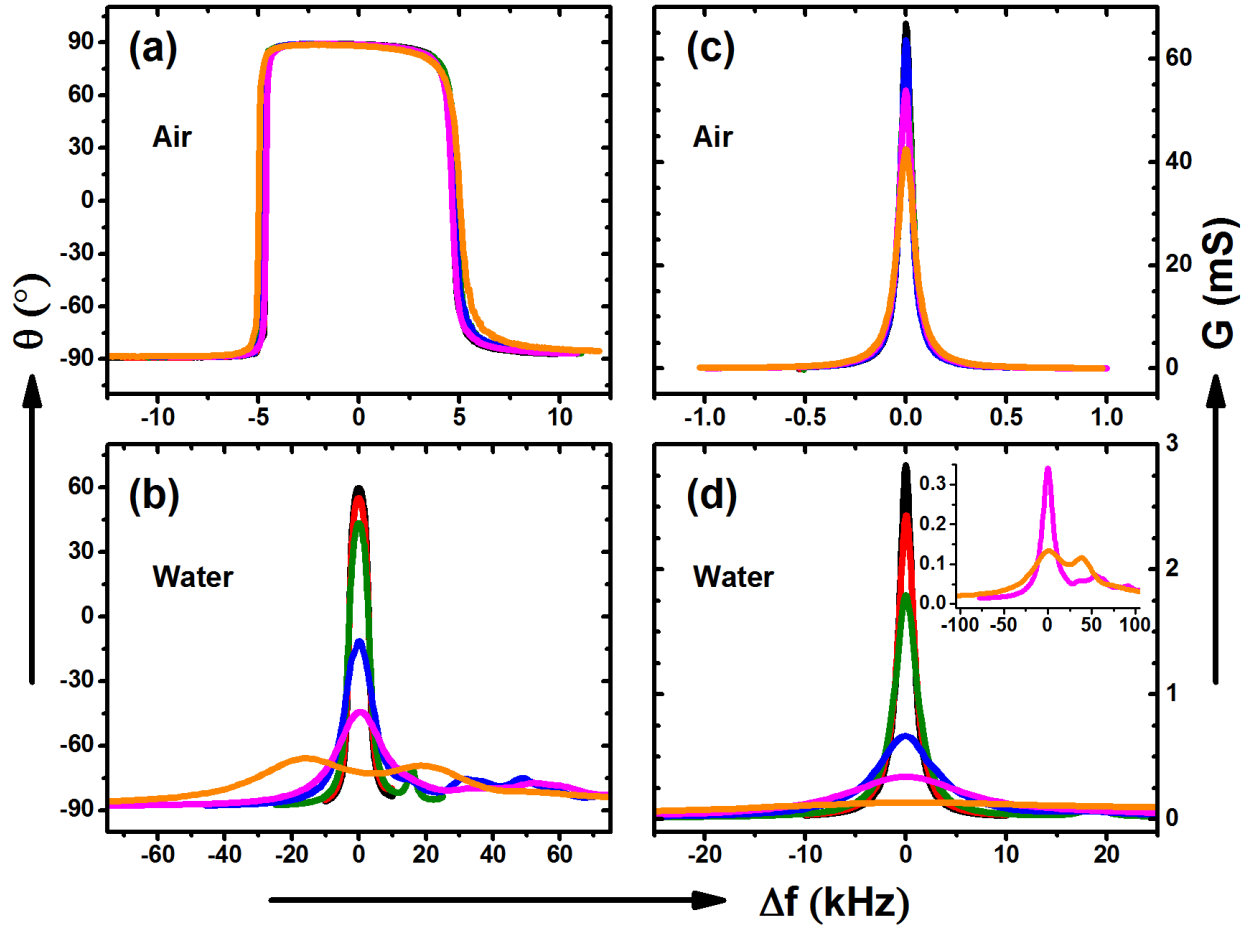

Figure 4.2: Impedance plots for a series of ionomer films of different dry thicknesses on Pt electrode 5 MHz AT-cut quartz crystals at room temperature (~ 21 °C). Average film thickness (nm): —— No film, —— 44 ± 13, —— 145 ± 13, —— 210 ± 13, —— 403 ± 27, —— 920 ± 40. θ-plots for the ionomer films in (a) air (b) de-ionized water. G-plots for the ionomer films in (c) air (d) de-ionized water. $\Delta f=f-(f_{Zmin}+f_{Zmax})/2$ for θ-plots and $\Delta f=f-f_{Gmax}$ for G-plots where f is the absolute frequency and f_{Zmin},f_{Zmax} and f_{Gmax} are the corresponding absolute frequencies at which Z has the minimum and the maximum and G has the maximum value respectively for a given ionomer film modified QCM electrode. The inset to (d) shows the expanded conductance plots for the 403 and the 920 nm films in water.

For the G-plots (Figure 4.2c and Figure 4.2d), the frequencies are specified relative to $\mathbf{f_{Gmax}}$ for the particular composite resonator, where $\mathbf{f_{Gmax}}$ is the absolute frequency at which the conductance **G** is maximum. The use of relative frequencies, as outlined above, allows for a direct comparison of the peak profiles without the effect of the resonant frequency shifts due to

the mass loading and the viscous loading (in water) of the QCM crystals and also compensates for the sample variations between the bare QCM electrodes.

Examining the θ-plots for the films in air (Figure 4.2a), it is seen that all the ionomer thin films conform to the θ-response typical of a rigid film. The phase angle θ is ~ -90 ° at frequencies far away from resonance, indicating the capacitive nature of the total impedance. At the series (**Δf** ≈ -5 kHz) and the parallel resonances (**Δf** ≈ 5 kHz), **θ** = 0° as required by the resonance condition. Between the series and the parallel resonance frequencies, **θ** ≈ 90 ° as the inductive load dominates the network impedance.

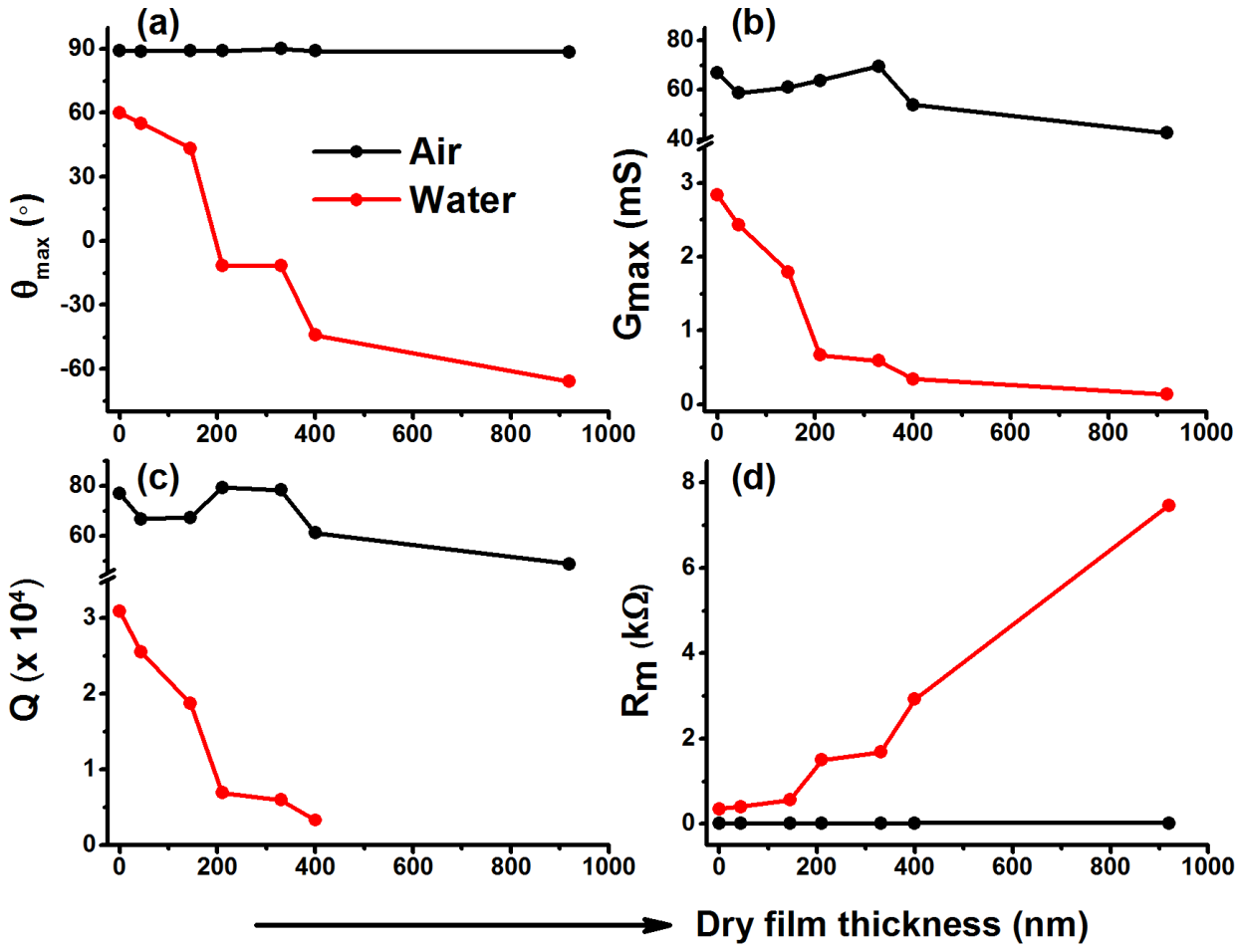

Figure 4.3: (a) θ_{max} (b) G_{max} (c) Q (d) R_m versus the dry thickness of the ionomer films. Experimental parameters same as in Figure 4.2. The legend for (a) is applicable for the rest of the figure. The value of Q for the 920 nm thick film is not computed.

As is apparent, the immersion of the ionomer thin films in water alters the **θ**-response significantly (Figure 4.2b). $\boldsymbol{\theta_{max}}$ – the maximum value of **θ** – is significantly less than 90 ° and decreases with increasing film thickness. The trend can also be followed by looking at Figure 4.3a. It is to be noted that the liquid operation of the QCM will invariably result in a lower $\boldsymbol{\theta_{max}}$ due to the viscous loading of the liquid (refer to the extended BVD model in section 2.2.1.d). This is evident from the θ-plot of the bare QCM electrode in water. The presence of the ionomer film introduces an additional viscoelastic loading due to the swelling of the film in water. This viscoelastic loading will add resistive and capacitive loads to the network (refer to the modified BVD model in Section 2.2.1.e) that will further reduce $\boldsymbol{\theta_{max}}$. The decrease in $\boldsymbol{\theta_{max}}$ will be accentuated with increases in the film thickness due to the increased viscoelasticity in thicker films. Above a critical film thickness, ca. 200 nm, $\boldsymbol{\theta_{max}}$ has a negative value implying that films much thicker than 200 nm would not be able to achieve a resonance condition. Thus, θ-plots can be conveniently used to deduce the range of film thicknesses that can be studied using QCM.

Another interesting trend in the θ-plots in water is the change in peak profile with film thickness. Compared to the stepped profile of the θ-plots in air, the θ-plots in water have a peaked appearance. Also to be noted is the fact that the width of the θ-peaks (20-50 kHz) in water is much larger than the width of the θ-plateau (~10 kHz) in air. Both these trends are related to the increased energy losses in the QCM or, equivalently, a decrease in the quality factor (**Q**) of the QCM due to its operation in a viscoelastic environment vis-à-vis air (vide infra). Briefly, the absence of steps and the broadness of the peaks in θ-plots in water signify that the resonance is not “sharp” due to the viscoelastic losses in the system. Finally, in case of severe viscoelastic loading, as in the case of the 920 nm film, there is splitting of the main peak and the

presence of additional peaks at higher frequencies indicating a complicated impedance response of the resonator. The origin of these extra peaks is not clear.

The G-plots (Figure 4.2c and Figure 4.2d) are highly diagnostic of the operational efficiency of a composite QCM resonator. The height of the conductance peak ($\mathbf{G_{max}}$) is inversely proportional to the motional resistance $\mathbf{R_m}$; hence, it can be used to quantify the viscoelastic resistance. The FWHM of the conductance peak is known as the bandwidth and is inversely proportional to the quality factor **Q** which is a measure of the QCM operational efficiency (refer to Section 2.2.1.f.iii). The trends can also be followed using Figure 4.3b, Figure 4.3c and Figure 4.3d. Clearly the composite resonators operating in air display close to ideal behavior. Their operation is characterized by high $\mathbf{G_{max}}$ values (~ 60 mS), narrow bandwidth (~ 75 Hz), high **Q** values (~70,000) and low $\mathbf{R_m}$ (~18 Ω). Importantly, these quantities do not vary greatly with film thickness (RSD ≈ 15-18 %).

On the other hand, in water, as is clear from Figure 4.3, there is an evident trend in the above-mentioned quantities with changing film thickness. Indeed, even without the film, the aqueous environment does affect these quantities as shown by the values for the case of the bare QCM electrode ($\mathbf{G_{max}}$ ~ 3 mS, FWHM ~ 1600 Hz, **Q** ~ 3000, $\mathbf{R_m}$ ~ 350 Ω). However, it is evident that the presence of the hydrated ionomer films dramatically affects the QCM performance parameters further. $\mathbf{G_{max}}$ and **Q** decrease while $\mathbf{R_m}$ and the bandwidth increase with an increase in film thickness; symptomatic of severe viscoelastic losses due to the hydrated film. For instance, the values of **Q** and $\mathbf{R_m}$ for the QCM electrode modified with the ionomer film with a thickness of 403 nm in water change by almost an order of magnitude compared to the values of the bare QCM electrode. Note that the value of **Q** is not computed for the 920 nm film in water due to the splitting of the conductance peak.

The admittance plots in Figure 4.4 conveniently summarize the effect of the hydrated ionomer thin films on the operation of the QCM in an aqueous environment. The decreasing radius of the admittance locus with increasing film thickness demonstrates the increase in the motional resistance $\mathbf{R_m}$ of the composite resonator due to the increased swelling in thicker films. It is straight-forward to ascertain the loss of resonance for the composite resonators incorporating thick ionomer films as indicated by the non-crossing of the x-axis by the admittance locus. Hence, the admittance plots can also be used to probe operational failures in composite resonators.

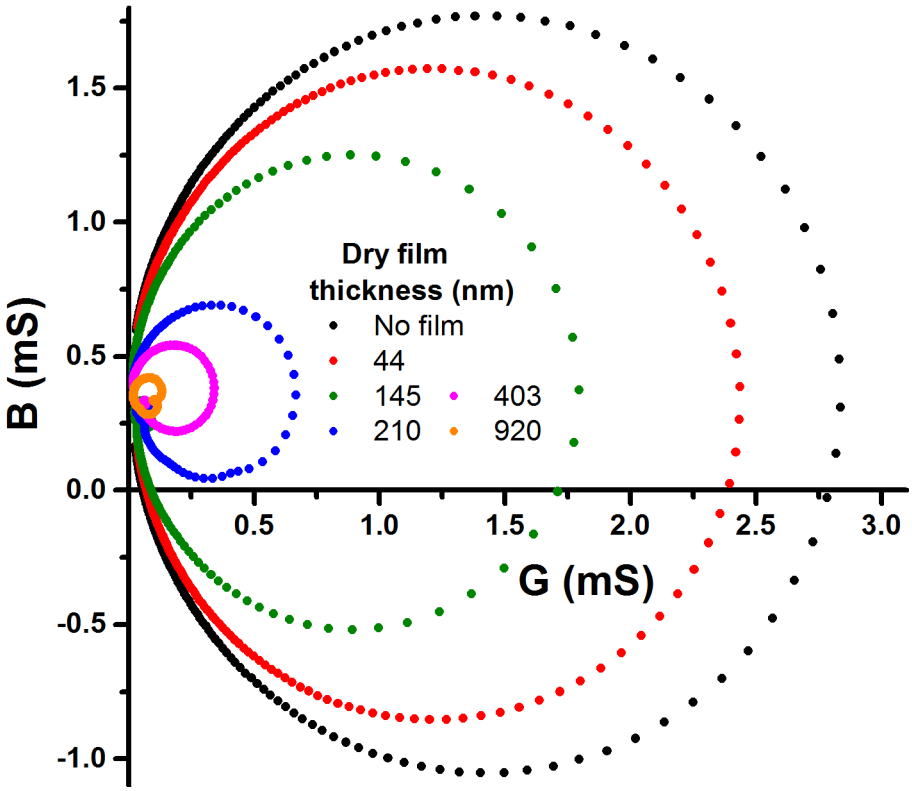

Figure 4.4: Admittance plots for the series of the ionomer-film modified QCM electrodes in water shown in Figure 4.2 and Figure 4.3. Experimental parameters same as in Figure 4.2.

Just as from the θ-plot (Figure 4.2), it is seen that for ionomer films thicker than ca. 200 nm, the ionomer-film modified QCM electrode ostensibly would not achieve resonance.

However, it should be pointed out that, experimentally, ionomer films up to approx. 350 nm can be studied using the QCM technique. This is because the SRS QCM 200 controller used for the QCM studies implements capacitance cancellation. Basically, a variable capacitor incorporated in the QCM oscillator circuit can be adjusted to effectively reduce the magnitude of the static capacitance $\mathbf{C_0}$ (refer to BVD model in section 2.2.1.c). This shifts the admittance locus downward. In favorable cases, the locus can now cross the x-axis allowing the circuit to achieve resonance.

4.3.2 EQCM Studies

The primary focus of the EQCM study was to investigate the carbonation process in ionomer thin films. At the outset, the objective was to detect and quantify any solid carbonate formation utilizing the QCM as the mass sensor. In the context of the current study, the carbonation is broadly defined as the incorporation of CO_3^{2-} ions in to the ionomer thin films which may or may not result in the formation of solid carbonate. As discussed in section 1.2.3, AAEM systems are expected to prevent the formation of solid carbonate precipitates due to the absence of mobile cations.

(a) Strategy

For the current analytical studies, the process of carbonation (as defined above) is simulated both chemically and electrochemically as shown in Figure 4.5. In both methods, the ionomer-film is kept in base solution and is initially in the OH^- form. In the chemical method (Figure 4.5a), the CO_3^{2-} is generated chemically; for example, by bubbling CO_2 gas through the base solution as shown in the figure. The frequency of the resonator is simultaneously recorded during this process allowing us to follow the carbonation process. Instead of passing CO_2, carbonation can also achieved by directly introducing small volumes of concentrated carbonate

solution. It is important to note that, in the chemical method, the solution concentration of CO_3^{2-} is altered. Hence, in this case, the inter-exchange of CO_3^{2-} with OH^- in the ionomer film (CO_3^{2-} ↔ OH^-) can only be followed in the forward direction.

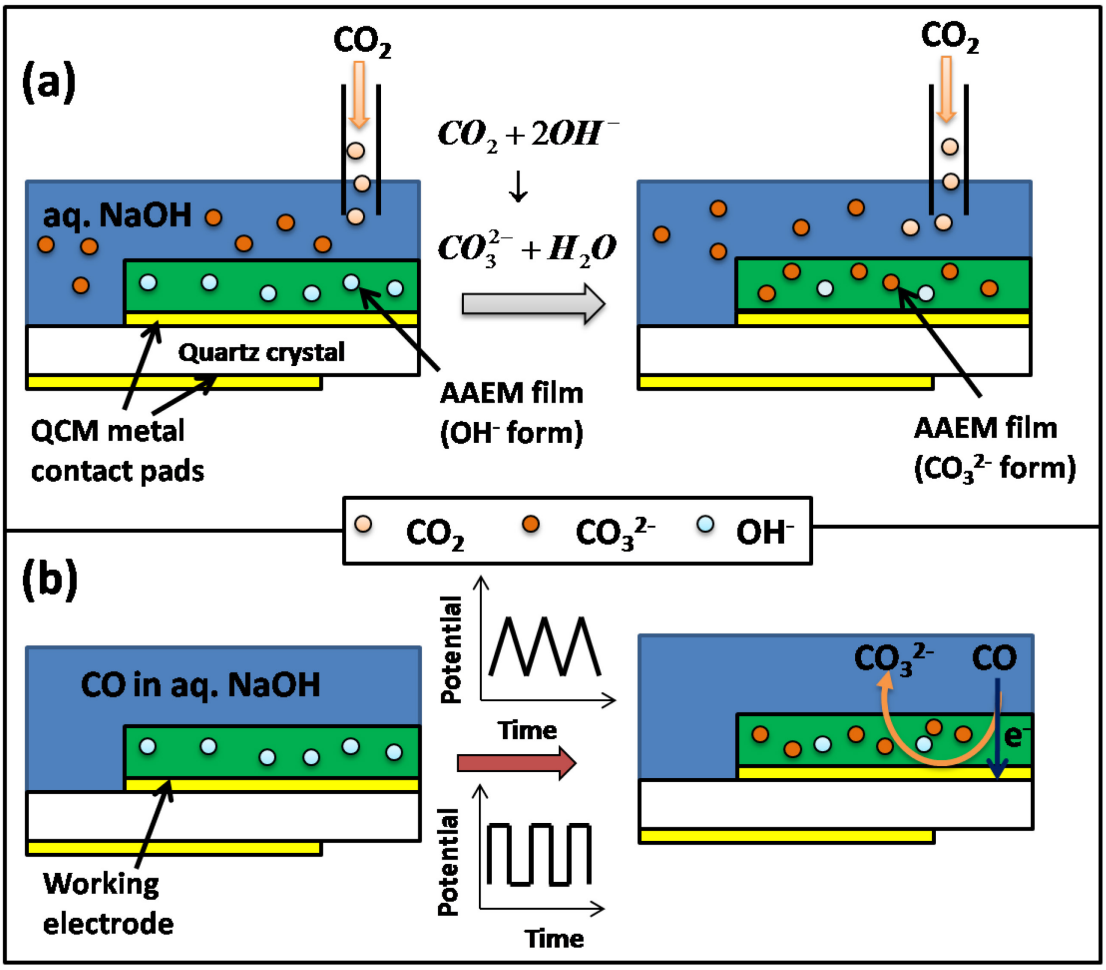

Figure 4.5: Strategies for the QCM investigations of anion incorporation in general in the ionomer thin films. The particular case of carbonation (incorporation of CO_3^{2-}) in the ionomer films is depicted using CO_2 and CO as sources of CO_3^{2-}. (a) CO_3^{2-} generated by chemical conversion of CO_2 in base solution (b) Electrochemical oxidation of CO to produce CO_3^{2-} at the film-electrode interface.

In the EQCM method (Figure 4.5b), CO_3^{2-} is generated electrochemically by the oxidation of a carbonaceous fuel such as CO or CH_3OH in basic media. Unlike the chemical method, in this case, the solution concentrations of the fuel, OH^- and CO_3^{2-} (≈ 0) are unaltered. Of course, the concentrations of the various species are expected to change in the ionomer thin

film which is in intimate contact with the electrode. Significantly, by controlling the electrochemical reactions at the film-electrode interface, the dynamics of the inter-exchange of anions in the film can be monitored. Cyclic voltammetry and chronoamperometry are the two commonly applied electrochemical methods used in conjunction with the QCM measurements.

Finally it should be noted that, in general, AAEMs can incorporate any anion not just CO_3^{2-}. This is the case, for example, when methanol is used as the source of CO_3^{2-}. The electrochemical oxidation of methanol produces, in addition to carbonate, formate anions (vide infra). The strategies outlined in Figure 4.5 are still relevant; only now, they are broadly applicable for monitoring anion incorporation in ionomer films.

(b) Method Validation - QCM Study of Carbonation using CO_2

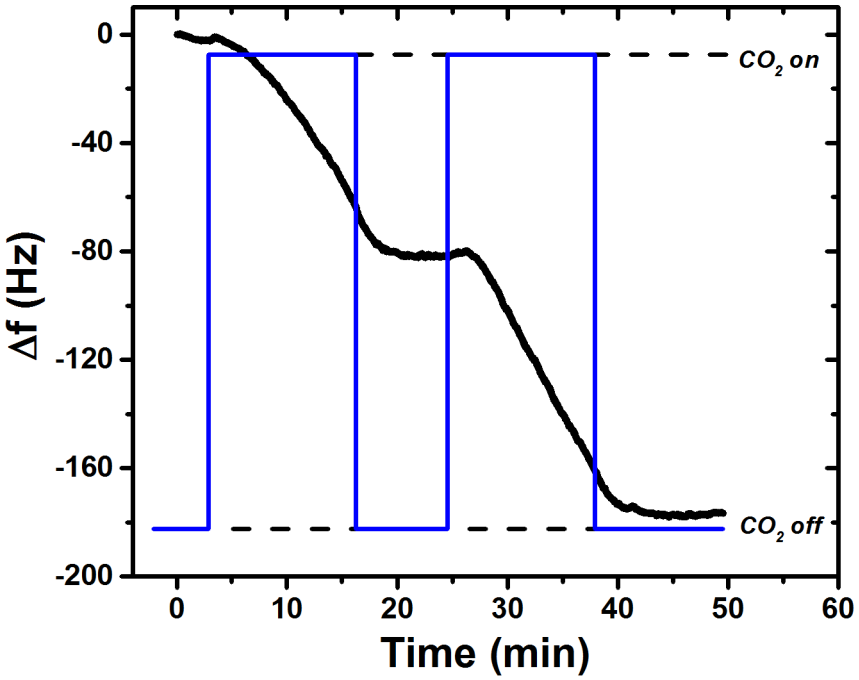

Figure 4.6: Frequency change (Black curve) for the ionomer-film modified Pt AT-cut 5 MHz QCM electrode in 1 M NaOH during the carbonation process. Ar or CO_2 gases are bubbled through the stirred solution as shown by the step profile in blue. When the CO_2 stream is off, the gas feed is switched to Ar and vice-versa.

To test the applicability of the QCM technique to the study of the carbonation process in ionomer thin films, the carbonation process was recreated by bubbling CO_2 gas through the base solution. The result is shown in Figure 4.6. Clearly, the observed frequency decrease of the ionomer-film modified QCM coincides with the introduction of CO_2 into the base solution initiating the carbonation process. Introduction of Ar which replaces CO_2 in the gas stream arrests the frequency decrease. The frequency reaches a steady value at longer times of purging with Ar. Re-introduction of CO_2 into the solution results in the decrease of the frequency signaling the re-initiation of the carbonation process. This experiment demonstrates the potential of the QCM technique in studying carbonation. It is to be noted that the neutralization of the NaOH solution by CO_2 will be a slow process. The CO_3^{2-} concentration in solution is therefore not expected to reach anywhere close to the saturation value in the time frame of the experiment.

(c) Ionomer-film Modified Pt QCM Electrode in NaOH Solution

The cyclic voltammograms and the corresponding frequency (**Δf**) and motional resistance (**ΔR_m**) changes for the bare Pt QCM electrode and the electrode with the ionomer film (dry film thickness: 210 nm) in 0.1 M NaOH are shown in Figure 4.7a and Figure 4.7b respectively. As can been see from Figure 4.7b, the presence of the ionomer film does not affect the surface voltammetric features of polycrystalline Pt in base solution. The major feature in the **Δf** curves is the frequency decrease (~ 12 Hz) is due to the formation of the Pt-oxide layer. Also, the frequency changes are similar between the bare and the modified electrodes suggesting that any mass changes in the film are small compared to those from the Pt surface processes.

The frequency response in the H-upd region is not straightforward to interpret. A frequency decrease should ostensibly correspond to a mass increase at the QCM electrode. Hence, a frequency decrease is expected on H-adsorption on Pt. It was consistently seen that H-

adsorption on the Pt QCM electrode is accompanied a small frequency increase of ~ 3 Hz and H-desorption by a frequency decrease of roughly the same magnitude. A similar response has been observed for the H-upd region on Pt in acidic solutions.[4] Possibly, the contact desorption of water molecules from the electrode surface as the H-monolayer is formed could be the cause for the observed frequency increase seen. It has been noted that the surface treatment and nature of the electrode could also play an important role in determining the frequency behavior. [4,5]

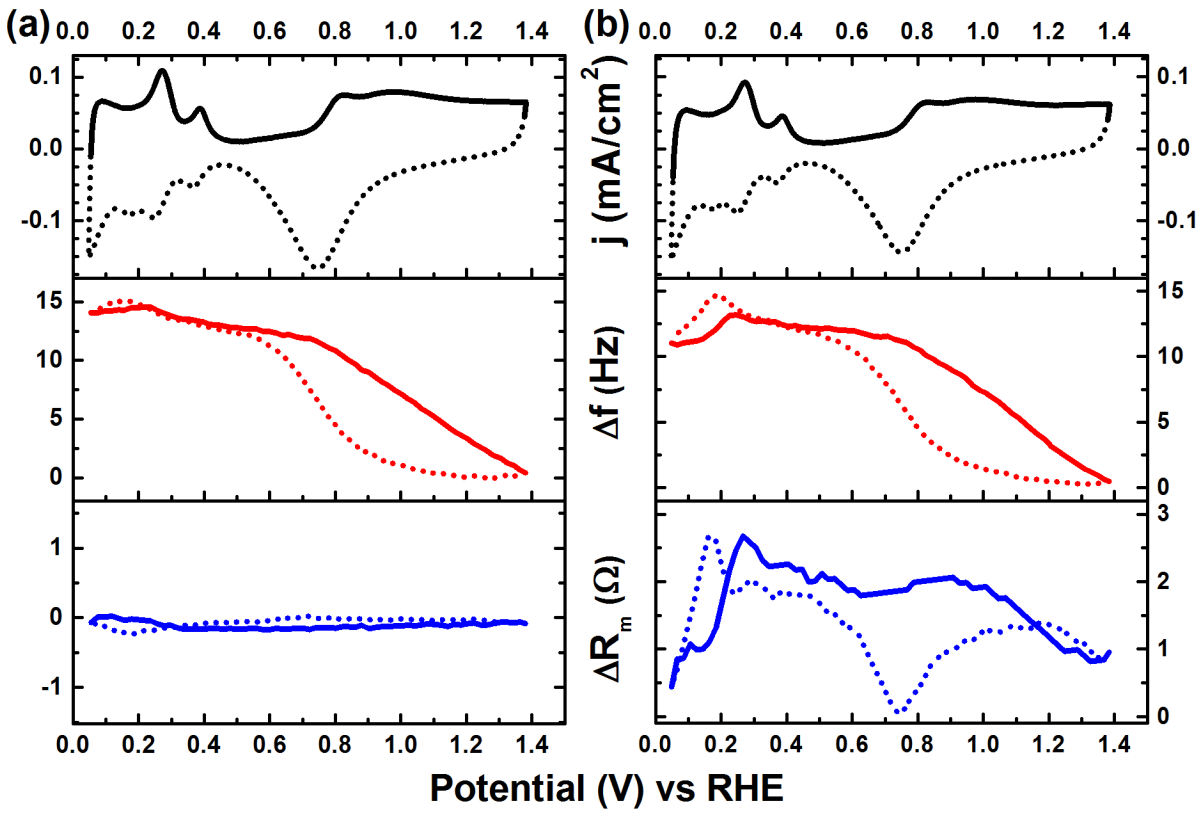

Figure 4.7: Cyclic voltammetry with simultaneous frequency (Δf) and motional resistance (ΔR_m) change measurement in 0.1 M NaOH for (a) bare Pt QCM electrode (b) the ionomer-film modified Pt QCM electrode. Dry film thickness: 210 nm. Scan rate: 20 mV/s. Solid line forward scan and broke line reverse scan. Solution stirring rate: 290 rpm.

It is interesting to compare the $\mathbf{\Delta R_m}$ plots for the bare and the modified electrodes. Evidently, due to the changes in the viscoelasticity of the ionomer film during cycling, the changes in the motional resistance for the modified electrode are significant vis-à-vis the bare

electrode. However, as will be evident later, these changes in $\mathbf{R_m}$ for the ionomer film modified electrode are still significantly smaller than those observed during fuel oxidation at the modified electrode. Interestingly, the $\mathbf{\Delta R_m}$ plot mirrors the Pt-oxide surface features in the CV to a large extent in the case of the modified electrode. It should be noted that Pt-oxide formation/reduction is accompanied by the production/consumption of H_2O and OH^- as in Equation 4.1. Thus, these surface reactions can drive mass and charge flows in the ionomer thin films changing the viscoelasticity of the film in step with the voltammetric profile.

Equation 4.1: $$Pt + 2OH^- \rightleftharpoons Pt - O + H_2O + 2e^-$$

(d) Methanol Oxidation at Ionomer-film Modified Pt QCM Electrode

i. Introduction

The use of methanol as a fuel represents an important avenue in fuel cell research since it can achieve higher volumetric energy densities, and being a liquid fuel has a better ease of handling, when compared to hydrogen.[6,7] It is particularly suited for alkaline fuel cells (AFCs) based on the reportedly faster kinetics of methanol oxidation in alkaline media vis-à-vis acidic media [8–11] and the lower fuel crossover effect compared to proton exchange membrane fuel cells due to the favorable direction of the electro-osmotic drag in AFCs.[6,7] However, methanol poses some challenges in its application in AFCs, in general, and in AFCs employing alkaline anion exchange membranes (AAEM-AFCs), in particular.[12]

Being a carbonaceous fuel, methanol, upon oxidation, is itself a source of carbonation in the polymer electrolyte at the anode. The buildup of CO_3^{2-} at the anode will lower the pH decreasing the overall cell voltage and deteriorating fuel cell performance. Due to the lower mobility of CO_3^{2-} compared to OH^-, the overall ionic conductivity of the membrane is also diminished. In light of these challenges, the current EQCM study of the methanol oxidation at

the ionomer-film modified Pt electrode assumes particular significance. An important aspect of AAEMs that has been overlooked, due to the intense focus on the carbonation issue, is the effect of non-carbonate anions on the performance of AAEM-AFCs. This point is again relevant to the use of methanol as fuel in these systems since incomplete oxidation of methanol can produce formate anion ($HCOO^-$). Besides, formate itself is a potential fuel for direct alkaline fuel cells.[13,14]

The mechanism of methanol oxidation on platinum in alkaline media has been inferred[15] to consist of primarily two reactions (Equation 4.2) and (Equation 4.3) producing CO_3^{2-} and $HCOO^-$, respectively, with $HCOO^-$ being indicated as the main product at high potentials (> 0.6V vs RHE).[16,17]

Equation 4.2: $$CH_3OH + 8OH^- \rightarrow CO_3^{2-} + 6H_2O + 6e^-$$

Equation 4.3: $$CH_3OH + 5OH^- \rightarrow HCOO^- + 4H_2O + 4e^-$$

ii. Cyclic Voltammetric Study

The oxidation of methanol drastically modifies the frequency response of the ionomer-film modified electrode. This is amply evident from comparing the results (Figure 4.8) to those in the absence of methanol (Figure 4.7) from the previous section. Figure 4.8 also serves to compare the response for the bare Pt electrode (Figure 4.8a) and the modified electrode (Figure 4.8b).

Examining the CV for the bare electrode (Figure 4.8a), it is seen that CH_3OH oxidation is inhibited at high potentials. This is due to the formation of a passivating oxide layer at the Pt electrode.[15] It is also generally seen that the onset of CH_3OH oxidation in the reverse scan (broken line) is delayed and the anodic peak current significantly lowered (~ 40 %) compared to

that in the forward sweep (solid line). This is attributed to the persistence of the inhibitory Pt-OH/oxide species formed at high potentials as mentioned earlier.

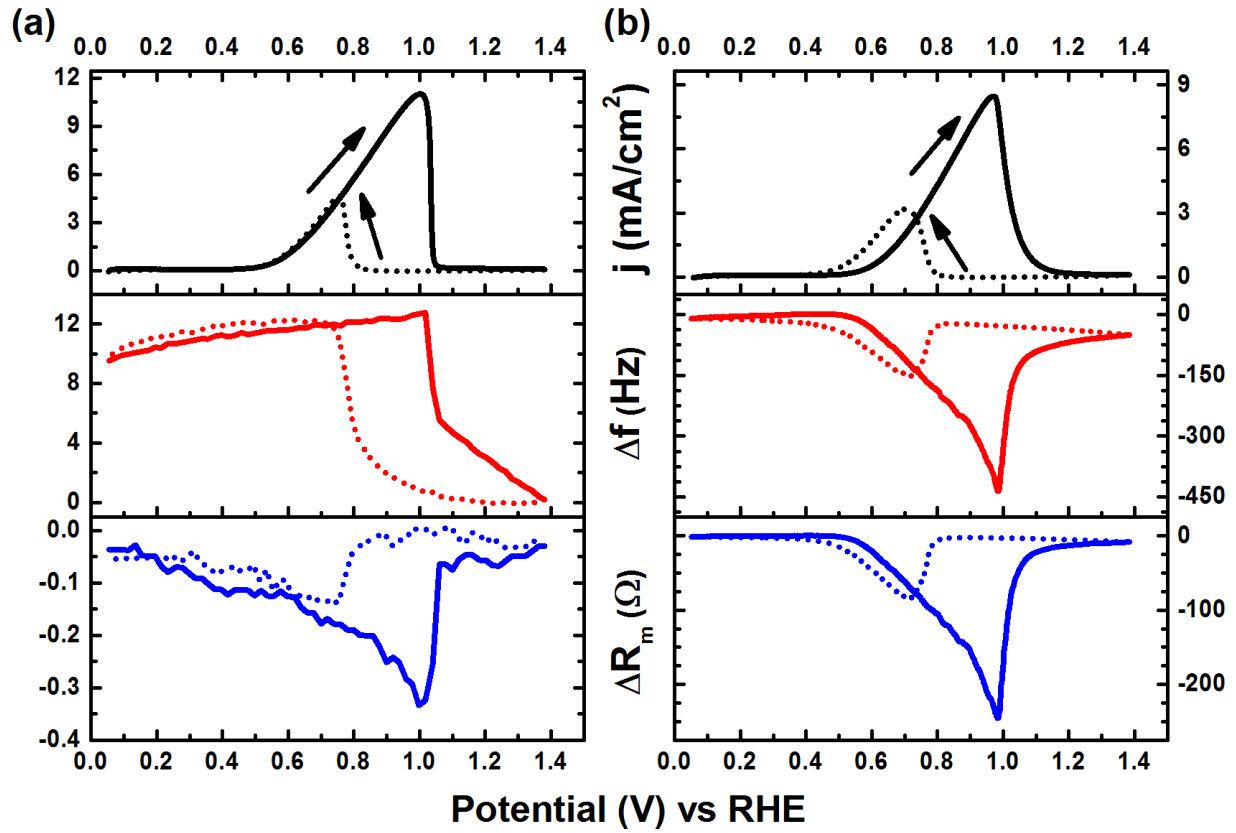

Figure 4.8: Cyclic voltammetry with simultaneous frequency (Δf) and motional resistance (ΔR_m) change measurement in 0.1 M CH_3OH/0.1 M NaOH for (a) bare Pt QCM electrode (b) the ionomer-film modified Pt QCM electrode. Dry film thickness: 210 nm. Scan rate: 20 mV/s. Solid line forward scan and broke line reverse scan. Solution stirring rate: 290 rpm.

It is apparent, from examining the CVs for the bare and the modified electrode, that the voltammetric profile is not altered markedly by the presence of the ionomer film. However, lower anodic peak currents (20-30 %) in the forward and the reverse scans are seen for the modified electrode. This may be attributed to the ionomer film on the Pt electrode acting as a blocking layer impeding the free transport of CH_3OH to the electrode surface. Due to partitioning of CH_3OH molecules at the film-solution interface, the concentration of CH_3OH may be different, likely lower, in the film than in the bulk solution.

The frequency response of the modified electrode is noticeably different from that of the bare electrode. First of all, for the bare electrode, the overall frequency change ($\mathbf{\Delta f_{max}}$: maximum value of $|\mathbf{\Delta f}|$) during potential cycling is much smaller (~ 13 Hz) compared to that at the modified electrode (~ 430 Hz). In fact, looking at Figure 4.7 and Figure 4.8, Δf_{max} at the bare electrode with and without CH_3OH are comparable. This suggests that the frequency changes even in the presence of CH_3OH are predominantly due to the Pt-oxide formation/reduction processes discussed previously. The introduction of the ionomer film at the electrode dramatically alters the frequency response. The frequency changes now reflect the CH_3OH oxidation voltammetric profile. Based on the previous results, the substantial frequency decrease ($\mathbf{\Delta f_{max}}$ ~ 430 Hz), signifying a mass increase of the composite electrode observed during CH_3OH oxidation, cannot be solely due to Pt-oxide formation. It is suspected that the apparent mass increase is due to the displacement of OH^- in the film by $CO_3^{2-}/HCOO^-$ ions generated during the oxidation process at the electrode. Results from a series of open-circuit QCM measurements, described later in this section, support this hypothesis. At the bare electrode, the changes in the motional resistance parameter ($\mathbf{R_m}$) are very small (maximum value of $|\mathbf{\Delta R_m}| \sim 0.3\ \Omega$). For the modified electrode, there is a significant decrease in $\mathbf{R_m}$ value during CH_3OH oxidation ($|\mathbf{\Delta R_m}|$ (max) ~ 250 Ω). Just as $\mathbf{\Delta f}$, $\mathbf{\Delta R_m}$ tracks the CH_3OH oxidation voltammetric profile strongly indicating that the viscoelastic changes are closely coupled to the Faradaic processes at the electrode.

The origin of the viscoelastic changes observed need to be determined. As discussed in section 2.2.1.e, for polymer films, the increase in the film viscoelasticity is generally attributed to solvent plasticization (swelling) of the film due to the influx of solvent molecules. EQCM studies of redox polymer films have indicated that the phenomenon of solvent transport simultaneous with the motions of ions during Faradaic processes is ubiquitous.[18–22] A theoretical

framework to understand the frequency changes in these systems has also been developed.[20,23–27] The studies emphasize the need to consider a variety of factors in analyzing the EQCM data such as the thermodynamic equilibria of species in the film, the kinetics of the electrochemical reactions in the film and the transport processes within the film. The salient point is that ensuring electroneutrality in the film by considering solely the movement of charged species is not sufficient to ensure global (quasi)-equilibrium in the film and the contributions of the neutral species (solvent molecules and ion-pairs) need to be evaluated.

In the current scenario, the analysis of EQCM results using the theoretical framework developed for the redox polymer films is not directly applicable due to two main reasons: (1) the ionomer film itself is electroinactive and the changes in the populations of species (both charged and neutral) in the film are directly influenced by the electrochemical processes occurring at the substrate electrode – film interface. This is in contrast to an electroactive film such as redox polymer films where the redox processes occur within the film (2) the viscoelasticity of the ionomer film changes significantly during fuel oxidation which precludes any reliable mass quantification from the frequency change. The EQCM studies of redox polymer films assumed the rigid film behavior in their analysis.

In the EQCM studies of redox polymers mentioned previously, the accounting for net mass fluxes in the film is simple since there is only the mass transport across the film-solution interface to consider; whereas for the ionomer-film modified electrodes, the mass fluxes at both the substrate electrode – film interface and the film-solution interface are relevant. This makes the analysis of mass changes in the latter system more complicated. Another problem in quantifying the EQCM data is the CH_3OH oxidation itself. The product distribution of the oxidation is not known which is needed to correlate the Faradaic charge to the apparent mass

change in the film. In view of these complications, only a qualitative treatment of the results is attempted here.

From the frequency decrease observed during CH_3OH oxidation, it appears that anions ($HCOO^-/CO_3^{2-}$) generated during the oxidation displace OH^- in the ionomer film registering an apparent mass increase of the film. Since there is a simultaneous decrease in $\mathbf{R_m}$, it is possible that anion incorporation in the film is accompanied by the efflux of water molecules such that there is a net mass increase due to the former process. This hypothesis is supported, to an extent, by the results of the auxiliary experiments described later.

iii. Chronoamperometric Study

The cyclic voltammetry study discussed above was complemented with potential-step experiments aimed at determining the time-dependent behavior of the film processes. A series of potential steps were performed between +0.7 V and +0.1 V vs RHE; thus, initiating or arresting the oxidation of CH_3OH, respectively (Figure 4.9).

The results from the potentiostatic experiment are in line with the $\mathbf{\Delta f}$ and the $\mathbf{\Delta R_m}$ changes that were already observed in the cyclic voltammetry study (Figure 4.8). On stepping to +0.7 V, where CH_3OH is oxidized, there is a precipitous decrease in both the frequency ($|\mathbf{\Delta f}| \sim$ 180 Hz) and the motional resistance ($|\mathbf{\Delta R_m}| \sim 70\ \Omega$). As discussed previously, these changes are suspected to be due to the incorporation of the oxidatively-generated anions into the film. When the potential is switched back to 0.1 V, CH_3OH is no longer oxidized and a slower recovery back to the original values is observed. The increase in the frequency and the resistance parameter on stepping back to 0.1 V is attributed to the displacement of the anions in the film by OH^- in solution.

A significant feature of the QCM response from the modified electrode is the difference in the rate of change of **f** and $\mathbf{R_m}$ during the positive and the negative potential steps. Assuming that the changes in **f** and $\mathbf{R_m}$ are due to anion inter-exchange (CO_3^{2-}/$HCOO^-$ ↔ OH^-) in the film, the smaller rate of recovery of **f** and $\mathbf{R_m}$ during the negative potential step indicates that it is more difficult for OH^- to displace CO_3^{2-}/$HCOO^-$ than for it to get displaced by the latter anions during the positive potential step. Such a phenomenon has been observed in case of redox polymer films.[26] For these systems, it was generally observed that, for a given species, egress from the film was more facile than ingress and the effect was termed 'kinetic permselectivity' of the film.

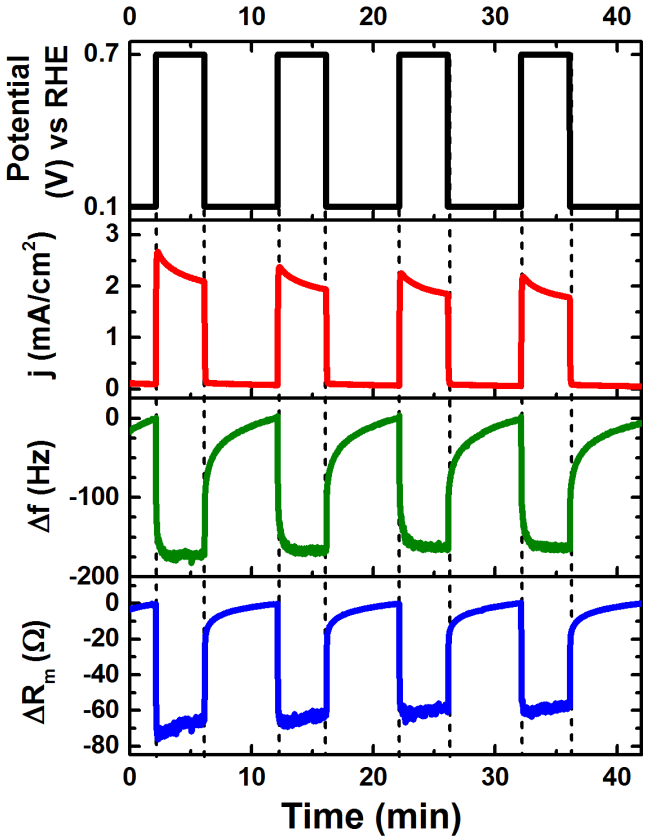

Figure 4.9: A series of potential steps with simultaneous frequency (Δf) and motional resistance (ΔR_m) change measurement in 0.1 M CH_3OH/0.1 M NaOH for the ionomer-film modified Pt QCM electrode. Dry film thickness: 210 nm. Solution stirring rate: 300 rpm.

iv. Effect of Film Thickness

Since the transport of reactants and products to and from the electrode would be controlled by the transport of species through the film, the film thickness will influence the rate of ion-exchange in the film. The effect of film thickness on the frequency response during CH_3OH oxidation was investigated by studying a thinner ionomer film (~ 50 nm dry thickness) and comparing the results (Figure 4.10) to those from the previous study (Figure 4.8 and Figure 4.9). It is clear that the frequency change observed for the thin ionomer film is significantly smaller (by a factor of ~ 15 for the cyclic voltammetric studies) compared to the thicker film. In fact, in contrast to the thicker film, the frequency increases (albeit to a smaller extent) during CH_3OH oxidation for the thinner film (Figure 4.10a). Also, the profile for the thin ionomer film resembles that of the bare electrode (Figure 4.8a) more than that of the thick ionomer film (Figure 4.8b).

A faster exchange of ions between the film and the solution as the film thickness decreases is expected. Consequently, the magnitude of the concomitant net mass changes in the film will also decrease with decreasing film thickness; eventually becoming small compared to even the mass changes from the electrochemical processes at the electrode. Hence, for sufficiently thin ionomer films, the Δf – potential profile of the modified electrode will resemble that of the bare electrode. Results from the potential step experiments (Figure 4.10b) also support these conclusions. The $\mathbf{\Delta R_m}$ versus potential plot is similar to that of the thicker film. However, the changes are much smaller. This was already anticipated from the viscoelastic studies previously described (Figure 4.4).

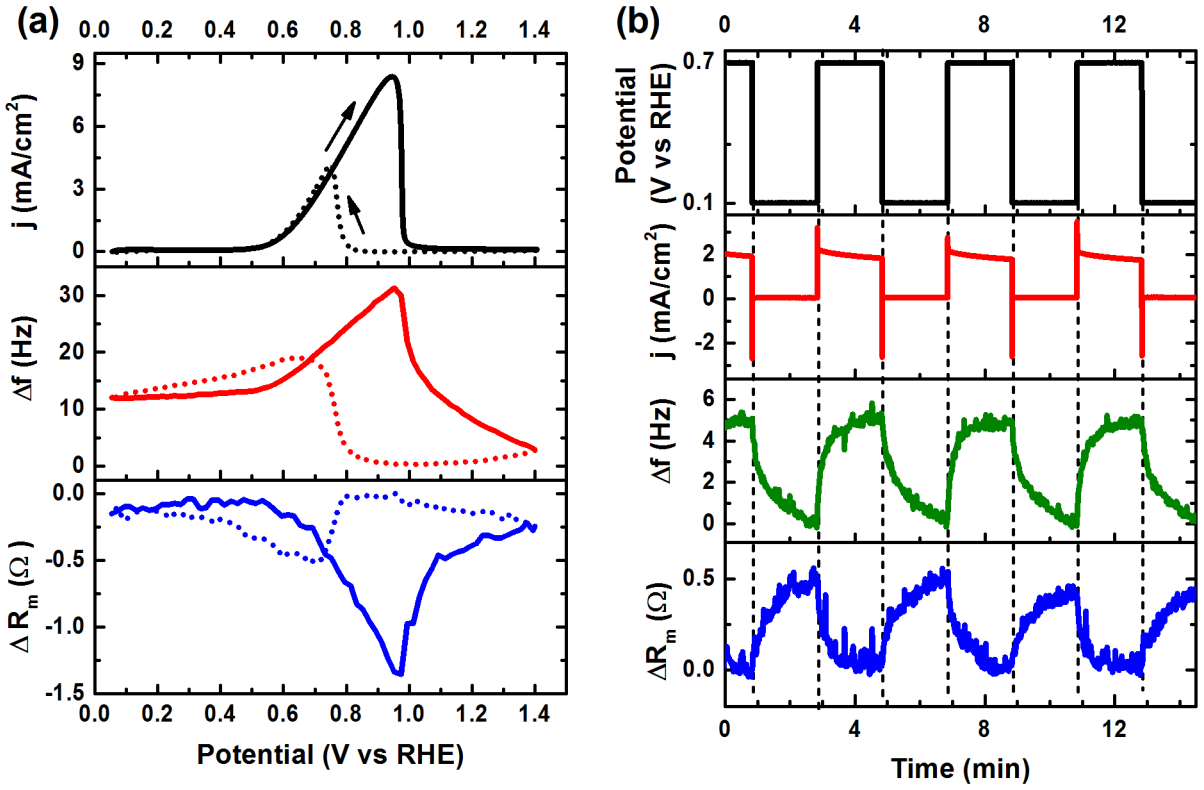

Figure 4.10: (a) Cyclic voltammetry and (b) potential step experiments with simultaneous frequency (Δf) and motional resistance (ΔR_m) change measurement in 0.1 M CH_3OH/0.1 M NaOH for a 50 nm (dry thickness) ionomer-film modified Pt QCM electrode. For (a): Scan rate – 20 mV/s. Solid line forward scan and broken line reverse scan. Solution stirring rate – 295 rpm. For (b): Solution stirring rate – 395 rpm.

(e) Frequency Measurements at Open Circuit

In order to understand the source of the mass and viscoelastic changes in the film observed during CH_3OH oxidation, QCM measurements were carried out at the ionomer film modified electrode at open circuit. The strategy was to introduce aliquots of concentrated solutions of the reactant (CH_3OH) or the products ($HCOO^-$/CO_3^{2-}) to the supporting electrolyte (0.1 M NaOH) in which the modified electrode is immersed and simultaneously monitor the changes in **f** and $\mathbf{R_m}$ resulting from the change in the concentration of the species in the film. This is similar to the experimental strategy depicted in Figure 4.5a. The intent here is, in a way, to simulate the effect of the concentration variation of the reactants/products in the film driven

by the CH_3OH oxidation at the electrode in the EQCM experiments discussed before. The benefit of the open circuit experiments is that the contributions of the product and the reactants to the QCM response can be individually analyzed. It should be remembered, however, that in these experiments the solution concentration of the species is deliberately altered to affect the species concentration in the film whereas in the EQCM experiments the species, concentration in the film is controlled largely by the applied potential and the species concentration in the solution is relatively unchanged during the course of the experiment.

i. CH_3OH Addition

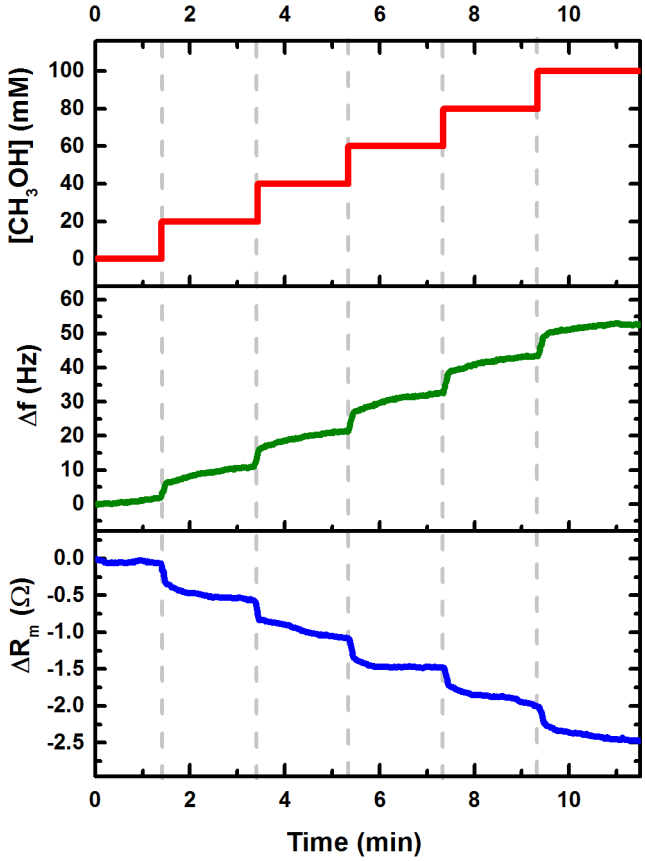

Figure 4.11: Δf and ΔR_m versus time during the addition of aliquots of 3 M CH_3OH to 0.1 M NaOH in the EQCM cell. A Pt QCM electrode coated with a 340 nm ionomer film is immersed in the solution. Initial volume of the solution (0.1 M NaOH) in the cell: ~ 90 mL. Each addition is an aliquot ~ 620 µL in volume added in ~ 5s (at 7 mL/min) to a stirred solution (~ 300 rpm) resulting in a concentration increment of CH_3OH in the solution of approximately 20 mM.

Increasing the concentration of CH_3OH in the solution in the range 0 – 0.1 M, and consequently, the concentration of CH_3OH in the film, results in a systematic increase in the frequency and a simultaneous decrease in $\mathbf{R_m}$. The frequency increased and the $\mathbf{R_m}$ decreased at a rate of ~ 10 Hz and ~ 0.5 Ω, respectively, for every 20 mM increment in the solution concentration of methanol. These changes are much smaller than those observed during the CH_3OH oxidation in the EQCM experiments (Figure 4.8 and Figure 4.9). Hence, the variation of the concentration of methanol in the film during oxidation cannot explain the significant decreases in **f** and $\mathbf{R_m}$ observed in the EQCM experiments.

ii. $HCOO^-/CO_3^{2-}$ Addition

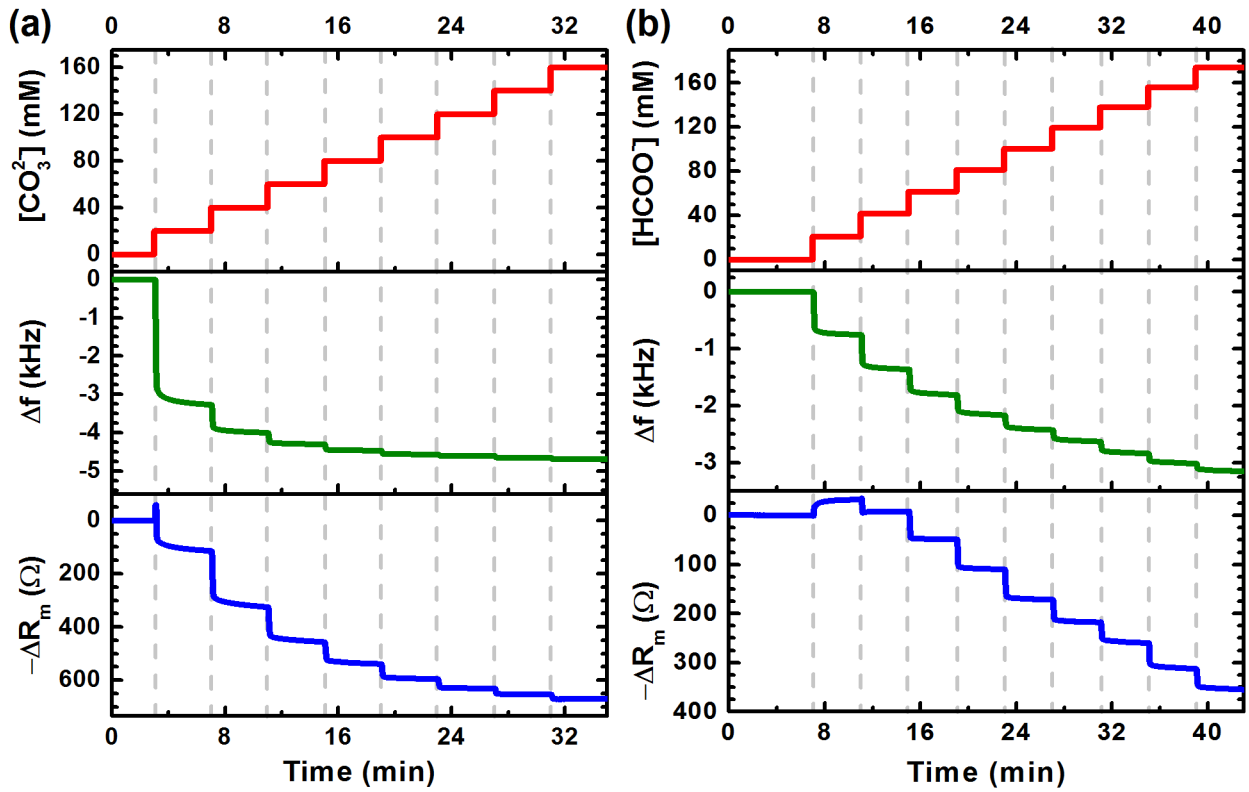

Figure 4.12: Δf and ΔR_m versus time during the addition of aliquots of (a) 2 M Na_2CO_3 (b) 2 M HCOONa to 0.1 M NaOH in the EQCM cell. A Pt QCM electrode coated with a 340 nm ionomer film is immersed in the solution. Initial volume of the solution (0.1 M NaOH) in the cell: ~ 85 mL. Each addition is an aliquot ~ 900 µL in volume added in ~ 5s (at 10.8 mL/min) to a stirred solution (~ 300 rpm) resulting in a concentration increment of $HCOO^-/CO_3^{2-}$ in the solution of approximately 20 mM.

Similar experiments were carried out using concentrated solutions of Na_2CO_3 and HCOONa to explore the effects of the incorporation of the product anions – CO_3^{2-} and $HCOO^-$ respectively – of CH_3OH oxidation in the film. As is evident from Figure 4.12, the effect of the anions on the ionomer film is drastically different from that of CH_3OH. Significantly, the addition of CO_3^{2-}/$HCOO^-$ results in a massive decrease in the frequency ($\Delta f \sim 3$-5 kHz) and the resistance parameter ($\Delta R_m \sim 350$-600 Ω) of the modified electrode. This observation strongly suggests that the incorporation of CO_3^{2-}/$HCOO^-$ generated during CH_3OH oxidation into the film is directly responsible for the apparent mass increase in the film and the decrease in the viscoelasticity of the film.

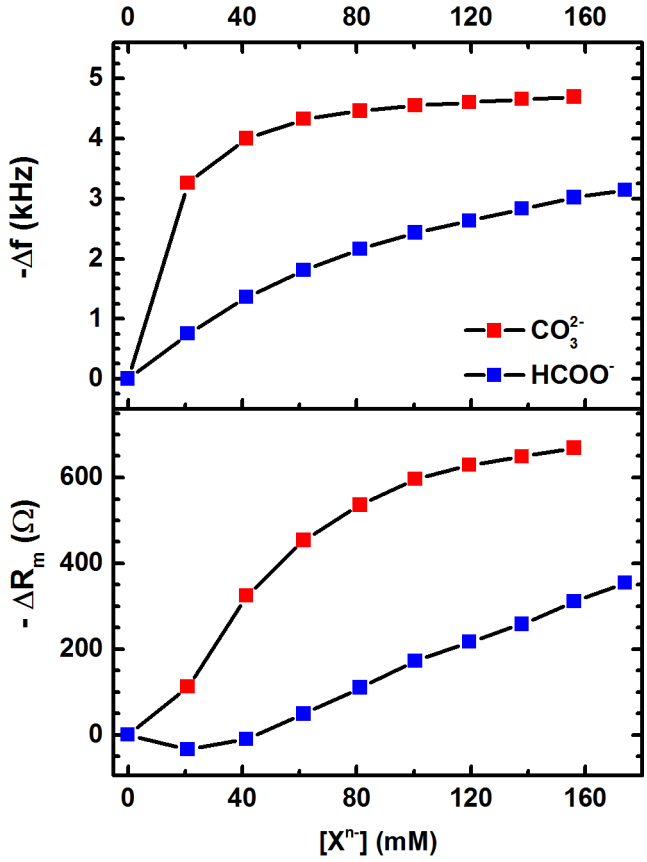

Figure 4.13: Plots of the steady-state values of Δf and ΔR_m versus the solution concentration of X^{n-} anion where $X^{n-} = CO_3^{2-}$ or $HCOO^-$ based on the data from Figure 4.12.

Due to the viscoelastic effects, mass quantitation of the anions in the film is not possible. However, the partitioning of the anions into the film dictated by the solution concentration can be studied by constructing pseudo-isotherms wherein the steady-state values of **Δf** and $\mathbf{\Delta R_m}$ are plotted against the solution concentration of the anion. This is shown in Figure 4.13. It is apparent that, for a given anion concentration in the solution, CO_3^{2-} uptake in the film causes apparently higher mass and viscoelastic changes in the film when compared to $HCOO^-$. A higher partition coefficient for CO_3^{2-} anions is also indicated based on the pseudo-isotherm as the saturation CO_3^{2-} concentration in the film is reached at lower solution concentrations of CO_3^{2-} vis-à-vis $HCOO^-$. Furthermore, it is seen that, for both CO_3^{2-} and $HCOO^-$, $\mathbf{\Delta R_m}$ does not attain a saturation value until a significantly higher solution anion concentration compared to that for Δf indicating that the changes in the film viscoelasticity is less affected by the change in the solution anion concentration. Importantly, the finite carbonate uptake in the film as indicated in Figure 4.13 validates the expected tolerance of AAEMs to carbonate precipitation.

(f) $HCOO^-$ Oxidation at Ionomer-film Modified Pd QCM Electrode

The interplay between $HCOO^-$ and CO_3^{2-} in the film can be probed by studying the $HCOO^-$ oxidation at the ionomer film modified electrode. To this end, the ionomer film was spin coated on a Pd thin film (~ 100 nm thick) sputtered deposited on Au QCM electrode. The combination of Pd thin layer electrode on Au QCM substrate was chosen as Pd is highly active for $HCOO^-$ oxidation where as Au is inactive.[28] It is to be noted that the deposited Pd thin film in contact with the Au QCM electrode still behaves as a rigid film during the QCM operation. Hence, any significant changes in R_m at the ionomer film modified electrode will be due to the changes in the viscoelasticity of the ionomer film.

The results from the EQCM studies of $HCOO^-$ oxidation at the ionomer film modified electrode are shown in Figure 4.14. The overall **Δf** and **ΔR_m** values for $HCOO^-$ oxidation at the ionomer film modified electrode are substantially higher than the corresponding values observed at the ionomer film modified electrode in the absence of $HCOO^-$ (ca. 15x and 20 x respectively) and at the bare Pd-Au composite QCM electrode in the presence of $HCOO^-$ (ca. 15x and 80x respectively). This implies that the apparent mass and the viscoelastic changes are due to the film processes driven by the $HCOO^-$ oxidation at the electrode.

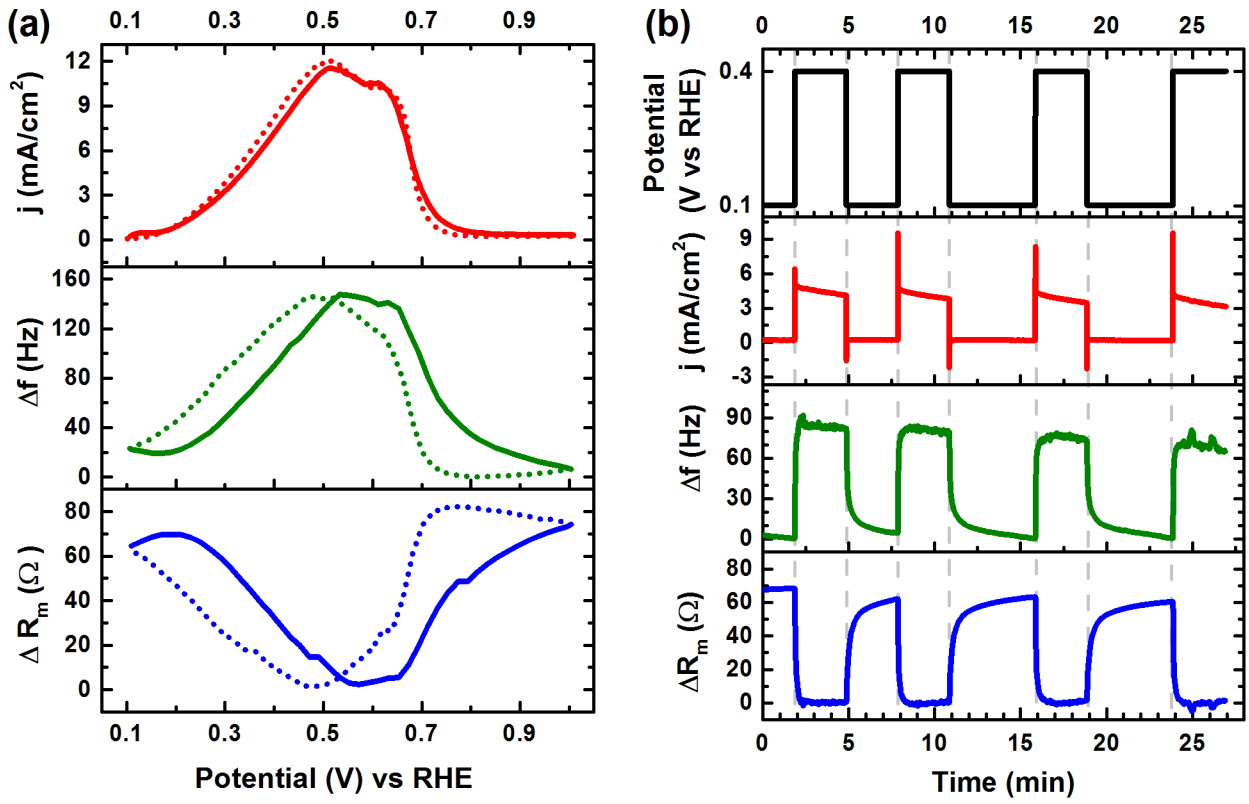

Figure 4.14: (a) Cyclic voltammetry and (b) potential step experiments with simultaneous frequency (Δf) and motional resistance (ΔR_m) change measurement in 50 mM HCOONa/0.5 M NaOH for a 330 nm (dry thickness) ionomer-film modified sputter deposited Pd (100 nm) on Au QCM electrode. For (a): Scan rate – 20 mV/s. Solid line forward scan and broken line reverse scan. Solution stirring rate for (a) and (b) – 210 rpm.

Equation 4.4: $HCOO^- + 3OH^- \rightarrow CO_3^{2-} + 2H_2O + 2e^-$

During oxidation, it is seen that there is an apparent mass decrease in the film. This could be due to the displacement of $HCOO^-$ in the film by CO_3^{2-} generated during $HCOO^-$ oxidation (Equation 4.4). From the results from the open-circuit QCM experiments discussed previously (Figure 4.12), it was already inferred that both $HCOO^-$ and CO_3^{2-} can easily displace OH^- from the film. Moreover, based on the pseudo-isotherms (Figure 4.13), the ionomer films seem to have a stronger affinity for CO_3^{2-} than $HCOO^-$ meaning that the exchange of $HCOO^-$ in the film by CO_3^{2-} should be a favored process. Based on these arguments, the apparent mass decrease in the film during oxidation can be understood. It is postulated that the dominant process could be the insertion of doubly charged CO_3^{2-} anions that will result in the expulsion of two $HCOO^-$ anions per CO_3^{2-} inserted to maintain electro-neutrality in the film. The overall apparent mass change (including any accompanying solvent transfer) during this process is postulated to be negative and consequently registered as a frequency increase during the oxidation. In a similar vein, the decrease in $\mathbf{R_m}$ during oxidation can also be explained by the same process. It is seen from Figure 4.13 that the magnitude of $\mathbf{\Delta R_m}$, on average, is 2-4 times higher for CO_3^{2-} compared to $HCOO^-$ for the same concentration of the anions in the solution.

(g) HCHO Oxidation at Ionomer-film Modified Pt QCM Electrode

Although not widely reported for CH_3OH oxidation in alkaline media, HCHO is a potential intermediate/product during oxidation on platinum. In acidic medium, the formation of HCHO during CH_3OH oxidation on Pt is known.[29] On platinum, it has been indicated that the oxidation of HCHO in alkaline medium predominantly yields $HCOO^-$ as the product (Equation 4.5).[30] Hence, in the conversion of CH_3OH to $HCOO^-$ in Equation 4.3, a route involving HCHO as the intermediate is a distinct possibility.

Equation 4.5: $HCHO + 3OH^- \rightarrow HCOO^- + 2H_2O + 2e^-$

Given this premise, HCHO oxidation at the ionomer film modified Pt QCM electrode was used as a probe reaction in an attempt to deconvolute the effect of $HCOO^-$ from that of CO_3^{2-} during the oxidation of CH_3OH. However, it should be pointed out that the nature of the interaction of HCHO with the ionomer film is complicated since, in the pH range (13-14) employed, HCHO (pKa=13.27) exists both as the neutral methylene glycol ($CH_2(OH)OH$) and the methylene glycolate anion ($(CH_2(OH)O^-$).

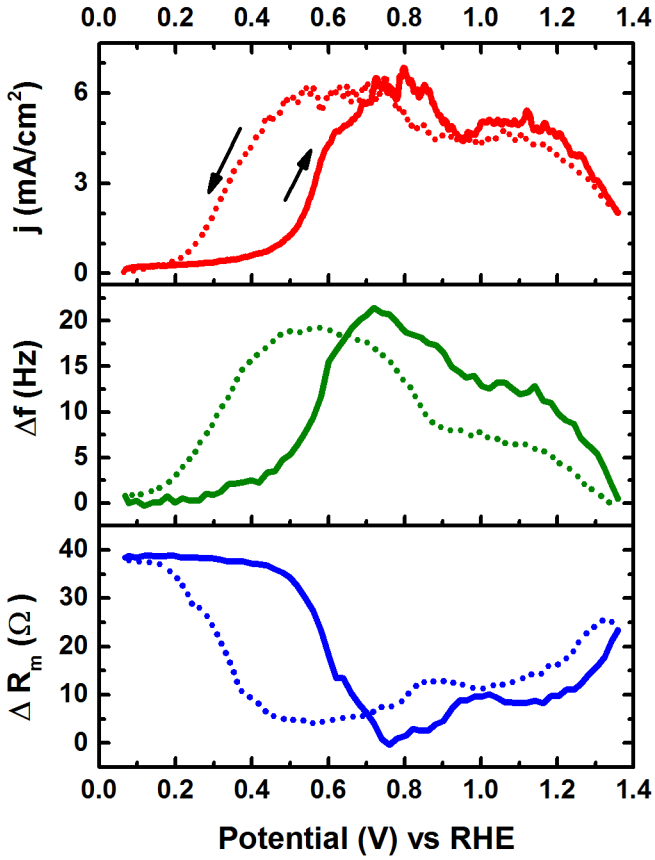

Figure 4.15: Cyclic voltammetry with simultaneous frequency (Δf) and motional resistance (ΔR_m) change measurement in 20 mM HCHO/0.5 M NaOH for a 340 nm thick ionomer-film modified Pt QCM electrode. Scan rate – 20 mV/s. Solid line forward scan and broken line reverse scan. Solution stirring rate – 210 rpm.

In any case, similar to $HCOO^-$ oxidation (Figure 4.14), a frequency increase is seen on oxidizing HCHO (Figure 4.15). However, the change ($\mathbf{\Delta f_{max}} \approx 20$ Hz) is about 3 times smaller than that of $HCOO^-$ oxidation (after normalizing for the current density). It should be noted that, unlike CO_3^{2-}, $CH_2(OH)O^-$ is singly charged same as $HCOO^-$ and also has almost the same nominal molecular mass. Hence, exchange of $CH_2(OH)O^-$ with $HCOO^-$ may not result in as significant a mass change in the film as that for $CO_3^{2-} \leftrightarrow HCOO^-$. The change in the film viscoelasticity during HCHO oxidation is comparable to that of $HCOO^-$ oxidation and the decrease in $\mathbf{R_m}$ is in line with the results of open circuit experiment for $HCOO^-$ (Figure 4.12).

4.4 Summary and Conclusions

Ex-situ acoustic impedance studies demonstrated that the ionomer thin films exhibited significant swelling in water. The solvent plasticization of the polymer film increases in magnitude with an increase in film thickness. In order to validate the tolerance of the ionomer material to carbonate precipitation, a strategy involving the use of QCM technique to monitor the mass changes due to carbonate uptake in the film, either electrochemically driven or otherwise, was devised. On simulating the carbonation process in the film, the technique was found to be responsive and sensitive to CO_3^{2-} insertion into the film; thus, validating the approach. In order to probe the dynamics of carbonation, in particular, and anion incorporation in the ionomer film, in general, EQCM experiments were carried out to monitor the mass changes in the film deposited on QCM electrodes in situ while relevant electrochemical reactions were driven at the electrode to generate anions that partition into the film.

The existence of severe viscoelastic effects in the ionomer thin films limited the quantitation of the mass changes in the film by the QCM technique. However, at the same time,

the measurement of the motional resistance parameter allowed the changes in the film viscoelasticity to be monitored simultaneously with mass changes. This afforded critical insights into the dynamic rheological changes in the polymer that were accompanying the anion insertion/de-insertion processes.

In the EQCM studies, the oxidation of CH_3OH at the ionomer film modified Pt QCM electrode was employed to generate anions viz. CO_3^{2-} and $HCOO^-$ to understand the dynamics of anion exchange in the ionomer film. The oxidation of CH_3OH was found to proceed with an apparent mass increase and a decrease in swelling of the film. The CO_3^{2-} /$HCOO^-$ uptake in the film was found to be reversible in that arresting the production of the anions resulted in the apparent mass and the viscoelastic changes being reversed with time. Open circuit QCM experiments were also carried out wherein the solution concentration of CH_3OH, $HCOO^-$ or CO_3^{2-} was changed systematically to establish the effects that each of these species, involved in CH_3OH oxidation, had on the mass and the viscoelastic changes in the ionomer thin film. CH_3OH was found not to influence the mass or the viscoelastic changes in the film significantly. However, the insertion of $HCOO^-$ and CO_3^{2-} into the ionomer film was observed to proceed with substantial increase in the apparent mass and decrease in swelling of the film. Reassuringly, the thin films were found to reach a saturation uptake of anions with an increase in the solution concentration of the anions; thus, validating the tolerance of AAEM towards precipitation of salts within the polymer matrix. Interestingly, CO_3^{2-} is indicated to have a higher partition coefficient than $HCOO^-$ which suggests a stronger interaction between CO_3^{2-} and the polymer.

In an effort to further separate out the dynamics of $HCOO^-$ and CO_3^{2-} insertion in the film, the oxidation of $HCOO^-$ and HCHO were carried out at the ionomer film modified QCM electrodes. $HCOO^-$ oxidation was found to proceed with an apparent mass decrease in the film

which may be attributed to the replacement of every two $HCOO^-$ anions in the film by a doubly charged CO_3^{2-} anion. HCHO oxidation resulted only in a slight apparent mass decrease in the film which could be due to $HCOO^-$ and $CH_2(OH)O^-$ being nominally comparable in charge and mass. The viscoelastic changes observed in these experiments, along with that from the previous experiments, point towards a ubiquitous phenomenon. Insertion of $HCOO^-/CO_3^{2-}$ into the ionomer film or equivalently the displacement of OH^- in the film by $HCOO^-/CO_3^{2-}$ invariably results in the deswelling of the film. It is inferred that the ionomer film in the OH^- form is more swollen than when in $HCOO^-/CO_3^{2-}$ form.

4.5 Future Work

There are some additional aspects of the anion incorporation into the ionomer films that need to be investigated. To this end, the methodology involving the use of EQCM that was developed in the current work can be conveniently extended for future studies. It is highly likely that the anion exchange in the ionomer films involves solvent transfer across the ionomer-solution interface. This point needs to be studied further. A well-know strategy employed in EQCM studies is to perform the experiments in H_2O and D_2O medium and compare the mass changes.[5] Any significant difference in the mass changes between the two experiments can be attributed to the presence of solvent transfer. Another aspect that warrants attention is the role of mobile cations during anion insertion. Admittedly, in an operational AAEM, there will be no mobile cations. Nevertheless, the studies along this direction will be useful for understanding the distribution of the fixed positive charges and the extent to which they are screened by the anions. A straight-forward exercise would be to conduct a series of EQCM studies using electrolytes whose cations differ in mass such as the series – LiOH, NaOH and KOH solutions.

4.6 References

(1) Kostalik, H. A.; Clark, T. J.; Robertson, N. J.; Mutolo, P. F.; Longo, J. M.; Abruña, H. D.; Coates, G. W. *Macromolecules* **2010**, *43*, 7147–7150.

(2) Pan, J.; Chen, C.; Zhuang, L.; Lu, J. *Accounts of chemical research* **2012**, *45*, 473–81.

(3) Hibbs, M. R.; Hickner, M. A.; Alam, T. M.; McIntyre, S. K.; Fujimoto, C. H.; Cornelius, C. J. *Chemistry of Materials* **2008**, *20*, 2566–2573.

(4) Gloaguen, F.; Léger, J.-M.; Lamy, C. *Journal of Electroanalytical Chemistry* **1999**, *467*, 186–192.

(5) Buttry, D. A.; Ward, M. D. *Chemical Reviews* **1992**, *92*, 1355–1379.

(6) Varcoe, J. R.; Slade, R. C. T. *Fuel Cells* **2005**, *5*, 187–200.

(7) Yu, E. H.; Krewer, U.; Scott, K. *Energies* **2010**, *3*, 1499–1528.

(8) Hao Yu, E.; Scott, K.; Reeve, R. W. *Journal of Electroanalytical Chemistry* **2003**, *547*, 17–24.

(9) Parsons, R.; VanderNoot, T. *Journal of Electroanalytical Chemistry and Interfacial Electrochemistry* **1988**, *257*, 9–45.

(10) Prabhuram, J.; Manoharan, R. *Journal of Power Sources* **1998**, *74*, 54–61.

(11) Tripković, A. V.; Popović, K. D.; Grgur, B. .; Blizanac, B.; Ross, P. N.; Marković, N. M. *Electrochimica Acta* **2002**, *47*, 3707–3714.

(12) Wang, Y.; Li, L.; Hu, L.; Zhuang, L.; Lu, J.; Xu, B. *Electrochemistry Communications* **2003**, *5*, 662–666.

(13) Bartrom, A. M.; Haan, J. L. *Journal of Power Sources* **2012**, *214*, 68–74.

(14) Bartrom, A. M.; Ta, J.; Nguyen, T. Q.; Her, J.; Donovan, A.; Haan, J. L. *Journal of Power Sources* **2013**, *229*, 234–238.

(15) Spendelow, J. S.; Wieckowski, A. *Physical chemistry chemical physics : PCCP* **2007**, *9*, 2654–75.

(16) Matsuoka, K.; Iriyama, Y.; Abe, T.; Matsuoka, M.; Ogumi, Z. *Electrochimica Acta* **2005**, *51*, 1085–1090.

(17) Morallón, E.; Rodes, A.; Vázquez, J. L.; Pérez, J. M. *Journal of Electroanalytical Chemistry* **1995**, *391*, 149–157.

(18) Varineau, P. T.; Buttry, D. A. *The Journal of Physical Chemistry* **1987**, *91*, 1292–1295.

(19) Lasky, S. J.; Buttry, D. A. *Journal of the American Chemical Society* **1988**, *110*, 6258–6260.

(20) Bruckenstein, S.; Wilde, C. P.; Shay, M.; Hillman, A. R. *The Journal of Physical Chemistry* **1990**, *94*, 787–793.

(21) Hillman, A. R.; Swann, M. J.; Bruckenstein, S. *Journal of Electroanalytical Chemistry and Interfacial Electrochemistry* **1990**, *291*, 147–162.

(22) Borjas, R.; Buttry, D. A. *Journal of Electroanalytical Chemistry and Interfacial Electrochemistry* **1990**, *280*, 73–90.

(23) Bruckenstein, S.; Hillman, A. R. *The Journal of Physical Chemistry* **1988**, *92*, 4837–4839.

(24) Bruckenstein, S.; Wilde, C. P.; Shay, M.; Hillman, A. R.; Loveday, D. C. *Journal of Electroanalytical Chemistry and Interfacial Electrochemistry* **1989**, *258*, 457–462.

(25) Bruckenstein, S. *Journal of The Electrochemical Society* **1990**, *137*, 1323.

(26) Hillman, A. R.; Loveday, D. C.; Bruckenstein, S.; Wilde, C. P. *Journal of the Chemical Society, Faraday Transactions* **1990**, *86*, 437.

(27) Hillman, A. R.; Swann, M. J.; Bruckenstein, S. *The Journal of Physical Chemistry* **1991**, *95*, 3271–3277.

(28) Nishimura, K.; Machida, K.; Enyo, M. *Journal of Electroanalytical Chemistry and Interfacial Electrochemistry* **1988**, *251*, 103–116.

(29) Korzeniewski, C.; Childers, C. L. *The Journal of Physical Chemistry B* **1998**, *102*, 489–492.

(30) Olivi, P.; Bulhões, L. O. S.; Beden, B.; Hahn, F.; Léger, J.-M.; Lamy, C. *Journal of Electroanalytical Chemistry* **1992**, *330*, 583–594.

CHAPTER 5
CHARACTERIZATION OF AN QUATERNARY AMMONIUM BASED ALKALINE ANION EXCHANGE MEMBRANE – PART II

5.1 Introduction

In a fuel cell, the ionomer in the catalyst layer has the critical function of interfacing the solid bulk membrane to the catalyst particles. Accordingly, the ionomer phase in the catalyst layer acts to transport ions between the catalyst particles and the membrane. Also, the ionomer phase should allow easy access of fuel or oxidant molecules to the catalyst particles. Hence, an important goal of the characterization studies of the AAEM ionomer material is to shed light on the mechanism of physical and charge transport in the ionomer. Rotating disc electrode (RDE) voltammetric studies of ionomer thin films using neutral redox probe molecules can yield insights into the physical transport mechanisms active in the ionomer films. For charge transport studies, negatively or positively charged redox molecules can be used as probes. The preliminary results from such studies carried out are reported herein. Ex-situ IR studies were also performed to better understand the ion-exchange process in the films.

In fuel cells, the surface pH at the catalyst-ionomer interface can be altered drastically from that in the bulk on driving the fuel cell reactions at the electrodes. The nature of these pH effects was investigated by employing DEMS (vide infra). The study of the morphology of the polymer membrane is crucial for understanding and tailoring mechanical and transport properties of the AAEMs. In fact, recent work in AAEMs has demonstrated that, unlike the general approach of increasing the ion-exchange capacity (IEC) of the membrane to improve its performance, strategies aimed at judiciously controlling the morphology of the membrane result in far more significant gains in the ionic conductivity of the membrane without simultaneously

compromising its structural integrity.[1] Given this premise, the morphology of the ionomer thin films was examined using ex-situ TEM and the initial results from that study are discussed herein.

5.2 Experimental

5.2.1 Rotating Disc Electrode Voltammetry

The RDE setup consisted of a rotator equipped with a control unit (Pine Model AFMSRX). The RDE electrodes were disks (5 mm in diameter) of glassy carbon or Pt inserted into the change disk type RDE tips (Pine E4QT Series ChangeDisk RDE tips). The change disk type tips allow the electrodes to be removed out of the tip for further characterization elsewhere. The ionomer thin films were deposited on the RDE electrodes by essentially employing the rotator as a spin-coater. For this purpose, the rotator assembly was mounted upside down on the support pillar. The rotator shaft (with the RDE electrode unit mounted) was then inserted into the rotator assembly such that the exposed face of the RDE electrode was facing up. An aliquot of the ionomer solution was then introduced on to the stationary electrode and subsequently the electrode rotated to the desired speed. Besides being used in the RDE studies, the ionomer-film modified electrodes thus prepared were also employed for the cyclic voltammetric studies using charged redox molecules.

5.2.2 DEMS

The DEMS apparatus has already been described in section 2.1. For the purpose of the experiment, a layer of the ionomer film was deposited by drop casting from the ionomer solution on a Pt sputtered porous Teflon membrane. This film electrode was then used in the DEMS flow cell configured for CO_2 detection in alkaline media as described in section 2.1.2.c.

5.2.3 Electrochemical Measurements

The potentiostats employed were the Pine AFCBP1 Bipotentiostat and the BASi CV-27 voltammograph. The data were recorded by home-made LabView/LabWindows programs using NI-DAQ cards to interface to the potentiostat. Solutions for the electrochemical experiments were prepared using chemicals that were ACS AR grade or higher and in high purity deionized water (18 MΩ cm Barnstead Nanopure Model No. 7148).

5.2.4 FTIR

The IR spectra of the spin-coated dry film samples on quartz crystal substrates (Au electrodes) were obtained using a Bruker Optics Vertex 80v FTIR. The spectra were collected in the ATR mode using the Miracle ATR accessory (PIKE) in an evacuated sample chamber (pressure: ≤ 2.5 hPa). The ATR accessory employed a diamond ATR crystal that was pressed into the sample. The angle of beam incidence at the sample was 60°. A liquid N_2-cooled MCT detector was used. A film-free Au quartz substrate was used for measuring the background spectrum. For the sample spectra, 1024 scans at a resolution of 4 cm^{-1} were co-added.

5.2.5 TEM

The ionomer films were drop-casted from the ionomer solutions in the I^- form (polymer loading ~ 0.1-1 wt %) onto Si TEM grids (5nm-thin amorphous Si TEM grid from temwindows.com). The films were subsequently allowed to air dry for 1-2 hrs before introducing into the microscope. For the case where the film was cast in the CO_3^{2-} form, the ion-exchange with I^- was carried out by immersing the grid in 1M KI with stirring for ~ 1 hr followed by repeated immersions of the grid in fresh batches of DI water for 3 times (20 mins each) to

remove any excess KI. Since I^- anions are preferentially incorporated into the hydrophilic regions of the ionomer, converting the film into the I^- form prior to the experiment serves to distinguish between the hydrophobic and the hydrophilic regions from Z-contrast TEM imaging. The TEM instrument used was a Tecnai F20 scanning transmission electron microscope (STEM) operated at 200keV. A high-angle annular dark field (HAADF) detector was employed for mass-thickness contrast (also known as 'Z-contrast') imaging. In this type of imaging, the image intensity is proportional to Z^a where Z is the atomic number and $a \approx 1.7\text{-}2$. Hence, in a Z-contrast image, the intensity due to an iodine atom should be about 40-80 times that of a carbon atom. Energy dispersive x-ray (EDX) measurements were carried out at beam current of roughly 10 pA, with 100 μs dwell time per pixel. The EDX maps of C, I and Ir were obtained by integrating peaks of C-K, I-L, Ir-L edges respectively.

5.2.6 Chemicals

N,N,N',N'- tetramethyl-p-phenylene diamine (TMPD) dihydrochloride (98% Aldrich), ferrocene - monocarboxylic acid (≥ 97% STREM chemicals), potassium ferricyanide (99.0% ACS reagent Sigma) were used without further purification. For making supporting electrolyte solutions and for ion-exchange procedures, potassium hydroxide (AR ACS Mallinckrodt), potassium chloride (99.7% AR ACS Macron chemicals), potassium iodide (≥ 99.0% puriss p.a. ACS Fluka), disodium hydrogen phosphate (ACS grade Mallinckrodt), sodium dihydrogen phosphate monohydrate (AR ACS Mallinckrodt), sodium carbonate (AR ARCS Mallinckrodt), sodium bicarbonate (AR ACS Mallinckrodt), and perchloric acid (70% redistilled Sigma Alrdich) were employed. High purity nitrogen, argon and hydrogen gases were obtained from Airgas.

5.3 Results and Discussion

5.3.1 RDE Study of the Transport of Neutral Redox Species – TMPD – in the Ionomer Film

The utility of RDE voltammetry in the investigation of the transport of molecules in film modified electrodes lies in its diagnostic value. The framework of analysis is well-established and invokes the theoretical constructs of *dynamical elements* and *characteristic currents*.[2] For the purposes of the discussion, these terms are explained in the context of the system under study. A more general description can be found elsewhere.[2] Consider the mass transport limited current i_l observed at a rotating-disc electrode coated with an electroinactive film (i.e. no charge transfer within the film). The rate at which the electroactive molecules arrive at the electrode, depending on the rotation rate ω is limited either by the *hydrodynamic transport in the solution* or by the *transport in the film* of the molecules. These are the *dynamical elements* of the system. The *characteristic current* associated with a particular *dynamical element* is the maximum current possible if the transport to the electrode is limited entirely by that *dynamical element*. In general, at a given ω, i_l is a combination of the *characteristic currents* associated with each rate-limiting step (*dynamical element*) and for the film modified electrode the general expression is

Equation 5.1:

$$\frac{1}{i_l} = \frac{1}{i_{soln}} + \frac{1}{i_{film}}$$

where i_{soln} and i_{film} are the limiting currents associated with the solution and the film transport respectively. Here, i_{soln} is the usual Levich current proportional to $\omega^{1/2}$. A plot of $1 / i_l$ vs $1/\omega^{1/2}$ will reveal any dependence of i_{film} on ω. Consequently, the plots yield insights into the nature of transport in the film through the application of various transport models. As must be evident, the

treatment above is identical to the Koutecký-Levich analysis; the only difference being that the currents are sampled in the mass-transport limited region.

A typical transport model for film modified electrodes is the membrane model (Figure 5.1a). In this model, the transport of molecules in the films is solely by diffusion and convective transport is ineffective in the film. The characteristic current associated with the diffusion in the film, i_{film}^{MM} is give by the expression

Equation 5.2:
$$i_{film}^{MM} = \frac{nFAD_s \kappa C^*}{\phi}$$

where n is the number of electrons involved in the Faradaic process, F is Faraday's constant, A is the geometric area of the electrode, κ is the partition coefficient, C^* is the solution concentration of the electroactive species and ϕ is the thickness of the film. Note that i_{film}^{MM} is independent of ω. The limiting current i_l is given by the same expression as previously (Equation 5.1) with i_{film}^{MM} in place of i_{film}. The diagnostic criterion for the applicability of the membrane model is the experimental observation of linear behavior in the $1 / i_l$ vs $1/\omega^{1/2}$ plot (Figure 5.1b). In the case of the membrane model, a linear plot with the same slope as that for the bare electrode and a non-zero y-intercept corresponding to $1 / i_{film}^{MM}$ is expected.

Another transport model of interest is the Landsberg or the pinhole model where the transport of molecules in the film occurs by both diffusion in the bulk film and permeation through channels/pinholes in the film. In this case, the corresponding characteristic current, i_{film}^{LM} is no longer independent of ω as the hydrodynamic transport in the solution can directly affect permeation of molecules in the channel. The analytical expressions for i_{film}^{LM} are more complicated

than that of i_{film}^{MM}.[2] However, from a diagnostic point of view, deviations from the linear behavior of the membrane model in the $1 / i_l$ vs $1/\omega^{1/2}$ plot can be taken to indicate the likely presence of channels/pinholes in the film.

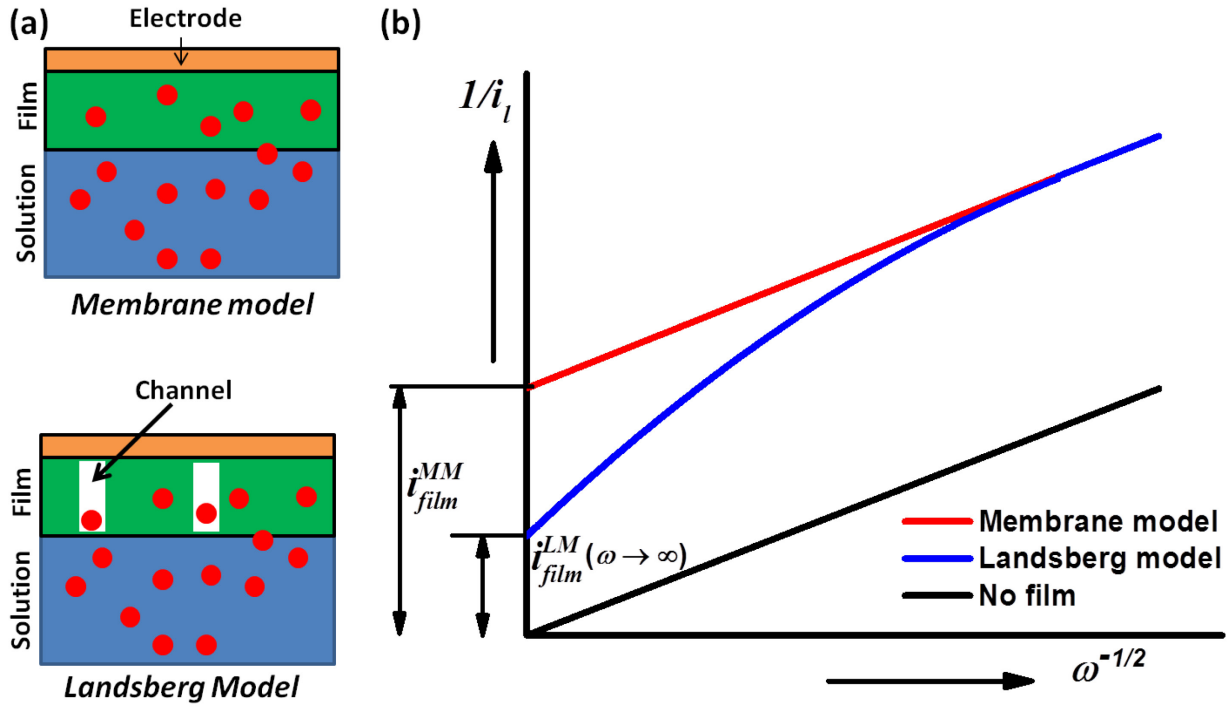

Figure 5.1: (a) Depiction of transport of molecules at film modified electrodes as per the membrane model and the Landsberg model. (b) Theoretical $1 / i_l$ vs $1/\omega^{1/2}$ plots for RDE studies according to the different transport models

Given this theoretical background, the results from the RDE studies of the oxidation of the neutral redox species – N,N,N′,N′-tetramethyl-p-phenylenediamine (TMPD) are analyzed (Figure 5.2). It is seen that for the ionomer film modified electrode, at low rotation rates, $1 / i_l$ varies linearly with $1/\omega^{1/2}$ and the plot is parallel to that of the bare electrode. Hence, at low rotation rates, the membrane model of transport in the ionomer film is applicable. However, as the rotation rate is increased, $1 / i_l$ deviates from the linear behavior. This signifies a transition from the diffusive mode of transport at low rotation rates to a faster method of transport

(possibly permeation along pinholes) at higher rotation rates. Such a non-linear behavior has been reported previously for the closely related system of Nafion coated electrodes.[3]

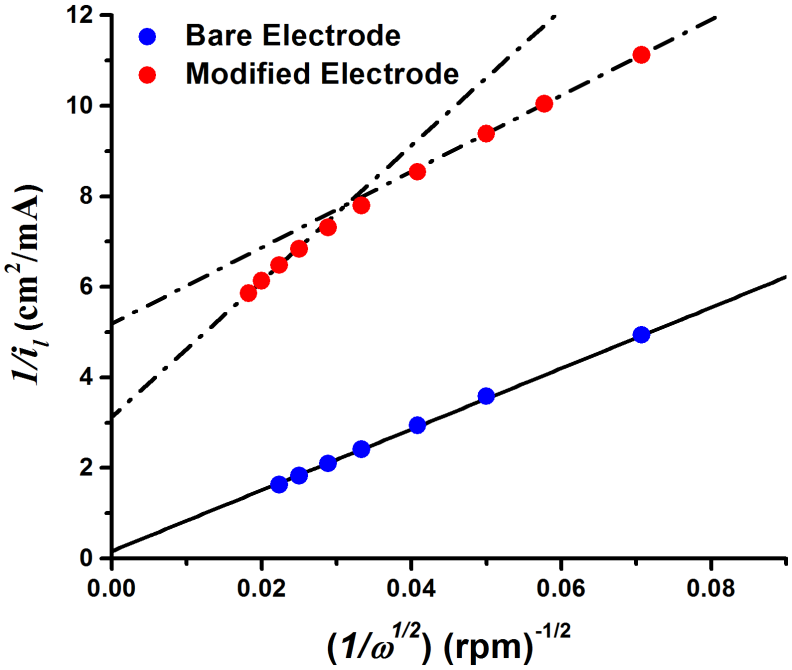

Figure 5.2: Transport behavior of TMPD through the ionomer film. $1 / i_l$ vs $1/\omega^{1/2}$ plot of ionomer film coated glassy carbon electrode in the mass transfer limited region of TMPD oxidation. 1mM TMPD in 0.1M KCl. Dry film thickness ~ 3.7μm.

5.3.2 Investigation of the Redox Chemistry of TMPD in the Ionomer Film

During the course of employing TMPD oxidation for the RDE studies described previously, it was noticed that the redox reaction of TMPD at the ionomer film modified electrode in quiescent solution showed significantly higher degree of irreversibility vis-à-vis the bare electrode. This is evident from Figure 5.3 where, compared to the anodic peak current ($i_{p,a}$), a smaller cathodic peak current ($i_{p,c}$) is observed at the modified electrode ($i_{p,c}/i_{p,a} \approx 0.8$).

Apparently, there is an irrecoverable loss of the oxidatively generated $TMPD^{\cdot+}$ species from the ionomer-electrode interface. This is suspected to be due to the presence of the ionomer

film as the redox reaction of TMPD is highly reversible at the bare electrode ($i_{p,c}/i_{p,a} \approx 1$). This phenomenon was investigated further by double potential step chronocoulometric (DPSCC) experiments that are generally useful for unraveling complications in a redox system.[4]

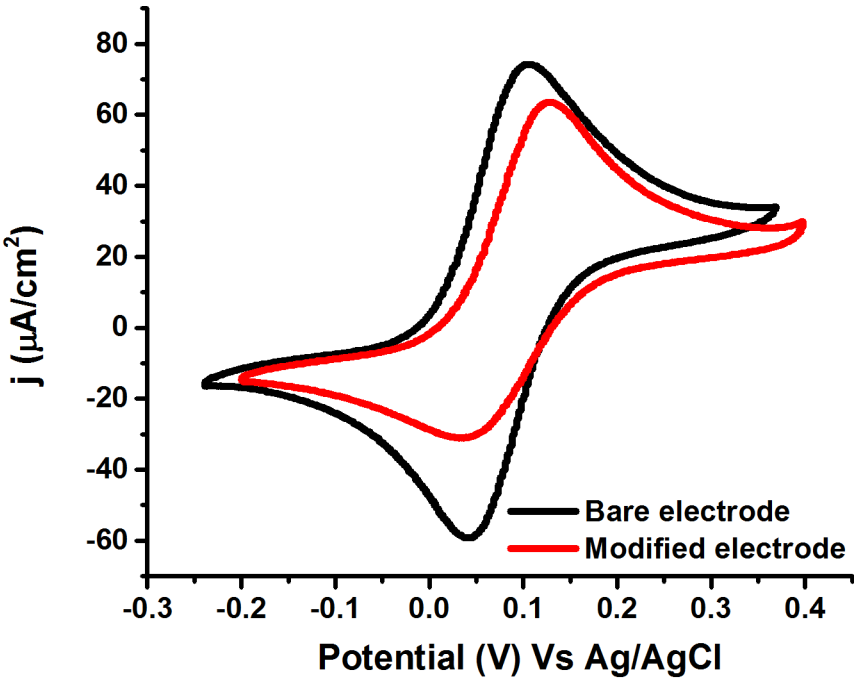

Figure 5.3: Cyclic voltammogram of 1 mM TMPD in 0.1 M KCl at (a) bare glassy carbon electrode (b) glassy carbon electrode coated with the ionomer film (dry film thickness ~ 3.7μm). Scan rate 10 mV/s.

The chronocoulometric plots from the DPSCC experiments are shown in Figure 5.4 and corroborate the existence of chemical complications following the oxidation process. Figure 5.4a demonstrates that the normalized cathodic charge $Q_R^*(t)$ recovered during the reversal step in DPSCC is significantly smaller at the modified electrode indicating the loss of electro-generated $TMPD^{\cdot+}$ by a secondary process. Similarly, the Anson plot (Figure 5.4b) shows that, during the reversal step in DPSCC, the chronocoulometric response of the TMPD redox system at the ionomer film modified electrode deviates significantly from that of the theoretical curve (dotted line) for a stable redox system. A plausible explanation for the quasireversibility of the redox reaction at the modified electrode is the repulsive interaction between the positively charged

$TMPD^{\cdot+}$ species and the cationic ionomer film that drives the rapid exodus of $TMPD^{\cdot+}$ from the ionomer-electrode interface resulting in the loss in the cathodic charge.

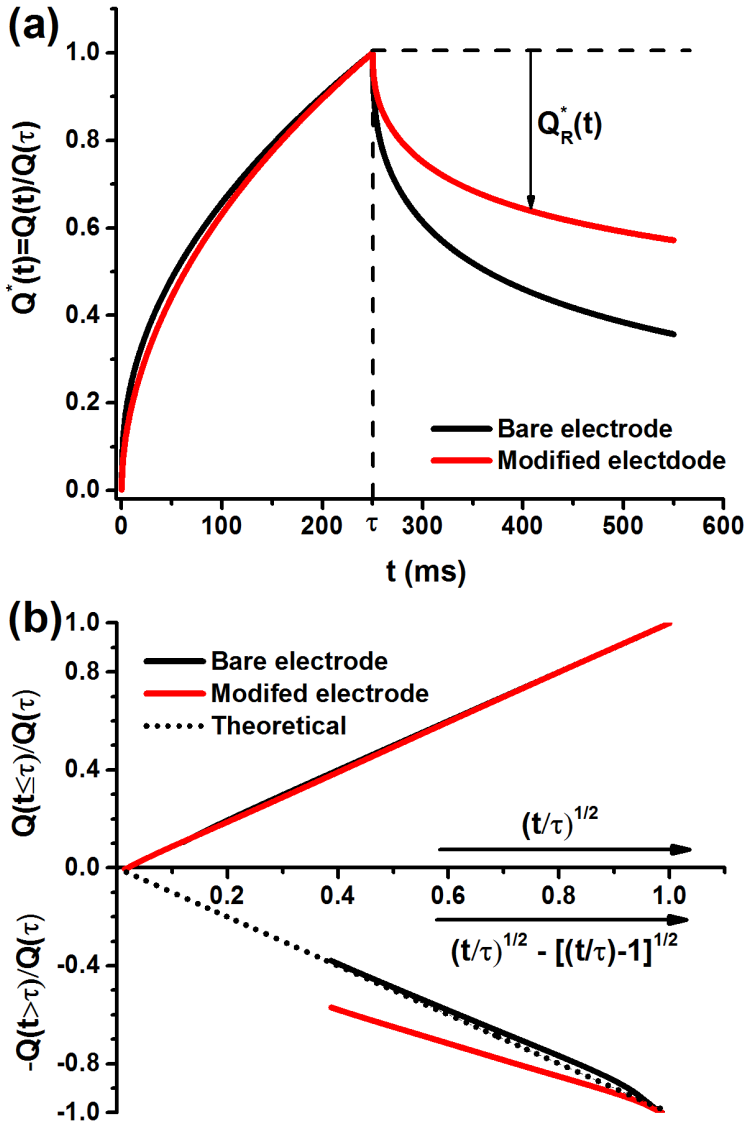

Figure 5.4: Double potential step chronocoulometry experiment at a glassy carbon electrode coated with the ionomer film (Dry film thickness ~ 3.7μm) in 1 mM TMPD/0.1 M KCl. Initial potential: -0.24 V vs Ag/AgCl. Forward step potential: 0.4 V vs Ag/AgCl. τ: 250 ms. Reverse step potential (after time, t= τ): -0.24 V vs Ag/AgCl.

5.3.3 Charge Transport Studies in Ionomer Thin Flims Using Negatively-charged Redox Probe Molecules

A series of cyclic voltammetric studies were carried out on ionomer thin films incorporated with negatively-charged redox probe molecules. The expectation was that the negatively charged redox molecules will pair with cationic sites in the film and thus, the electrochemical response of the film in this form can be used to probe the mechanism of charge transfer between the cationic sites. Since the goal was to investigate the inter-site charge transfer, the cyclic voltammetric studies were carried out in the absence of the redox species in the solution (i.e. in the supporting electrolyte solution). This ensures that there is no contribution from the solution species to the Faradaic charge observed. Accordingly, the preparation of the redox species incorporated ionomer film involved (1) immersion of the ionomer film modified electrode in a bathing solution of the redox species (2) followed by rinsing with water and/or supporting electrolyte and immersion in supporting electrolyte to ensure removal of any excess amount of redox species and (3) finally immersion of the modified electrode in fresh supporting electrolyte for the cyclic voltammetric experiment. Ferrocene-carboxylate ($Fc\text{-}COO^-$), ferricyanide ($[Fe(CN)_6]^{3-}$) and I^- were the redox species used for the studies. The corresponding bathing solutions employed were 1 mM Fc-COOH / 0.2 M Na_2HPO_4, 1 mM $K_3[Fe(CN)_6]$ / 0.1 M KOH and 1 mM KI / 0.1 M $HClO_4$ respectively.

The results from the cyclic voltammetric studies for all the redox species studied are compiled in Figure 5.5. For the $Fc\text{-}COO^-$ incorporated ionomer film (Figure 5.5a), a broad surface oxidation peak is seen at ~0.45 V vs Ag/AgCl. Intriguingly, the corresponding reduction peak (~0.35 V vs Ag/AgCl) is extremely small. It maybe that since the oxidation of $Fc\text{-}COO^-$

generates a zwitter-ion with no net charge, the oxidized species may no longer be associated with the cationic site.

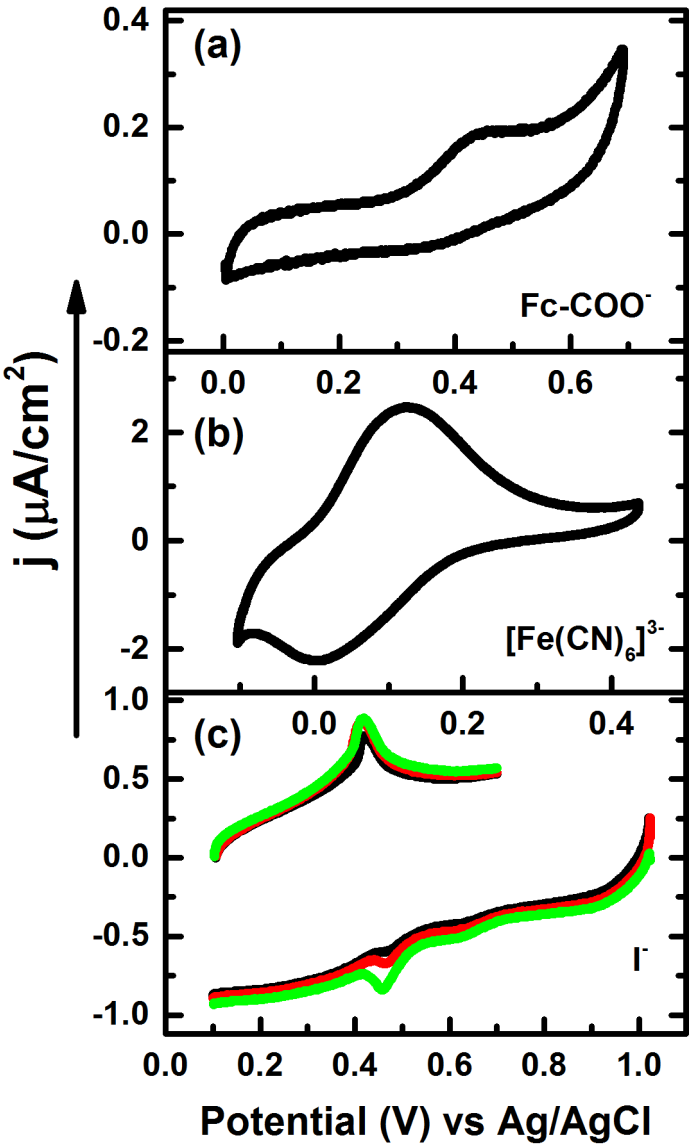

Figure 5.5: Cyclic voltammetry of (a) glassy carbon electrodes coated with ferrocene-carboxylate (Fc-COO-) incorporated ionomer film in the bare supporting electrolyte solution (0.025 M Na_2HPO_4/0.025 M NaH_2PO_4). Scan rate: 0.5 mV/s. (b) Pt polycrystalline electrodes coated with ferricyanide ($[Fe(CN)_6]^{3-}$) incorporated ionomer film in 0.1 M KOH. Scan rate: 0.5 mV/s. (c) Positive and negative-going scans of glassy carbon electrodes coated with Iodide (I^-) incorporated ionomer film in 0.1 M $HClO_4$ after holding at 0.1 V (vs Ag/AgCl) and 1V (vs Ag/AgCl) respectively for 5 (Black), 10 (Red), 20 (Green) mins. Scan rate: 1 mV/s.

The $[Fe(CN)_6]^{3-}$ incorporated ionomer film does show a pair of broad redox peaks (Figure 5.5b) at ~ 0.1 V vs Ag/AgCl. These peaks match well with those of the bulk oxidation of $[Fe(CN)_6]^{3-}$ at the modified electrode. However, quantification of charges associated with the redox processes is problematic due to the contributions from the Pt-surface features in the same potential range.

The results from the I^- incorporated ionomer film are interesting. Relatively sharp redox peaks are observed at ~0.45 V vs Ag/AgCl. The reduction peak potential is shifted slightly positive w.r.t to the oxidation peak. This may be due to the chemical conversion of I_2 to I_3^-. The I_3^-/I^- couple has a slightly more positive standard potential than the I_2/I^- couple.[5] This hypothesis is further supported by the observed temporal dependence of the reduction peak. It was seen that an increase in the time spent at potentials positive of the oxidation peak (where I_2 is generated) by either holding the potential or decreasing the scan rate resulted in an increase in the charge under the reduction peak in the subsequent negative-going scan. It should be noted that, just as in the case of $Fc\text{-}COO^-$, the oxidation of I^- results in the neutral I_2 species which may not interact with the cationic site. Hence, the chemical conversion of I_2 to the negatively charged I_3^- may be required to re-associate the oxidized species with the cationic site.

In summary, it was generally observed that for, all the redox species studied, the Faradaic charges associated with the film redox processes were small. This could be due to a variety of reasons. The partitioning of the redox species into the film might be low, resulting in a low concentration of redox active sites in the film. The distribution of the cationic sites may not be optimal in communicating the charge from the film to the electrode and/or the energetics of inter-site charge transfer may not be favorable. In the future, it will be worthwhile to carry out RDE studies involving the use of negatively charged redox probe molecules to gauge the relative

contributions of the physical transport of molecules in the film and the self-exchange mechanism to the overall charge propagation in the film.

5.3.4 DEMS Study of H_2 Oxidation in Carbonate/bicarbonate Buffer at Ionomer-film Modified Pt Sputtered Teflon Membrane

In an AFC, OH^- is generated at the cathode by the ORR and consumed at the anode through oxidation of H_2 (HOR) or other fuels. Hence, there is a OH^- concentration gradient between the cathode and the anode resulting in a finite difference between the interfacial pHs at the cathode and the anode; the anode being at a lower pH. This difference is larger in an AAEM-AFC due to the lower mobility of ions in the membrane vis-à-vis the liquid electrolyte. If using ambient air as the oxidant, the presence of CO_2 in the oxidant stream will also contribute to the decrease in pH at the anode due to the accumulation of CO_3^{2-} at the anode.[6] At the anode itself, if carbonaceous fuels – such as CH_3OH – are used, the pH drop at the anode is even more pronounced since the oxidation of the fuel results in both the consumption of OH^- and production of CO_3^{2-}. The pH difference for methanol AAEM-AFCs is estimated at 4-6 pH units and therefore a voltage loss of about 240-360 mV.[7] An interesting effect associated with the CO_3^{2-} accumulation and the concomitant pH drop at the anode is the self-purging phenomenon were the CO_3^{2-} at the anode is expelled as CO_2.[8]

In order to investigate the above-mentioned pH effects, the oxidation of H_2 in a relatively low pH medium ($NaHCO_3/Na_2CO_3$ buffer, pH≈10.2) at a Pt-sputtered Teflon membrane coated with the ionomer film (3-4 μm) was studied using DEMS. The modified electrode is used in the dual thin layer flow cell in the configuration for CO_2 detection in alkaline media (section 2.1.2.c). The results from the DEMS measurements for the bare and the modified electrode during a series of current steps in a H_2-saturated buffer solution are compared in Figure 5.6.

Since the ionomer film acts as a transport barrier, significantly lower limiting currents (~ 3x) were observed at the modified electrode compared to the bare electrode. This necessitated the use of a smaller value of the current step for the modified electrode (top panels in Figure 5.6).

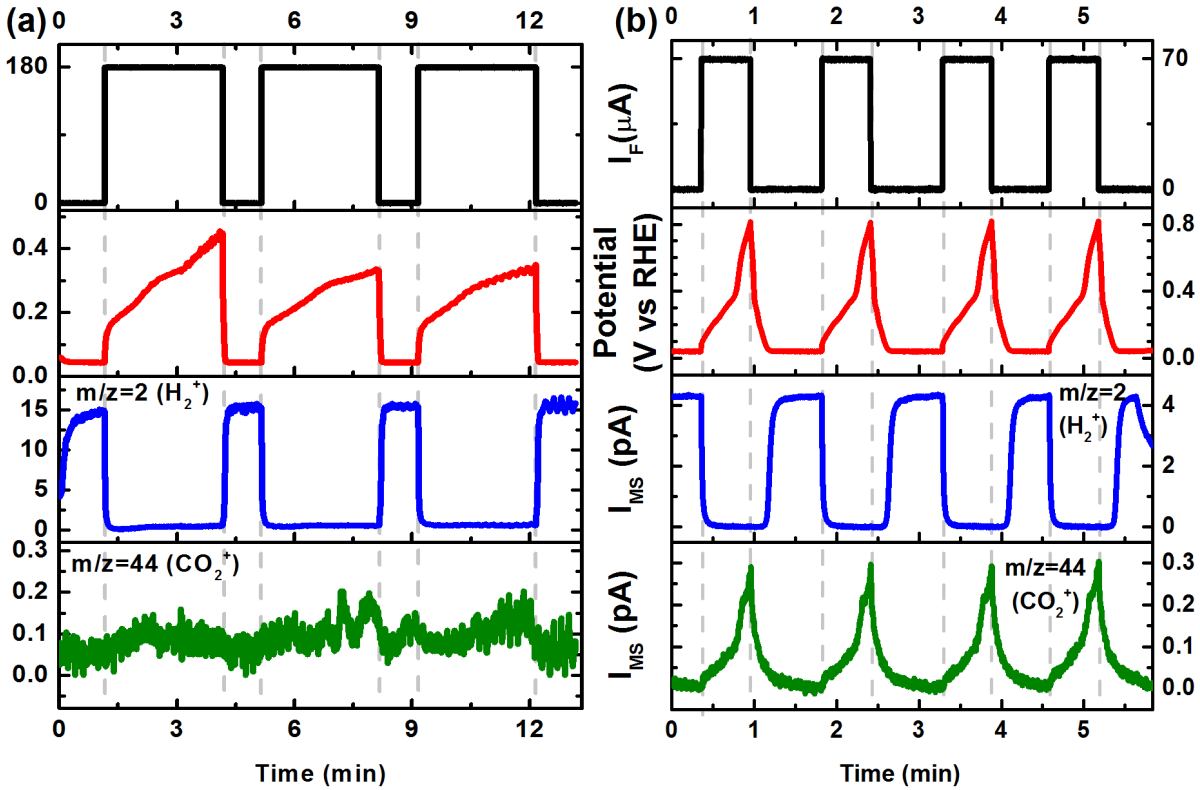

Figure 5.6: Series of current steps in 0.25 M Na_2CO_3/0.25 M $NaHCO_3$ solution saturated with H_2 at (a) Pt sputtered porous Teflon membrane (b) ionomer film coated Pt sputtered porous Teflon membrane in the dual thin layer DEMS flow cell. Simultaneous DEMS measurements yield the mass spectrometric currents for H_2^+ (m/z=2) and CO_2^+ (blue and green curves respectively). Ionomer film thickness (dry) ~ 3-4 µm. Solution flow rates: (a) 1.7 mL/min (b) 3 mL/min

The transport constraint imposed by the ionomer film on H_2 oxidation at the Pt sputtered membrane is also apparent on comparing the potential response (top second panels in Figure 5.6) during the current steps. In response to the current demand, the potential of the modified electrode increases rapidly with time to relatively high values (~ 0.8 V vs RHE) without reaching a steady state value. This is in contrast to the behavior of the potential at the bare electrode where the rise in potential is small and more gradual with time; eventually approaching a steady state

value (~ 0.3 V vs RHE) at longer times. The mass spectrometric current for H_2^+ (m/z=2) can be used to monitor the shielding effect due to the oxidation at the working electrode (bottom second panels in Figure 5.6). It is apparent that due to higher oxidation currents attainable at the bare electrode, the shielding of the H_2^+ mass spectrometric signal is higher compared to that at the modified electrode.

A comparison of the simultaneously acquired mass spectrometric current for CO_2^+ (m/z=44) (Bottom panels in Figure 5.6) show a higher amount of CO_2 being produced during H_2 oxidation at the modified electrode. The reason behind this enhanced CO_2 production needs to be carefully investigated. Prima facie, the self-purging phenomenon driven by the pH changes that accompany HOR can be cited as the reason. However, due to the low overall CO_2 signal observed and the high sensitivity of mass spectrometric detection, the oxidation of carbon contaminants in the ionomer film could be a significant source of the CO_2 signal. As documented in the literature, a more fruitful approach to study the self-purging phenomenon would be to monitor the CO_2 evolution from the anode in an operational fuel cell by analyzing the anode exhaust.[8]

5.3.5 Ex-situ IR Characterization of the Ionomer Thin Films

The IR spectra of dry ionomer thin films were obtained following the procedure outlined in section 5.2.4. Since CO_3^{2-}/HCO_3^- have strong absorption bands, the efficacy of the ion-exchange procedure was investigated by acquiring IR spectra of the ionomer thin film before and after ion-exchange with I^- (Figure 5.7). The bands were assigned based on the literature values for quaternary ammonium salts and alkanes.[9–11] The strongest bands are from the methylene groups in the polyethylene backbone of the ionomer (see Figure 4.1). Interestingly, a strong sharp band is observed at 966 cm^{-1} that has been assigned to the breathing mode ν_B(C-N) of the

quaternary ammonium group and is expected to shift based on the counter-anion of the ammonium group.[9] However, in the current case, the ion-exchange procedure did not affect the position of this band. The broad band at ~ 1340 cm^{-1} is significant since this band disappears on ion-exchange with I^-. Based on the IR spectra of inorganic carbonate and bicarbonate salts both in the solid[12] and the solution phase,[13] this band has been assigned to the stretching mode (ν_{COO}) of HCO_3^-. The CO_3^{2-} band expected to appear at 1400 cm^{-1} is not discernible. It is indicated that, under ambient conditions, HCO_3^- may be preferentially paired with the mono-charged cationic site; most likely due to the electro-neutrality requirement.

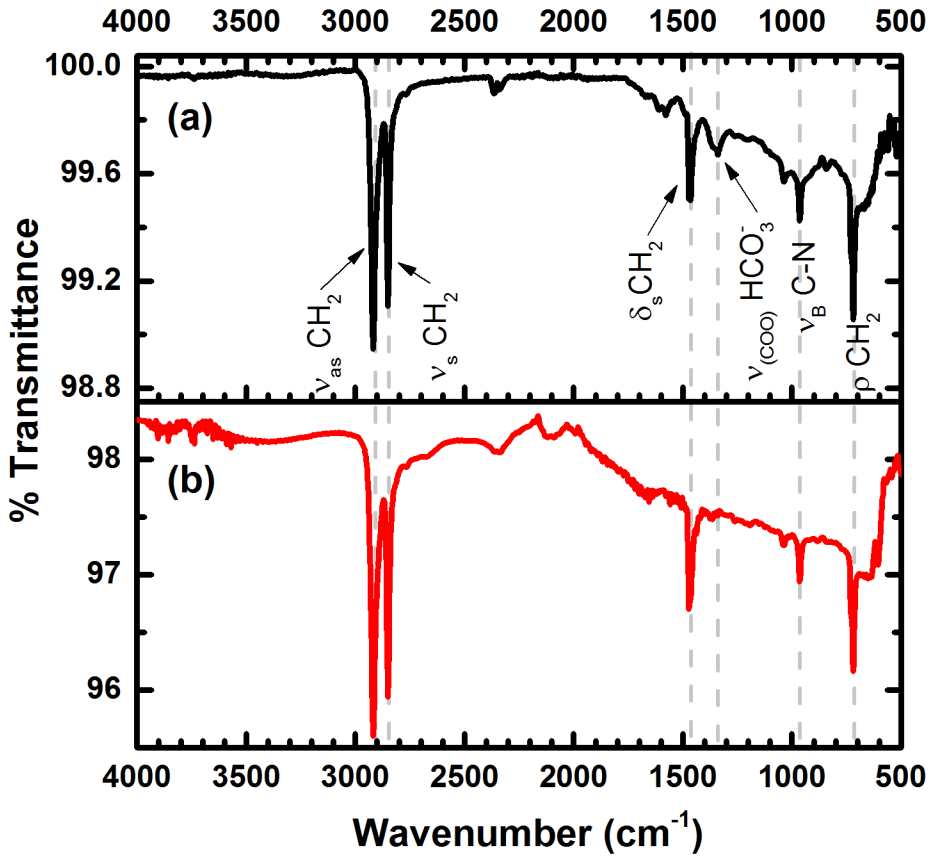

Figure 5.7: Transmittance spectra of the dry ionomer thin film (a) before ion-exchange with I^- (b) after ion-exchange with I^-.

5.3.6 Ex-situ TEM Studies of the Ionomer Thin Films

The morphology of the ionomer thin films was studied by TEM. The procedures for casting the films on the TEM grids and the subsequent ion-exchange with I^- (if needed) were already described in Section 5.2.5. During the course of the study, it was found that the nature of the counter-anions profoundly affects the solubility of the solid polymer in the solvent (for making ionomer solutions). I^- form of the solid polymer was found to be less soluble in n-propanol than the CO_3^{2-}/HCO_3^- form. Further, TEM studies showed that the morphology of the film differed depending on whether the films were cast in the I^- or the CO_3^{2-}/HCO_3^- form (Figure 5.8). It should be pointed out that for imaging purposes the films cast in the CO_3^{2-}/HCO_3^- form were also finally converted into the I^- form by ion-exchange (see section 5.2.5) in order to selectively stain the hydrophilic regions of the ionomer film. Due to Z-contrast, in HAADF-STEM images, the I^- rich regions will be brighter thus the hydrophilic regions can be identified.

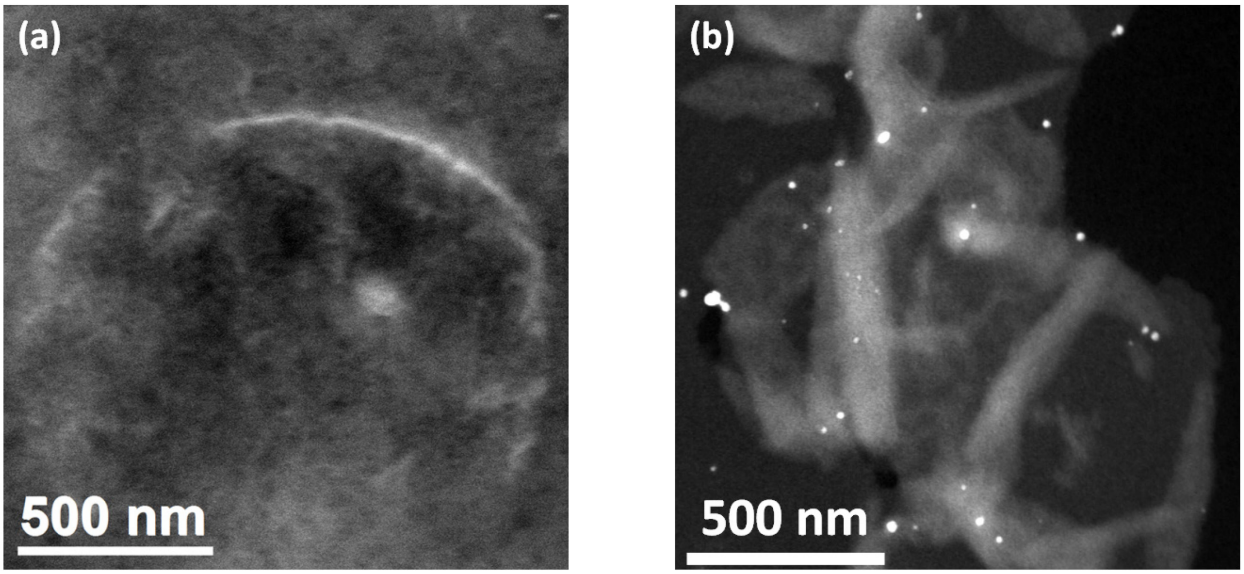

Figure 5.8: Representative dark field TEM images of the ionomer film cast on the TEM grid in (a) the CO_3^{2-}/HCO_3^- form and subsequently exchanged with I^-(b) I^- form directly.

For the films cast in the CO_3^{2-}/HCO_3^- form, the hydrophilic regions seemed to be uniformly distributed as evident from the more or less even distribution of bright regions in the

dark field TEM image (Figure 5.8a). However, for the films cast directly in the I^- form, the hydrophilic domains seemed to be larger and there appeared to be significant microphase separation between the hydrophilic and the hydrophobic regions (Figure 5.8b and Figure 5.9a). This observation assumes significance in the light of previously reported studies suggesting that driving microphase separation in AAEM materials may lead to significant gains in the ionic conductivity due to the formation of inter-connected ionic channels.[1]

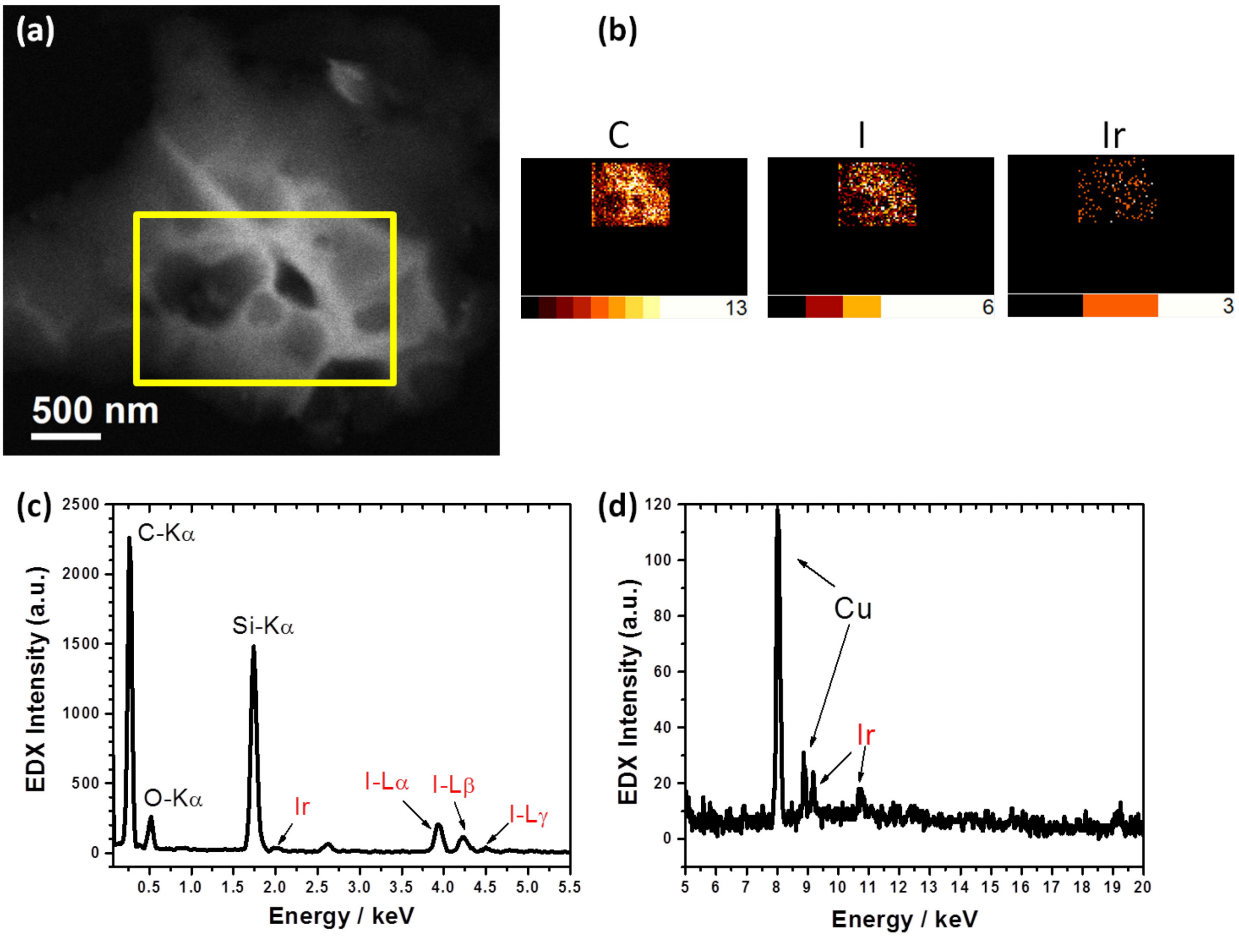

Figure 5.9: (a) Dark field STEM image of the dry ionomer film cast on the TEM grid in the I^- form directly. (b) EDX map of the region marked by the rectangle in (a). (c) and (d) EDX spectra of the dry ionomer film.

During TEM imaging of the ionomer films in the I^- form, it was noticed that there were bright spots 30-50 nm in size (see Figure 5.8b) spread throughout the sample. Further

investigations of the ionomer films by EDX (Figure 5.9) indicated the presence of Ir in the sample. In the synthesis of the AAEM polymer, an Ir-based catalyst is used during the hydrogenation step.[14] The bright spots could be residual catalyst particles that remain trapped in the polymer sample at the end of the synthesis. At the same time, it should be pointed out that the presence of Ir does not seem to inhibit I^- incorporation into the film. This becomes clear on comparing the EDX maps of I and Ir to the corresponding region (marked by the yellow rectangle in Figure 5.9a) of the dark field STEM image. It is apparent that the distribution of I conforms well to the bright regions of the image; more so than that of Ir. This means that the previous assignment of the bright regions of the dark field STEM image to the hydrophilic regions in the film remains valid.

5.4 Summary

Electrochemical and ex-situ characterization studies of the ionomer films were carried out to supplement the carbonation studies in the previous chapter. The RDE and the cyclic voltammetric studies employing redox probe molecules were important in gaining an understanding of the important functional aspects of the ionomer materials namely the mechanism of the physical transport of molecules and the charge transport in the ionomer. The RDE studies demonstrated that the physical transport mechanism in the ionomer does not adhere to a simple membrane model. Besides diffusion in the bulk of the ionomer, a secondary means of transport involving the permeation of molecules along pinholes/micro-channels may be active in the ionomer film. The charge transport studies conducted so far indicate that charge transfer in the ionomer film mediated by inter-site movement of anions is not significant. The interfacial pH changes during fuel oxidation in an AAEM-AFC fuel cell and the associated self-purging phenomenon was simulated by driving hydrogen oxidation reaction at the ionomer modified Pt

electrode under low pH conditions. The consumption of H_2 and the evolution of CO_2 during HOR were monitored by DEMS. An increase in the production of CO_2 was observed during HOR that may indicate the self-purging phenomenon.

Ex-situ IR characterization of the ionomer film provided information on the interaction between the counter-anion and the cationic sites in the ionomer. The ion-exchange process in the ionomer was studied by measuring the IR spectra of the dry ionomer film (initially stored under ambient conditions) before and after exchange with I^-. It seems that under ambient conditions the cationic sites in the ionomer prefers to pair with HCO_3^- rather than CO_3^{2-}. TEM studies importantly revealed the remarkable effect of the counter-anions on the microstructure of the ionomer films. The presence of I^- in the ionomer as the counter-anion is indicated to drive significant microphase separation in the ionomer.

5.5 Outlook

The physical and the charge transport studies need to be developed further. The RDE studies of HOR and ORR at the ionomer film modified electrodes have to be performed due to their relevance to fuel cell operation. The transport studies also need to be performed on films of varying thickness. For charge transport studies, RDE voltammetry at the ionomer film modified electrodes employing both positively and negatively charge redox molecules to decouple different charge transfer mechanisms constitutes a potentially fruitful direction to pursue in the future.

In situ spectroscopic/microscopic studies building on the ex-situ results would be immensely useful. The advanced in situ FTIR capabilities developed in our laboratory (see chapter 6) is expected to be central to in situ IR studies of the ionomer films in the future. The investigation of the dynamics of anion exchange in situ is the obvious area of application for

these techniques. In a similar vein, the capabilities being currently available in the area of in situ TEM and X-ray techniques in our laboratory will be tremendously useful in researching the critical aspect of polymer morphology.

Lastly, fuel cell testing and optimization of the membrane-electrode assembly (MEA) using the AAEM membrane and the ionomer interface material remain an area to be critically addressed. In this regard, it is important to note that the functional requirements of the ionomer interfacial material and the AAEM membrane are not the same and consequently the strategies to optimize them will also differ. For instance, the AAEM membranes need to be mechanically robust and prevent fuel crossover. For the ionomer interface material, mechanical strength is not as critical; however, the ionomer phase in the catalyst layer needs to be sufficiently permeable to fuel so that it can reach the catalyst particles. Even more important for MEA fabrication is the catalyst ink formulation. The catalyst particles and the ionomer need to be homogeneously mixed in the ionomer solution. Aggregation of either the catalyst particles or the ionomer is not desirable. The choice of solvents and the solubility of the ionomer in the solvents will be critical in optimizing the formulation. To this end, some of the metrics of the AAEM material such as the IEC and the average molecular weight may need to be optimized separately for the membrane and the ionomer interface material. A case in point was that, during the studies, it was found that the average molecular weight of the ionomer samples had to be decreased from that of the membrane to increase the solubility of the ionomer and obtain a homogeneous ionomer solution (section 4.2.1.d).

5.6 References

(1) Pan, J.; Chen, C.; Zhuang, L.; Lu, J. *Accounts of chemical research* **2012**, *45*, 473–81.

(2) Bard, A. J.; Faulkner, L. R. In *Electrochemical Methods: Fundamentals and Applications*; Wiley, 2001; pp. 608–623.

(3) Porchet, F.; Javet, P. *Electrochimica Acta* **1995**, *40*, 2569–2577.

(4) Bard, A. J.; Faulkner, L. R. In *Electrochemical Methods: Fundamentals and Applications*; Wiley, 2001; pp. 207–216.

(5) Bard, A. J.; Parsons, R.; Jordan, J. *Standard Potentials in Aqueous Solutions*; Taylor & Francis, 1985.

(6) Siroma, Z.; Watanabe, S.; Yasuda, K.; Fukuta, K.; Yanagi, H. *ECS Transactions* **2010**, *33*, 1935–1943.

(7) Wang, Y.; Li, L.; Hu, L.; Zhuang, L.; Lu, J.; Xu, B. *Electrochemistry Communications* **2003**, *5*, 662–666.

(8) Fukuta, K.; Inoue, H.; Watanabe, S.; Yanagi, H. *ECS Transactions* **2009**, *19*, 23–27.

(9) Harmon, K. M.; Gennick, I.; Madeira, S. L. *The Journal of Physical Chemistry* **1974**, *78*, 2585–2591.

(10) Rizzarelli, E.; Theophanides, T. M. *Chemistry and Properties of Biomolecular Systems*; Kluwer Academic, 1991.

(11) Silverstein, R. M.; Webster, F. X.; Kiemle, D. J. *Spectrometric identification of organic compounds*; John Wiley & Sons, 2005.

(12) Miller, F. A.; Wilkins, C. H. *Analytical Chemistry* **1952**, *24*, 1253–1294.

(13) Iwasita, T.; Nart, F. C. *Progress in Surface Science* **1997**, *55*, 271–340.

(14) Kostalik, H. A.; Clark, T. J.; Robertson, N. J.; Mutolo, P. F.; Longo, J. M.; Abruña, H. D.; Coates, G. W. *Macromolecules* **2010**, *43*, 7147–7150.

CHAPTER 6
DEVELOPMENT AND TESTING OF ADVANCED IN SITU FTIR SETUPS

6.1 Introduction

The application of in situ FTIR endows chemical specificity to electrochemical measurements allowing correlations to be made between the electrochemical response and the chemically specific spectroscopic signal. In in situ FTIR techniques, this is achieved by acquiring the IR spectra of species adsorbed on or near the electrode surface during the course of electrochemical experiments. In this sense, in situ FTIR techniques are complimentary to DEMS as the former allow us to look at adsorbed intermediates and non-volatile products of a reaction while the latter helps us monitor the volatile products.

Over the years, the application of in situ FTIR techniques has contributed greatly to our understanding of interfacial electrochemistry.[1] Particularly, in the field of electrocatalysis, in situ FTIR has been invaluable in gaining mechanistic insights into electrocatalytic reactions. In the case of the model electrocatalytic reaction of the oxidation of adsorbed CO, an in-depth knowledge has been developed over the years about the surface species distribution and the reaction mechanism from in situ FTIR experiments.[1] Significant progresses were also made in elucidating the mechanisms of the oxidation of small organic molecules such as HCOOH,[2] CH_3OH[3] and C_2H_5OH[4,5] via the spectroscopic identification of adsorbed intermediates involved. Finally, the study of the electrochemical double layer is another area that has benefited from the use of in situ FTIR.[1]

In the literature, one can find a proliferation of in situ FTIR techniques.[6,7] In this chapter, however, only the three techniques currently active in our laboratory will be discussed. The

IRRAS technique, which is the most widely used in situ FTIR technique and that has been traditionally employed in our laboratory, will be introduced first. This will be a prelude to the description of the more sensitive techniques, namely PM-IRRAS and ATR-SEIRA, which were recently implemented and tested in our laboratory.

6.2 IRRAS

6.2.1 Introduction

Infrared reflection absorption spectroscopy (IRRAS) is an external reflection technique where the incoming IR beam is reflected off a specular working electrode. Thus, the beam samples IR-active species at or near the electrode surface. The schematic of the IRRAS cell used in our laboratory shown in Figure 6.1 illustrates the technique. The incoming beam first passes through an IR transparent window (CaF_2 prism) and then through a layer of solution before being incident on the working electrode surface.

Due to the heavy absorption of the IR beam by the solvent (typically water), the path length of the beam through the solution needs to be as short as possible to achieve high surface sensitivity. Consequently, as shown in Figure 6.1, a thin layer of solution (1-2 μm) is established between the working electrode and the window by pressing the working electrode against the window. Although this allows for a better sampling of the adsorbed species, the thin layer restricts mass transport to and from the working electrode. In this way, the thin layer is said to be *diffusionally decoupled*[1] from the rest of the electrolyte in the cell.

Due to the increased solution resistance in the thin layer, the time constant (τ) of the cell is large and necessitates use of concentrated electrolytes ($\tau \sim 50$ ms for 1 M aqueous electrolyte).[8] Another important consequence of the stagnant thin layer configuration is the

artificial concentration and pH effects due to the *diffusional decoupling* mentioned earlier. Compared to a typical electrochemical cell with no diffusion constraints, in the IRRAS cell, the depletion of the reactants, the buildup of the products and the bulk pH changes (in the thin layer) are accentuated by the thin layer configuration and has to be taken into consideration when designing the experiment and analyzing the results.

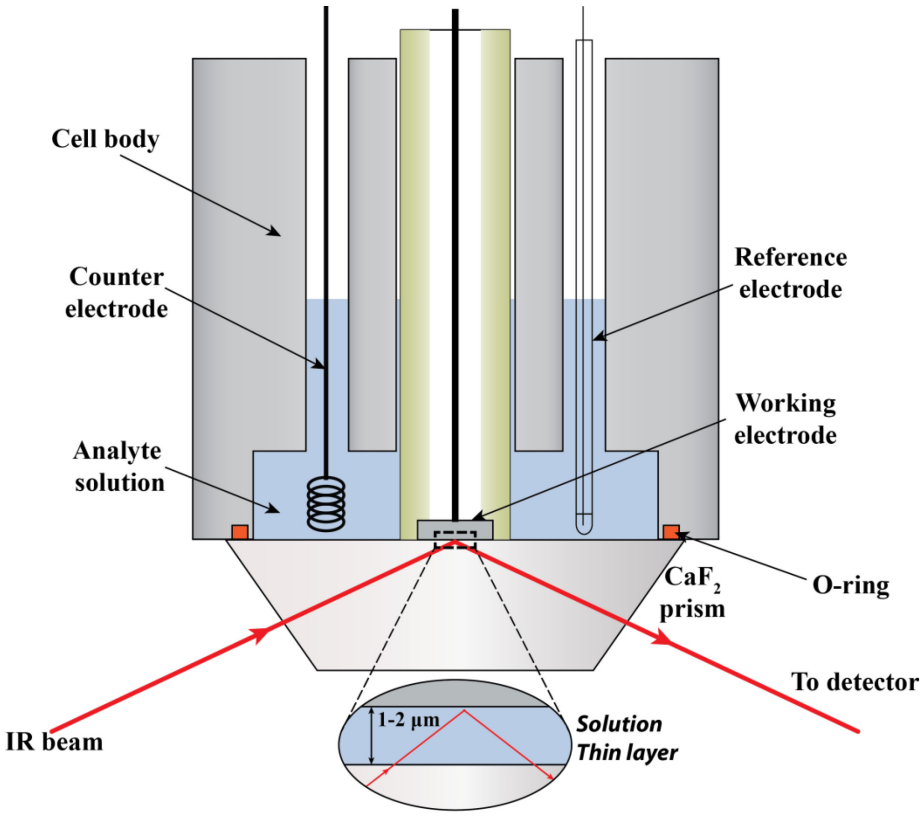

Figure 6.1: IRRAS cell. IR beam path shown in red. Also shown is the magnified view of the thin layer of solution between the electrode and the prism.

6.2.2 Surface selection rule (SSR)

An incoming IR beam can be thought of as composed of two components with their electric field vectors ($\mathbf{E_i}$) mutually perpendicular. Since for IRRAS the relevant surface is that of the electrode, the beam is usually decomposed w.r.t the *plane of incidence* into orthogonal components viz.: (a) s-polarized beam with its electric field vector ($\mathbf{E_{s,i}}$) perpendicular to the

plane of incidence (b) p-polarized beam with the field ($\mathbf{E_{p,i}}$) oriented parallel to the plane of incidence (see Figure 6.2). Note that the electric field vector is always perpendicular to the direction of propagation. The plane of incidence is the plane containing the incident and the reflected beam (xz plane in Figure 6.2).

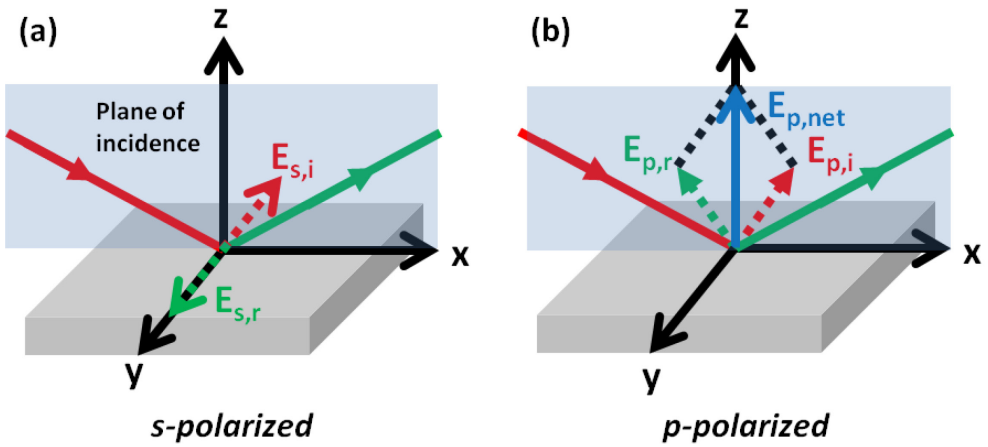

Figure 6.2: Surface selection rule for IRRAS on a metal electrode – (a) s-polarized and (b) p-polarized beam incident on the electrode surface.

In a metal there is a high concentration of mobile electrons. When the IR beam is incident on a metallic surface, the electrons at the surface move under the influence of the electric field of the incident beam creating an induced field. The induced field acts to counter $\mathbf{E_{s,i}}$ – the electric field vector parallel to the surface. Hence, for an s-polarized beam, the net electric field at the surface is close to zero (see Figure 6.2a). For a p-polarized beam at the surface, however, there is a net non-zero electric field ($\mathbf{E_{p,net}}$) normal to the surface. Thus, the IR beam has an effective electric field only perpendicular to the surface on a metal electrode. Consequently, *for an adsorbed species on a metal surface to be IR active, it should have a non-zero component of its dynamic dipole moment perpendicular to the surface*. This is the surface selection rule for IRRAS on metallic surfaces. Due to the much lower carrier concentrations in semiconductors,

the tangential electric field ($\mathbf{E_{s,i}}$) of the beam is not effectively shielded at the surface and this rule is not strictly applicable on semiconductor electrodes.[6]

6.2.3 Experimental

(a) IRRAS Cell

The typical IRRAS cell used in our laboratory is depicted in Figure 6.1. The cell body is made of Teflon. A 60° dovetail CaF_2 prism (United Crystals) is employed as the optical element. The prism is supported in an Al holder. The Al holder is attached to the Teflon cell body using screws pressing the prism firmly against the bottom face of the cell. On the bottom face, a circular groove is made in which a CAPFE O-ring (Ace Glass Inc) is placed to make a good seal between the bottom face and the prism. The electrodes are placed into the main chamber from the top through channels machined in the cell body. The working electrode is pressed against the prism by operating a screw gauge acting on the top flat face of the electrode.

(b) FTIR Setup

A Biorad/Varian Excalibur FTS 3000 spectrometer was used. To direct the beam in and out of the IRRAS cell, an in-line specular reflectance accessory (Pike Veemax II) was placed in the sample compartment of the spectrometer. The signal throughput was optimized by adjusting the position of the IRRAS cell. This is achieved by attaching the cell to a composite positioning stage consisting of a linear stage (Newport Model 462-XYZ-M) and a tilt and rotation platform (Newport Model 36). A liquid N_2-cooled mercury-cadmium-telluride (MCT) detector was used. The spectral data were collected using Resolutions Pro software (Varian). The sample compartment and the optics chamber of the spectrometer were kept purged with dry CO_2 free air from the laboratory compressed air supply passed through a purge gas generator (Parker Balston

75-62NA). Although the use of p-polarized radiation theoretically should afford higher surface sensitivity, the beam throughput was unacceptably low. Hence, no polarizer was used.

(c) Electrochemical Measurement

The working electrode was a polished disc electrode of polycrystalline platinum (1 cm in diameter) sealed in a glass tube. A RHE and a Pt wire were the reference and the counter electrodes respectively. The potentiostat used was BASi CV-27 voltammograph. The data were recorded by a home-made LabVIEW program using a NI-DAQ card.

(d) Spectroelectrochemical Data Conventions

The IR data are displayed as a set of potential difference spectra (PDS) obtained by subtracting the absorbance spectrum at a given potential (**E**) from that of a spectrum at a reference potential ($\mathbf{E_{ref}}$). Consequently, the spectra are expressed as in Equation 6.1.

Equation 6.1:
$$A(E) = -\log\left(\frac{I(E)}{I(E_{ref})}\right)$$

where **I(E)** and $\mathbf{I(E_{ref})}$ are the observed signal intensities at potentials **E** and $\mathbf{E_{ref}}$. By this convention, a negative-going peak in the PDS indicates the consumption of a species that is present at $\mathbf{E_{ref}}$ and a positive-going peak the generation of a species that is absent at $\mathbf{E_{ref}}$. Typically, the spectra acquired over a small potential range (30-50 mV) are co-added to improve SNR and the average potential used to label the spectra. The spectral resolution is typically set at 8 cm^{-1}.

6.2.4 CO Oxidation

The oxidation of adsorbed CO on Pt monitored by IRRAS is a typical experiment that demonstrates the utility of the technique. A series of potential difference spectra obtained during

CO oxidation at polycrystalline Pt are shown in Figure 6.3 . The consumption of adsorbed CO (linearly bonded) by oxidation at high potentials is clearly seen from the growth of the negative-going lobe of the bipolar peak at ~ 2070 cm^{-1} (ν^{l} (CO)) in Figure 6.3a. The concomitant generation of the product CO_2 is also observed from the growth of the positive-going peak at ~ 2343 cm^{-1}.

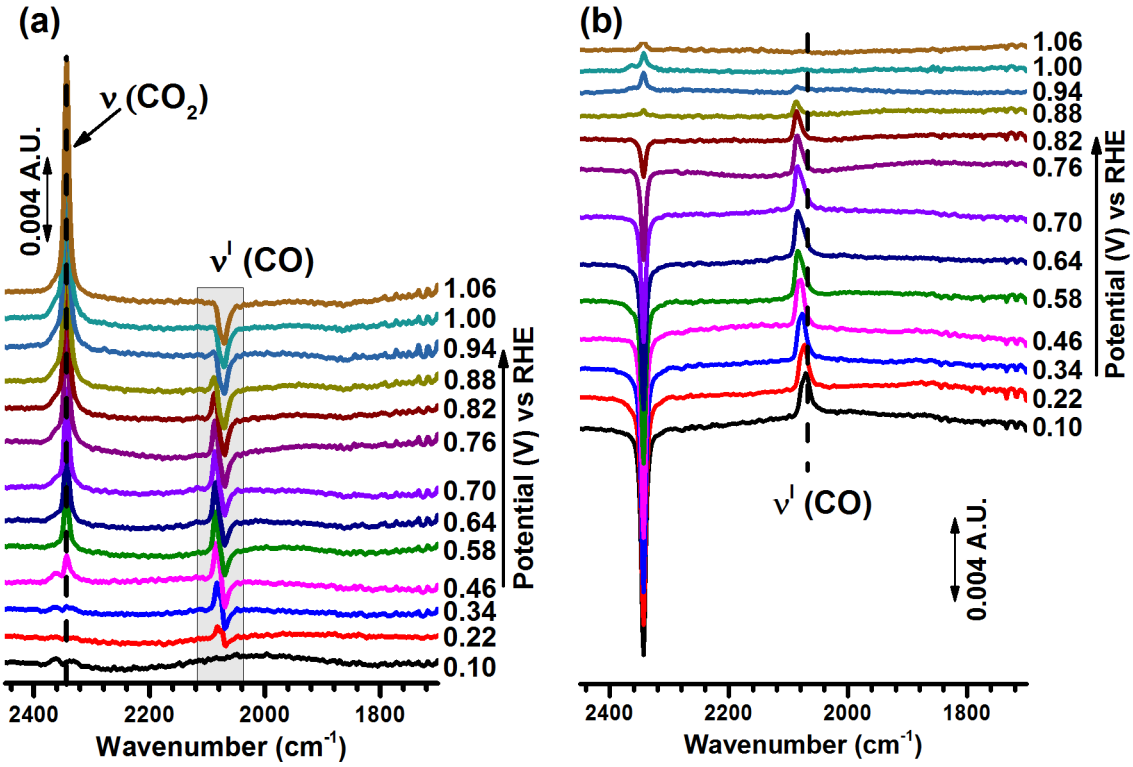

Figure 6.3: Potential difference spectra (absorbance) collected during CO oxidation in CO saturated 0.1 M H_2SO_4 at polycrystalline Pt. Scan rate : 1 mV/s. (a) Reference potential: 0.05 V vs RHE. (b) Reference potential: 1.09V vs RHE.

An explanation of the origin of the bipolar nature of the CO peak is worthwhile for understanding IRRAS results in general. Bipolar peaks are exhibited only by *adsorbed / interfacial species* and occur when (a) the species is present at both the reference potential ($\mathbf{E_{ref}}$) and the sampling potential (**E**) and (b) the peak/band center shifts in frequency with potential. For the experiment under discussion, the first condition is satisfied since at the reference

potential chosen (0.05 V vs RHE) a saturated layer of CO_{ads} is expected to be present. The phenomenon of potential-dependent peak shift is known as *Stark tuning* and has been attributed to either metal-CO backbonding and/or Stark effect.[1] Note that the peak corresponding to the solution species – CO_2 does not exhibit stark tuning.

If a potential is known at which the adsorbed species of interest is absent, it should be chosen as the reference potential for the sake of simplifying analysis. This is demonstrated in Figure 6.3b where the same data as in Figure 6.3a is re-plotted now w.r.t to the reference potential of 1.09V vs RHE. At this potential, no CO_{ads} is present. Only unipolar positive-going peaks for CO_{ads} are observed facilitating straightforward interpretation of the data. The Stark tuning is also more clearly visible in Figure 6.3b.

6.3 PM-IRRAS

6.3.1 Introduction

Polarization modulation – IRRAS (PM-IRRAS) is a variation of the IRRAS technique that can, in principle, afford better surface sensitivity and SNR. As the name suggests, it involves the rapid modulation of the IR beam polarization between the s and the p – polarized states as defined previously (see section 6.2.2). PM-IRRAS spectra are cast in the form expressed below.

Equation 6.2:

$$\frac{\Delta I}{\langle I \rangle} = \frac{I_p - I_s}{(I_s + I_p)/2}$$

where $\mathbf{I_s}$ and $\mathbf{I_p}$ are the component signal intensities at the detector for the s and the p-polarization beams. $\mathbf{\Delta I}$ and $\langle \mathbf{I} \rangle$ are known as the difference and the average signals respectively.

The advantages of employing polarization modulation can be explained using Equation 6.2 and Figure 6.4. Any randomly oriented IR active species in the beam path will absorb the s

and the p-polarized light to the same extent. Hence, for such species, the difference signal, $\mathbf{\Delta I} \approx 0$. This will be the case for any IR active solution species and also for any water vapor or CO_2 in the beam path. But, based on the surface selection rule for metal electrodes (section 6.2.2), p-polarized beam will be preferentially absorbed by species either adsorbed or near the electrode. Hence, $\mathbf{\Delta I} \neq 0$ for interfacial species. Thus, PM-IRRAS is able to achieve higher surface sensitivity by eliminating background contributions from the ambient atmosphere and to a large extent from the solution species. The average signal, $\langle \mathbf{I} \rangle$, is the background spectrum to which the difference spectrum is ratioed. Since, in effect, both the surface specific spectrum, $\mathbf{\Delta I}$, and the background spectrum, $\langle \mathbf{I} \rangle$, are obtained simultaneously, PM-IRRAS also has the advantage of obtaining absolute spectra without the need to initially collect a background spectrum. This is especially advantageous for long-duration time resolved experiments where the background signal can change over time and the background spectrum collected initially is no longer relevant.

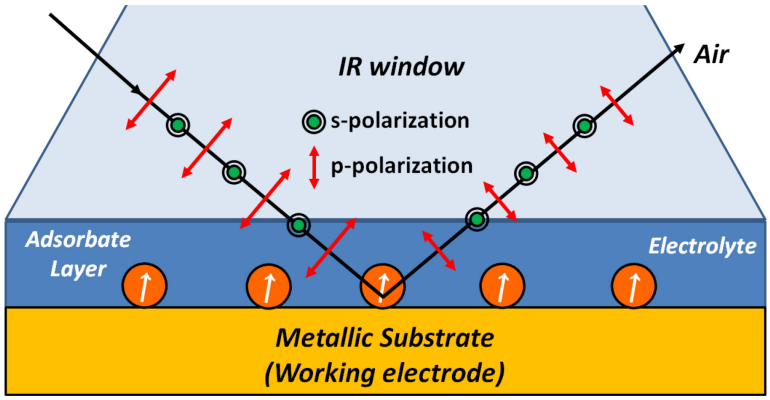

Figure 6.4: Principle of PM-IRRAS operation at a metal electrode.

It is to be noted that though having better surface selectivity than conventional IRRAS, PM-IRRAS still samples the metal-electrolyte interface up to ~ 1 μm from the surface.[9] Consequently, the spectrum still includes a strong solvent background signal. In addition, the operation of the photoelastic modulator (PEM), which provides the polarization modulation,

introduces another slowly varying background in the spectrum. This point will be discussed in the next section.

6.3.2 Operation of PEM

The critical component of the PM-IRRAS setup is the photoelastic modulator (PEM) unit since it provides the required polarization modulation of the IR beam. The operational scheme of a PEM unit is shown in Figure 6.5. It consists of an optical element (such as ZnSe or CaF_2 crystal) which exhibits birefringence when mechanically stressed. Birefringence is the property of a material exhibiting anisotropy in refractive index with the result that light travels in the material with different speeds depending on the direction of propagation. Since this can result in a change in the polarization of the light, birefringent materials can be employed as polarizers.

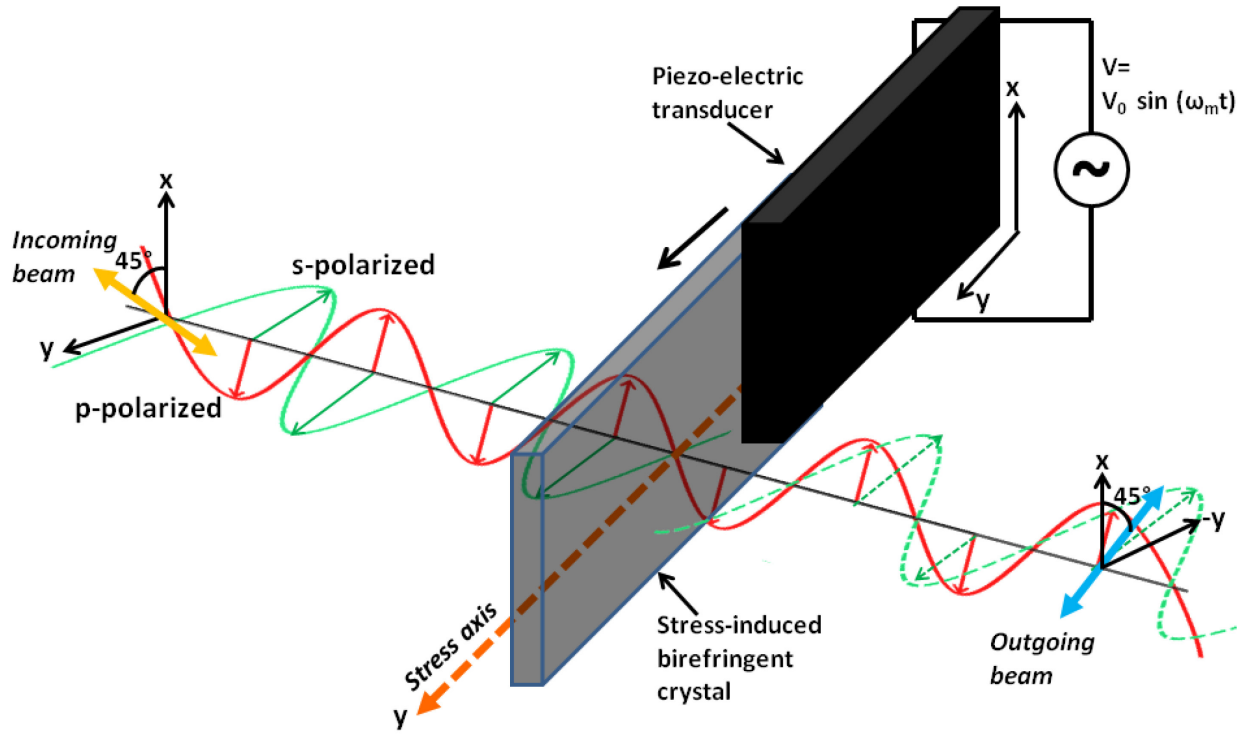

Figure 6.5: Operation of a photoelastic modulator (PEM) unit.

The optical element in the PEM unit is periodically stressed by the motion of an attached piezoelectric transducer to which a sinusoidal voltage is applied at a modulation frequency ω_m. Thus, the crystal undergoes cyclic compression and elongation resulting in periodically changing refractive index (birefringence) along the stress axis (y-axis in Figure 6.5) at the same frequency ω_m.

For a typical PEM operation, the incident beam is linearly polarized (45° w.r.t x-axis in Figure 6.5). This incoming beam can be decomposed into two mutually perpendicular s and p components. Anticipating the orientation of the metal electrode surface in the spectroelectrochemical cell (section 6.3.3.d), the component along the x-axis is set as the s-polarized beam (normal to the plane of incidence at the electrode surface) and the component along the y-axis as the p-polarized beam (parallel to the plane of incidence at the electrode surface). Note that y-axis coincides with the stress axis of the crystal.

The principle of polarization modulation by PEM can be understood from Figure 6.6. When no voltage is applied, the crystal is unstressed and the incident beam passes through unchanged. When the crystal is stressed by the application of voltage across the transducer, the p-component of the incident beam is phase shifted w.r.t to the s-component. The s-component is unperturbed. The p-component is retarded in phase when the crystal is compressed and vice-versa. This phase shift can be expressed either as a phase angle (φ) or as a path-length difference known as the *retardation* (**R**). Typically, **R** is given in units of the wavelength, λ. In any case, the phase shift is proportional to the applied voltage.

Two values of **R** are important in the operation of PEM. These are $|\mathbf{R}| = \lambda/4$ and $|\mathbf{R}| = \lambda/2$ know as quarter-wave and half-wave retardation respectively. At $|\mathbf{R}| = \lambda/4$, the s-polarization is out of phase w.r.t the p-polarization by 90 °. This results in a circularly polarized beam. For $|\mathbf{R}| =$

λ/2, the phase shift is 180 ° and the outgoing beam is still linearly polarized. However, the plane of polarization is rotated by 90 °. For PM-IRRAS, the PEM is typically operated with the maximum phase shift, $|\mathbf{R}_{max}|$ (or φ_0) set to **λ/2** (or π) to provide for the common signal rejection capability of the PM-IRRAS setup. In this mode, as can be seen from Figure 6.6, the polarization of the beam is flipped twice between s and p-polarizations in one voltage cycle and thus ensuring that the **ΔI** signal (Equation 6.2) contains only the anisotropic contributions. It should be noted that the polarization modulation occurs at twice the frequency of the crystal oscillation i.e. 2 ω_m.

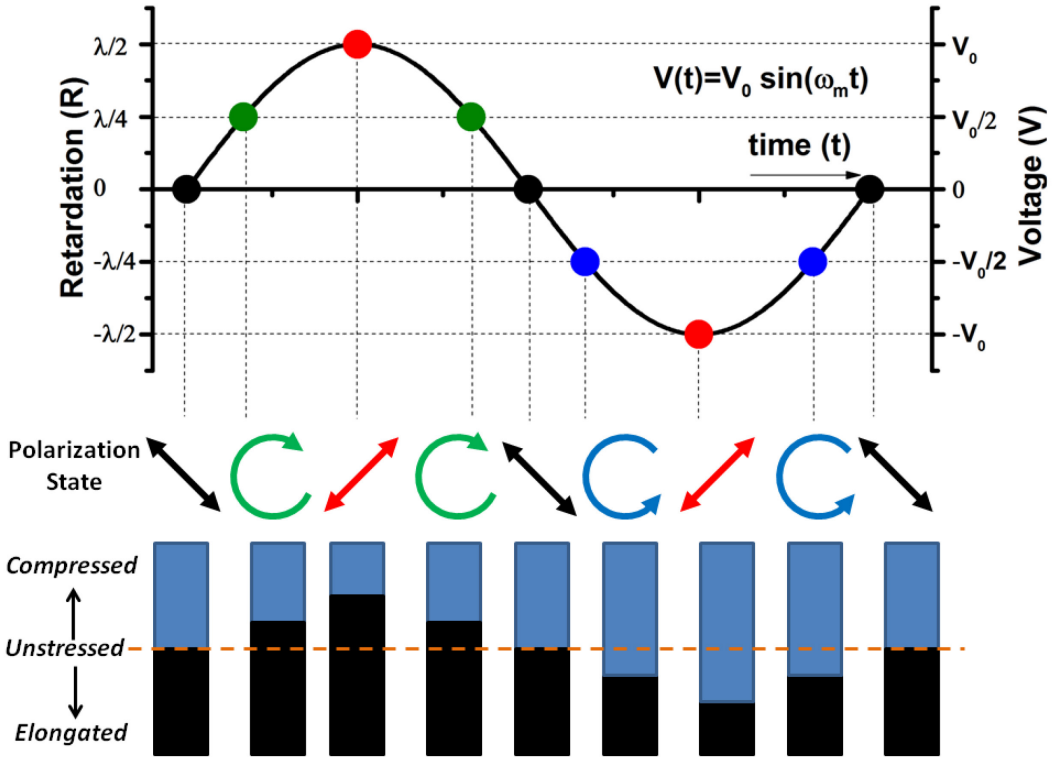

Figure 6.6: Polarization modulation during PEM operation.

6.3.3 Experimental

(a) Optics Layout

PM-IRRAS experimental layout was developed using the newly acquired Varian 670-IR. The experimental layout is shown in Figure 6.7. The PM-IRRAS setup is assembled on an

external optical bench interfaced with the main spectrometer. The IR beam from the spectrometer is deflected into the external bench by a flipping mirror in the optics chamber.

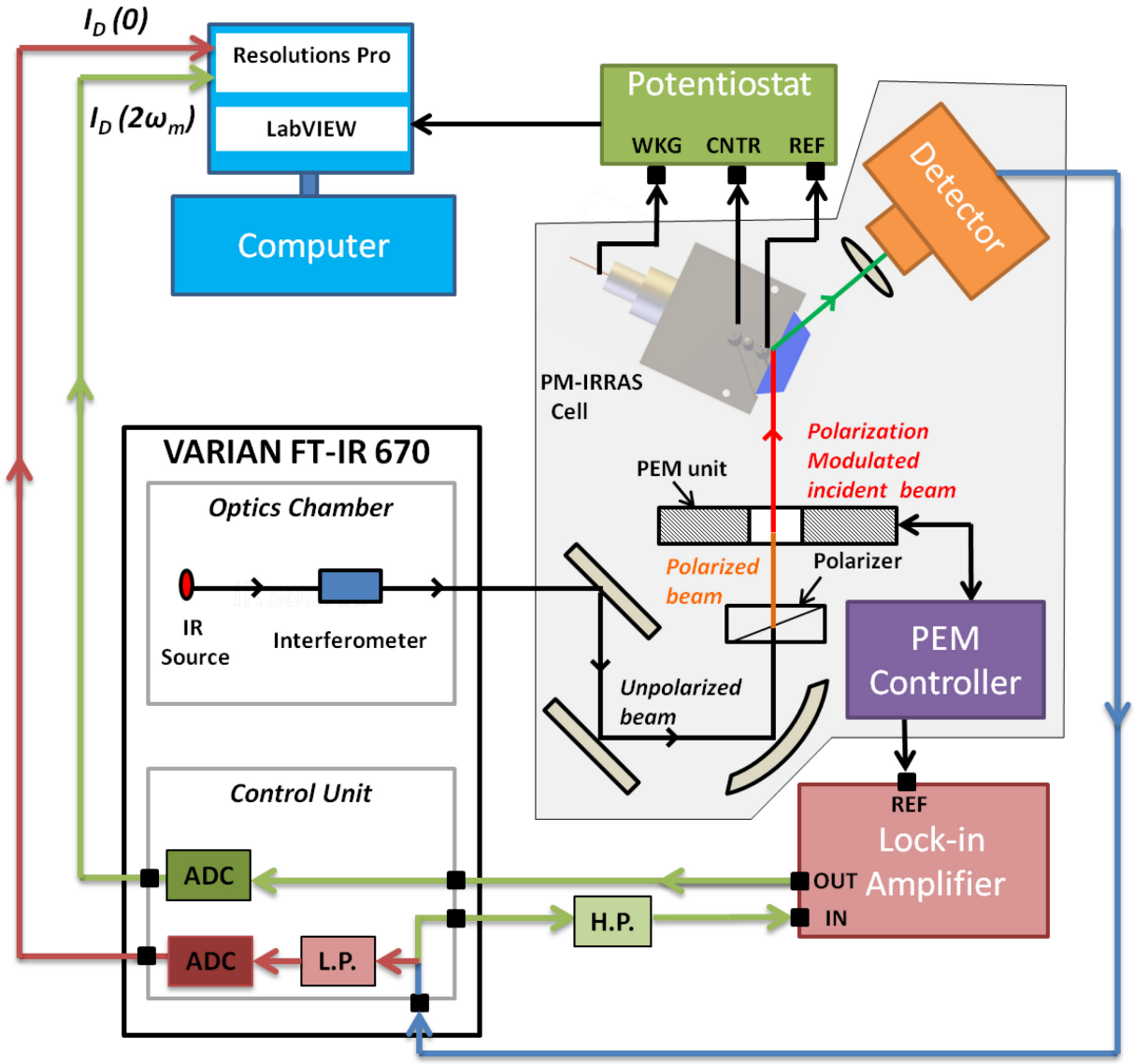

Figure 6.7: PM-IRRAS experimental scheme. H.P. – High pass filter, L.P. – Low pass filter, ADC – Analog-to-digital converter.

In the external bench, the beam is guided and focused by a set of flat and parabolic mirrors. The unpolarized beam passing through a gold grid polarizer is linearly polarized with the plane of polarization parallel to the electrode surface. The linearly polarized beam incident on the photoelastic modulator (Hinds Model ZS-37 – ZnSe crystal, operating frequency- ω_m: 37

kHz) is modulated (at frequency $\mathbf{2\omega_m}$) before being directed into the PM-IRRAS cell. It is important not to use intervening mirrors between the PEM unit and the PM-IRRAS cell in order to maintain the fidelity of the polarization state of the beam. After sampling the electrode surface and the thin solution layer in the cell, the modulated beam exiting the cell is focused on to the detector (Liquid N_2-cooled MCT) by a ZnSe lens. Both the optics chamber of the spectrometer and the enclosed external optical bench was kept purged with dry CO_2 free air supplied from the laboratory compressed air line passed through a purge gas generator (Parker Balston 75-62 NA).

An important experimental consideration is the choice of the interferometer mirror velocity. The mirror velocity needs to be as low as possible to avoid cross talk between the Fourier frequencies ($f_{\bar{\nu}}$ - see Equation 6.3 below) and the PEM modulation frequency $\mathbf{2\omega_m}$.

Equation 6.3: $$f_{\bar{\nu}} = 2V_M\bar{\nu}$$

where $f_{\bar{\nu}}$ is the Fourier frequency, V_M is the mirror velocity and $\bar{\nu}$ is the corresponding wavenumber. As a rule of thumb, the Fourier frequency should be at least an order of magnitude lower than the PEM frequency. For instance, at $\bar{\nu}$ =4000 cm^{-1} and $\mathbf{\omega_m}$=37 kHz, $V_M \leq 0.93$ cm/s.

(b) PM-IRRAS Signal Processing

(i) Instrumentation

The signal from the detector consists of a high frequency component and a low frequency component. The high frequency component includes the signal of interest $\mathbf{I_D(2\omega_m)}$ (also known as the ac component) at twice the modulation frequency due to PEM. The low frequency component includes $\mathbf{I_D(0)}$ (also known as the dc component).The composite signal encompassing both $\mathbf{I_D(2\omega_m)}$ and $\mathbf{I_D(0)}$ from the detector is fed into the control unit of the spectrometer. The high frequency and the low frequency components are separated by passing

the signal through a high pass and a low pass filter, respectively. $\mathbf{I_D(2\omega_m)}$ is separated out from the rest of the high frequency signal by a lock-in amplifier (Stanford Research Systems SR 830) that uses the reference signal at $\mathbf{2\omega_m}$ from the PEM controller. After further filtering of noise by band pass filters (not shown), the ac, $\mathbf{I_D(2\omega_m)}$ and the dc, $\mathbf{I_D(0)}$ components are converted into digital signals by analog-to-digital converters (ADC) and recorded by the FTIR software (Varian Resolutions Pro).

(ii) Spectral Data Processing

It should be pointed out that $\mathbf{I_D(2\omega_m)}$ and $\mathbf{I_D(0)}$ obtained experimentally as described above are related to but not identical to $\mathbf{\Delta I}$ and $\langle \mathbf{I} \rangle$ respectively defined in Equation 6.2. The relationships between the two sets of quantities, when a lock-in amplifier is employed, have been derived[10] and are given below.

Equation 6.4:
$$I_D(2\omega) = \Delta I * J_2(\varphi_0)$$

Equation 6.5:
$$I_D(0) = \langle I \rangle + \frac{\Delta I}{2} * J_0(\varphi_0)$$

where $\mathbf{J_0(\varphi_0)}$ and $\mathbf{J_2(\varphi_0)}$ are the first-order and the second-order Bessel functions of the maximum phase shift $\boldsymbol{\varphi_0}$ between the s and the p-polarizations (see section 6.3.2). The nodes and the slowly varying background in the PM-IRRAS spectra introduced by the operation of the PEM are captured in the Bessel functions mentioned above. $\mathbf{I_D(2\omega_m)}$ and $\mathbf{I_D(0)}$ are usually ratioed as shown in Equation 6.6 to give the experimental PM-IRRAS spectra (devoid of any background corrections). A constant C is incorporated into the expression in Equation 6.6 to account for any electronic gain values used in signal processing.

Equation 6.6:
$$S = \frac{I_D(2\omega)}{I_D(0)} = C\frac{\Delta I * J_2(\varphi_0)}{\langle I \rangle + \frac{\Delta I}{2} * J_0(\varphi_0)}$$

For a highly reflective surfaces such as the metal electrodes used in our studies, $\langle \mathbf{I} \rangle >> \mathbf{\Delta I}$ and $\mathbf{J_0(\varphi_0)} \leq 1$. Hence, **S** can be approximated as

Equation 6.7:
$$S \approx C \frac{\Delta I * J_2(\varphi_0)}{\langle I \rangle}$$

If the absolute spectrum is desired, **S** needs to be corrected for the PEM background (i.e. $\mathbf{J_0(\varphi_0)}$ and $\mathbf{J_2(\varphi_0)}$). There are several procedures outlined in the literature that can be followed to achieve this.[9] However, for the electrochemical PM-IRRAS tests that were carried out in the current study, potential difference spectra were calculated to eliminate the PEM background and any solution background, as outlined below. Using Equation 6.7, the PM-IRRAS spectrum, **S(E)** acquired at the sample potential (**E**) is subtracted from the reference spectrum, $\mathbf{S(E_{ref})}$ at the reference potential ($\mathbf{E_{ref}}$) and ratioed to $\mathbf{S(E_{ref})}$ to finally obtain the potential difference spectra as shown in Equation 6.8.

Equation 6.8:
$$\frac{\Delta S(E)}{S(E_{ref})} = \frac{S(E) - S(E_{ref})}{S(E_{ref})}$$

(c) Electrochemical Measurement

The scheme and the instrumentation for acquiring the electrochemical data is same as that described for IRRAS (section 6.2.3). The PM-IRRAS cell is designed differently from the IRRAS cell (Figure 6.1) and will be discussed separately below.

(d) PM-IRRAS Cell

(i) Design

A new spectroelectrochemical cell (Figure 6.8) was developed for the PM-IRRAS setup. Just as in the IRRAS cell, the cell body is fabricated out of Teflon and a 60 ° dovetail CaF_2 prism is used as the IR window. The salient feature of the PM-IRRAS cell is that it is horizontally

configured (electrode surface perpendicular to the optical bench) as to allow ease of placement and manipulation of the PM-IRRAS setup in the external optical bench (see Figure 6.7). This is in contrast to the conventional IRRAS cell (Figure 6.1) used in our laboratory where the cell is vertically oriented (i.e. electrode surface parallel to the base of the sample chamber). The conventional IRRAS experiments are carried out in the sample chamber of the spectrometer using the specular reflectance accessory. This necessitates the vertical configuration of the IRRAS cell.

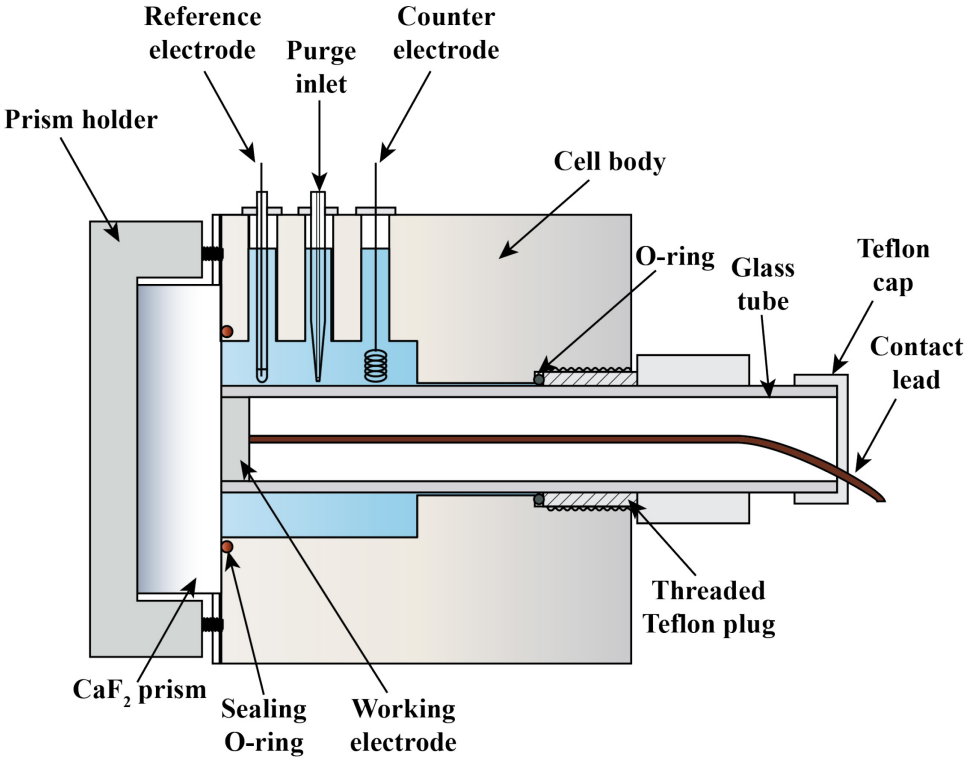

Figure 6.8: PM-IRRAS cell

Due to the horizontal configuration of the PM-IRRAS cell, the chamber containing the solution needed to be properly sealed. For this purpose, a syringe-barrel mechanism of electrode insertion as shown in Figure 6.8 is employed. The working electrode (encased in a glass tube) is inserted through a closely fitting Teflon plug that is screwed into the body of the cell. An O-ring

sandwiched between the plug and the cell body helps create a good seal. The auxiliary electrodes are introduced through channels drilled in the cell body from the top face.

(ii) Mounting and Alignment Stage

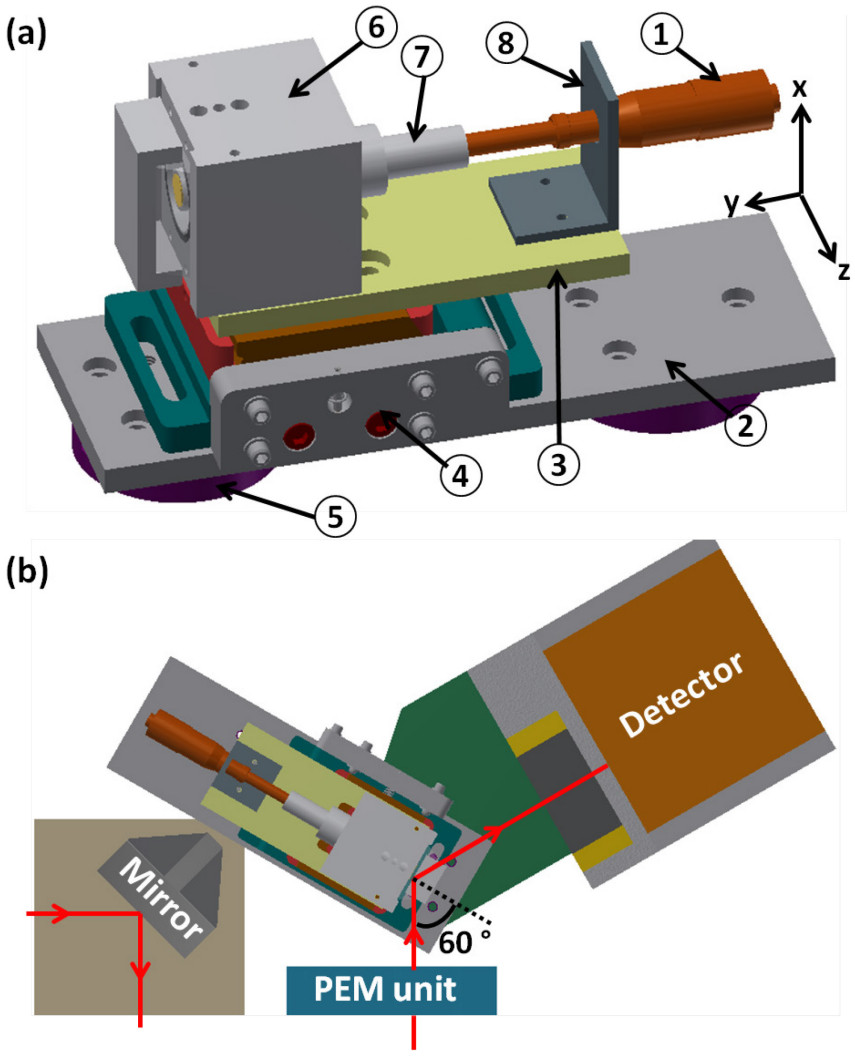

Figure 6.9: (a) Mounting and positioning stage for PM-IRRAS cell (b) top view of the optical bench layout with the PM-IRRAS cell aligned. 1- Micrometer, 2 – Bridge, 3 – Cell mounting base plate, 4 – Wide 5-axis aligner, 5- Pivot, 6 – PM-IRRAS cell, 7 – Working electrode, 8 – Micrometer support. CAD models for micrometer (1) and aligner (4) courtesy of Newport.

In order to properly position the cell, a mounting and alignment stage was designed (Figure 6.9a). The cell is mounted on an aluminum base plate (Part 3). Just as in the IRRAS cell, the working electrode is pressed against the IR window by means of a micrometer secured to the

base plate. The base plate itself is mounted on a wide 5-axis aligner (Newport Model 9082 – Part 4). There are grooves machined lengthwise on the base plate that allows it and in turn the cell to be moved along the y-axis. The wide 5-axis aligner enables further alignment of the cell along all the three axes and also additionally provides tilt and pivot adjustment. The aligner is fixed on another piece of machined aluminum plate called the "bridge" (Part 2). The bridge is supported on two cylindrical aluminum pieces which are in turn bolted to the optical bench. One of the legs (Part 5) acts as the pivot around which the detector unit can be rotated to maximize the signal (see Figure 6.9b). The center of the pivot lies on the path of the beam exiting the PEM unit. It is to be noted that the long axis (y-axis) of the bridge is aligned at a nominal angle of 60 ° w.r.t to the incoming beam. This is so as to ensure normal beam incidence on the 60 ° dovetail CaF_2 prism.

6.3.4 Preliminary Testing

After the design and the subsequent deployment of the PM-IRRAS setup in our laboratory, initial experiments were carried out results from which are reported herein. To achieve the enhanced surface sensitivity promised by the use of PM-IRRAS, experimental parameters need to be judiciously set. As pointed out earlier, unlike IRRAS, the data obtained from PM-IRRAS need to be processed more elaborately to obtain the desired information from the experiment.

An important aspect of PEM operation is the fact that PEM is chromatic. To explain, the desired rapid switching of the linear polarization by 180 ° of the beam incident on the PEM is achieved only at specific wavelength (or wavenumber), λ_0 (or $\bar{\nu}_0$) known as the center wavelength (or wavenumber). At all other wavelengths, the PEM operates at less than the

maximum efficiency. Hence, operationally, when using PEM with Fourier transform spectrometers, $\bar{\nu}_0$ may need to be adjusted to the spectral region of interest and multiple spectra taken varying $\bar{\nu}_0$ to cover the entire spectral range desired.

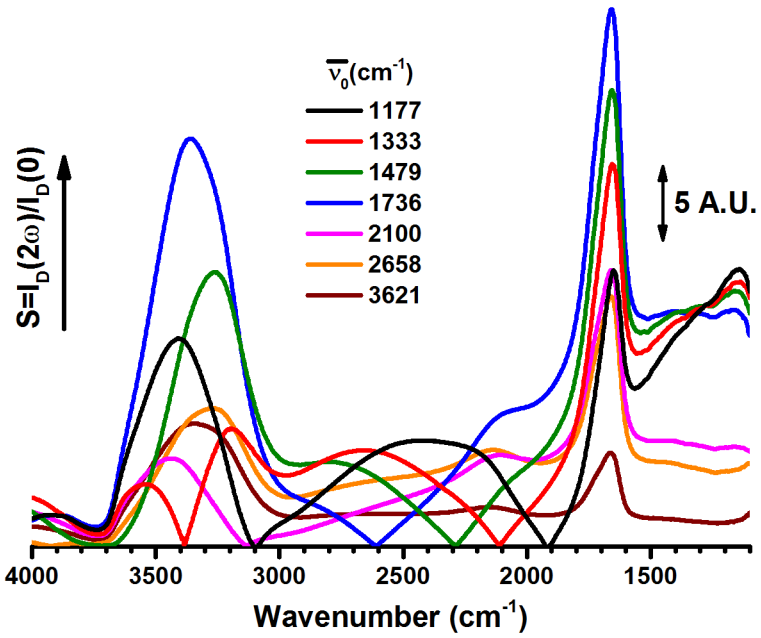

Figure 6.10: Ratioed spectra, $S = I_D(2\omega_m) / I_D(0)$ of de-ionized water in contact with a Pt electrode in the PM-IRRAS cell. The plot shows the variation of the spectra on changing the center wavenumber $\bar{\nu}_0$ of PEM operation. PEM maximum retardation ($|R_{max}|$) set to 0.5 λ_0 where $\lambda_0 = 1 / \bar{\nu}_0$. Spectra uncorrected for lock-in amplifier gains (variably set).

The above-mentioned feature of the PEM is apparent from Figure 6.10 where the PM-IRRAS spectra, $S = I_D(2\omega_m) / I_D(0)$ of de-ionized water in contact with a Pt electrode in the PM-IRRAS cell at various $\bar{\nu}_0$ is shown. $\bar{\nu}_0$ is varied in the spectral range typically used for the IRRAS experiments (4000-1100 cm^{-1}). The broad peaks at ~ 1640, 2150 and 3300 cm^{-1} are those associated with water superimposed on the slowly varying PEM background. The nodes in the spectra created by the operation of the PEM are also clearly visible. At the nodes, the PEM efficiency is essentially zero. By changing $\bar{\nu}_0$, these nodes can be shifted away from the spectral

region of interest. For instance the node at ~ 1900 cm^{-1} (for $\bar{\nu}_0$=1177 cm^{-1}) is systematically blue-shifted by increasing $\bar{\nu}_0$. Since the inter-conversion between two linear polarization states (s and p) is desired, the maximum retardation ($|\mathbf{R_{max}}|$) is always set to 0.5 λ_0.

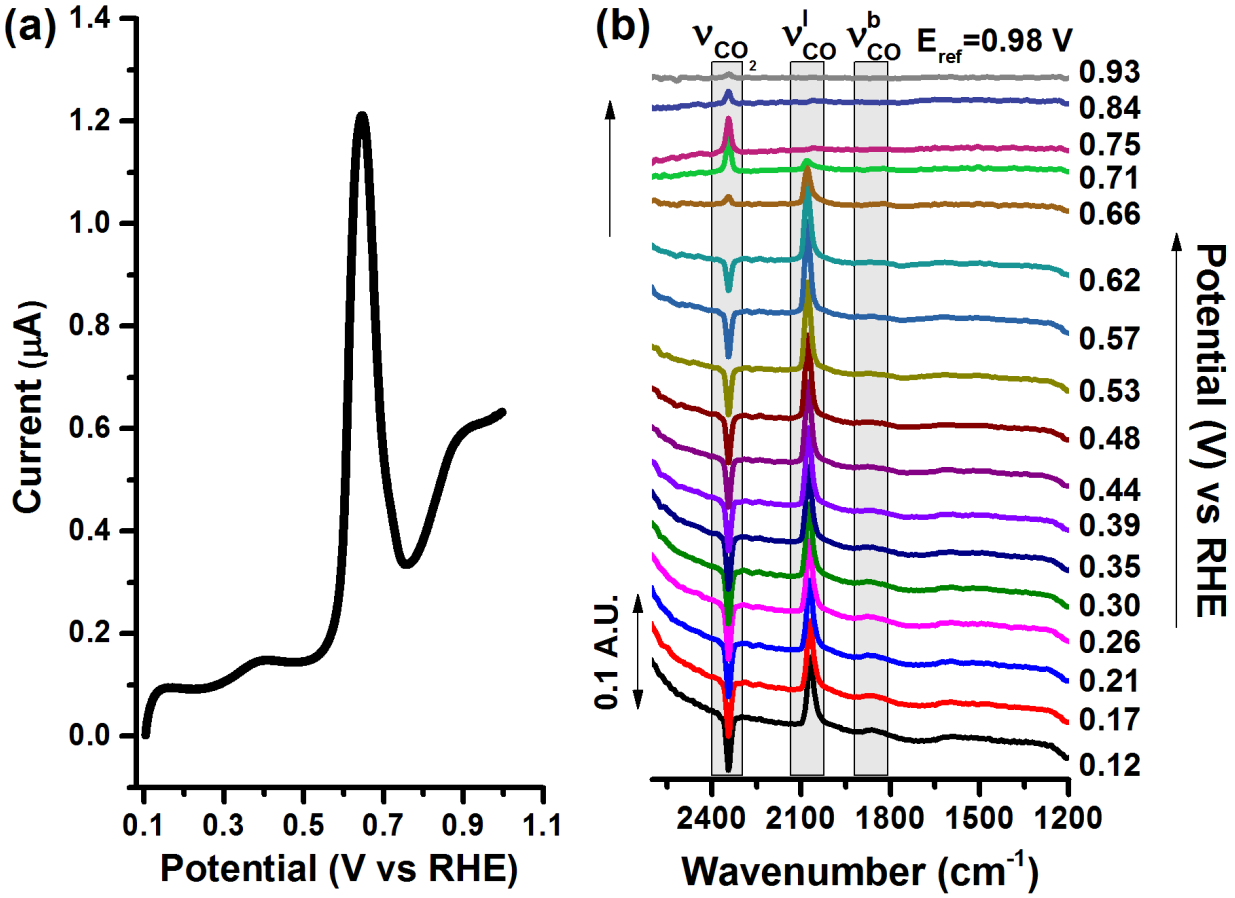

Figure 6.11: (a) Stripping of adsorbed CO from a polycrystalline Pt electrode in 0.1 M H_2SO_4 in PM-IRRAS cell. Dosing potential: 0.1 V vs RHE. Scan rate: 0.25 mV/s. (b) simultaneously acquired potential difference PM-IRRAS spectra ($\Delta S(E)/S(E_{ref})$). Sampled potential indicated alongside each spectrum. Reference potential (E_{ref}): 0.98 V vs RHE.

Finally, to validate the operation of the PM-IRRAS setup in conjunction with the performance of electrochemical measurements, the archetypical oxidation of adsorbed CO from a polycrystalline platinum electrode was carried out in the PM-IRRAS cell. The results are shown in Figure 6.11. The PM-IRRAS spectra are cast in the form of the potential difference spectra, $\Delta S(E)/S(E_{ref})$, as defined in Equation 6.8. The reference potential used was 0.98 V vs

RHE at which potential adsorbed CO is completely oxidized. Hence, as explained earlier (section 6.2.4), only unipolar CO bands are seen. In addition to the strong peak at ~ 2070 cm^{-1} due to the linearly-bonded CO, a very weak broad band is detected at ~ 1860 cm^{-1} corresponding to bridge-bonded CO.

6.4 ATR-SEIRAS

6.4.1 Introduction

Another surface-sensitive FTIR scheme is the attenuated total internal reflection – surface enhanced infrared absorption spectroscopy (ATR-SEIRA). The essential idea behind this technique is depicted in Figure 6.12. The technique has several salient features that set it apart from the other FTIR techniques. A thin metal film (thickness 20 – 50 nm), acting as the working electrode, is deposited on the flat face of an IR window (usually a hemicylinder or hemisphere). The IR window is of a high refractive index material (such as Si, Ge or ZnSe) so that the beam incident at the window – metal film undergoes total internal reflection. This is the so-called Kretschmann geometry. Although the beam is highly attenuated due to absorption in the metal film (hence attenuated total internal reflection), the evanescent waves can still penetrate through the thin metal film to sample the metal-solution interface. Thus, adsorbed and interfacial species can be detected.

In a manner similar to surface enhanced Raman scattering (SERS), the presence of the metal film amplifies the IR signal from the adsorbed molecules. This effect is known as the surface enhanced infrared absorption (SEIRA). Although the source of this effect is still a matter of research, from an experimental point of view, the short distance range from the metal film within which the enhancement is active implies that the SEIRA effect selectively amplifies the

signal from species close to the surface.[11] This endows the ATR-SEIRAS technique with superior surface sensitivity. It should be pointed out that the surface selection rule of IRRAS is still generally applicable for ATR-SEIRAS i.e. only vibration modes having a non-zero component of the dynamic dipole moment normal to the surface are detected. [11]

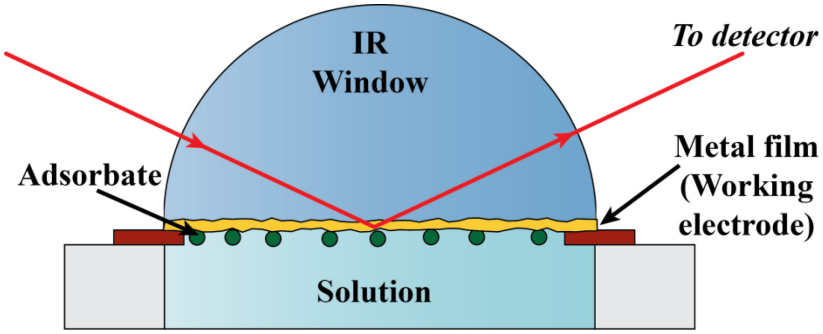

Figure 6.12: ATR-SEIRA scheme

In addition to the enhanced surface sensitivity, due to the Kretschmann beam geometry employed, the ATR-SEIRAS affords greater experimental flexibility compared to IRRAS. The critical advantage is the irrelevance of the thin layer configuration in ATR-SEIRAS due to the backside illumination of the working electrode. This means that, unlike IRRAS, standard cell configurations that allow free diffusion of solution species to the working electrode can be employed. Hence, the problems associated with reactant depletion, product build-up and solution resistance effects due to the thin layer configuration in IRRAS are avoided completely in ATR-SEIRAS. In the same vein, in situ experiments that involve exchange of solutions can easily be implemented by integrating the ATR-SEIRAS technique with flow cells.[12]

The ATR-SEIRAS technique has been recently implemented in our laboratory. A brief description of the development of the technique in our laboratory and the results of the initial testing is given below.

6.4.2 Experimental

(a) Preparation of Thin Metal-film Electrode

Si hemicylinder IR windows (20 mm in diameter and 20 mm long) were obtained from Crystran Optics (UK). The preliminary testing was carried out on Au metal film electrodes. To this end, Au was deposited by magnetron Ar sputtering onto the flat face of the hemicylinder. To improve adhesion of the Au layer to Si, a thin layer of Ti (5 nm) was initially sputter deposited on Si at 0.5 Å/s. On top of the Ti layer, Au was then finally deposited to a thickness of 20 nm at ~ 0.8 Å/s. Although not studied here, the film morphology is critical in achieving the SEIRA effect. Apparently, it has been noted that the films with an island surface structure and nanometer-scale roughness (roughness factor 2-7) show high SEIRA activity.[11]

(b) ATR-SEIRA Cells

(i) ATR Glass Cell

Two spectroelectrochemical cells were designed and fabricated. The first cell, shown in Figure 6.13 is a horizontal-type glass cell based on the design previously reported in the literature.[13] The Si prism with the Au film deposited on the flat face is firmly held to the flange (inner diameter = 15 mm) of the glass cell using two Al pieces that are screwed together. The top plate is machined so as not to obstruct the beam path. Note that, as per Figure 6.13, the plane of incidence of the beam is the y-z plane (i.e. normal to the plane of the paper). Silicone spacers are inserted between the top plate and the prism and also the bottom plate and the flange to provide sufficient compression. Between the flat face of the prism and the glass flange, an annular piece of Al foil to provide working electrode contact and an annular silicon gasket (inner diameter ~ 15 mm) for the purpose of sealing is sandwiched. In this manner, a circular area about 15 mm in diameter of the working electrode is exposed to the solution. The reference (RHE) and the

counter electrodes (Pt wire) are inserted via standard ground glass joints in the cell. A glass frit at the end of the cell can be used to purge the cell as show in Figure 6.13.

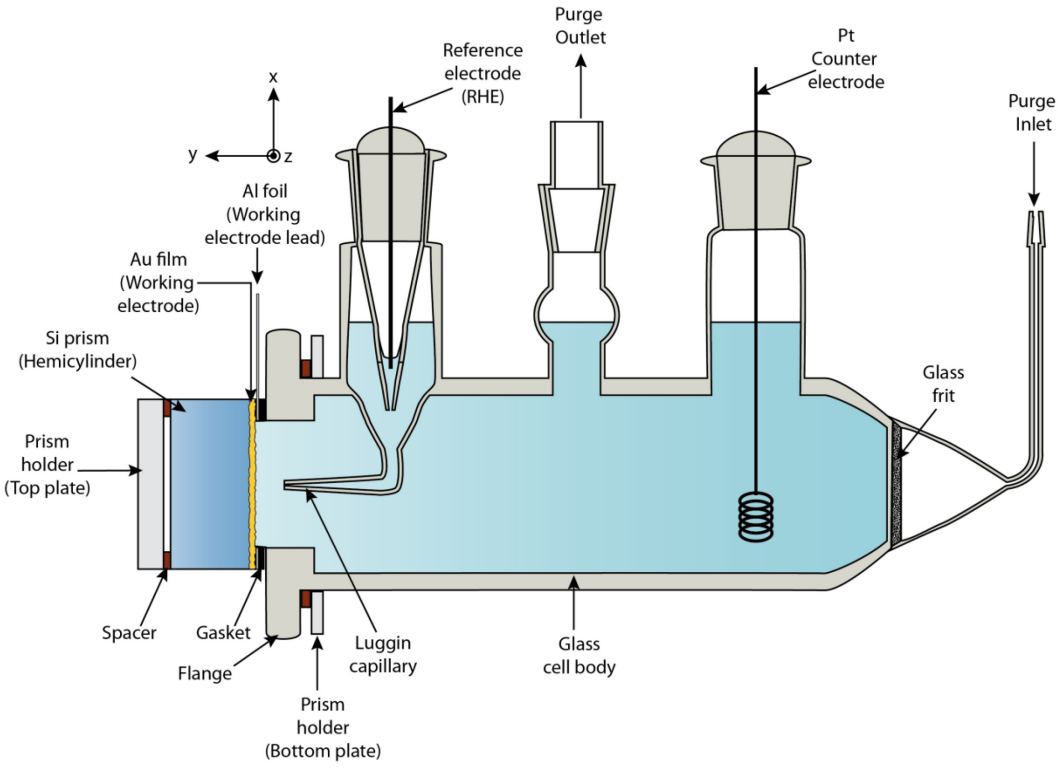

Figure 6.13: Cross-sectional view of the ATR-SEIRA glass cell. The thickness of the Au thin film is greatly exaggerated for schematic purposes.

(ii) ATR Flow Cell

As an extension of the ATR-SEIRA experimental scheme shown before, a flow cell was also designed and fabricated. A flow cell is useful for studying electrochemical reactions under dynamic mass transport conditions. A schematic of the cell is shown in Figure 6.14. The construction of the flow cell is essentially the same as that of the dual thin layer DEMS flow cell that was described in section 2.1.2.b. The cell body and the inlet and the outlet port T-pieces were made of KEL-F. As shown in Figure 6.14, due to the similar construction as the DEMS cell, the bottom chamber of the cell can be used for DEMS if so desired. The upper chamber is

employed for in situ FTIR as per the ATR-SEIRA scheme. A similar approach has been reported previously in the literature.[14] The two chambers are connected by a series of capillaries just as in the dual thin layer cell. Si prism/metal film working electrode is held firmly against the top face of the cell using a machined Al piece (Part 10) that is screwed into the main cell body. A circular area of the metal film (working electrode) about ~12 mm in diameter is exposed to the solution. The plane of incidence of the beam is along the y-z plane as per Figure 6.14.

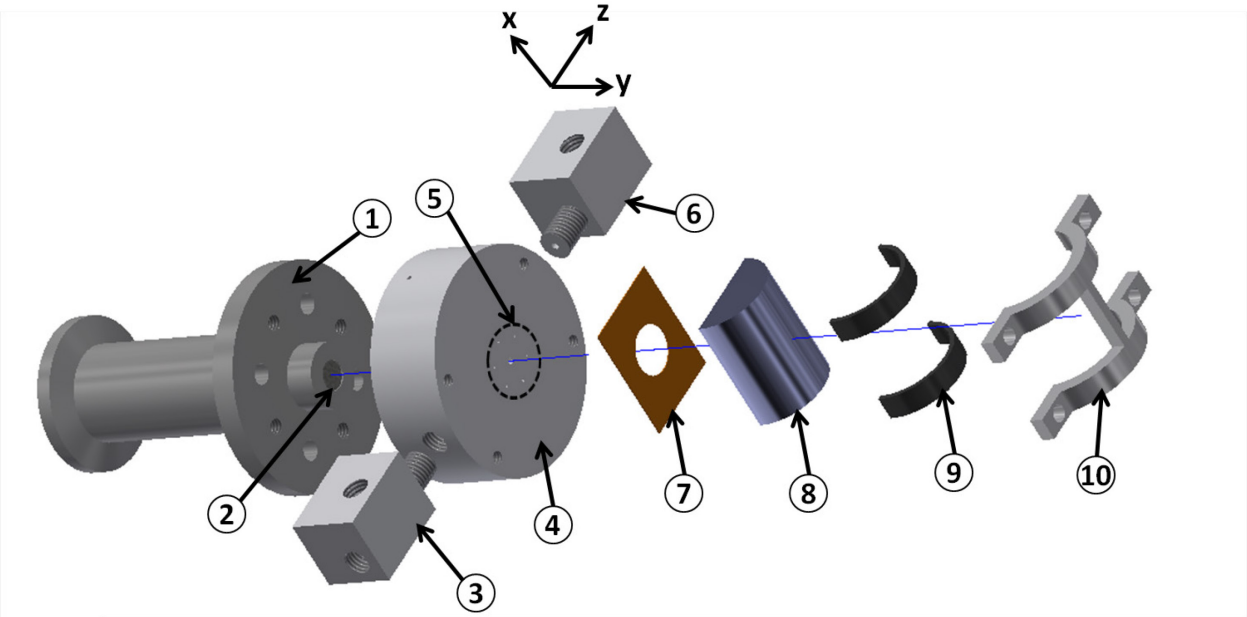

Figure 6.14: Exploded view of the ATR flow cell. 1- Stainless steel support with vacuum flange, 2- Steel frit, 3- Inlet port T-piece, 4- Main cell body, 5- set of 6 capillaries, 6- Outlet port T-piece, 7- Silicone Gasket, 8 – Si prism, 9 – Spacer, 10- Prism holder.

(c) Instrumentation

The Varian FTIR 670 system used for the PM-IRRAS testing was also used for the ATR-SEIRA experiment. Unlike PM-IRRAS, the experiment was conducted in the sample chamber of the spectrometer than on the external optical bench. In the sample chamber, a series of guiding mirrors were used to direct the incoming beam from the optics chamber of the spectrometer onto the Si prism and the outgoing beam from the prism into the detector chamber. An MCT detector

was used. The spectra were recorded by Resolutions Pro (Varian) software and are reported as potential difference absorbance spectra; same as that of IRRAS. The instrumentation for the electrochemistry segment of the experiment was same as that for IRRAS experiments (section 6.2.3).

(d) Preliminary Testing

In order to verify the operation of the ATR-SEIRA setup, an initial set of in situ electrochemical experiments were carried out using the ATR glass cell described above. The potential-dependent adsorption of HSO_4^-/SO_4^{2-} and rearrangement of interfacial water at the Au metal film electrode was monitored using the ATR-SEIRA setup. The angle of incidence of the IR beam was set to 60 °. The potential difference absorbance spectra obtained are shown in Figure 6.15. The band at ~ 1120 cm^{-1} is assigned to the stretching mode of the S-O bond (ν_{S-O}) in HSO_4^-.[1] Clearly, the increase of the bisulfate band with the increase in potential is due to the adsorption of HSO_4^- at the positively charged electrode. The broad band in the range 3600-3000 cm^{-1} is due to the O-H stretching mode (ν_{O-H}) of H_2O. The bending mode of H_2O (δ_{H-O-H}) appears at ~ 1620 cm^{-1}. The origin of the sharp negative-going peak at 2900 cm^{-1} was not immediately apparent. Due to the sharpness of the peak, it is most likely not due to H_2O. The same feature has been observed previously in other studies and has been attributed to the stretching of C-H bond (ν_{C-H}) in hydrocarbon contaminants.[13,15]

Simultaneous with the growth of the bisulfate band ~ 1120 cm^{-1}, the H_2O bands also undergo significant change. With the increase in potential, δ_{H-O-H} band grows in the negative direction. This is most likely due to the displacement of the interfacial water by the adsorption of HSO_4^-/SO_4^{2-}. Note that the band at ~ 1120 cm^{-1} has been assigned to HSO_4^- based on the argument that at low pH conditions (nominal pH=1) of the experiment HSO_4^- should be the

dominant species.[1] With increase in potential, the broad ν_{O-H} band increases and resolves into two peaks (~ 3495 cm^{-1} and ~ 3000 cm^{-1}). The reason for the latter phenomenon is unclear. However, the significant increase in the integrated band intensity with potential has been attributed to the potential-dependent reorientation of the water dipoles.[13,15] At low potentials, the water dipole is thought to be oriented more or less parallel to the surface resulting in a comparatively weak ν_{O-H} band. At high potentials, it is postulated that the water dipole tend to orient normal to the surface and thus, a stronger band is seen.

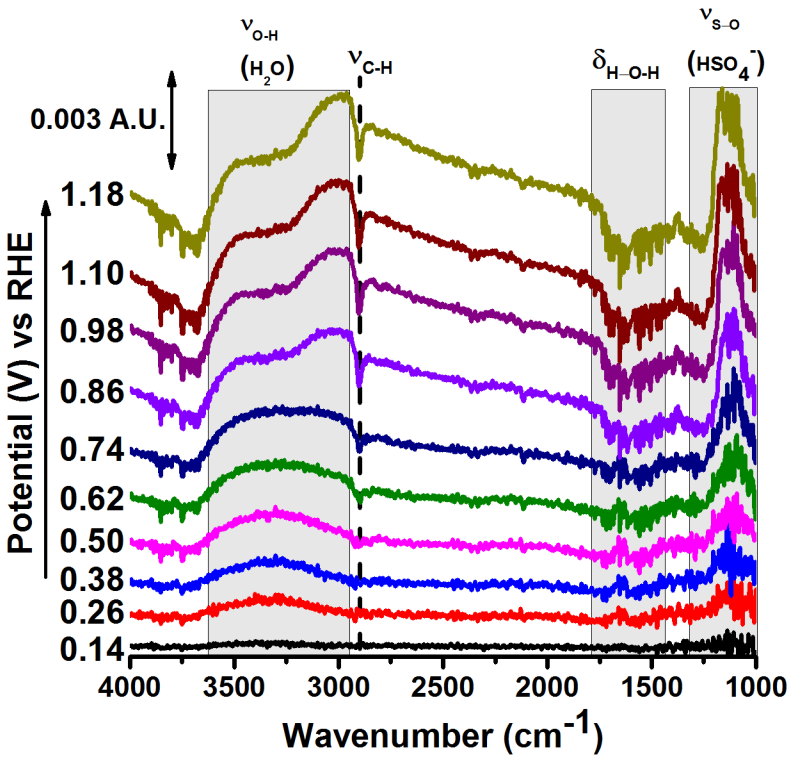

Figure 6.15: SEIRA spectra of 0.1 M H_2SO_4 at Au film electrode during a positive-going scan at 5 mV/s. Reference spectrum taken at 0.11 V vs RHE.

6.5 Summary and Outlook

In this chapter, the traditional IRRAS method used in our laboratory was introduced first. The IRRAS technique can be extended to achieve potentially higher surface sensitivity by introducing polarization modulation as realized in PM-IRRAS. The development and the

implementation of this technique using the recently acquired Varian FTIR 670 system were described in this chapter. The experimental setup for the highly surface sensitive ATR-SEIRA technique was also successfully deployed adding to the advanced characterization capabilities in our laboratory. Preliminary experiments carried out on both the PM-IRRAS and the ATR-SEIRA experimental setups verified their operation.

Further ground work need to be carried out in the future to fully optimize the systems. For the PM-IRRAS setup, additional calibration procedures need to be made part of the experimental protocol to obtain the full benefit of the technique.[9] The ATR-SEIRA setup was tested using the Au metal film electrode on Si prism. However, it would be extremely beneficial to apply the ATR-SEIRA technique to the study of other electrocatalyst materials. A future direction that needs to be pursued is to augment the sputtering deposition method of electrode fabrication with other metal deposition techniques such as electroless plating[16] and electrochemical deposition.[17] Looking forward, the application of these surface sensitive techniques to problems in different areas of electrochemical research pursued in our laboratory would be extremely useful.

6.6 References

(1) Iwasita, T.; Nart, F. C. *Progress in Surface Science* **1997**, *55*, 271–340.

(2) Beden, B.; Bewick, A.; Lamy, C. *Journal of Electroanalytical Chemistry and Interfacial Electrochemistry* **1983**, *148*, 147–160.

(3) Beden, B.; Lamy, C.; Bewick, A.; Kunimatsu, K. *Journal of Electroanalytical Chemistry and Interfacial Electrochemistry* **1981**, *121*, 343–347.

(4) Perez, J. M.; Beden, B.; Hahn, F.; Aldaz, A.; Lamy, C. *Journal of Electroanalytical Chemistry and Interfacial Electrochemistry* **1989**, *262*, 251–261.

(5) Leung, L.-W. H.; Chang, S.-C.; Weaver, M. J. *Journal of Electroanalytical Chemistry and Interfacial Electrochemistry* **1989**, *266*, 317–336.

(6) Tolstoy, V. P.; Chernyshova, I. V.; Skryshevsky, V. A. *Handbook of Infrared Spectroscopy of Ultrathin Films*; John Wiley & Sons, Inc.: Hoboken, NJ, USA, 2003.

(7) *Advances in Electrochemical Science and Engineering*; Alkire, R. C.; Kolb, D. M.; Lipkowski, J.; Ross, P. N., Eds.; Wiley-VCH Verlag GmbH: Weinheim, Germany, 2006; Vol. 9.

(8) Foley, J. K.; Korzeniewski, C.; Daschbach, J. L.; Pons, S. In *Electroanalytical Chemistry: A series of advances, vol. 14*; Bard, A. J., Ed.; Marcel Dekker Incorporated, 1986; pp. 309–433.

(9) Zamlynny, V.; Lipkowski, J. In *Advances in Electrochemical Science and Engineering*; Wiley-VCH Verlag GmbH, 2008; pp. 315–376.

(10) Hipps, K. W.; Crosby, G. A. *The Journal of Physical Chemistry* **1979**, *83*, 555–562.

(11) Osawa, M. In *Advances in Electrochemical Science and Engineering*; Wiley-VCH Verlag GmbH, 2008; pp. 269–314.

(12) Chen, Y. X.; Heinen, M.; Jusys, Z.; Behm, R. J. *Angewandte Chemie (International ed. in English)* **2006**, *45*, 981–5.

(13) Ataka, K.; Yotsuyanagi, T.; Osawa, M. *The Journal of Physical Chemistry* **1996**, *100*, 10664–10672.

(14) Heinen, M.; Chen, Y. X.; Jusys, Z.; Behm, R. J. *Electrochimica Acta* **2007**, *52*, 5634–5643.

(15) Ataka, K.; Osawa, M. *Langmuir* **1998**, *14*, 951–959.

(16) Miki, A.; Ye, S.; Osawa, M. *Chemical Communications* **2002**, 1500–1501.

(17) Yan, Y.-G.; Li, Q.-X.; Huo, S.-J.; Ma, M.; Cai, W.-B.; Osawa, M. *The Journal of Physical Chemistry B* **2005**, *109*, 7900–6.

CHAPTER 7
HYDROGEN OXIDATION ON PtPb INTERMETALLIC IN ACIDIC MEDIUM

7.1 Introduction

Alloys and ordered intermetallics are two classes of materials extensively researched as prospective electrocatalysts that can functionally replace the precious metal catalysts in fuel cells. Intermetallic materials are especially attractive as they can potentially address some of the shortcomings of alloys. In an alloy, the atomic positions are randomly occupied by the constituent elements in the unit cell whereas in ordered intermetallics the atomic positions in the unit cell are uniquely occupied by the constituent elements. Hence, due to the ordered structure of the latter, a stable, pristine intermetallic will be expected to have on the surface a distribution of identical catalytic sites, unlike alloys. Additionally, intermetallics generally have high enthalpies of formation which endow potentially better material stability in contact with aqueous solutions vis-à-vis alloys.

In particular, the PtPb intermetallic has been found to be especially promising as an anode electrocatalyst for direct fuel cells due to its high catalytic activity for HCOOH and CH_3OH oxidation.[1–3] Importantly, the fuel oxidation reactions have been shown to proceed on PtPb surfaces without the formation of CO_{ads} which will deactivate a pure Pt catalyst.[3] Given its promising performance, the catalytic activity of PtPb for the archetype anode reaction – hydrogen oxidation reaction (HOR) – was studied using RDE voltammetry. The CO tolerance of the catalyst was also investigated by conducting the RDE studies of the oxidation of H_2 in the presence of CO. For the sake of comparison, similar studies were conducted on bulk Pt electrodes.

7.2 Experimental

7.2.1 Chemicals

Supporting electrolyte solutions were made from high purity sulfuric acid (99.999% Sigma Aldrich) and perchloric acid (70% redistilled Sigma Aldrich) in ultrapure de-ionized (DI) water (Millipore Milli-Q, 18 MΩ cm). High purity H_2, H_2 (2% CO), Ar and N_2 gases were obtained from Airgas.

7.2.2 Electrode Preparation

The Pt and PtPb RDEs were fabricated as described previously.[4] Cylindrical slugs of polycrystalline Pt or PtPb (3, 5 or 7 mm in diameter) were inserted into Teflon rods appropriately drilled in the center to house the slugs. The Teflon rods were heated to ~ 350 °C prior to insertion of the slug to ensure a tight seal. For electrical contact, the inside of the hollow Teflon rod was filled with graphite felt and the end sealed with a stainless steel piece. The stainless steel piece was machined such that it could be mounted on the shaft of the rotator unit. The RDEs were polished to a mirror finish using diamond paste (METADI-Buehler, 1 μm). The electrodes were subsequently rinsed with and sonicated in DI water to remove any residues. Finally, the electrodes were subjected to electrochemical cleaning by potential cycling in the range 0.05-1.4 V (vs RHE) for Pt and 0.05-0.8 V (vs RHE) for PtPb electrodes at 50 or 100 mV/s in the supporting electrolyte (0.1 M H_2SO_4). In particular, the choice of the upper limit of cycling for PtPb electrodes was guided by previous experimental work which indicated bulk PtPb to be stable up to ~ 0.8 V (vs Ag/AgCl) in 0.1 M H_2SO_4.[3,5]

7.2.3 Electrochemical Measurements

The RDE voltammetric studies were carried out in a typical RDE setup (Pine Model AFMSRX). The measurements were performed in a standard three-electrode configuration with a reversible hydrogen electrode (RHE) as the reference and a large area Pt wire as the counter electrode. A custom made three-chambered RDE glass cell with the chambers separated by porous glass frits to minimize interference from the counter and the working electrodes was used. A combination of an EG&GModel 173 potentiostat/galvanostat and a Model 175 universal or a Pine AFCBP1 Bipotentiostat was employed for the measurements. The analog signals from the potentiostat were converted by a NI-DAQ card and subsequently recorded by a home-made LabWindows program (CV-EI400). For the H_2 oxidation RDE experiments, the solutions were aerated for at least 30 mins with either H_2 or H_2 (2% CO) as desired. During the experiment, the headspace above the solution in the cell was kept purged with the corresponding gases to ensure a saturation concentration of H_2 in the solution. The potentials are referenced to RHE and the current densities are reported based on the geometric area of the electrodes.

7.3 Results and Discussion

7.3.1 Cyclic Voltammogram of PtPb in 0.1 M H_2SO_4

Representative CVs of PtPb and Pt polycrystalline electrodes are shown in Figure 7.1. Typical surface features associated with H-adsorption/desorption and Pt-oxide formation/reduction are clearly visible in the CV of Pt. However, in the case of PtPb, there are no discernible surface voltammetric features in the potential range examined. Moreover, it is apparent that, for the same geometric area, PtPb electrode exhibit significantly higher double layer capacitance compared to Pt. This effect was consistently observed during the studies (also

in previous studies[3]) and is clearly due to the higher electrochemically active surface area (ECSA) of PtPb vis-à-vis Pt electrode. This is despite the visually comparable mirror finishes achieved for both electrodes. The roughness of the PtPb electrode could be intrinsic to the sample or induced by the small amount of leaching and re-deposition of Pb occurring during the electrochemical cleaning procedure, in spite of the restricted potential range of cycling.[5]

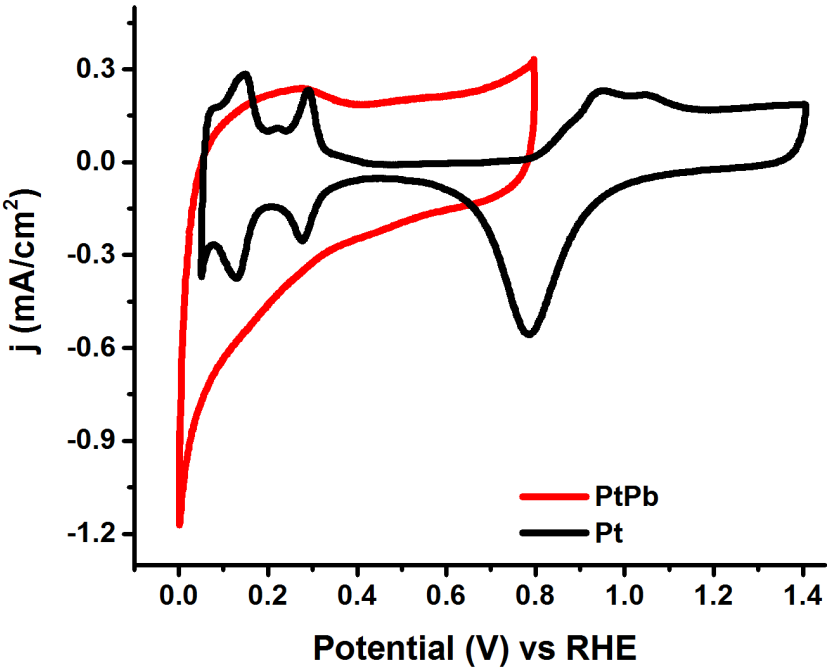

Figure 7.1: CVs of Pt and PtPb electrodes in 0.1 M H_2SO_4. Scan rate: 10 mV/s.

On a related note, based on the initial few experiments carried out on PtPb electrode in 0.2 M $HClO_4$, the use of perchloric acid solutions as supporting electrolyte is advised against. It was noticed that the double layer capacitance of the PtPb electrode increased dramatically after cycling in 0.2 M $HClO_4$ on comparing the CVs of PtPb in 0.1 M H_2SO_4 before and after the experiment. Evidently, cycling in perchloric acid solution induced surface roughening of the electrode. It is known from previous XPS studies of PtPb in H_2SO_4 solutions that the surface of PtPb electrode is far from being phase pure.[5] It was determined that the top layer (about 2-3 nm) of PtPb is a mixture of Pt and Pb salts ($PbCO_3$ and $PbSO_4$). In light of this knowledge, it is easy

to understand the surface roughening of the electrode in $HClO_4$ solutions. It is inferred that, due to the substantially higher solubility of $PbClO_4$ compared to either $PbSO_4$ (~ 5 orders of magnitude larger) or $PbCO_3$ (~ 6 orders of magnitude larger),[6] the exposed surface of the PtPb electrode is not stable in $HClO_4$ solutions and the Pb salts are leached out from the top layer into the solution causing the surface roughening.

7.3.2 Hydrogen Oxidation Reaction

The results of the RDE studies of HOR on Pt and PtPb bulk electrodes are shown in Figure 7.2. The facile kinetics of hydrogen oxidation on Pt is apparent from the polarization curves at different rotation rates (Figure 7.2a). The mass transport limited currents are reached at $\eta \leq 50$ mV where η is the overpotential. In contrast, HOR on PtPb is kinetically hindered. A significantly higher overpotential ($\eta \geq 350$ mV) is needed to drive the HOR at mass transport limited rates (Figure 7.2b). Levich and Koutecký-Levich (K-L) plots (Figure 7.2c and Figure 7.2d) were employed to further investigate the kinetic limitation for HOR on PtPb. The Levich plot (***j*** vs $\boldsymbol{\omega^{1/2}}$ where j is the current density and $\boldsymbol{\omega}$ is the rotation rate of the electrode) for Pt in the mass transport limited region (0.5 V vs RHE) shows the linear relationship between ***j*** and $\boldsymbol{\omega^{1/2}}$ as expected from the Levich equation (Equation 7.1).[7]

Equation 7.1: $$j_l = (0.62nFD^{2/3}\nu^{-1/6}C^*)\omega^{1/2}$$

where $\boldsymbol{j_l}$ is the mass-transport limited current density, ***n*** is the number of electrons transferred in the electrode reaction (***n*** = 2 for HOR), ***F*** is Faraday's constant, ***D*** is the diffusion coefficient of the electroactive species in solution, $\boldsymbol{\omega}$ is the rotation rate of the electrode, ***v*** is the kinematic viscosity of the solution and ***C**** is the concentration of the electroactive species in the solution.

Based on the literature data,[6] at 25 °C, $\boldsymbol{D}$ = 5.11 x 10^{-5} cm^2/s for H_2 in water, $\boldsymbol{\nu}$ = 8.9 x 10^{-3} cm^2/s for water and $\boldsymbol{C^*}$ = 8.08 x 10^{-4} M for H_2 at saturation concentration in water.

Satisfactorily, the PtPb electrode also show linear behavior in the mass transport limited region (0.5 V vs RHE) and the Levich plots for PtPb and Pt are more or less coincident as expected. When currents are sampled in the kinetically-limited region of the polarization curve on PtPb, Levich analysis clearly shows the deviation from the linear behavior at high rotation rates.

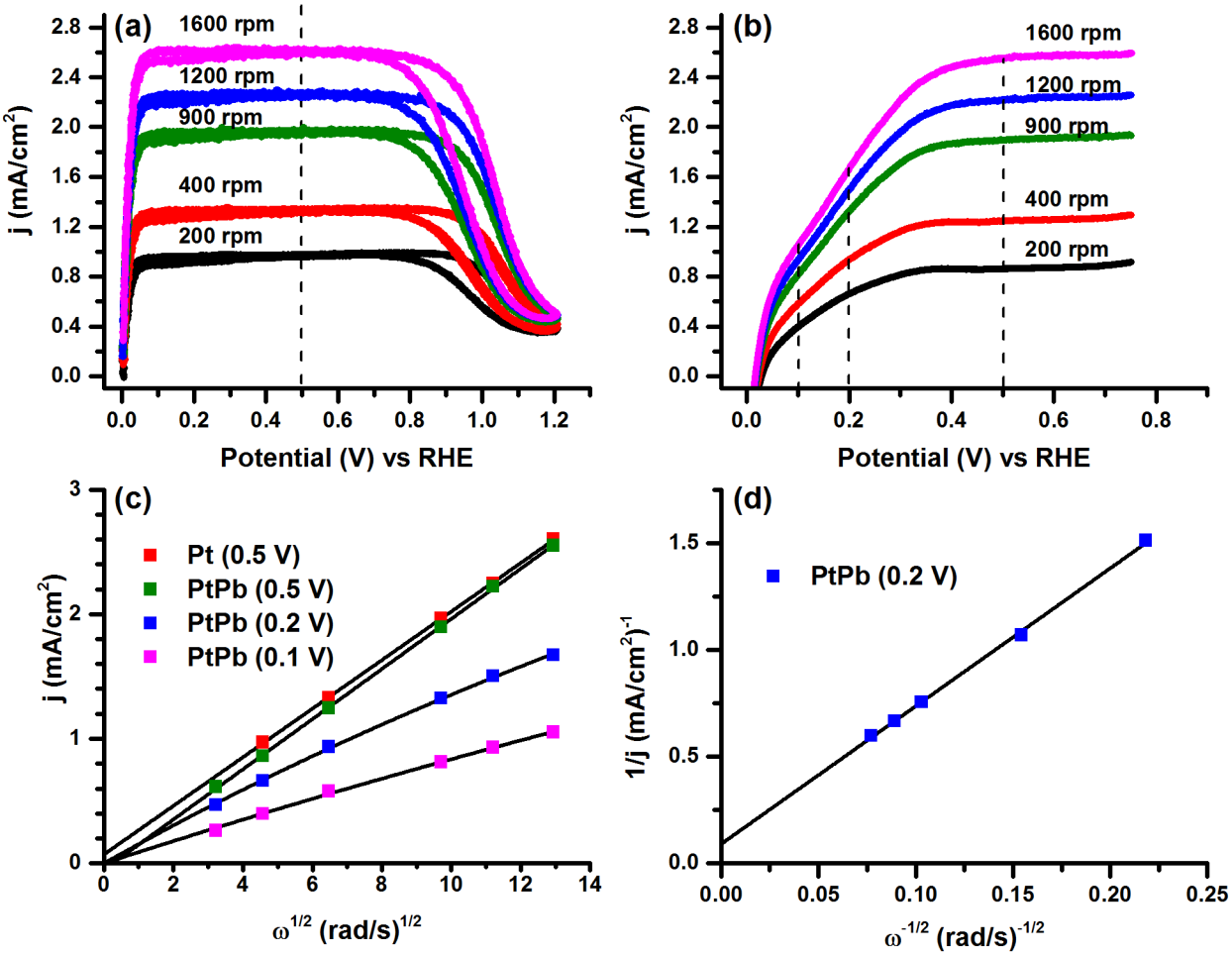

Figure 7.2: Family of HOR polarization curves in 0.1 M H_2SO_4 saturated with H_2 at different rotation rates on (a) Pt bulk electrode (b) PtPb buk electrode. Scan rate: 10 mV/s. (c) Levich and (d) Koutecký-Levich plots based on (a) and (b). Potentials at which the currents are sampled for (c) and (d) are marked by broken lines in (a) and (b). In (b), for the sake of clarity, the positive and the negative-going scans are averaged to eliminate the double layer charging current.

If the electrode reaction is assumed to be limited only by either the kinetics or the mass transport in solution, then the current ***j*** can be expressed by the Koutecký-Levich (K-L) equation[7] (Equation 7.2) as shown below.

Equation 7.2:
$$\frac{1}{j} = \frac{1}{j_k(E)} + \frac{1}{j_l(\omega)}$$

where j_k is the kinetic current independent of ω and j_l is the mass-transport limited current as previously defined (Equation 7.1). For the sake of clarity, the functional dependence of j_k on the potential E and j_l on the rotation rate ω is explicitly shown in Equation 7.2. Based on the K-L equation, it is straightforward to see that a plot of **1/j** vs 1/ $\omega^{1/2}$ (K-L plot) will be a straight line even in the kinetically limited region. K-L plots in the kinetically-limited region result in a non-zero y-intercept (=$1/j_k$) that depends on the potential E. If an analytical expression is available for j_k, then the K-L plots can be used to obtain kinetic parameters.[7] Examining the K-L plot for PtPb electrode in the kinetically limited region (Figure 7.2d), it is seen that the linear relationship between $1/j$ and $1/\omega^{1/2}$ is preserved for HOR and that a non-zero y-intercept is obtained. Further experiments need to be carried out to understand the reason for the kinetic limitation of HOR and appropriate models developed before kinetic parameters can be derived from the current RDE studies.

7.3.3 Hydrogen Oxidation Reaction in Presence of CO

The tolerance of PtPb catalyst to CO poisoning during H_2 oxidation was tested by conducting polarization measurements in a supporting electrolyte solution (0.1 M H_2SO_4) aerated with H_2 (2 % CO). From the window opening CVs shown in Figure 7.3, it is seen that up to ~ 0.8 V vs RHE, PtPb does not show any activity either for hydrogen or CO oxidation. Apparently, CO present in the solution completely deactivates PtPb. This is also amply evident on comparing

the window opening CVs in the presence of CO in solution to that in the CO-free H_2 saturated solution (black curve in Figure 7.3). Beyond ~ 0.8 V vs RHE, an oxidation wave is observed that is attributed to the oxidation of H_2 on PtPb. It is likely that the onset of this oxidation wave coincides with the onset of the oxidative removal of CO_{ads} from PtPb at high potentials. The removal of CO_{ads} will result in the reactivation of HOR at the free sites on PtPb. Lack of immunity of PtPb to poisoning by free CO present in solution has been previously documented [8] and is possibly due to the adsorption of CO at the free Pt sites in the surface layer of the PtPb electrode.[5] In fact, if the onset of the oxidation wave in Figure 7.3 is assumed to be the onset of CO_{ads} oxidation (~ 0.8 V vs RHE) on PtPb, then the oxidative removal of CO_{ads} is initiated on PtPb and Pt at around the same potential.

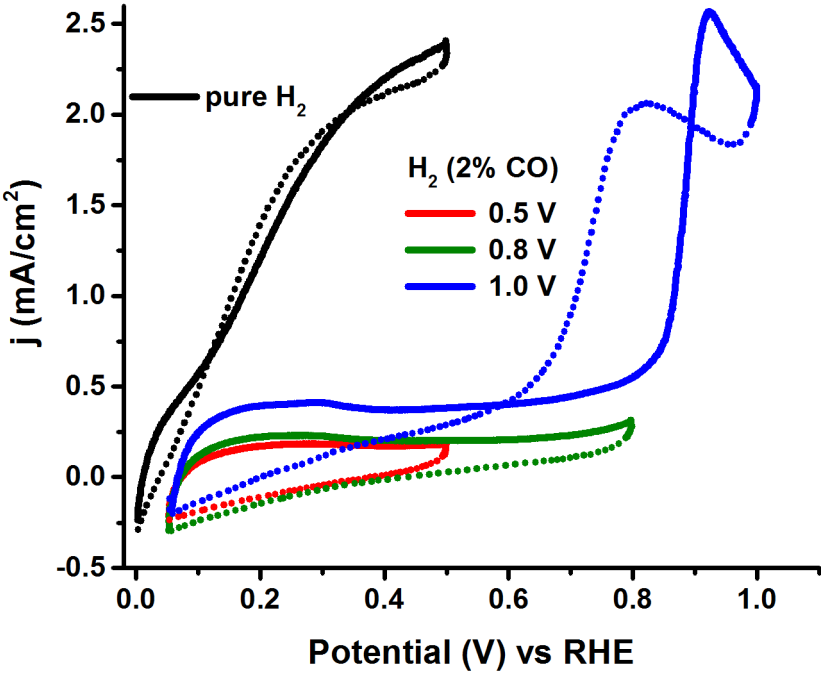

Figure 7.3: Polarization curves for HOR in the presence of CO on PtPb bulk electrode in 0.1 M H_2SO_4 solution saturated with H_2 (2 % CO). Scan rate: 10 mV/s. Electrode rotation rate: 1600 rpm. Polarization curve for HOR in the absence of CO on PtPb bulk electrode also shown (black) for reference. Solid lines and broken lines represent positive and negative-going scans, respectively.

7.4 Conclusions

The RDE studies conducted on the PtPb bulk electrode showed the hydrogen oxidation reaction to be kinetically hindered. The presence of CO completely poisons the PtPb electrode for the hydrogen oxidation reaction. In this respect, it is worthwhile to discuss the subtle point of CO tolerance of an electrocatalyst using the example of PtPb. The reported immunity of PtPb to CO poisoning during the oxidation of HCOOH or CH_3OH is due to the reaction proceeding through a non-CO_{ads} pathway on PtPb. In other words, the tolerance of PtPb to CO poisoning is pre-emptive in nature in that it acts to prevent the formation of CO in the first place. Based on the current study, it seems that free CO in solution will bind strongly to the catalyst surface and deactivate it. In this respect, PtPb can be seen as not strictly CO-tolerant. The results from the current study also validate the early indications from DFT studies of CO adsorption on PtPb where it was found that CO adsorbs on the Pt-terminated PtPb(001) plane even more strongly than on Pt(111).[9,10]

7.5 References

(1) Casado-Rivera, E.; Volpe, D. J.; Alden, L.; Lind, C.; Downie, C.; Vázquez-Alvarez, T.; Angelo, A. C. D.; DiSalvo, F. J.; Abruña, H. D. *Journal of the American Chemical Society* **2004**, *126*, 4043–9.

(2) Matsumoto, F.; Roychowdhury, C.; DiSalvo, F. J.; Abruña, H. D. *Journal of The Electrochemical Society* **2008**, *155*, B148.

(3) Wang, H.; Alden, L.; Disalvo, F. J.; Abruña, H. D. *Physical chemistry chemical physics : PCCP* **2008**, *10*, 3739–51.

(4) Casado-Rivera, E.; Gál, Z.; Angelo, A. C. D.; Lind, C.; DiSalvo, F. J.; Abruña, H. D. *Chemphyschem : a European journal of chemical physics and physical chemistry* **2003**, *4*, 193–9.

(5) Blasini, D. R.; Rochefort, D.; Fachini, E.; Alden, L. R.; DiSalvo, F. J.; Cabrera, C. R.; Abruña, H. D. *Surface Science* **2006**, *600*, 2670–2680.

(6) Haynes, W. M.; Lide, D. R.; Bruno, T. J. *CRC Handbook of Chemistry and Physics 2012-2013*; CRC Press, 2012.

(7) Bard, A. J.; Faulkner, L. R. In *Electrochemical Methods: Fundamentals and Applications*; Wiley, 2001; pp. 331–367.

(8) De-los-Santos-Álvarez, N.; Alden, L. R.; Rus, E.; Wang, H.; DiSalvo, F. J.; Abruña, H. D. *Journal of Electroanalytical Chemistry* **2009**, *626*, 14–22.

(9) Ranjan, C.; Hoffmann, R.; DiSalvo, F. J.; Abruna, H. D. *Journal of Physical Chemistry C* **2007**, *111*, 17357–17369.

(10) Wang, L.-L.; Johnson, D. D. *Journal of Physical Chemistry C* **2008**, *112*, 8266–8275.